# Université de Strasbourg

### UNIVERSITÉ DE STRASBOURG



#### ÉCOLE DOCTORALE DES SCIENCES CHIMIQUES

Institut de Chimie et Procédés pour l'Energie, l'Environnement et la Santé ICPES (UMR 7515 CNRS / Univ. Strasbourg)

# THÈSE présentée par :

Qingyang XI

soutenue le : 17 octobre 2023

pour obtenir le grade de : Docteur de l'université de Strasbourg

Discipline/ Spécialité: Chimie Physique / Chimie du Solide

## TiO<sub>2</sub> co-dopé avec des métaux de transition et de l'azote pour la photocatalyse à large spectre activé par la lumière solaire

Transition metal and nitrogen co-doped TiO<sub>2</sub> for broad spectrum solar light activation photocatalysis

THÈSE dirigée par :

Mr COTTINEAU Thomas Chargé de Recherche, HDR, CNRS, (ICPEES, Strasbourg)

**RAPPORTEURS:** 

**EXAMINATEURS:** 

Mme DELVILLE Marie Hélène Directrice de Recherche, HDR, CNRS (ICMCB, Bordeaux)
M. BONNET Pierre Directrice de Recherche, HDR, CNRS (ICMCB, Bordeaux)
Maitre de conférences, HDR, Univ. Clermont Ferrand

Mme LEBEAU Bénédicte

Directrice de Recherche, HDR, CNRS, (IS2M, Mulhouse)

## Acknowledgments

This thesis was performed under the supervision of Dr. Valérie Keller and Dr. Thomas Cottineau at Institute of Chemistry and and Process for Energy, Environment and Health (ICPEES), UMR-7515, CNRS. First of all, I would like to sincerely thank my supervisors. I would like to thank Dr. Valérie Keller for providing me with an opportunity to work in your laboratory and complete my Ph.D. Thank you for your warm welcome and the overall design of my PhD thesis project. I appreciate your guidance and support throughout all stages of my research. Great appreciation for Dr. Thomas Cottineau, for your guidance through my PhD journey. I am impressed by your profound knowledge and passionate attitude toward science. Thanks for your patience, explanation, and encouragement. There is no doubt that the numerous discussions with you have helped me to develop both research skills and critical thinking.

The China Scholarship Council (CSC) is greatly acknowledged for this PhD project, which not only provided me the financial support for my work but also gave me a chance to experience different cultures and lives in France.

Sincere thanks would be given to my jury members: Dr. Marie Hélène Delville, Dr. Pierre Bonnet and Dr. Bénédicte Lebeau. Their feedback and suggestions have significantly improved the quality of this work. The interesting discussion during my defense has helped me have a better understanding of this scientific project.

I am grateful for all the people who have contributed to the progress of this work: Thierry Dintzer for the SEM images, Driss Ihiawakrim for the TEM images, Vasiliki Papaefthimiou for the XPS analysis, Marc Lenertz for the in-situ XRD measurements and Rietveld refinement, Fabrice Vigneron for the BET tests, and Christophe Mélart for the TGA analysis. Special thanks would be given to Dr. Bunsho Ohtani and Dr. Mai Takashima for their important contribution to the RDB-PAS measurements, and to Dr. Nolwenn Le Breton and Dr. Bertrand Vileno for their support of EPR measurements. I am also thankful to the technicians: Alain Rach, Sécou Sall and Michel Wolf, for their kind help in solving any technical problem.

I would like to thank other lab members. The communication with Dr. Nicolas Keller and Dr. Valérie Caps at group meetings provided critical advice for this work. Great appreciation to my office colleagues: Leila Hammoud, Javier Iváñez, Laura Ávila, Poonam Chaturvedi, Laura Claro, Maria Anagnostopoulou, Eliane Khoury, Olivier Smith, Hamza El Marouazi, Jean-Philippe Brach, Charlotte Jonis, Marie Duflot, Justine Quinet, Maël Morguen, Caroline Mary, Clément Marchal, Nina Rouviere, Steven Bardy, Florian Gelb, Marvin Motay, Thomas Favet and Fany Ouali. I will always remember the enjoyable moments that we shared and wish you all the best in your future lives and careers.

I would also like to thank my former supervisors in Nanjing University of Aeronautics and Astronautics: Dr. Jinsong Liu and Dr. Ziquan Li, with whom I started my research for the first time and entered the field of catalysis.

In the end, I would like to express my gratitude to my family for their constant support and forever love.

# Table of contents

Résumé	i
List of Abbreviations	xxi
General introduction	1
Chapter-1: Bibliography and context	7
1. General context	9
1.1 Global demand for energy transition	9
1.2 Solar energy	10
2. Solar energy conversion via photocatalysis	11
2.1 Principle of photocatalysis	11
2.2 Photocatalytic degradation of pollutants	12
2.3 Photocatalytic water splitting	
2.4 Fundamental requirements for photocatalysts	14
2.4.1 Absorption of sunlight	14
2.4.2 Band position	15
2.4.3 Charge separation and transfer	16
2.4.4 Stability and cost	17
3. TiO <sub>2</sub> as photocatalyst	17
3.1 Crystal structure	17
3.2 Electronic band structure:	19
4. Band engineering of TiO <sub>2</sub> by doping	19
4.1 Cation-doping	20
4.2 Anion-doping	22
4.3 Cation-anion co-doping	23
4.3.1 Theoretical study	24
4.3.2 Experimental study	28
5. Outline and scope of this thesis	35
6. References	37

1	. Introduction	5
2	. Material preparation	5
	2.1 Synthesis of TiO <sub>2</sub> and Nb-doped sample	5
	2.1.1 Sol-gel synthesis procedure	5
	2.1.2 Determination of annealing conditions	5
	2.2 Synthesis of N-doped and (Nb,N) co-doped samples	5
3	. Material characterization	5
	3.1 Crystal structure analyzed by XRD	5
	3.2 Study of the morphology	5
	3.2.1 SEM and TEM	5
	3.2.2 Specific surface area	5
	3.3 UV-vis spectroscopy	6
	3.4 X-ray photoelectron spectroscopy	6
	3.5 Electron paramagnetic resonance spectroscopy	6
	3.6 Discussion on the charge compensation mechanism	6
	3.7 Reversed double-beam photoacoustic spectroscopy	6
	3.7.1 Experimental setup	6
	3.7.2 Result and discussion	6
	3.7.3 Proposed electronic band structure	7
	3.8 X-ray absorption and emission spectroscopy with synchrotron irradiate	ion7
•••	3.8.1 Principle of X-ray Absorption and Emission Spectroscopy (XAS	
	3.8.2 Experimental parameters	7
	3.8.3 Experimental results	7
	3.8.4 Conclusion on synchrotron measurement.	7
4	. Photocatalytic activity for methylene blue degradation	7
	4.1 Experimental conditions.	7
	4.2 Photocatalytic activity measurements	7
	4.2.1 Control experiments	7
	4.2.2 Result discussion	8
5	. Conclusion	(

6. R	eferences	85
Chapter- 3	: Characterizations of M-doped TiO2 and (M,N) co-doped	ł TiO <sub>2</sub> (M
-	y) materials	,
1. In	ntroduction	92
2. M	laterial preparation	93
2.	1 Preparation of M-doped TiO <sub>2</sub> materials	93
	2.1.1 Sol-gel synthesis	93
	2.1.2 Determination of calcination condition	94
2.	2 Preparation of co-doped TiO <sub>2</sub> materials	95
3. M	Saterial characterization	95
3.	1 Characterization of M-doped TiO <sub>2</sub>	95
	3.1.1 XRD analysis	95
	3.1.2 in-situ temperature-dependent XRD analysis	97
	3.1.3 Morphology study:	102
	3.1.4 Optical property	103
	3.1.5 Surface chemical composition by XPS	104
	3.1.6 Identification of defects in M-doped samples by EPR	106
3.	2 Conclusion on the M-doped TiO <sub>2</sub>	107
3.	3 Characterizations of the (M,N) co-doped samples	108
	3.3.1 Crystal structure by XRD	108
	3.3.2 Morphology study	110
	3.3.3 Optical properties	111
	3.3.4 Surface chemical composition by XPS	116
	$3.3.5$ Defects identification in the (M,N) co-doped $TiO_2$ samples	119
3.	4 Conclusion on the (M,N) co-doped samples	121
4. Ir	n-situ characterization of UV-visible properties during the thermal	
4.	1 Experimental section	122
	4.1.1 Apparatus	122
	4.1.2 Calibration of temperature	123
	4.1.3 Data treatment	124
4.	2 Results and discussion	124
	4.2.1 Cleaning pre-treatment	124

4.2.2 In-situ observation of nitridation process	126
4.2.3 In-situ observation of the oxidation process	131
4.3 Conclusion on the in-situ UV-visible.	133
5. Conclusion	134
6. References	136
r- 4 : Photocatalytic performance of M-doped TiO2 and (M,N) I=Nb, Ta or W) materials	_
1. Introduction	144
2. Photocatalytic performance for MB degradation	145
2.1 Experimental part	145
2.2 Photocatalytic activities of M-doped materials	145
2.2.1 Effect of cation doping on the adsorption of MB	145
2.2.2 Photocatalytic degradation of MB under UV irradiation	147
2.3 Photocatalytic activities of (M,N) co-doped TiO <sub>2</sub>	147
2.3.1 Effect of co-doping on the adsorption for MB	147
2.3.2 Photocatalytic degradation of MB under UV irradiation	148
2.3.3 Photocatalytic degradation of MB under visible irradiation	150
2.4 Conclusion on photocatalytic MB degradation	151
3. Photocatalytic hydrogen production	152
3.1 Experimental part	152
3.1.1 Photocatalytic test platform	152
3.1.2 Analysis of products on compact GC	153
3.1.3 Data treatment	154
3.2 Photoreduction vs. chemical reduction for Pt co-catalyst deposition.	155
3.2.1 Context	155
3.2.2 Experimental method for Pt deposition	155
3.2.3 Characterization of the Pt co-catalyst	156
3.2.4 Photocatalytic activity	158
3.3 Effect of M-doping and N-doping on the photocatalytic activities	160
3.3.1 Characterization of the co-catalyst	160
3.3.2 Photocatalytic activities	162
3.4 Effect of (M.N)-co-doping on the photocatalytic activities	163

3.4.1 Characterization of the co-catalyst	163
3.4.2 Photocatalytic activities	165
3.5 Conclusion on photocatalytic hydrogen production	166
4. Photocatalytic performance for water oxidation	167
4.1 Experimental part	167
4.2 Characterization of RuO <sub>x</sub> -deposited TiO <sub>2</sub> materials	167
4.2.1 Elemental analysis	167
4.2.2 TEM characterization	168
4.2.3 XPS analysis	168
4.3 Photocatalytic activities for water oxidation	169
4.4 Conclusion on photocatalytic water oxidation.	170
5. Dual co-catalysts modified TiO <sub>2</sub> material	170
5.1 Context	170
5.2 Experimental part	171
5.2.1 Preparation of dual co-catalyst modified TiO <sub>2</sub>	171
5.2.2 Photocatalytic experiment	171
5.3 Photocatalytic activities of dual co-catalyst deposited TiO <sub>2</sub>	171
6. Conclusion	172
7. References	175
Conclusion and perspectives	179
Annexes	186

#### Résumé

#### 1. Introduction

L'utilisation des combustibles fossiles a apporté des contributions significatives au développement de la société humaine au cours des deux derniers siècles. <sup>1</sup> Cependant, les crises environnementales et climatiques causées par la combustion massive de combustibles fossiles ont commencé à se manifester. Par conséquent, le développement des énergies renouvelables est la résolution fondamentale pour résoudre les crises climatiques et environnementales auxquelles l'humanité est confrontée au 21e siècle. En tant que source d'énergie renouvelable importante, le développement et l'utilisation de l'énergie solaire ont suscité un intérêt généralisé au sein de la communauté scientifique, car elle a un énorme potentiel à exploiter. Théoriquement, l'énergie fournie annuellement par le rayonnement solaire est plus de 1200 fois supérieure à la quantité totale d'énergie demandée par l'humanité.<sup>2</sup> Actuellement, la technologie de conversion de l'énergie solaire la plus largement utilisée est la photovoltaïque, qui la convertit en électricité. Le rendement de conversion photovoltaïque est d'environ ~20% et il peut être limité par les fluctuations du rayonnement solaire et de la météo et de la localisation géographique.<sup>3</sup> Ainsi, pour exploiter pleinement l'énergie solaire, il est essentiel de développer des technologies émergentes pour la collecte, la conversion et le stockage de l'énergie solaire. La photocatalyse est une technique prometteuse pour la conversion de l'énergie solaire, dans laquelle des semi-conducteurs sont utilisés comme catalyseurs et les électrons et trous photogénérés sont utilisés pour favoriser diverses réactions chimiques.<sup>4,5</sup> D'autre part, la photocatalyse est largement utilisée pour la remédiation environnementale grâce au processus d'oxydation photocatalytique avancé, dans lequel divers radicaux actifs dotés d'une forte capacité d'oxydation sont générés pour la dégradation des polluants dans l'eau ou l'air. 6,7

Le TiO<sub>2</sub> est l'un des photocatalyseurs les plus largement utilisés en raison de son abondance, de sa stabilité chimique et de sa disponibilité facile dans la nature. La découverte de la division photocatalytique de l'eau sur une électrode en TiO<sub>2</sub> sous lumière UV a été publiée pour la première fois par Fujishima et Honda,<sup>8</sup> ce qui a inspiré de nombreuses études sur les photocatalyseurs à base de TiO<sub>2</sub>. Cependant, le principal inconvénient du TiO<sub>2</sub> en tant que photocatalyseur est le manque d'absorption visible. En raison de sa large bande interdite (3,2 eV pour l'anatase),<sup>9</sup> seule l'énergie des photons dans la région UV (~5% du spectre solaire) peut être utilisée pour les réactions photocatalytiques.

Au cours des dernières décennies, des efforts ont été consacrés à l'augmentation de la réponse à la lumière visible des photocatalyseurs à base de TiO<sub>2</sub>. L'une des stratégies de modification les plus largement étudiées est le dopage avec d'autres éléments, comprenant le dopage cationique, le dopage anionique et le dopage cation-anion. Le dopage cationique implique le remplacement des ions Ti<sup>4+</sup> dans la structure par des cations étrangers. En raison de la simplicité de la méthode de synthèse et de son faible coût, le dopage avec des métaux de transition est largement étudié. Dans la littérature précédente, une absorption accrue dans le visible a été obtenue en dopant le TiO<sub>2</sub> avec des éléments tels que le V,<sup>10</sup> Co,<sup>11</sup> Fe,<sup>12</sup> Nb,<sup>13</sup> Ta<sup>13</sup>

et W,<sup>14</sup> etc. Le dopage anionique, représenté par le dopage en azote, est considéré comme plus efficace pour améliorer les performances activées par la lumière visible du TiO<sub>2</sub>.<sup>15</sup> Cependant, ces catalyseurs mono-dopés présentent une faiblesse en termes de transport interne inefficace des charges, ce qui peut être attribué aux états N 2p localisés et/ou aux défauts agissant comme des pièges à porteurs. Les chercheurs ont constaté que les matériaux dopés à l'azote de TiO<sub>2</sub> présentant une absorption accrue dans le visible montrent une performance photocatalytique réduite sous irradiation UV.<sup>16–18</sup>

Pour surmonter les inconvénients du mono-dopage, une autre approche consistant à codoper à la fois un cation et un anion dans la structure cristalline du  $TiO_2$  a été développée, dans laquelle  $Ti^{4+}$  et  $O^{2-}$  sont respectivement substitués par le cation et l'anion. Cette stratégie de modification a été proposée par plusieurs calculs ab initio au début des années 2010. Il est démontré qu'en introduisant des quantités stœchiométriques de cation ( $M^{n+}$ ) et d'anion ( $A^{p-}$ ), la structure optoélectronique du  $TiO_2$  peut être profondément modifiée, permettant ainsi d'obtenir des photocatalyseurs  $TiO_2$  sensibles à la lumière visible. De plus, grâce à la compensation de charge entre le cation et l'anion (**l'équation 1**)<sup>20</sup>:

$$Ti_{(1-x)}^{4+}M_x^{(4+n)+}O_{(2-\frac{n}{p}x)}^{2-}A_{\frac{n}{p}x}^{(2+p)-}$$
 (éq. 1.)

Les défauts agissant comme des centres de recombinaison de charge peuvent être limités. Un autre avantage de la co-dopage est qu'il permet d'insérer une plus grande quantité d'espèces dopantes par rapport au mono-dopage. Cela pourrait favoriser une hybridation suffisante entre les niveaux d'énergie des dopants et ceux du TiO<sub>2</sub>, créant un continuum de niveaux d'énergie se chevauchant avec la sommet de la bande de valence (VBT) et la bas de la bande de conduction (CBB) du TiO<sub>2</sub> (**Figure 1**). Les matériaux de TiO<sub>2</sub> résultants sont connus sous le nom de TiO<sub>2</sub> co-alliés. Par rapport à la situation de mono-dopage avec des états donneurs ou accepteurs localisés, on s'attend à ce que les matériaux co-alliés présentent une mobilité des porteurs de charge plus élevée.

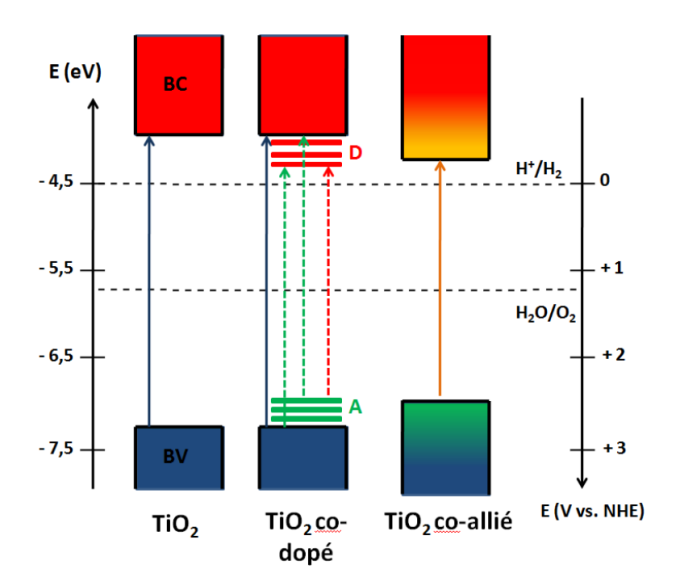


Figure 1: Structures de bandes du TiO<sub>2</sub>, du TiO<sub>2</sub> co-dopé et du TiO<sub>2</sub> coallié .<sup>21</sup>

Au cours des décennies passées, des résultats prometteurs ont été publiés par différents groupes dans le monde entier. Malheureusement, la disparité des approches de synthèse et d'analyse rend difficile la compréhension du mécanisme sous-jacent aux propriétés améliorées des TiO<sub>2</sub> co-dopé. Par conséquent, dans ce travail, basé sur des caractérisations systématiques de matériaux TiO<sub>2</sub> co-dopé avec (M, N) préparés par la méthode sol-gel (M=Nb, Ta ou W), nous visons à comprendre l'effet de chaque dopant et des défauts associés sur les propriétés physico-chimiques et les activités photocatalytiques des matériaux co-dopé. Tout d'abord, le TiO<sub>2</sub> co-dopé (Nb, N) a été étudié en tant que système co-dopé représentatif. L'accent est mis sur l'effet des conditions de nitruration sur les propriétés physico-chimiques et les activités photocatalytiques du TiO<sub>2</sub> co-dopé (Nb, N). Ensuite, nous avons modifié le choix du cation dans la combinaison de co-dopage (M, N). En comparant les propriétés physico-chimiques des matériaux TiO<sub>2</sub> co-dopé avec (Nb, N), (Ta, N) et (W, N), le rôle du cation dans les systèmes codopé a été étudié. Enfin, les différents matériaux TiO<sub>2</sub> co-dopé avec (M, N) ont été appliqués à la dégradation photocatalytique du bleu de méthylène (MB), à la réaction d'évolution de l'hydrogène (HER) et à la réaction d'évolution de l'oxygène (OER) par oxydation de l'eau, respectivement. Nous visons à déterminer un photocatalyseur adapté à chaque type spécifique de réaction et à analyser le mécanisme de la réaction correspondante.

#### 2. Résultats et discussions

# 2.1 Influence des paramètres de nitruration sur les propriétés photocatalytiques du TiO<sub>2</sub> co-dopé avec (Nb,N) pour la dégradation du bleu de méthylène

Dans le Chapitre 2, nous rendons compte de la synthèse de TiO2 co-dopé avec Nb et N (Nb/Ti at. = 0,25) par une méthode sol-gel suivie d'une nitruration thermique dans une atmosphère d'ammoniac. En se basant sur une combinaison de méthodes de caractérisation (UVvis et XPS, EPR, RDB-PAS), les propriétés photoélectrochimiques du TiO<sub>2</sub> co-dopé (Nb, N) synthétisé (0,25NbNTi) ainsi que leurs activités photocatalytiques pour la dégradation du bleu de méthylène (MB) ont été étudiées et comparées à celles du TiO2, du TiO2 dopé au Nb (0,25NbTi) et du TiO<sub>2</sub> dopé au N (NTi). Un objectif essentiel de ce chapitre est d'étudier l'influence des conditions de nitruration sur les propriétés physico-chimiques et les performances photocatalytiques des photocatalyseurs à base de TiO<sub>2</sub> synthétisés, un aspect largement négligé jusqu'à présent par la communauté scientifique. En particulier, outre les dopants azotés, les défauts associés à l'insertion de l'azote sur le matériau spécifique ont été étudiés en détail afin de comprendre les mécanismes de compensation de charge pour un système de dopage/co-dopage spécifique. Pour mettre en évidence l'influence des conditions de nitruration, deux ensembles de conditions thermiques de nitruration (douces et intenses) ont été réalisés, et la température spécifique et la durée du processus de nitruration pour le TiO<sub>2</sub> dopé au N et le TiO2 co-dopé (Nb, N) ont été déterminées sur la base des spectres UV-vis des échantillons après la nitruration. Comme illustré dans la Figure 2, les échantillons après une nitruration douce (NTi-m et 0,25NbNTi-m) présentent une couleur jaune avec une absorption principalement dans la région avant 550 nm, tandis que les échantillons après une nitruration intense (NTi-h et 0,25NbNTi-h) virent au foncé, avec une absorption supplémentaire dans les longueurs d'onde plus longues.

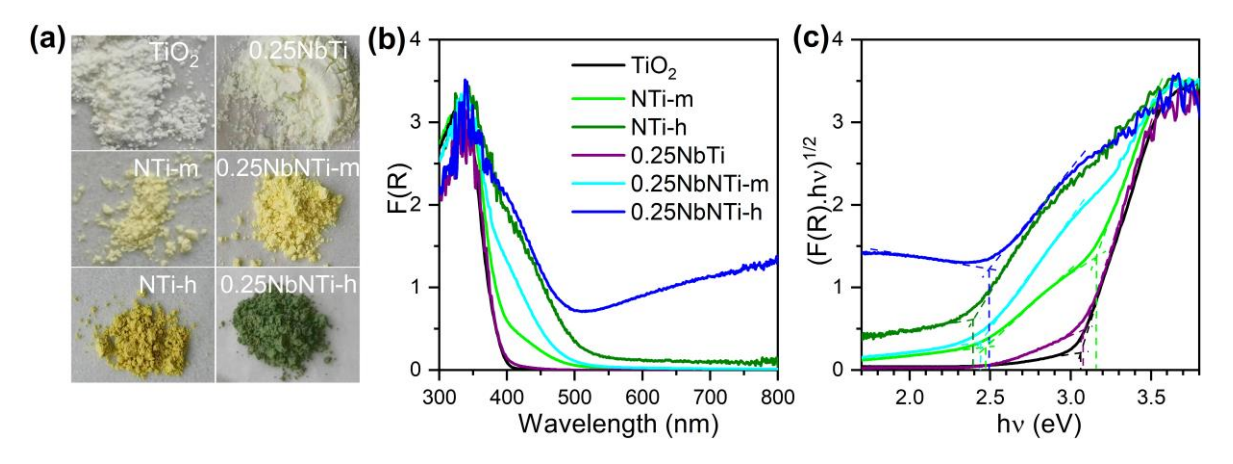


**Figure 2:** (a) Images optiques des échantillons de TiO<sub>2</sub>, TiO<sub>2</sub> dopé au N, dopé au Nb et co-dopé au (Nb, N). (b) Spectres d'absorption UV-visible de chaque échantillon. (c) Tracés de Tauc de (F(R).hv)<sup>1/2</sup> vs (hv) pour estimer la bande interdite indirecte de chaque échantillon.

Les résultats de l'analyse de diffraction des rayons X (DRX) montrent que le TiO<sub>2</sub> non dopé cristallise principalement en phase anatase, avec une petite quantité d'allotropes de rutile et de brookite. Pour les échantillons dopés au N, le rapport de la phase rutile augmente avec la condition thermique de nitruration, indiquant la facilitation de la transition de phase de l'anatase au rutile pendant la nitruration. À l'opposé, le dopage au Nb inhibe la transition de phase de l'anatase au rutile, conduisant à une anatase pure pour les échantillons dopés au Nb et (Nb, N). Les résultats de la raffinement de Rietveld suggèrent une extension du volume moyen du réseau de 1,764 % pour les échantillons contenant du Nb, ce qui est une première indication de l'insertion réussie de Nb5+ dans la structure cristalline du TiO2, car Nb5+ a un rayon ionique légèrement plus grand que Ti<sup>4+</sup>. La spectroscopie de photoélectrons à rayons X (XPS) a été utilisée pour analyser la composition chimique de surface des échantillons synthétisés. Uniquement Ti<sup>4+</sup> est observé pour les échantillons de TiO<sub>2</sub> et de TiO<sub>2</sub> dopé au N, tandis que le dopage au Nb et les traitements de nitruration contribuent à la réduction partielle de Ti<sup>4+</sup> en Ti<sup>3+</sup> dans les échantillons de TiO2 dopé au Nb et (Nb,N). Pour 0.25NbTi, 0.25NbNTi-m et 0.25NbNTi-h, les dopants de niobium existent sous forme de Nb<sup>5+</sup>. D'autre part, deux types de spécies d'azote (l'azote interstitiel et l'azote substitutif) sont présents dans le TiO2 dopé au N et le TiO<sub>2</sub> co-dopé (Nb, N), déterminés par les conditions de nitruration. La nitruration thermique douce n'introduit de l'azote qu'aux positions interstitielles dans le réseau de TiO2, tandis que la nitruration thermique intense entraîne un azote de substitution supplémentaire. Pour estimer davantage si ces espèces d'azote sont situées à la surface ou au cœur des nanoparticules, les spectres N 1s mesurés avec l'anode Mg ont été comparés à ceux enregistrés en utilisant l'anode Al. Les résultats obtenus indiquent une distribution plus homogène de l'azote de substitution dans les particules, par rapport à l'azote interstitiel. En complément de la XPS, des mesures de résonance paramagnétique électronique (RPE) ont été réalisées pour étudier les défauts avec une signature paramagnétique pour l'échantillon spécifique (Figure 3). Les résultats révèlent que les mécanismes de compensation de charge pour le TiO<sub>2</sub> dopé au N et le TiO<sub>2</sub> co-dopé (Nb, N) sont déterminés par les conditions de nitruration. Sous des conditions douces, pour le TiO<sub>2</sub> dopé au N, les vacance d'oxygène  $(V_O^+)$  sont les principaux défauts qui compensent la charge négative apportée par  $N^{3-}$ . Dans le cas de l'échantillon co-dopé, en raison de l'effet de compensation de  $Nb^{5+}$ , une meilleure passivation des défauts est obtenue. Sous des conditions intenses, pour les échantillons dopés au N et co-dopé avec (Nb, N), à la fois  $V_O^+$  et  $Ti^{3+}$  sont impliqués dans le mécanisme de compensation de charge.

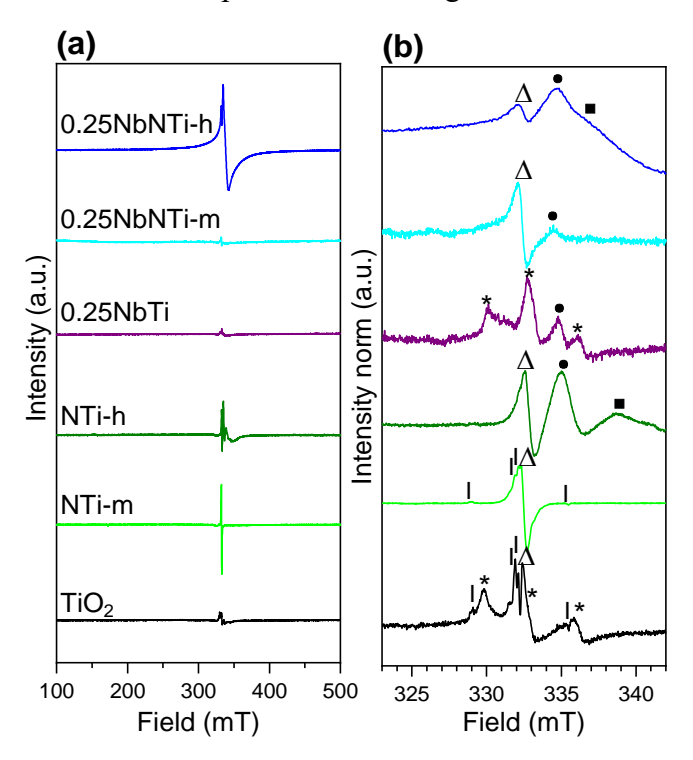


**Figure 3:** Spectres RPE pour différents échantillons : (a) spectres à large champ normalisés en fonction de la masse de l'échantillon et (b) spectres à haute résolution avec normalisation crête à crête.

Pour étudier la modification des espèces de dopage et des défauts identifiés sur la structure électronique de bande de différents échantillons, des mesures de spectroscopie photoacoustique à double faisceau inversé (RDB-PAS) ont été réalisées. Cette technique nous permet de détecter la bande interdite et les états d'énergie agissant comme pièges à électrons (ETs) dans un échantillon spécifique, comme illustré dans la Figure 4. En combinant les résultats de RDB-PAS avec d'autres caractérisations, la structure électronique de bande des matériaux synthétisés a été proposée (Figure 5). Les bandes interdites estimées de TiO<sub>2</sub> et de 0.25NbTi sont d'environ 3,0 eV, et les ETs sont distribués principalement près de la CBB, ce qui pourrait être principalement attribué à  $V_0^+$ . La densité accrue d'ETs pour 0.25NbTi pourrait être due à l'ajout d'états orbitaux vides de Nb 4d à proximité de la CB. Après la nitruration, la bande interdite des matériaux est réduite à ~2,5 eV. Dans le cas de NTi-m, seule une petite contribution, possiblement des états N 1s au-dessus de la VB, est observée. Pour les échantillons co-dopé avec (Nb, N), la distribution des ETs est plus homogène entre 3,8 et 2,4 eV, indiquant une densité d'états plus élevée induite par l'azote au-dessus de la VB. 0.25NbNTi-h présente une densité d'ETs trois fois inférieure à celle de 0.25NbNTi-m, ce qui pourrait être attribué aux centres de recombinaison de charge constitués par Ti<sup>3+</sup> et/ou l'azote de substitution.

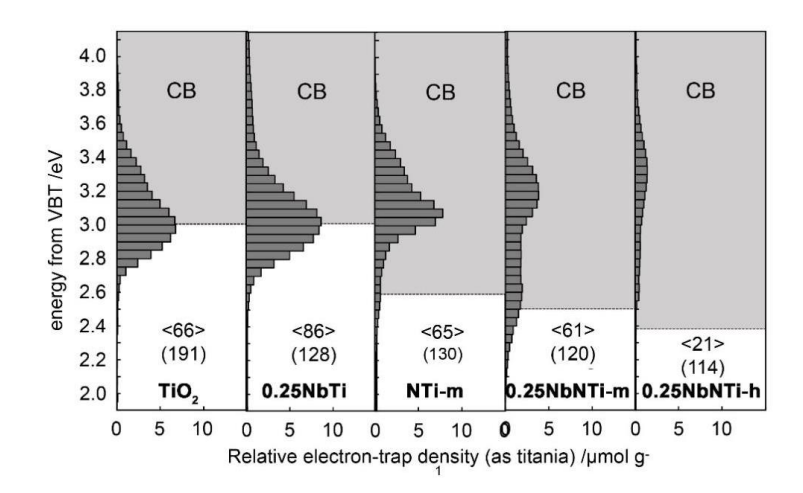


**Figure 4:** Schémas ERDT/CBB de TiO<sub>2</sub>, NTi-m, 0.25NbTi, 0.25NbNTi-m et 0.25NbNTi-h. Les valeurs <XX> indiquent la densité totale des ET en μmol.g<sup>-1</sup>. La surface spécifique en m<sup>2</sup>.g<sup>-1</sup> est indiquée par (YY). L'ordonnée représente les états d'énergie des ETs en comptant à partir du sommet de la bande de valence (VBT). La longueur des barres représente la densité relative des pièges à électrons.

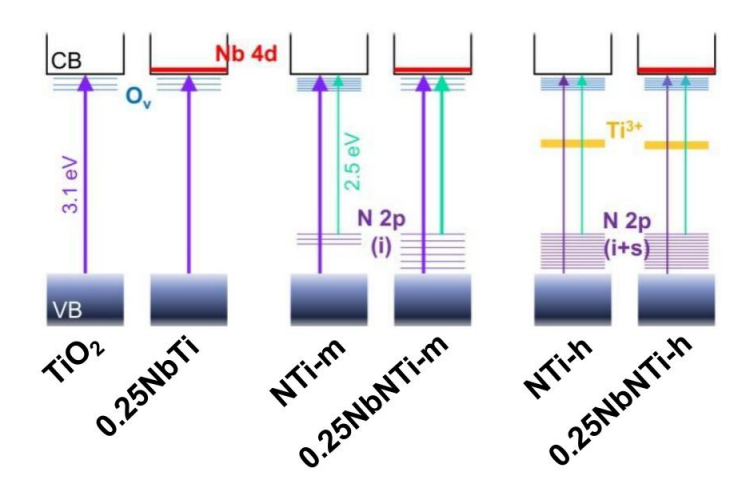


**Figure 5:** Structures de bandes électroniques proposées et position des défauts pour TiO<sub>2</sub>, 0.25NbTi recuit à l'air, et traité par nitruration douce et intense dans NH<sub>3</sub>. (i et s pour les états N 2p correspondent à l'azote interstitiel et substitutif)

Pour enquêter sur l'emplacement de l'azote dans le réseau d'anatase, nous avons réalisé des mesures de spectroscopie d'absorption des rayons X (XAS) et de spectroscopie d'émission des rayons X (XES). À la limite K du titane, aucun changement de signal pouvant être attribué au ligand azote n'a été observé. À la limite K du niobium (**Figure 6**), une évolution de l'émission Kβ" dépendante du ligand avec l'augmentation de la température de nitruration a été observée sur les spectres de XES des échantillons co-dopé. Bien que cet effet reste faible puisque l'oxygène et l'azote sont tous deux en coordination avec les cations, nos résultats suggèrent que cet azote de substitution interagit préférentiellement avec le Nb<sup>5+</sup>, créant ainsi des paires de défauts Nb-N.

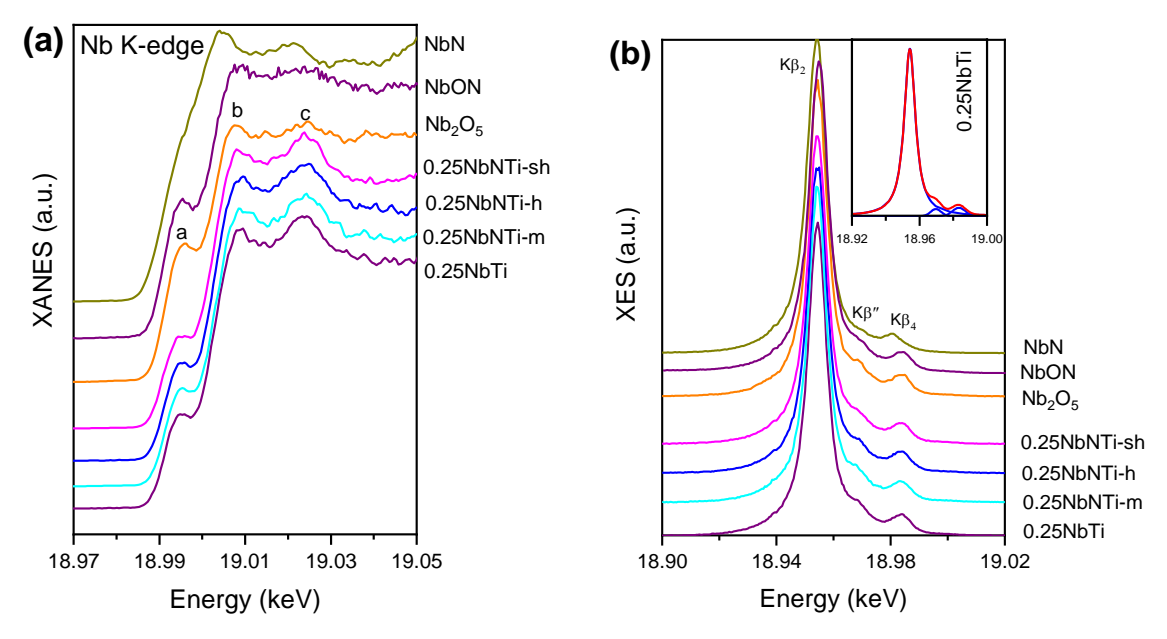


Figure 6: Spectres XANES (a) et spectres d'émission de rayons X (b) à la limite K du Nb pour les matériaux synthétisés, NbN et Nb<sub>2</sub>O<sub>5</sub>. (L'encadré en (b) montre l'ajustement à 0,25NbTi. Les trois pics ajustés représentent Kβ2, Kβ" et Kβ4.)

La photo-dégradation du bleu de méthylène a été réalisée dans différentes régions spectrales (UV, visible et lumière solaire simulée AM 1.5G) pour évaluer les propriétés photocatalytiques des photocatalyseurs préparés. Comme présenté dans la **Figure 7**, 0.25NbNTi-m présente la meilleure activité, notamment sous l'éclairage de la lumière visible et de la lumière solaire simulée, pour laquelle la cinétique de la photodégradation est presque 4 fois plus rapide que celle du TiO<sub>2</sub>. Les résultats corroborent les rapports antérieurs, dans lesquels l'activité photocatalytique améliorée était généralement attribuée au rétrécissement de la bande interdite dû au co-dopage de TiO<sub>2</sub> par Nb et N. De plus, dans le présent travail, nous mettons en évidence l'importance d'ajuster la condition thermique de la nitruration pour produire l'échantillon co-dopé spécifique avec une activité améliorée. Les échantillons soumis à des conditions intense de nitruration (0.25NbNTi-h) voient leurs activités photocatalytiques réduites dans la région UV, mais aussi dans la région visible par rapport à 0.25NbNTi-m, même s'ils présentent une meilleure absorption de la lumière optique dans la région visible. Nous supposons que la concentration plus élevée de Ti<sup>3+</sup> agissant comme des centres de recombinaison de charges conduit à cette détérioration de l'activité photocatalytique.

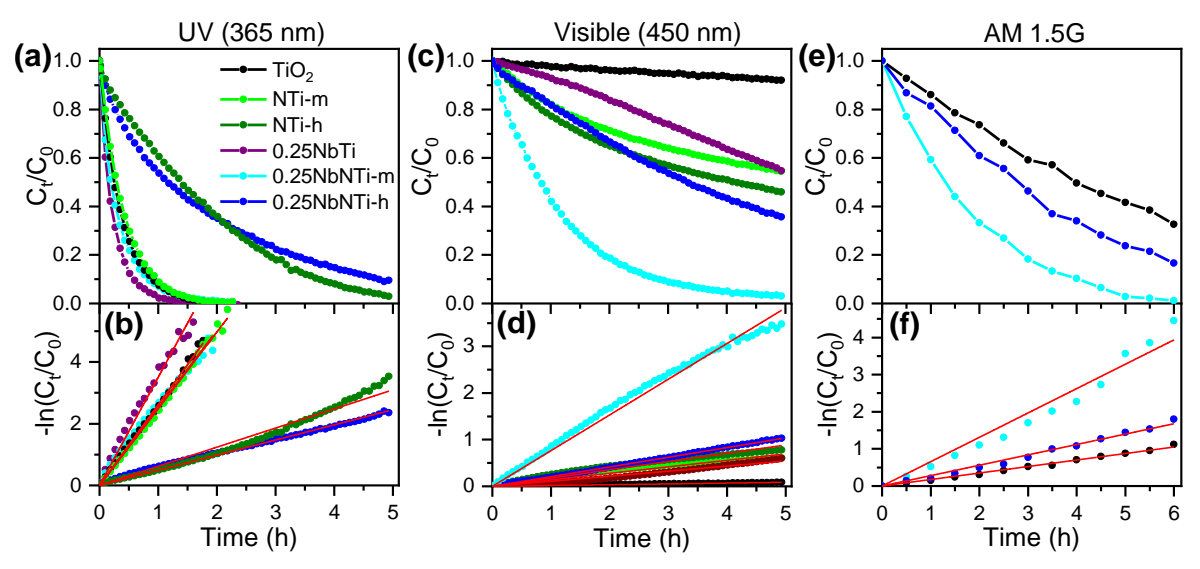
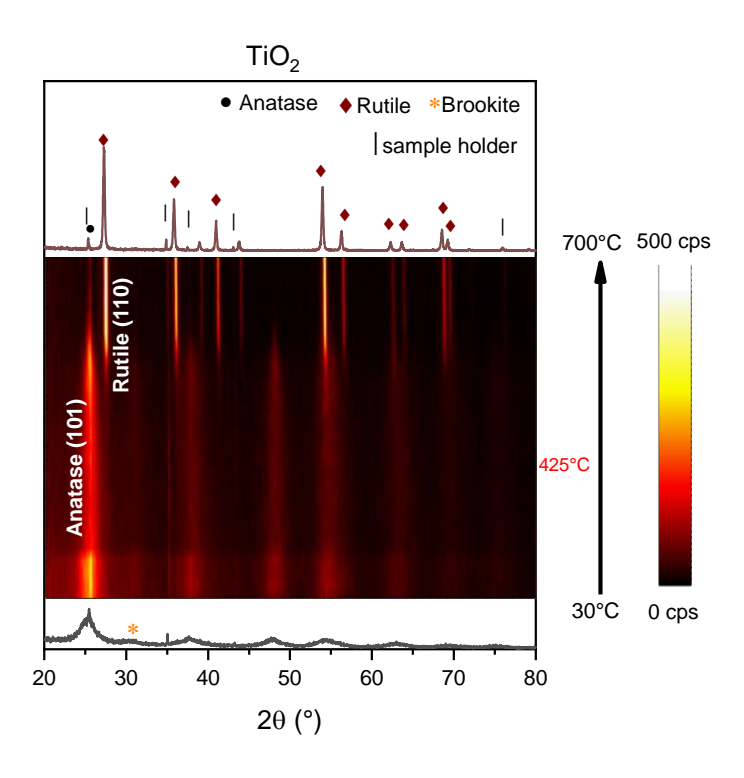


Figure 7: Activités photocatalytiques de la cinétique de dégradation de MB pour les différents échantillons sous irradiation par LED UV (365 nm) (a et b), LED visible (450 nm) (c et d) et lumière solaire simulée AM 1,5G (e et f)..

# 2.2 Caractérisation des matériaux TiO<sub>2</sub> dopé par M et TiO<sub>2</sub> co-dopé avec (M,N) (M=Nb, Ta, W)

Dans le Chapitre 3, nous avons cherché à changer le cation de dopage du TiO<sub>2</sub> co-dopé avec (M,N). En suivant la même stratégie de synthèse, nous avons préparé des photocatalyseurs TiO<sub>2</sub> co-dopé avec (Nb,N), (Ta,N) et (W,N). Dans chaque système co-dopé avec (M,N), nous avons également effectué la nitruration dans des conditions douces et intenses, respectivement. La combinaison de plusieurs méthodes de caractérisation a été utilisée pour déterminer l'influence du cation sur la formation du TiO<sub>2</sub> co-dopé avec (M,N) et ses propriétés. En particulier, nous avons essayé de déterminer comment le cation affecte l'insertion de l'azote et si les deux comportements déterminés par les conditions de nitruration qui ont été observés au Chapitre 2 pour le TiO<sub>2</sub> avec (Nb,N) sont observés dans le cas du Ta et du W. Les propriétés optoélectroniques de chaque TiO<sub>2</sub> avec (M,N) et les défauts associés à l'insertion de l'azote ont également été analysés.

En suivant la méthode de synthèse sol-gel, les matériaux TiO<sub>2</sub> dopé par M (M/Ti at.= 0.25 ou 0.1) ont été synthétisés avec succès avec Nb, Ta et W. Les résultats du MEB suggèrent que tous les TiO<sub>2</sub> dopé par M présentent une morphologie sphérique uniforme similaire à celle du TiO<sub>2</sub>. En combinant les résultats de DRX et BET, il est démontré que la taille des nanoparticules de TiO<sub>2</sub> pour un échantillon spécifique dopé par M augmente avec la concentration de dopage au cation, conduisant à une légère diminution de la surface spécifique BET. D'après les résultats des spectres UV-vis, le dopage avec Nb ou Ta n'a guère d'impact sur la structure de la bande interdite des matériaux TiO<sub>2</sub> obtenus. En revanche, la bande interdite du TiO<sub>2</sub> dopé au W a été réduite à 2,79 eV (0,1WTi) et à 2,72 eV (0,25WTi). Les résultats RPE suggèrent une diminution du V<sub>O</sub><sup>+</sup> dans tous les TiO<sub>2</sub> dopé par M, ce qui est favorisé par la compensation de la charge positive supplémentaire apportée par les cations dopants.



**Figure 8:** Schéma TDXRD du TiO<sub>2</sub>. L'image DRX bidimensionnelle est représentée au milieu de la figure. Les diagrammes DRX du premier (à 30°C) et du dernier balayage (à Tm=700°C) sont représentés respectivement en bas et en haut de la figure.

Les résultats DRX confirment l'inhibition de la formation de la phase rutile due à l'introduction du cation. Cet effet d'inhibition est observé de manière plus significative sur le TiO<sub>2</sub> dopé au W, et il est également renforcé avec l'augmentation de la concentration du dopage cationique. Ainsi, afin de déterminer plus quantitativement le rôle des types de cations et de leur concentration de dopage sur la cristallinité de la structure cristalline pour les matériaux TiO<sub>2</sub> dopé par M spécifiques en fonction de la température, une technique d'analyse DRX insitu en fonction de la température (TDXRD) a été mise au point. La température de transition de phase (TPT) de l'anatase au rutile est déterminée par la première apparition du pic caractéristique du rutile (110). Pour le TiO<sub>2</sub>, la transition de phase apparaît à 425°C, comme le montrent les diagrammes TDXRD (Figure 8). Tous les TiO<sub>2</sub> dopé par M ont une température de transition de phase plus élevée que le TiO<sub>2</sub>, comme le montrent les diagrammes TDXRD de la **Figure 9**. Pour le  $TiO_2$  dopé par M avec la même concentration de dopage, les valeurs de  $T_{PT}$ suivent l'ordre suivant : W>Ta>Nb. Dans le cas de 0,25WTi, le TPT devrait être supérieur à 900°C. D'autre part, une ségrégation de phase sous forme d'oxydes correspondants est observée pour tous les échantillons dopés par M. Cela suggère une solubilité limitée du cation dans le réseau TiO<sub>2</sub>, qui diminue avec la température et qui est probablement due à la nature métastable de la phase anatase.

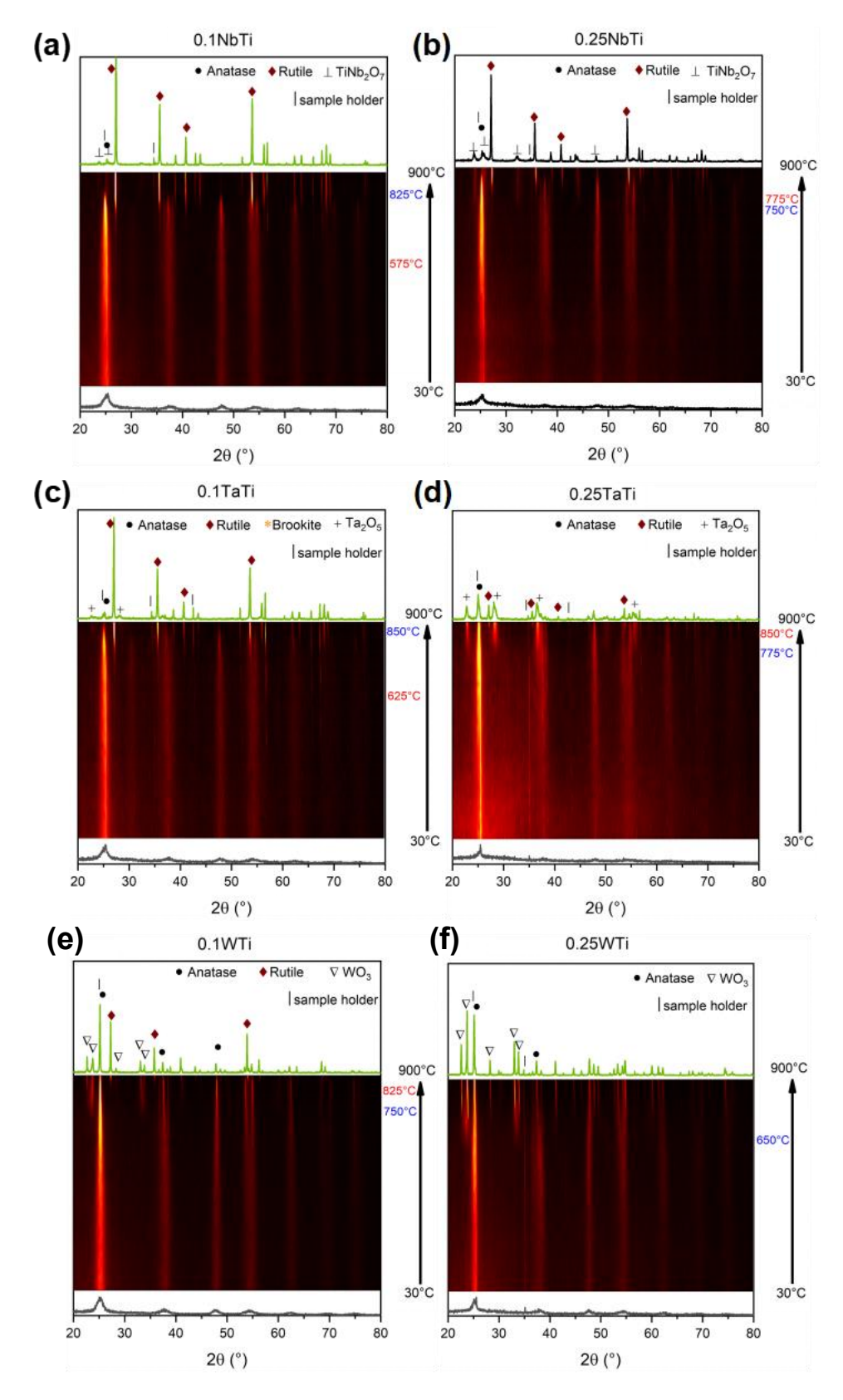


**Figure 9 :** Les diagrammes TDXRD des échantillons dopé par M. (a) et (b) pour le TiO<sub>2</sub> dopé par Nb ; (c) et (d) pour le TiO<sub>2</sub> dopé par Ta ; (e) et (f) pour le TiO<sub>2</sub> dopé par W.

Pour les matériaux TiO<sub>2</sub> co-dopé avec (M,N), par rapport au TiO<sub>2</sub> dopé par M, la modification de la morphologie des échantillons co-dopé avec (M,N) par le processus de nitruration est limitée. Les résultats XPS confirment une insertion réussie de l'azote dans le TiO<sub>2</sub> co-dopé avec (M,N) par le traitement de nitruration, et la formation de l'azote substitutif nécessite des conditions plus intenses que celle de l'azote interstitiel. L'échantillon co-dopé avec (W,N) contient une plus grande quantité de N que les échantillons co-dopé avec (Nb,N), comme le montre la charge 6+ de W. Les résultats RPE (**Figure 10**) ont confirmé un comportement différent des défauts pour l'échantillon (W,N) par rapport aux échantillons co-dopé avec (Nb,N) et (Ta,N). Dans les conditions intenses de nitruration, Ti<sup>3+</sup> a été généré pour les matériaux co-dopé avec (Nb,N) et (Ta,N), mais pas pour les échantillons co-dopé avec (W,N). Au contraire, le schéma de compensation de charge pour le codopage (W,N) peut impliquer V<sub>O</sub><sup>+</sup> et W<sup>5+</sup>.

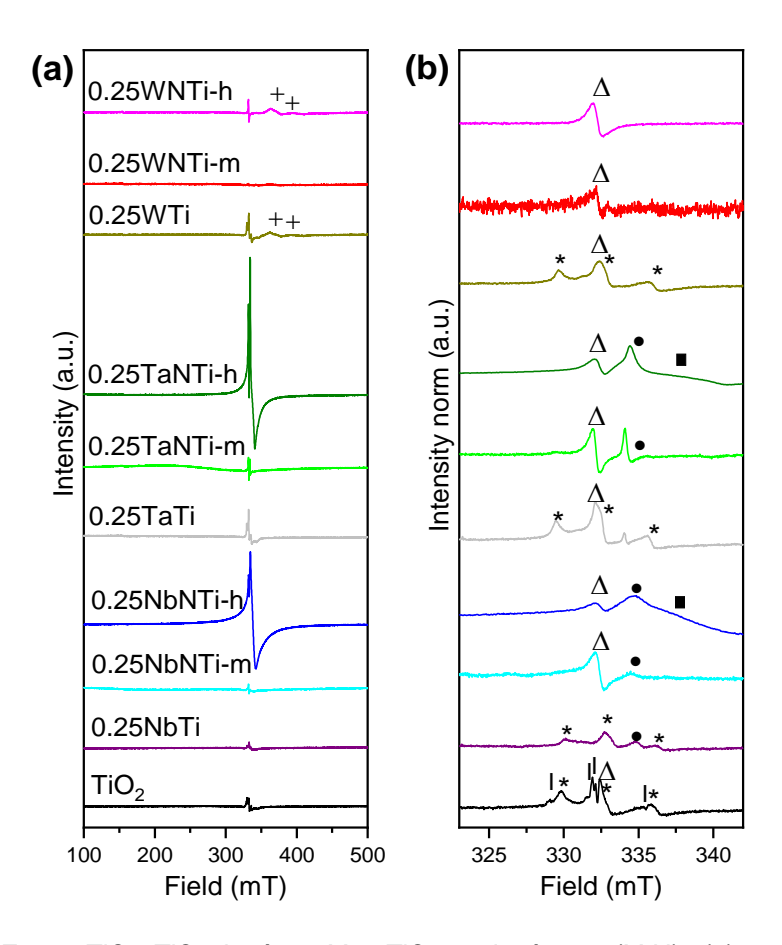


**Figure 10:** RPE pour TiO<sub>2</sub>, TiO<sub>2</sub> dopé par M et TiO<sub>2</sub> co-dopé avec (M,N) : (a) spectres à large gamme normalisés par la masse de l'échantillon, (b) spectres à haute résolution avec normalisation crête à crête.

Les propriétés d'absorption du TiO<sub>2</sub> co-dopé avec (M,N) synthétisé ont été caractérisées par spectroscopie UV-vis. Deux types différents de caractéristiques d'absorption sont également observés sur tous les échantillons co-dopé avec (M,N). La nitruration douce a entraîné une augmentation de l'absorption visible avant 550 nm (couleur jaune), qui est attribuée au dopage N. La nitruration intnese a entraîné une augmentation de l'absorption visible avant 550 nm (couleur jaune), qui est attribuée au dopage N. La nitruration intense a entraîné une augmentation de l'intensité de l'absorption visible avec une absorption apparaissant après 550 nm (couleur sombre), ce qui est principalement attribué à la génération d'états défectueux dans

la bande interdite. En outre, le TiO<sub>2</sub> co-dopé (W,N) présente une bande interdite plus courte (2,26 eV pour 0,25WNTi-m, 2,1 eV pour WNTi-h) que les échantillons co-dopé avec (Nb,N) et (Ta,N), ce qui peut être dû à une distribution différente des états N 2p ou à l'énergie plus faible de l'orbitale W 5d. Pour surveiller le changement des propriétés spectrales de l'échantillon au cours des processus de recuit ou de nitruration, nous avons également développé une méthode *in-situ* basée sur la spectroscopie UV. Les mesures ont été effectuées sous flux d'ammoniac et d'air. D'après les spectres UV-vis des différents échantillons obtenus dans l'ammoniac (**Figure 11**), deux mécanismes de dopage associés à l'insertion d'azote et à l'apparition de Ti<sup>3+</sup>/W<sup>5+</sup> ont été identifiés. Ces derniers apparaissent à des températures plus élevées et ont été facilement identifiés. Leur apparition dépend du cation dopant dans l'ordre de température W < Nb < Ta. Nous avons également observé que l'apparition des centres de couleur jaune prend plus de temps, probablement en raison d'un phénomène de diffusion, mais qu'ils sont plus stables à l'oxydation que les défauts des centres sombres.

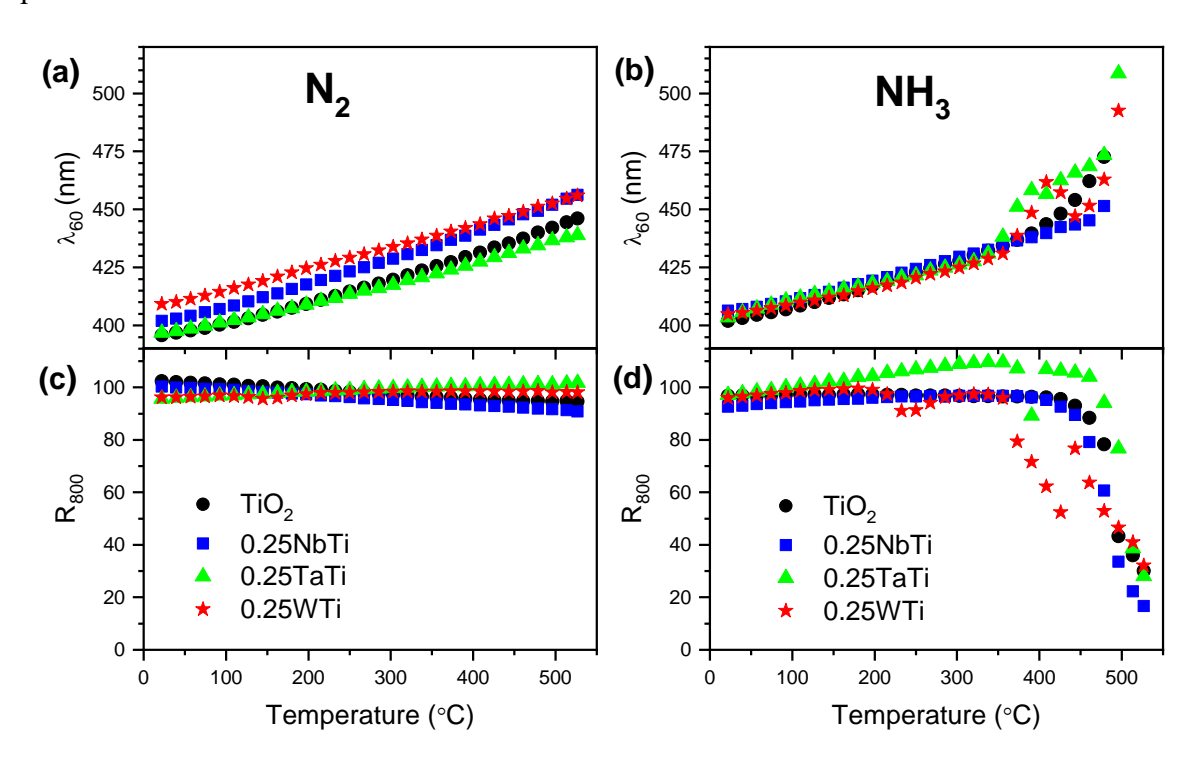


**Figure 11:** Valeurs de  $\lambda_{60}$  et  $R_{800}$  en fonction de la température (a et c correspondent aux spectres enregistrés dans  $N_2$ ; b et d correspondent aux spectres enregistrés dans  $NH_3$ )

# 2.3 Performance photocatalytique des matériaux TiO<sub>2</sub> dopé par M et TiO<sub>2</sub> co-dopé avec (M,N) (M=Nb, Ta ou W)

Le Chapitre 4 présente les résultats expérimentaux liés aux performances photocatalytiques des matériaux synthétisés dans le Chapitre 3. Tout d'abord, les activités photocatalytiques des différents matériaux TiO<sub>2</sub> dopé par M et co-dopé avec (M.N) pour la dégradation de MB ont été évaluées afin de clarifier l'effet des différents types de dopage ou de co-dopage sur l'activité photocatalytique résultante. De plus, l'influence des défauts (Ti<sup>3+</sup>, V<sub>O</sub><sup>+</sup> et W<sup>5+</sup>) sur le processus de dégradation photocatalytique a également été discutée. Ensuite, ces matériaux ont été appliqués aux deux demi-réactions de la division photocatalytique de l'eau : la réaction d'évolution de l'hydrogène (HER) et la réaction d'évolution de l'oxygène (OER).

Les résultats de la dégradation photocatalytique de MB ont montré que le TiO<sub>2</sub> co-dopé (Nb,N) et le TiO<sub>2</sub> co-dopé (Ta,N) présentent des comportements photocatalytiques similaires, où la condition de nitruration influence significativement l'activité photocatalytique. En revanche, la performance photocatalytique du TiO<sub>2</sub> co-dopé (W,N) est à peine affectée par les conditions de nitruration. Sous l'éclairage de la lumière UV (**Figure 12**), une détérioration de l'activité photocatalytique a été observée pour les échantillons (Nb,N) et (Ta,N) soumis à une nitruration intense, mais pas pour 0.25WNTi-h. Le résultat confirme que Ti<sup>3+</sup> pourrait agir comme des centres de recombinations de charges, entraînant une diminution du taux de dégradation. À l'inverse, V<sub>O</sub><sup>+</sup> et W<sup>5+</sup> identifiés dans le Chapitre 3 ont été proposés comme ayant une influence négligeable sur le processus de dégradation photocatalytique.

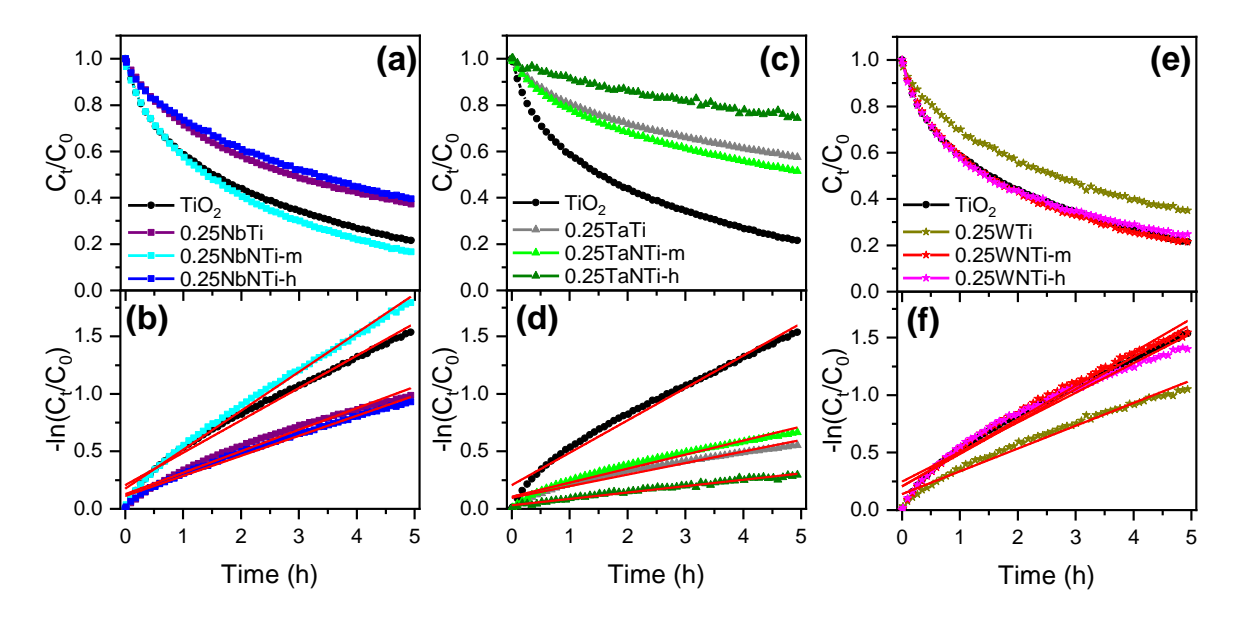


**Figure 12:** Profils et cinétique de dégradation du MB pour les échantillons de TiO<sub>2</sub>, de TiO<sub>2</sub> dopé par M et de TiO<sub>2</sub> co-dopé avec (M,N) sous irradiation par LED UV (365 nm): (a, b) pour les échantillons de Nb. (c, d) pour les échantillons de Ta et (e, f) pour les échantillons de W.

En comparant les résultats photocatalytiques obtenus dans ce chapitre avec ceux du Chapitre 2, nous avons souligné l'influence importante de l'adsorption de MB sur le résultat expérimental de la dégradation photocatalytique. Il est proposé que, pour un rapport MB/photocatalyseur plus élevé, des molécules de colorant excessives peuvent être adsorbées à la surface de l'échantillon. Par conséquent, la génération d'espèces radicalaires pourrait être ralentie en raison de cette couverture de la surface du matériau par les molécules de MB adsorbées (ou leurs produits de dégradation), entraînant une diminution du taux de dégradation. Ce phénomène dépend des propriétés de surface du photocatalyseur. La zétamétrie (**Figure 13**) indique que les échantillons dopés par M ont davantage souffert de cette adsorption excessive de MB que le TiO<sub>2</sub>, car leurs surfaces sont plus négativement chargées.

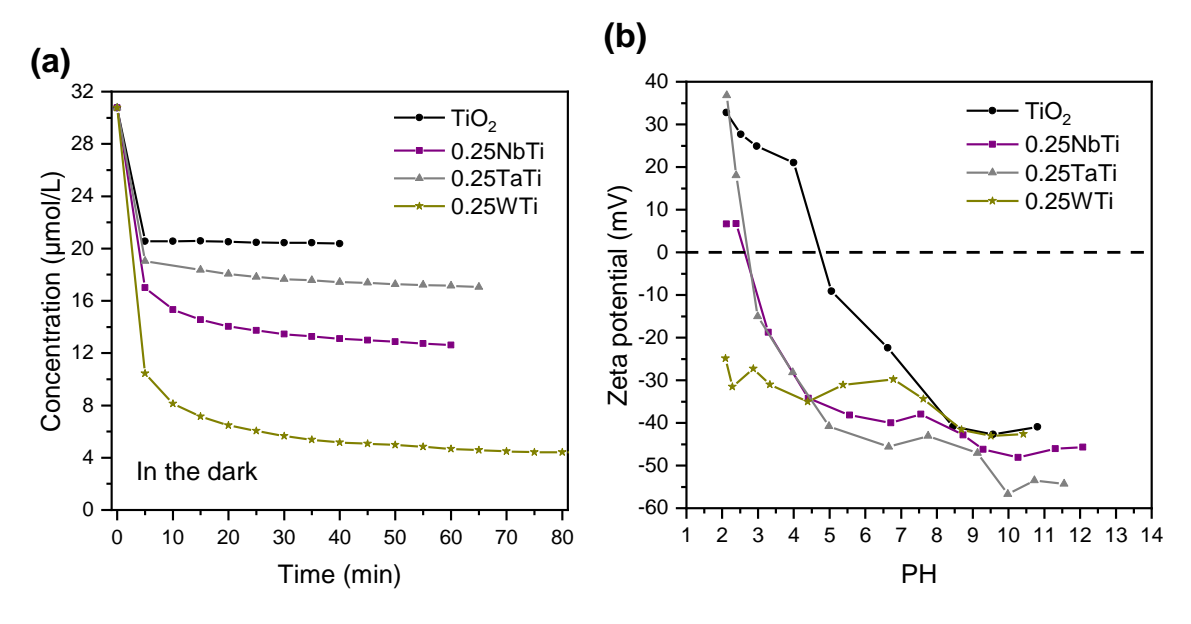


**Figure 13:** (a) Courbes d'adsorption à l'équilibre de MB pour TiO<sub>2</sub> et les échantillons dopés par M. (b) Potentiel zêta du TiO<sub>2</sub> et des échantillons dopés au M en fonction du pH.

Pour la réaction de HER, nanoparticules de Pt (NPs) et le méthanol ont été utilisés comme co-catalyseur et donneur d'électrons sacrificiel, respectivement. Il a été démontré que la méthode de dépôt de Pt a un effet significatif sur le taux de production d'hydrogène. En utilisant le TiO<sub>2</sub> comme matériau de référence, nous avons constaté que la méthode de photoréduction est plus favorable à la production d'hydrogène par rapport à la méthode de réduction chimique en raison de la plus petite taille des particules de co-catalyseur, la présence de Pt0. Il a également été observé que différentes stratégies de dopage ont un impact significatif sur la forme des NPs de Pt déposées. Une concentration élevée de dopage au Nb a entraîné une forte réduction de la charge de Pt. Ce phénomène a également été attribué à la charge plus négative à la surface du matériau. D'autre part, on note que les NPs de Pt ont tendance à s'agréger sur les surfaces du TiO2 dopé au N et du TiO2 co-dopé (Nb,N). Comme le montre la Figure 14, tous les matériaux soumis au dopage et au co-dopage présentent des activités réduites par rapport au TiO<sub>2</sub>. Les raisons pourraient être l'absence totale de rutile dans ces échantillons par rapport au TiO2 et au TiO2 dopé au N, ainsi qu'un changement dans le pouvoir réducteur des électrons photo-générés dû au déplacement de CBB provoqué par l'orbital d de l'ion dopant. À l'exception des échantillons à base de Nb, il n'y a pas d'amélioration évidente de l'activité photocatalytique du TiO<sub>2</sub> co-dopé avec (M,N) par rapport à leurs homologues dopés par M, ce qui pourrait être attribué à l'agrégation des NPs de Pt.

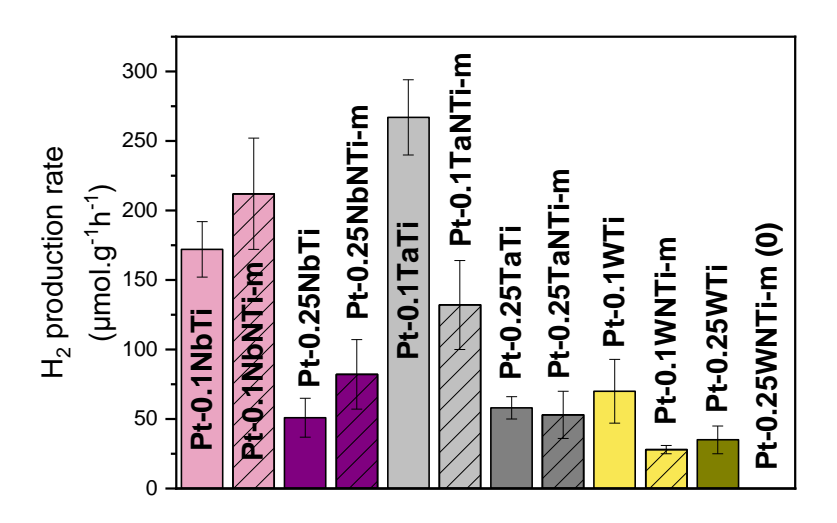


**Figure 14:** Taux de production d'hydrogène photocatalytique des échantillons de Pt-MTi et de Pt-MTi-m.

Les matériaux TiO<sub>2</sub> synthétisés, dopé par M et co-dopé avec (M,N), ont également été utilisés pour catalyser la réaction de OER, dans laquelle des NPs de RuO<sub>x</sub> et NaIO<sub>3</sub> ont été utilisés comme co-catalyseur et accepteur d'électrons sacrificiel. Les résultats de la TEM confirment que des NPs de RuO<sub>x</sub> extrêmement fines et dispersées ont été déposées avec succès à la surface des matériaux TiO<sub>2</sub> par la méthode de photo-déposition. Les taux de production d'oxygène des différents échantillons (**Figure 15**) indiquent que le TiO<sub>2</sub> dopé au Ta et le TiO<sub>2</sub> dopé au Nb sont plus avantageux pour l'oxydation photocatalytique de l'eau. De manière similaire à la réaction de production d'hydrogène photocatalytique, aucune amélioration supplémentaire de l'activité n'a été obtenue sur les matériaux co-dopé avec (M,N). Cela indique que l'augmentation de l'absorption visible ne contribue pas à une activité photocatalytique globale améliorée. Des caractérisations supplémentaires sont nécessaires pour révéler la corrélation entre le dépôt de co-catalyseur, les défauts intrinsèques du photocatalyseur et l'activité photocatalytique.

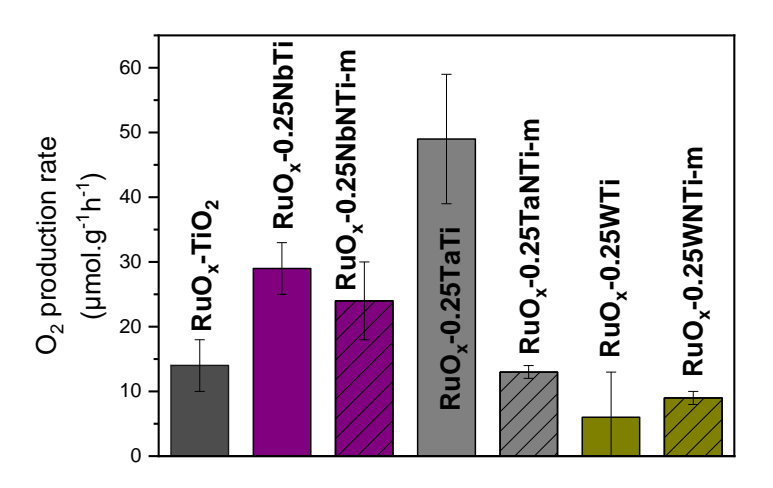


**Figure 15:** Taux de production d'oxygène photocatalytique du RuOx-TiO<sub>2</sub>, RuOx-0.25MTi et RuOx-0.25MNTi-m.

Pour améliorer l'efficacité de la séparation des porteurs de charge, nous avons également réalisé une étude préliminaire sur une stratégie de dépôt de double co-catalyseur en utilisant le TiO<sub>2</sub> comme matériau de référence. Les photocatalyseurs à base de TiO<sub>2</sub> ont été déposés avec à la fois du Pt et du RuO<sub>x</sub>. Les résultats photocatalytiques (**Figure 16**) suggèrent une perspective pour améliorer davantage l'activité photocatalytique du matériau TiO<sub>2</sub> par la stratégie de dépôt de double co-catalyseur, surtout pour les réactions d'oxydation de l'eau. Nous supposons que la combinaison de la stratégie de dépôt de double co-catalyseur et du dopage/co-dopage pourrait constituer un sujet intéressant pour l'avenir.

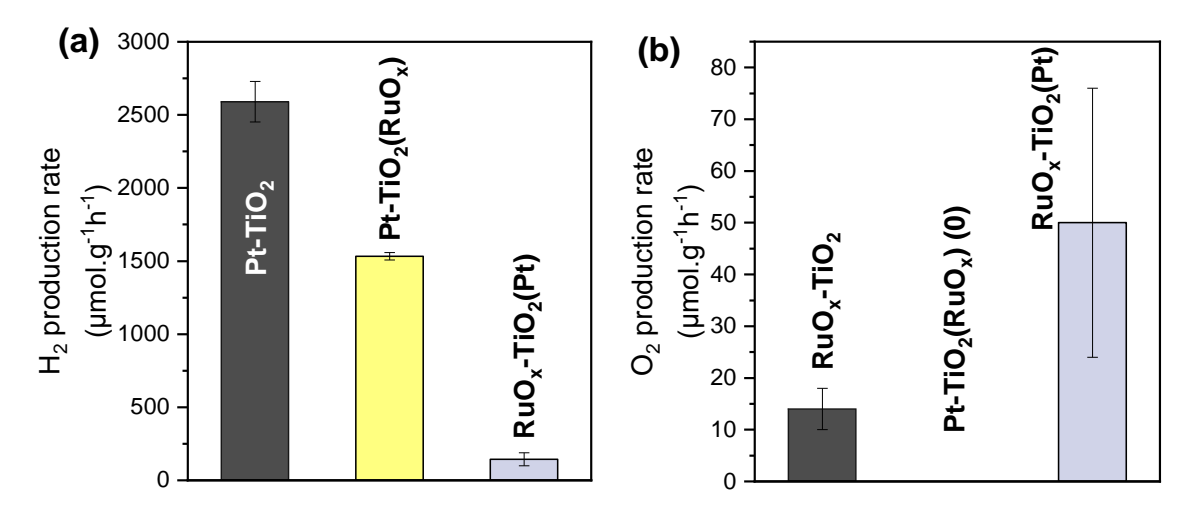


**Figure 16:** Taux de production photocatalytique d'hydrogène (a) et d'oxygène (b) du TiO<sub>2</sub> déposé avec double co-catalyseur.

#### 3. Conclusions général

Dans ce travail, nous avons étudié la stratégie de co-dopage avec une combinaison cation-anion. L'objectif de cette thèse était de modifier la structure de bande électronique du photocatalyseur TiO<sub>2</sub> par co-dopage avec des métaux de transition (M = Nb, Ta ou W) et de l'azote, dans le but d'améliorer la réponse à la lumière visible et l'activité photocatalytique des matériaux TiO<sub>2</sub> co-dopé avec (M,N). En particulier, des efforts ont été déployés pour comprendre l'effet des différents types de dopage/co-dopage sur les propriétés des matériaux et leurs activités pour des réactions photocatalytiques spécifiques. En contrôlant les paramètres de synthèse, différents matériaux co-dopé avec (M,N) avec une morphologie et une structure cristalline comparables ont été produits, nous permettant de nous concentrer sur l'effet du co-dopage lui-même.

Tout d'abord, nous nous sommes concentrés sur les matériaux TiO<sub>2</sub> co-dopé avec (Nb,N), qui représentent la combinaison cation-anion la plus représentative. Le rôle de la nitruration dans la détermination des propriétés et des activités photocatalytiques pour la dégradation du bleu de méthylène (MB) des photocatalyseurs TiO<sub>2</sub> co-dopé avec (Nb,N) a été étudié. Nous avons constaté que l'échantillon co-dopé après une nitruration douce présente la

meilleure activité sous l'éclairage de la lumière visible et de la lumière solaire simulée, ce qui pourrait être attribué au rétrécissement de la bande interdite dû au co-dopage (Nb,N). En revanche, les échantillons soumis à des conditions de nitruration intenses ont subi une détérioration des activités photocatalytiques, ce qui pourrait être attribué à la génération de Ti<sup>3+</sup> agissant comme des centres de recombinations de charges. Ensuite, une étude comparative visant à comprendre le rôle du cation dans les matériaux TiO<sub>2</sub> dopés par M et co-dopé avec (M,N) (M = Nb, Ta ou W) a été menée. Nous avons confirmé que la structure cristalline et la morphologie des matériaux dopés par M et co-dopé avec (M,N) synthétisés dépendent principalement du cation. Tous les cations sélectionnés augmentent la température de transition de phase de l'anatase au rutile. Un mécanisme de dopage similaire entre le co-dopage (Nb,N) et (Ta,N) a été observé, dans lequel Ti<sup>3+</sup> a été généré sous une nitruration intense. Pour le codopage (W,N), le schéma de compensation de charge peut impliquer V<sub>0</sub><sup>+</sup>, W<sup>5+</sup> et des lacunes cationiques. Les matériaux synthétisés ont été utilisés pour catalyser des réactions photocatalytiques : dégradation du MB, production d'hydrogène et oxydation de l'eau. Sur la base des résultats de dégradation du MB, nous avons conclu que Ti<sup>3+</sup> agit comme des centres de recombinations de charges, tandis que V<sub>O</sub><sup>+</sup> et W<sup>5+</sup> n'influencent négligeablement la cinétique de dégradation photocatalytique. Pour la production d'hydrogène, une diminution de l'activité pour tous les échantillons dopés par M et co-dopé avec (M,N) par rapport au TiO<sub>2</sub> a été observée. La raison possible pourrait être le changement de la charge de Pt et/ou le déplacement vers le bas du CBB dû au dopage avec M. De plus, nous avons constaté que les TiO2 dopés avec Nb et Ta présentent des perspectives pour l'oxydation de l'eau.

#### 4. Références

- (1) Wrigley, E. A. Energy and the English Industrial Revolution. Philosophical Transactions of the Royal Society A: Mathematical, Physical and Engineering Sciences 2013, 371 (1986), 20110568. https://doi.org/10.1098/rsta.2011.0568.
- (2) Ritchie, H.; Roser, M.; Rosado, P. Energy. Our World in Data 2022.
- (3) Photovoltage-an overview: ScienceDirect Topics. https://www.sciencedirect.com/topics/chemistry/photovoltage (accessed 2023-11-17).
- (4) Li, J.; Wu, N. Semiconductor-Based Photocatalysts and Photoelectrochemical Cells for Solar Fuel Generation: A Review. Catal. Sci. Technol. 2015, 5 (3), 1360–1384. https://doi.org/10.1039/C4CY00974F.
- (5) Chen, X.; Shen, S.; Guo, L.; Mao, S. S. Semiconductor-Based Photocatalytic Hydrogen Generation. Chem. Rev. 2010, 110 (11), 6503–6570. https://doi.org/10.1021/cr1001645.
- (6) Sharma, S.; Kumar, R.; Raizada, P.; Ahamad, T.; Alshehri, S. M.; Nguyen, V.-H.; Thakur, S.; Nguyen, C. C.; Kim, S. Y.; Le, Q. V.; Singh, P. An Overview on Recent Progress in Photocatalytic Air Purification: Metal-Based and Metal-Free Photocatalysis. Environmental Research 2022, 214, 113995. https://doi.org/10.1016/j.envres.2022.113995.
- (7) Liu, H.; Wang, C.; Wang, G. Photocatalytic Advanced Oxidation Processes for Water Treatment: Recent Advances and Perspective. Chem. Asian J. 2020, 15 (20), 3239–3253. https://doi.org/10.1002/asia.202000895.
- (8) Dambournet, D.; Belharouak, I.; Amine, K. Tailored Preparation Methods of TiO<sub>2</sub> Anatase, Rutile, Brookite: Mechanism of Formation and Electrochemical Properties. Chem. Mater. 2010, 22 (3), 1173–1179. https://doi.org/10.1021/cm902613h.
- (9) Cromer, D. T.; Herrington, K. The Structures of Anatase and Rutile. J. Am. Chem. Soc. 1955, 77 (18), 4708–4709. https://doi.org/10.1021/ja01623a004.
- (10) Zhou, W.; Liu, Q.; Zhu, Z.; Zhang, J. Preparation and Properties of Vanadium-Doped TiO<sub>2</sub> Photocatalysts. J. Phys. D: Appl. Phys. 2010, 43 (3), 035301. https://doi.org/10.1088/0022-3727/43/3/035301.
- (11) Das, K.; Sharma, S. N.; Kumar, M.; De, S. K. Morphology Dependent Luminescence Properties of Co Doped TiO<sub>2</sub> Nanostructures. J. Phys. Chem. C 2009, 113 (33), 14783–14792. https://doi.org/10.1021/jp9048956.
- (12) Wu, Q.; Yang, C.-C.; van de Krol, R. A Dopant-Mediated Recombination Mechanism in Fe-Doped  $TiO_2$  Nanoparticles for the Photocatalytic Decomposition of Nitric Oxide. Catalysis Today 2014, 225, 96–101. https://doi.org/10.1016/j.cattod.2013.09.026.
- (13) Emeline, A. V.; Furubayashi, Y.; Zhang, X.; Jin, M.; Murakami, T.; Fujishima, A. Photoelectrochemical Behavior of Nb-Doped TiO<sub>2</sub> Electrodes. J. Phys. Chem. B 2005, 109 (51), 24441–24444. https://doi.org/10.1021/jp055090e.
- (14) Chen, H.; Wang, L.; Guan, L.; Ren, H.; Zhang, Y.; Tao, J. Tungsten and Nitrogen Co-Doped  $TiO_2$  Nanobelts with Significant Visible Light Photoactivity. Surf Interface Anal 2018, 50 (2), 146–153. https://doi.org/10.1002/sia.6351.
- (15) Asahi, R.; Morikawa, T.; Ohwaki, T.; Aoki, K.; Taga, Y. Visible-Light Photocatalysis in Nitrogen-Doped Titanium Oxides. Science 2001, 293 (5528), 269–271. https://doi.org/10.1126/science.1061051.
- (16) Pomoni, K.; Vomvas, A.; Trapalis, Chr. Dark Conductivity and Transient Photoconductivity of Nanocrystalline Undoped and N-Doped TiO<sub>2</sub> Sol-Gel Thin Films. Thin Solid Films 2008, 516 (6), 1271–1278. https://doi.org/10.1016/j.tsf.2007.05.040.
- (17) Yamanaka, K.; Ohwaki, T.; Morikawa, T. Charge-Carrier Dynamics in Cu- or Fe-Loaded Nitrogen-Doped TiO<sub>2</sub> Powder Studied by Femtosecond Diffuse Reflectance Spectroscopy. J. Phys. Chem. C 2013, 117 (32), 16448–16456. https://doi.org/10.1021/jp404431z.

- (18) Yamanaka, K.; Morikawa, T. Charge-Carrier Dynamics in Nitrogen-Doped TiO<sub>2</sub> Powder Studied by Femtosecond Time-Resolved Diffuse Reflectance Spectroscopy. J. Phys. Chem. C 2012, 116 (1), 1286–1292. https://doi.org/10.1021/jp209210u.
- (19) Gai, Y.; Li, J.; Li, S.-S.; Xia, J.-B.; Wei, S.-H. Design of Narrow-Gap TiO<sub>2</sub>: A Passivated Codoping Approach for Enhanced Photoelectrochemical Activity. Phys. Rev. Lett. 2009, 102 (3), 036402. https://doi.org/10.1103/PhysRevLett.102.036402.
- (20) Brancho, J. J.; Bartlett, B. M. Challenges in Co-Alloyed Titanium Oxynitrides, a Promising Class of Photochemically Active Materials. Chem. Mater. 2015, 27 (21), 7207–7217. https://doi.org/10.1021/acs.chemmater.5b02357.
- (21) Favet, T. Conversion de l'énergie solaire en carburant H<sub>2</sub> par photoélectrolyse de l'eau sur des matériaux nanohybrides à base de TiO<sub>2</sub>/nanoparticules. phdthesis, Université de Strasbourg; Institut national de la recherche scientifique (Québec, province), 2019. https://theses.hal.science/tel-03186944 (accessed 2023-08-30).

## List of Abbreviations

TiO<sub>2</sub>: Titanium dioxide

MB: Methylene blue

HER: Hydrogen evolution reaction

OER: Oxygen evolution reaction

NPs: Nanoparticles

CO<sub>2</sub>: Carbon dioxide

ppm: Parts per million

·O<sub>2</sub><sup>-</sup>: Superoxide radicals

·OH: Hydroxyl radicals

·OOH: Hydroperoxyl radicals

OH<sup>-</sup>: Hydroxyl ion

 $\Delta G_0$ : Standard Gibbs free energy

VB: Valence band

CB: Conduction band

VBT: Valence band top

CBB: Conduction band bottom

V<sub>O</sub><sup>+</sup>: Oxygen vacancy

Ti<sup>3+</sup>: Titanium interstitials

V<sub>Ti</sub>: Titanium vacancy

PL: Photoluminescence

NTs: Nanotube arrays

MO: Methylene orange

IPCE: Photo-to-current efficiency

RhB: Rhodamine B

NWs: Nanowire arrays

FTO: Fluorine-doped tin oxide

EDX: X-ray spectroscopy

XPS : X-ray photoelectron spectroscopy

EPR: Electron paramagnetic resonance

XRD: X-Ray diffraction

SEM: Scanning electron microscopy

TEM: Transmission electron microscopy

HRTEM: High-resolution transmission

electron microscopy

BET<sub>SSA</sub>: BET surface area

ERDT: Energy-resolved distribution of

electron traps

PAS: Photoacoustic spectroscopy

RDB-PAS: Reversed double-beam

photoacoustic spectroscopy

ETs: Electron traps

DOS: Density of states

XAS : X-ray Absorption Spectroscopy

EXAFS: Extended X-ray Absorption Fine

Structure

XANES: X-ray Absorption Near Edge

Structure

XES: X-ray Emission Spectroscopy

VTC: Valence-to-core

TDXRD: Temperature-dependent XRD

 $T_{PT}$ : Temperature for the phase transition

 $T_{PS}$ : Temperature for the phase segregation

 $E_g$ : Bandgap energy

FWHM: Full width at half maximum

DR spectra: Diffuse reflectance spectra

CompactGC: Compact-chromatograph

FID: Flame Ionization Detector

TCD: Thermal Conductivity Detector

ICP-AES: Inductively Coupled Plasma

Atomic Emission Spectroscopy

## General introduction

The use of fossil fuels has made significant contributions to human society's development over the past two centuries. Coal, oil, and natural gas have dominated energy production since the Industrial Revolution. The chemical energy contained in fossil fuels can be released through combustion, and used in electricity production, transportation and industrial processes. This has allowed for the rapid industrialization and modernization of societies, leading to increased standards of living and economic development. However, these contributions have come with not only benefits but also drawbacks. As the Earth's population and industrial manufacturing have grown exponentially, the environmental and climate crises caused by the massive combustion of fossil fuels have begun to emerge. On the one hand, pollutants from industrial production processes are released into the ecosystem through wastewater and exhaust gas emissions, which directly threaten human health. On the other hand, the use of fossil fuels inevitably emits large amounts of carbon dioxide, which is the main contributor to the increasing greenhouse effect. In addition, fossil fuels are finite resources, which are predicted to be depleted over the next centuries. Therefore, developing renewable energy is the fundamental resolution to solve the climate and environmental crises faced by mankind in the 21st century.

Solar energy is one of the most important renewable energy sources because the total amount of energy reaching the earth is enormous. Theoretically, the energy provided annually by sunlight radiation is more than 1200 times greater than the total amount of energy demanded by mankind. But one difficulty is to convert solar energy flux into other forms of energy that can be used directly by humans. Currently, the most widely used solar energy conversion technology is photovoltaics, which converts it into electricity. It accounts for only 0.46% of primary energy production and 2.7% of total electricity production. The current photovoltaic conversion efficiency is about ~20% but photovoltaic technology is limited by the fluctuation of solar radiation with the seasons, weather, and geographic location. This can result in unstable electricity generation. Therefore, in order to exploit solar energy more sufficiently, emerging solar energy conversion technologies have attracted extensive attention from the scientific community.

Through photocatalytic reactions in which semiconductors are used as catalysts, the photogenerated electrons and holes can be used to promote a variety of chemical reactions. In 1972, Fujishima and Honda found that hydrogen and oxygen were produced on a titanium dioxide (TiO<sub>2</sub>) photoanode in an aqueous electrolyte, under UV irradiation. Despite its limited efficiency, this process showed for the first time the possibility of converting solar energy directly into storable chemical energy. The application of photocatalysis was also extended to environmental remediation. It has been shown that the photogenerated charge carirers (electrons and holes) can react with oxygen or water molecules adsorbed on the photocatalyst surface to generate active radicals with strong oxidizing power, which can used for pollutant degradation in water or air. The main disadvantage of TiO<sub>2</sub> used as a photocatalyst is the lack of visible absorption. Due to its wide band gap (3.2 eV for anatase), only the energy of photons in the UV region (~5% of the solar spectrum) could be used for photocatalytic reactions.

The main objective of this thesis is to modify TiO<sub>2</sub> nano-photocatalysts via a strategy of co-doping with transition metals (M=Nb, Ta or W) and nitrogen to extend its photoresponse range over the solar spectrum. This approach was first proposed in theoretical studies as a way to overcome the limitations of classical N-doping. If promising results were obtained by different groups around the world, the disparity of synthetic and analytic approaches makes it difficult to understand the mechanism behind the improved properties of co-doped TiO<sub>2</sub>. In this work, based on systematic characterizations of the solgel prepared (M,N) co-doped TiO<sub>2</sub> materials, we aim to understand the effect of each dopant and associated defects on the physicochemical properties and the photocatalytic activities of the co-doped materials. First, (Nb,N) co-doped TiO<sub>2</sub> was studied as a representative co-doped system. The effect of (Nb,N) co-doping on the crystal structure, light absorption properties, and electronic band structure of TiO<sub>2</sub> was analyzed. Then, we changed the choice of cation in the (M,N) co-doping combination. By comparing the physicochemical properties of the (Nb,N), (Ta,N) and (W,N) co-doped TiO<sub>2</sub> materials, the role of cation in determining the nitrogen doping process and the associated defects involved in the charge compensation mechanism was studied. Finally, the different (M,N) co-doped TiO<sub>2</sub> materials were applied to photocatalytic degradation of methylene blue (MB), hydrogen evolution reaction (HER) and oxygen evolution reaction (OER) from water oxidation, respectively. We aim to determine a suitable photocatalyst for each specific type of reaction and analyze the corresponding reaction mechanism. For this the thesis is divided into four chapters:

The first chapter is a bibliographic review aiming to introduce the context of this work: the current situation of global energy consumption, the way to reduce the consumption of fossil fuels, the potential of solar energy and the prospects of photocatalytic technologies are presented. Then the fundamental principle of photocatalysis, two specific reaction processes (photocatalytic pollutant degradation and photocatalytic water splitting) are illustrated. Furthermore, after a brief introduction to the properties of TiO<sub>2</sub>, a detailed review of band engineering of TiO<sub>2</sub> by doping with foreign elements is presented. Emphasis is placed on the cation-anion co-doping strategies. Based on the theoretical calculation and experimental studies reported in the literature, we point out the challenges that remain in the research area of co-doped TiO<sub>2</sub> materials.

The second chapter concerns the synthesis, characterization and the evaluation of photocatalytic activity of the (Nb,N) co-doped TiO<sub>2</sub> material. The Nb dopants were introduced into TiO<sub>2</sub> first by a sol-gel method and the N dopants were inserted successively through a thermal nitridation process in ammonia. By controlling the calcination temperature and duration, the TiO<sub>2</sub> and Nb-doped TiO<sub>2</sub> with comparable crystal structure and morphology were prepared, allowing us to highlight the photoelectrochemical property of a specific sample with its chemical composition and intrinsic defects due to the doping/co-doping modification. Besides, the effect of nitridation conditions on the type of nitrogen species and the associated defects are analyzed. By comparing the characterization results of TiO<sub>2</sub>, Nb or N-doped TiO<sub>2</sub> and (Nb,N) co-doped TiO<sub>2</sub>, the charge compensation mechanisms for different types of doping/co-doping are proposed.

Then, we analyzed the impacts of different types of dopants and defects on the photocatalytic activity for MB degradation.

Chapter 3 presents a comparative study involving three different co-doping combinations: (Nb,N), (Ta,N) and (W,N). The objective is to investigate the effect of cation on the structure, morphology, and photoelectrochemical properties of the resultant TiO<sub>2</sub> materials. This chapter is divided into two main parts. The first part concerns the characterization of the M-doped samples. The focus of this part is to study the effect of the cation type and doping concentration on the crystal structure of the resultant M-doped TiO<sub>2</sub>. An *in-situ* temperature-dependent XRD technique was developed, to reveal the evolution of the crystalline phase of the M-doped samples with increasing temperature. The second part presents the comparison of the characterization results of different (M.N) co-doped TiO<sub>2</sub>. The crystal structure and morphology of the co-doped samples were first compared with the corresponding M-doped samples. Then, based on the results of UV-vis spectroscopy, the role of cation in determining the light absorption properties of the resultant co-doped materials was analyzed. Combining the results of XPS and EPR, we detected the nitrogen species and associated defects in different (M,N) co-doped TiO<sub>2</sub> The charge compensation mechanisms corresponding to each (M,N) family are discussed. Finally, an *in-situ* UV-vis reflectance spectroscopy technique is presented. This technique helps to understand and optimize the thermal nitridation process.

Before a general conclusion and perspective chapter, the 4<sup>th</sup> chapter presents the experimental results related to the photocatalytic performances of the M-doped TiO<sub>2</sub> and (M,N) co-doped TiO<sub>2</sub> materials synthesized and characterized in Chapter 3. This chapter can be divided into three parts, corresponding to three different types of photocatalytic reactions: photocatalytic degradation of methyl blue, photocatalytic hydrogen production and photocatalytic water oxidation. The prepared materials were used to catalyze photocatalytic degradation of MB. Combining the characterization results obtained in Chapter 3, the effect of different types of doping/co-doping on the resultant degradation kinetics was studied. Besides, the role of different types of defects, such as Ti<sup>3+</sup>, V<sub>0</sub><sup>+</sup> and W<sup>5+</sup> in determining the charge carrier separation and transfer efficiency was also discussed. In addition to the nature of the photocatalyst itself, we also studied the influence of photocatalytic experimental conditions, especially the initial dye concentration, on the photocatalytic degradation kinetics. Then, the photocatalytic activities of the prepared materials were evaluated by conducting photocatalytic HER and OER. Pt and RuO<sub>x</sub> nanoparticles (NPs) were deposited on the sample surface as a co-catalyst for HER and OER, respectively. For the co-catalyst deposition, we used an in-situ photo-deposition method followed by the photocatalytic test. According to the HER result using TiO<sub>2</sub> as reference material, this method produced smaller Pt sizes than the chemical deposition method. After that, we investigated the effects of different types of doping/co-doping on the morphology, distribution, and loading of the co-catalysts. The photocatalytic activities were discussed considering both the effect of co-catalyst and the nature of the material itself. Finally, we have conducted a preliminary exploration of the TiO2 decorated with dual co-catalysts (Pt and RuO<sub>x</sub> NPs) for the application of HER and OER.

PhD	XI	Qingyang

"We are just an advanced breed of monkeys on a minor planet of a very averag star. But we can understand the Universe. That makes us something very special."	ıe
– Stephen Hawkin	ıg

Chapter- 1 Bibliography and context

## Summary

1. General context	9
1.1 Global demand for energy transition	9
1.2 Solar energy	10
2. Solar energy conversion via photocatalysis	11
2.1 Principle of photocatalysis	11
2.2 Photocatalytic degradation of pollutants	12
2.3 Photocatalytic water splitting	13
2.4 Fundamental requirements for photocatalysts	14
2.4.1 Absorption of sunlight	14
2.4.2 Band position	15
2.4.3 Charge separation and transfer	16
2.4.4 Stability and cost	17
3. TiO <sub>2</sub> as photocatalyst	17
3.1 Crystal structure	17
3.2 Electronic band structure:	19
4. Band engineering of TiO <sub>2</sub> by doping	19
4.1 Cation-doping	20
4.2 Anion-doping	22
4.3 Cation-anion co-doping	23
4.3.1 Theoretical study	24
4.3.2 Experimental study	28
5. Outline and scope of this thesis	35
6 References	37

### 1. General context

## 1.1 Global demand for energy transition

The exploitation and utilization of energy are closely related to the development of human society. Fossil fuels (such as coal, oil, and natural gas) have played an important role in driving industrial progress and social development. Almost all of the great inventions of the first and second technological revolutions, such as the steam engine, the internal combustion engine, the train, and the airplane, are directly driven by the energy released via the combustion of fossil fuels.<sup>2</sup> However, with the rapid growth of the world's population and economy since the mid-19th century, the use of fossil fuels increased rapidly (Figure 1.1), leading to the emergence of the climate crisis. Fossil fuel combustion has released large amounts of carbon dioxide (CO<sub>2</sub>) which is the main greenhouse effect gases, which is considered the major cause of climate change. It is shown that atmospheric CO<sub>2</sub> concentrations have risen from ~290 parts per million (ppm) at the beginning of the Industrial age to the current level of 412 ppm. Simultaneously, more than 1°C increase in global average temperature has occurred since 1880 due to this global warming.<sup>3,4</sup> Besides, extreme weather events (such as hurricanes, droughts, and heatwaves) have been recorded more frequently in recent decades, as well as the rise of the sea-level, and the loss of ecosystems and biodiversity.<sup>5,6</sup> On the other hand, environmental pollution caused by industrial production activities is another major challenge for humanity in the 21st century. A variety of toxic pollutants, such as heavy metals, organic solvents, pesticides, and pharmaceuticals could enter the ecosystem with the discharge of wastewater and waste gas, which in turn pose a risk to human health. It is reported that long-term exposure to the contaminated environment could cause organ damage, neurological disorders, and an increased risk of cancer.<sup>7–9</sup>

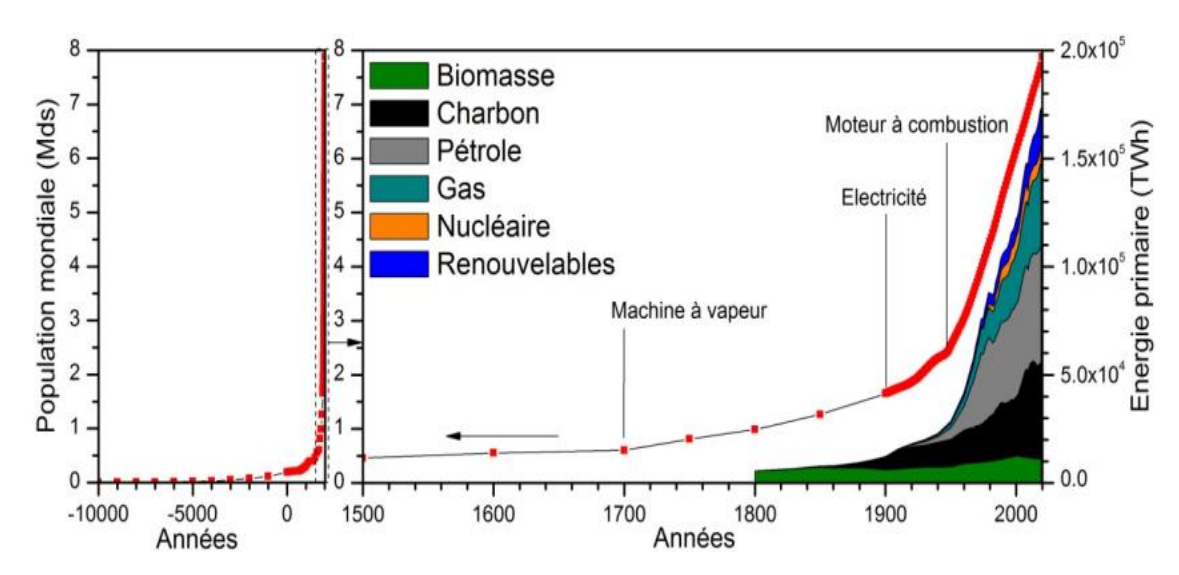


**Figure 1.1**: Evolution of the world population and annual consumption of primary energy., (biomass: traditional biomass mainly firewood; renewables: solar, biofuels, wind, hydraulic)<sup>10</sup>

The increasing concerns about the environment and climate have led to the focus on the transition towards renewable energies (solar energy, wind energy, hydro energy, tidal energy, geothermal energy, biomass energy). The extraction and utilization of renewable energy sources produce little to no greenhouse gas emissions as well as minimal environmental pollution. It can help to mitigate climate change and lead to more sustainable development of our society. 11,12 Although the technologies of renewable energy conversion have undergone rapid development with an increasing proportion of renewable energy consumption in the past few decades, non-renewable sources still dominate the global current energy consumption (> 80% of global primary energy consumption), as shown in Figure 1.2.<sup>11</sup> The main difficulty in the development of renewable energies is economic viability, since initial investment and installation costs for renewable energy systems can be significant, and the return on investment may take a long time. In addition, the intermittency and variability of some renewable energy sources, such as solar and wind, pose challenges to a stable and reliable energy supply. 12,13 Therefore, advanced technologies for efficient conversion and storage of renewable energy are urgently demanded, and research in the field will certainly contribute towards achieving the global climate goals outlined in "The Paris Agreement". 14

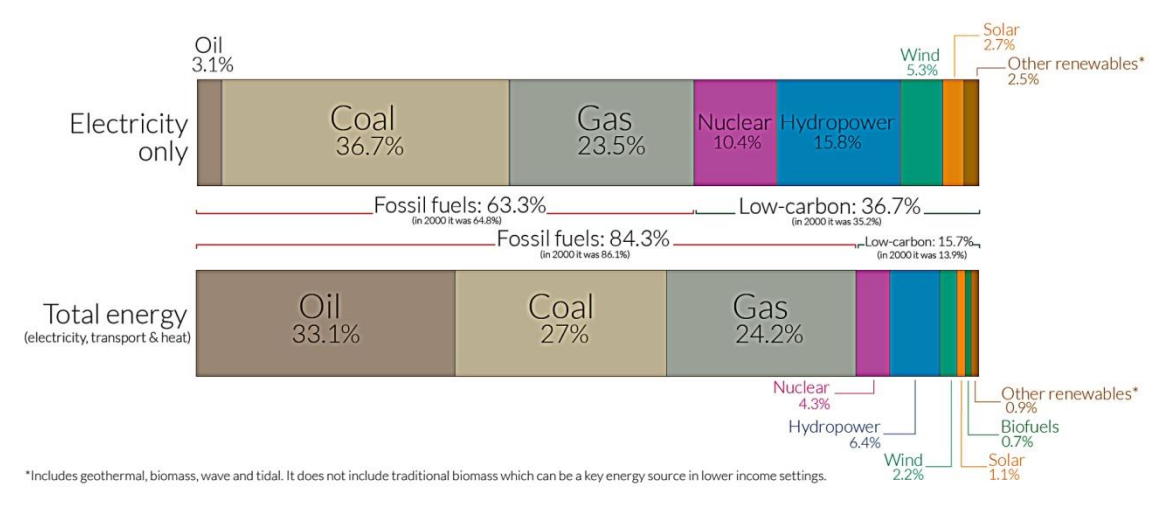


**Figure 1.2 :** World primary energy consumption by type of resource in 2019 and the share of these energies in global electricity production.<sup>15</sup>

# 1.2 Solar energy

Among the mentioned renewable energies, solar energy is by far the largest sustainable source available. **Figure 1.3** shows the theoretical annual production potential of various renewable energies as well as the remaining stocks in fossil fuels and uranium. Wind and hydro power, including tidal power, could reach 45 000 TWh (considering the installation of windmills at all offshore and onshore sites with a wind speed  $> 10 \text{ m.s}^{-1}$  and all potential dam sites). By comparison, considering only the land surface, the solar energy reaching the earth's surface annually is  $200 \times 10^6$  TWh, which is 1,200 times the annual primary energy consumption. On a clear day, at a latitude of 48° the power received is 1000 W.m<sup>-2</sup> (the value used to define the AM1.5G spectrum, which is the standard for evaluating

solar cells). On the other hand, the existing fossil fuel reserves are limited and may be depleted in the near future. In fact, the production of fossil fuels was also inherently influenced by the input of solar energy to the Earth. About 0.1% of the solar energy that reaches the surface is absorbed by plants and then stored into biomass via photosynthesis, at least some of which has been transformed into fossil fuels over a long geological evolution. In other words, the use of fossil fuels consumed, in less than two centuries, the solar energy stored on Earth over millions of years. To fully utilize solar energy and reduce dependence on fossil fuels, the development of emerging technologies for harvesting, converting, and storing solar energy has attracted scientific attention.

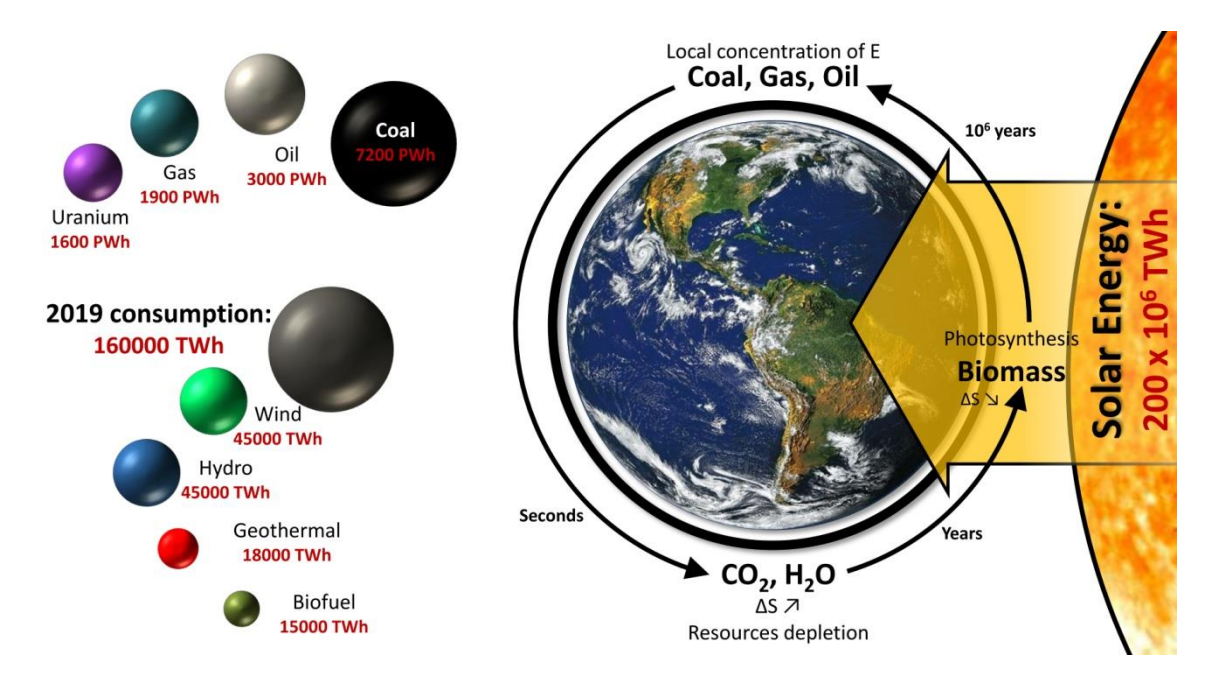


**Figure 1.3 : Left :** Representation of the theoretical energy resources that can be exploited on Earth (for the fossils + uranium: exploitable stock remaining in 2015, for the renewables: annual production potential). <sup>16</sup> **Right:** simplified representation of the carbon cycle by considering the Earth as a closed thermodynamic system. <sup>10</sup>

# 2. Solar energy conversion via photocatalysis

Photocatalysis is one of the most promising strategies for solar energy conversion. On the one hand, photocatalysis has been widely used for environmental remediation through the advanced photocatalytic oxidation process. On the other hand, solar energy can be converted and stored in the form of "solar fuels" via reactions such as photocatalytic hydrogen production from water splitting and photocatalytic CO<sub>2</sub> reduction into hydrocarbons. On the other hand, solar energy can be converted and stored in the form of "solar fuels" via reactions such as photocatalytic hydrogen production from water splitting and photocatalytic CO<sub>2</sub> reduction into hydrocarbons.

# 2.1 Principle of photocatalysis

The important steps of the photocatalytic reaction are illustrated in **Figure 1.4.** When the photocatalyst absorbs photons with an energy equal to or higher than the band gap of the semiconductor, electrons can be excited from the valence band to the conduction band,

leaving holes behind in the valence band (zoom-in region). After the generation of electron-hole pairs, the photo-induced electrons and holes could transfer to the reaction sites located on the surface of the semiconductor (process 1 and 3). However, the migration process may suffer from the charge recombination taking place both in the bulk and on the surface (process 2 and 4), accompanied by releasing the adsorbed energy of charge carriers in the form of vibration of lattice atoms (phonons) and fluorescence (photons).<sup>22</sup> These recombinations can be enhanced, by a variety of defects existing in the photocatalytic materials and acting as charge recombination centers, and this has made the effective separation of electrons and holes a challenging topic in photocatalysis. Finally, the photogenerated electrons and holes that successfully reach the reaction sites will promote specific chemical reactions. In more detail, the electrons or holes could be utilized to drive reduction or oxidation reactions respectively, depending on the redox potential required for the target reaction.<sup>23</sup>

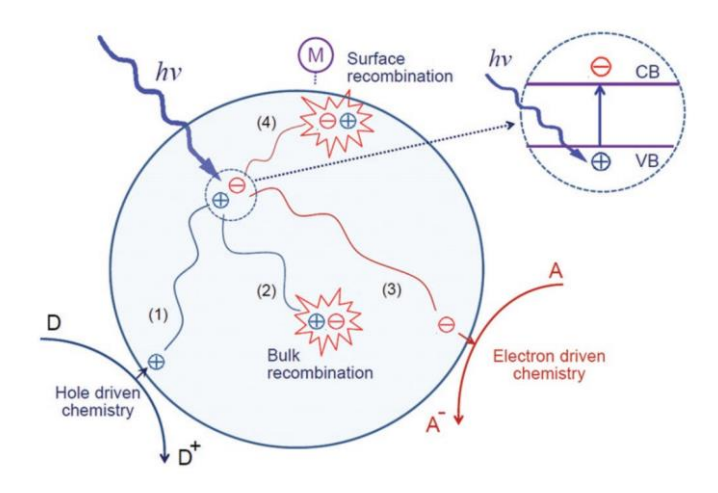


**Figure 1.4:** Important processes in photocatalysis: electron-hole pair generation, charge transfer, electron-hole pair recombination in the bulk or at the surface, and electron and hole-induced chemistry at the surface.<sup>22,23</sup>

## 2.2 Photocatalytic degradation of pollutants

photocatalytic degradation of pollutants is achieved by various active radicals species with strong oxidizing power (illustrated in **Figure 1.5**), such as superoxide radicals ( $\cdot$ O<sub>2</sub> $^{-}$ ), hydroxyl radicals ( $\cdot$ OH) and hydroperoxyl radicals ( $\cdot$ OOH), which could be generated by a series of photo-redox reactions (**eq. 1.1 to 1.8**) involving the photo-induced charges and the corresponding reactant adsorbed on the catalyst surface. For example, the holes could oxidize hydroxyl ion (OH $^{-}$ ) or a water molecule to produce  $\cdot$ OH. The electrons could reduce an oxygen molecule to generate O<sub>2</sub> $^{-}$ , which may further produce  $\cdot$ OOH and  $\cdot$ OH. The photogenerated holes may also directly participate in the oxidation of pollutants, although the efficiency is limited by the diffusion of holes in the reaction medium.<sup>24</sup>

$$semiconductor + hv \rightarrow e^- + h^+$$
 (eq. 1.1)

$$e^- + O_2 \rightarrow O_2^-$$
 (eq. 1.2)

$$\cdot O_2^- + H^+ \to \cdot OOH$$
 (eq. 1.3)

$$\begin{array}{lllll} 2 \cdot 00H & \rightarrow & O_2 + H_2O_2 & (eq. \ 1.4) \\ H_2O_2 + \cdot O_2^- & \rightarrow \cdot OH^- + OH^- + O_2 & (eq. \ 1.5) \\ H_2O_2 + h\nu & \rightarrow & 2 \cdot OH & (eq. \ 1.6) \\ h^+ + H_2O & \rightarrow \cdot OH + H^+ & (eq. \ 1.7) \\ h^+ + OH^- & \rightarrow \cdot OH & (eq. \ 1.8) \end{array}$$

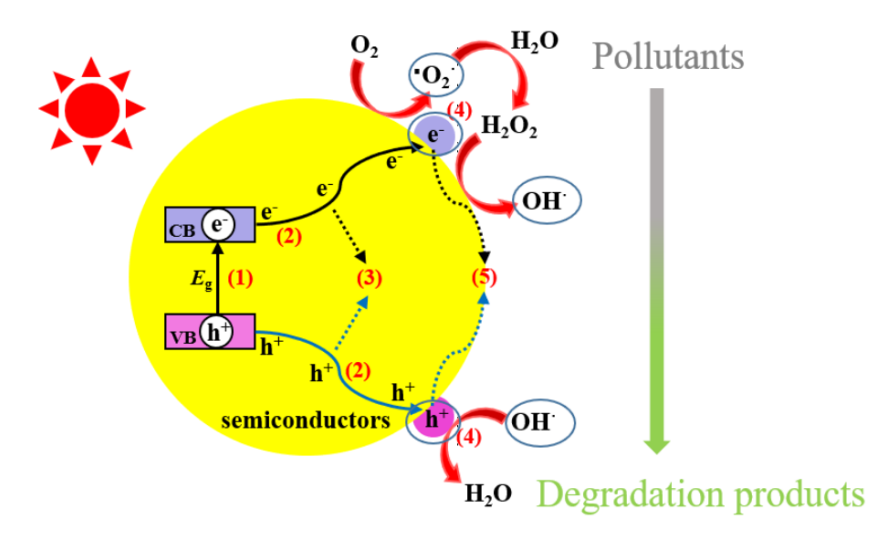


Figure 1.5: Schematic of photocatalytic degradation of organic pollutants.24

### 2.3 Photocatalytic water splitting

The reaction of water splitting (eq. 1.9) is thermodynamically uphill, requiring a standard Gibbs free energy ( $\Delta G_0$ ) of 237 kJ/mol<sup>25</sup>, and it is comprised of 2 half-reactions: hydrogen evolution reaction (HER, eq. 1.10) and oxygen evolution reaction (OER, eq. 1.11). The reaction pathway of OER is more complicated and commonly considered as the primary limitation for the overall kinetic of water splitting reaction. It requires a transfer of 4 electrons to form an oxygen molecule, causing the high energy barrier and the slow kinetics. The overall photocatalytic water splitting can be achieved through photoexcitation, in which case the HER and OER occur on the surface of the same semiconductor (Figure 1.6 left). On the other hand, the half-reaction of HER (OER) can be performed by adding electron donors (electron acceptors) as the sacrificial agent into the reaction medium to consume the photogenerated holes (electrons). Due to the lower redox potential required for the reaction of a sacrificial agent, working in the presence of the sacrificial agent provides a possibility to produce hydrogen or oxygen using semiconductors that are not capable of overall water splitting. Seq. 28,29

$$2H_2O \to 2H_2 + O_2$$
 ( $\Delta E=1.23V \text{ vs NHE}$ ) (eq. 1.9)

$$4H^+ + 4e^- \rightarrow 2H_2$$
 (0V vs NHE) (eq. 1.10)

$$2H_2O \rightarrow O_2 + 4H^+ + 4e^-$$
 (1.23V vs NHE) (eq. 1.11)

Furthermore, with the participation of shuttle redox mediators, the overall water splitting can be achieved by constructing a 2-step photoexcitation system (**Figure 1.6 right**).

Under this circumstance, the shuttle redox mediators with higher (lower) oxidation states work as the sacrificial agent for OER (HER), respectively. In addition, the deposition of co-catalysts is usually indispensable for both HER and OER reactions for most photocatalysts. The main function of the co-catalyst is decreasing the overpotential as well as creating active sites for the reaction. Generally, noble metals, such as Pt, Pd, Rh are widely used to promote HER, 33–37 whereas metal oxides of Co, Ni, Ir, and Ru are proven effective in promoting OER. 38–41

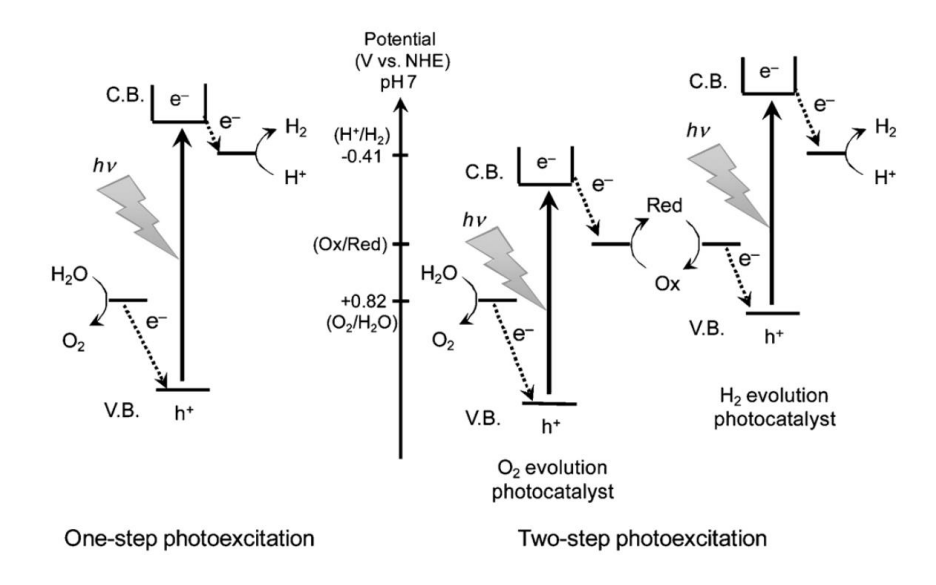


**Figure 1.6**: Schematic of photocatalytic water splitting for one-step (left) and two-step (right) photoexcitation systems. 42,43

# 2.4 Fundamental requirements for photocatalysts

As outlined above, a complete photocatalytic reaction is comprised of photon absorption, charge carrier migration, and surface redox reactions. The overall activity of a specific photocatalyst is determined by each of these steps. Thus, several fundamental requirements for an efficient semiconductor photocatalyst are listed below.

### 2.4.1 Absorption of sunlight

All photocatalytic reactions require the excitation of electrons from the valence band (VB) to the conduction band (CB) of the semiconductor. In other words, the energy of photons provides the driving force for photocatalytic reactions. The solar spectrum energy distribution is shown in **Figure 1.7**; the energy of photons in the UV region only accounts for 5% of the entire spectrum, compared to 43% in the visible region and 52% in the near-infrared region. From the perspective of efficient use of photons in the spectrum simultaneously overcoming the associated overpotential, photocatalysts with visible light response are preferable. The performance of some traditional photocatalysts, such as TiO<sub>2</sub>, ZnO, and SiC are limited by their wide band gap, leading to activation only under UV illumination. Over the past few decades, great efforts have been devoted to modifying

the band gap of semiconductors with a wide intrinsic band gap, to enhance visible light activation, and the details are present latter in this chapter.

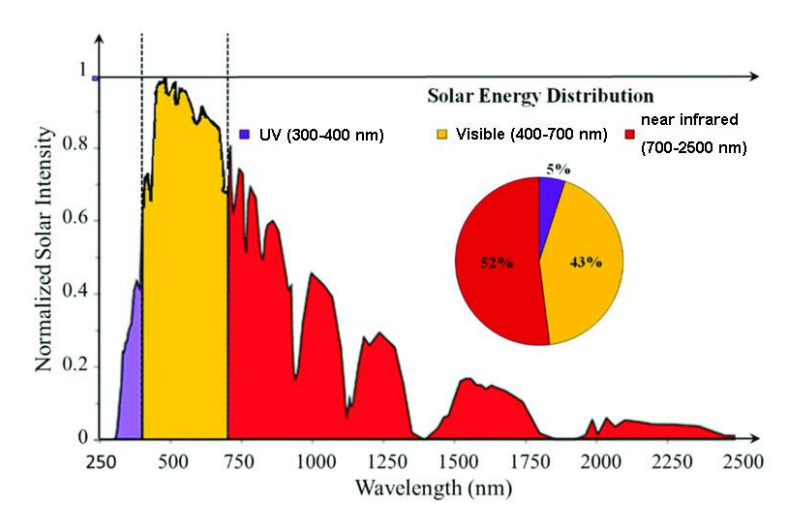
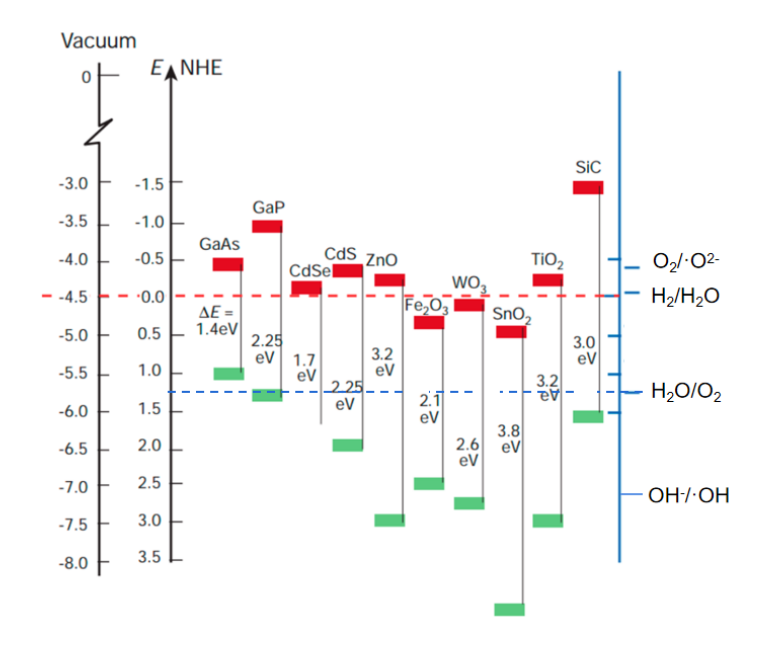


Figure 1.7: Energy distribution of solar spectrum.44

#### 2.4.2 Band position

Besides the band gap determining the capacity of photon absorption, the position of the valence band top (VBT) and conduction band bottom (CBB) of the semiconductor must be well-matched with the target reaction (**Figure 1.8**). The CBB should be located at an potential more negative than that required for the reduction reaction, while the VBT should be more positive than the potential required for the oxidation reaction. This proper placement of CBB and VBT endows the photogenerated electrons and holes with sufficient energy, thermodynamically ensuring the feasibility of the target reactions.

For the reactions of advanced photocatalytic oxidation that are applied for environmental purification, an important requirement is that the VBT should be positive enough (+2.7 V vs NHE) to generate sufficient ·OH radicals that are used for the degradation of pollutants. On the other hand, the potential required to generate ·O2<sup>-</sup> radicals is too negative (-0.33 V vs NHE) for many widely-used semiconductors such as TiO2, WO3, and CdSe, and the productivity of ·O2<sup>-</sup> is largely limited by the diffusion of oxygen in the solution and the adsorption of oxygen on the semiconductor surface.<sup>47</sup> As for water splitting, The energy of CBB should be more negative than the proton reduction potential (0 V vs NHE), and the VBT should be more positive than the water oxidation potential (1.23 V vs NHE).<sup>48</sup> Aiming for the photocatalytic overall water splitting, the CBB and the VBT of the photocatalyst must straddle the potentials required for both half-reactions.



**Figure 1.8**: Band gap and band position of the typical semiconductors (Vs NHE and Vacuum), The right axis presents the potential required for typical redox reactions. 47,49

### 2.4.3 Charge separation and transfer

The photogenerated carriers must be efficiently separated and transferred to the semiconductor surface. Otherwise, the recombination of electrons and holes will severely diminish photocatalytic performance. Time-resolved analysis has shown that the lifetime of photogenerated carriers is extremely short (ns-ps).<sup>50,51</sup>

The crystalline structure has a significant effect on the activity of the catalyst. Nanoscale materials tend to have superior activity compared to conventional bulk catalysts, and the nano-processing strategy has been already applied not only to photocatalysis but also to other traditional catalysis.<sup>52</sup> Reducing the crystalline size directly shortens the distance required for the photogenerated carriers to diffuse from the bulk to the surface, thus reducing the probability of charge carrier recombination. Simultaneously, the resultant large surface area exposes more active sites for accepting the reactant molecules. In the past decades, photocatalysts with various nanostructures, including 1D nanotubes and nanowires,<sup>53</sup> 2D nanosheets,<sup>54</sup> mesoporous materials,<sup>55</sup> have been developed.

Crystal facet engineering is another important strategy to optimize the charge carrier transfer process, in which the spatial separation of photogenerated electrons and holes is promoted by synthesizing the photocatalysts with specific anisotropic crystal facets. <sup>56,57</sup> By surface photovoltage imaging technique, J. Zhu *et al.* have confirmed that the photogenerated electrons and holes can be sufficiently separated to {010} and {011} facets of BiVO<sub>4</sub> crystals, driven by the surface built-in electric fields. <sup>58</sup> For anatase TiO<sub>2</sub> nanocrystals, the photoexcited electrons and holes preferentially transfer to {101} and {001} facets, respectively, as demonstrated by single-molecule fluorescence probe<sup>59</sup> and photochemical deposition study<sup>60</sup>.

#### 2.4.4 Stability and cost

The photocatalysts should be environmentally friendly and highly chemically stable, which is an important criterion for scaling-up. Besides, from an economic point of view, the photocatalyst should preferably be made from earth-abundant elements. In general, semiconductors containing elements harmful to the environment or human health should be avoided to exclude the potential risks. The photocatalysts must be capable of resisting corrosion from the specific working environment. For example, the composition of the wastewater is very complex and may contain a variety of corrosive chemicals, like heavy metals, strong acids, and bases. The chemical salts and impurities in seawater may shorten the service life of the photocatalysts used for seawater splitting.

On the other hand, a good photocatalyst should have sufficient resistance to photocorrosion, in which the structure of the photocatalyst itself may be damaged by the reactive or oxidative species generated by charge carriers under a long-term illustration. <sup>65</sup> Many promising novel catalysts have shown enhancement of visible light photocatalytic/photoelectrochemical activity, such as CdS, MoS<sub>2</sub>, and Cu<sub>2</sub>O. However, the photocorrosion phenomena lead to a decrease in the performances with the prolongation of illumination. It is illustrated that the decomposition of sulfide semiconductors can be caused by the oxidation of S<sup>2-</sup> ion to S<sup>0</sup> or SO<sub>4</sub><sup>2-</sup> (in the presence of oxygen). <sup>66,67</sup> The deactivation of Cu<sub>2</sub>O could be attributed to the oxidation of Cu<sub>2</sub>O to CuO by the photogenerated holes and/or the reduction of Cu<sub>2</sub>O to Cu by the photogenerated electrons. <sup>68,69</sup> For the practical applications of these catalysts, additional modifications, such as heteroatom doping <sup>70,71</sup> and heterojunction construction, <sup>72,73</sup> are indispensable to inhibit photocorrosion and thus ensure a stable activity during a long-term operation.

# 3. TiO<sub>2</sub> as photocatalyst

TiO<sub>2</sub> is commercially manufactured by millions of tons to be widely utilized as a pigment, paint additive, and sunscreen to name a few uses, due to its abundance, chemical stability, and easy availability in nature. The use of TiO<sub>2</sub> as a photocatalyst dates back to 1972. The discovery of the photocatalytic splitting of water on a TiO<sub>2</sub> electrode under UV light was first published by Fujishima and Honda.<sup>74</sup> This discovery has inspired numerous studies on TiO<sub>2</sub> photocatalysts. The photocatalytic properties of TiO<sub>2</sub> are closely related to its crystal structure and electronic band structure.

## 3.1 Crystal structure

The crystal structure of TiO<sub>2</sub> can be described using TiO<sub>6</sub> octahedra as a basic unit.<sup>75</sup> TiO<sub>2</sub> mainly exists in the form of three crystalline phases: anatase, rutile, and brookite, with different physical properties depending on the specific lattice structure (**Table 1.1**). In each phase, the octahedra are distorted in different symmetries and arrangements.<sup>76</sup> A unit cell of anatase includes four TiO<sub>2</sub> motifs, consisting of edge-sharing TiO<sub>6</sub> octahedra. Both cornersharing and edge-sharing TiO<sub>6</sub> octahedra are present in the unit cell of rutile and brookite, with two and eight TiO<sub>2</sub> motifs included, respectively.<sup>77,78</sup>

In the bulk form, rutile is the most thermodynamically stable among these three phases, while anatase and brookite are metastable phases and they can be transformed irreversibly to rutile by elevating the temperature. However, the stability of different phases can be varied due to the change in crystalline size. Zhang and Banfield reported that in the temperature range of 325°C to 750°C, anatase is the most thermodynamically stable phase once the particle size is below 11 nm. When the particle size is between 11 to 35 nm, brookite becomes the most stable phase. When the particle is bigger than 35 nm, it is rutile that has the highest stability. The higher stability of anatase in the nanoscale is ascribed to its lower surface energy compared to that of rutile nanocrystalline, reported by a theoretical study of DFT calculation. Besides, Zhang *et al.* 2 have noticed that the behavior of phase transition from anatase to rutile of TiO<sub>2</sub> crystalline is strongly size-dependent. As shown in **Figure 1.9**, the onset phase transition temperature increases with the initial particle size. In addition, the nucleation of rutile only takes place at the interfaces of the contacting anatase particles (< 60 nm). For bigger anatase particles (> 60 nm), the rutile nucleation can extend to the free surface and the bulk sites.

Anatase Rutile Brookite Ref. 83 Crystal structure Orthorhombic Tetragonal Tetragonal 84 I4<sub>l</sub>/amd P4<sub>2</sub>/mnm Space group Pbca a = 9.1600a = b = 3.7842a = b = 4.5937Lattice parameter 85–87 b = 5.4300c = 2.9581(nm) c = 9.5146c = 5.130085-87 Band gap(eV) 3.20 3.00 3.26 88-90 Density(g/cm<sup>3</sup>) 3.79 4.13 4.12

**Table 1.1:** Properties of TiO<sub>2</sub> crystalline in three phases: anatase, rutile and brookite

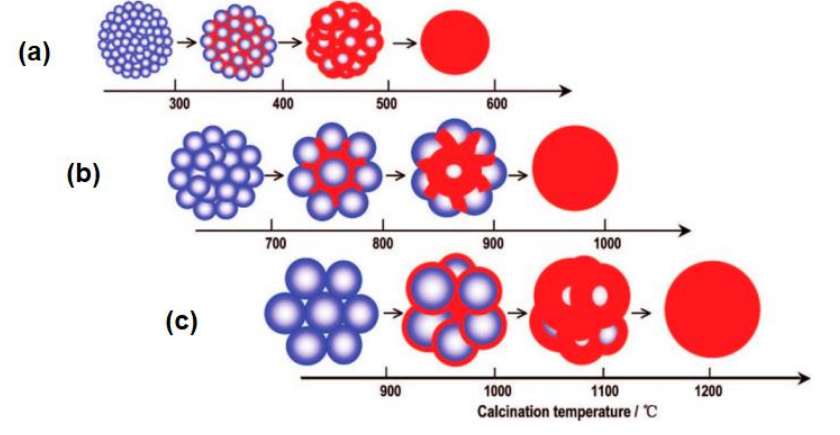


**Figure 1.9:** Proposed scheme for the phase transformations of TiO<sub>2</sub> with particle size (a) smaller than 10 nm, (b) in the range 10−60 nm, and (c) larger than 60 nm (blue: anatase; red: rutile).<sup>82</sup>

#### 3.2 Electronic band structure:

The optical property of a semiconductor is primarily defined by its electronic band structure. Band gap and defect states have an important influence on its absorption and responsivity to the photons in the specific region of the solar spectrum. From a theoretical perspective, the electronic band structure of  $TiO_2$  in different phases has been widely researched by previous studies.  $^{91-93}$  Rutile and brookite have a direct band gap while anatase has an indirect band gap. The corresponding band gap features have been proved by both theoretical and experimental work.  $^{91-93}$  As presented in **Figure 1.10 a**, The CBB of  $TiO_2$  is mainly composed of Ti 3d. The lower energy portion of Ti 3d can be further degenerated to  $e_g$  and  $e_g$  states due to the crystal field splitting. The VBT of  $TiO_2$  is comprised of O 2p, and the higher energy portion of O 2p is mainly the  $P_{\pi}$  orbital.  $^{94}$ 

Different intrinsic defects, depending on the specific synthetic process, including oxygen vacancy  $(V_{O}^{+})$ , titanium interstitials  $(Ti^{3+})$  and/or titanium vacancy  $(V_{Ti})$  are present in the materials, leading to a non-stoichiometric  $TiO_2$  crystalline. These intrinsic defects donate additional energy states in the band gap of  $TiO_2$  (**Figure 1.10 b**), which may affect the light harvest, charge carrier migration, and photocatalytic activity of  $TiO_2$ .  $^{95-97}$ 

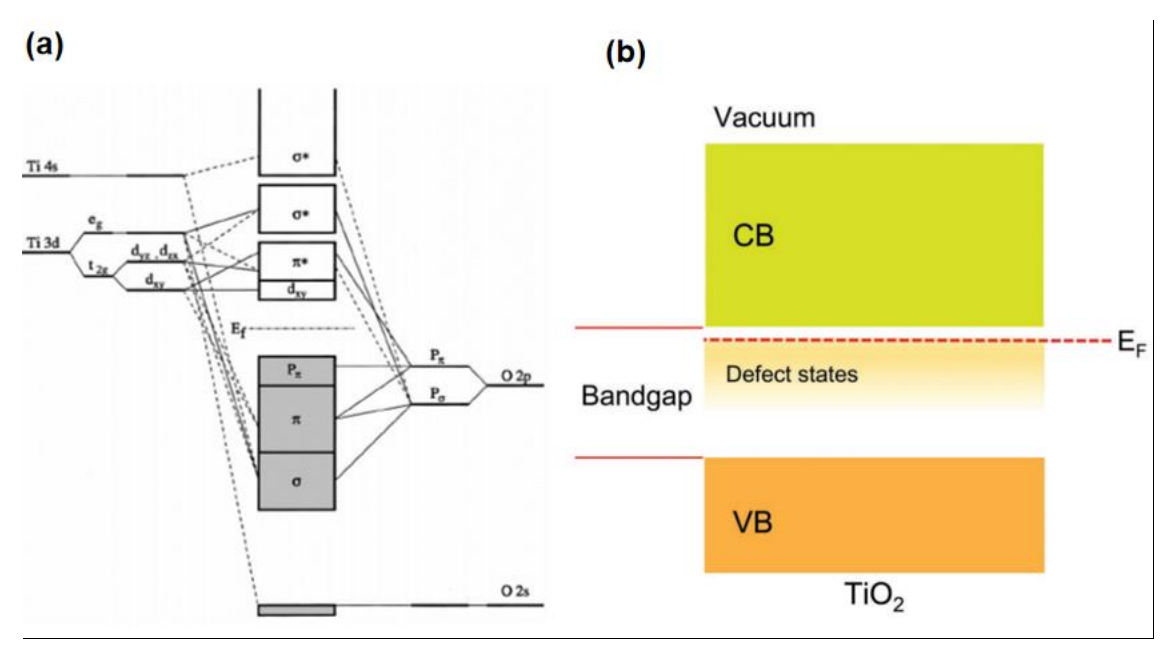


**Figure 1.10 :** (a) Detailed molecular orbital diagram of anatase TiO<sub>2</sub>.<sup>94</sup> (b) Schematic diagram of the electronic structure of TiO<sub>2</sub>.<sup>22</sup>

# 4. Band engineering of TiO<sub>2</sub> by doping

One of the disadvantages that limit the application of TiO<sub>2</sub> photocatalyst is its wide band gap, leading to extremely low utilization efficiency of photons in the visible region. To increase its overall activity, in the past few decades, much effort has been devoted to the development of advanced TiO<sub>2</sub>-based photocatalysts with visible-light response. One of the most widely studied modification methods is doping. This section highlights three

approaches to modifying the band structure TiO<sub>2</sub> for the materials to absorb longer wavelengths of light: (i) Cation-doping (ii) Anion-doping and (iii) Cation-anion co-doping.

## 4.1 Cation-doping

Cation-doping involves the replacement of Ti<sup>4+</sup> ions in the lattice by foreign cations. Transition metals are the most commonly used for cation-doped TiO<sub>2</sub>. Depending on the type of cation dopants, additional energy states could be introduced in the band gap. The types of cation dopants can be generally divided into two types: transition metals and rare-earth metals. Due to the simple synthetic method and low cost, doping with transition metals is more widely researched.

As 3d transition metal as Ti, studies focusing on TiO<sub>2</sub> doped by V<sup>98,99</sup>, Co<sup>100–102</sup>, and or Fe<sup>103–105</sup> have been widely carried out. Yu et al. <sup>98</sup> prepared V-doped TiO<sub>2</sub> via a modified sol-gel method and the synthesized material exhibits enhanced activity toward photocatalytic degradation of methylene blue (MB) under visible light illumination. Multiple oxidation states of V (V<sup>4+</sup> and V<sup>5+</sup>) were observed, and the energy states V<sup>4+</sup> and V<sup>5+</sup> in the band gap were proposed responsible for the increase in visible absorption. Das et al. 100 synthesized Co-doped TiO<sub>2</sub> using a simple hydrothermal method. In addition to the defect state of Co<sup>2+</sup>, the scheme for the extension of optical absorption also involves the ligand field transitions of  $Co^{2+}$ ,  $4T_{1g}(4F)$ - $4T_{1g}(4P)$ , as well as the generation of  $V_0^+$  associated with Co doping. It is worth noting that besides the type of cation, doping concentration also plays an important role in determining the photocatalytic activity of the cation-doped TiO<sub>2</sub>. Zhang et al. <sup>106</sup> observed that the intensity of the photoluminescence (PL) signal decreases with the increase of Fe doping concentration within the limit of 4% (Figure 1.11), which may related to the suppression of charge carrier recombination. The authors proposed that the doped Fe<sup>3+</sup> and the host Ti4+ act as hole traps and electron traps, respectively, thereby facilitating the separation of photogenerated carriers.

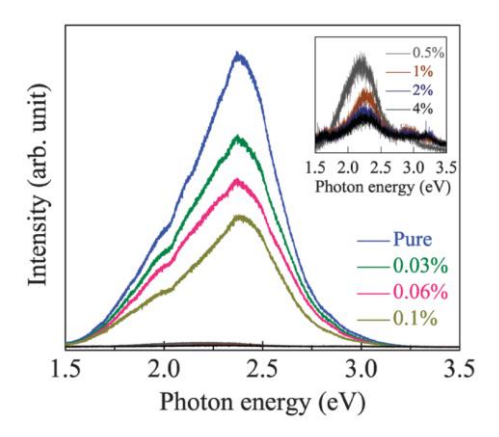


**Figure 1.11:** Room temperature PL emission spectra of Fe/TiO<sub>2</sub> films with increasing Fe concentration. Inset: enlarged PL emissions of the Fe/TiO<sub>2</sub> films ([Fe] = 0.5%, 1%, 2%, and 4%).<sup>106</sup>

Besides, some 4d and 5d transition metals (particularly Nb, Ta, W) have attracted widespread attention in the cation-doping of TiO<sub>2</sub>. The ionic radius of Nb<sup>5+</sup> (0.640 Å), Ta<sup>5+</sup> (0.640 Å) and W<sup>6+</sup> (0.600 Å) are close to that of Ti<sup>4+</sup> (0.605 Å),  $^{107}$  making it prospective to

produce the cation-doped TiO<sub>2</sub> with less lattice distortion, which is favorable for improving the doping concentration.

Nb or Ta doping is considered an effective way to enhance the carrier mobility of TiO<sub>2</sub>, and it has been utilized to improve the performance in the application of transparent conducting oxides, 108,109 photoelectrochemical systems, 110,111 solar cells 112-114 and Li batteries. 115,116 As a photocatalyst, the enhanced conductivity due to the introduction of Nb or Ta with a proper content generally favors the improvement of photocatalytic performance. 117-120 Qian et al. 119 synthesized Nb-doped TiO<sub>2</sub> nanotube array (NTs) via an anodization method followed by annealing at 550°C. The prepared material exhibited excellent activity for photocatalytic CO<sub>2</sub> reduction towards acetaldehyde (~500 μmol·g<sup>-1</sup>·h<sup>-1</sup>) with a high selectivity (99%) under simulated solar light illumination. Zhang et al. 120 reported the Nb-doped TiO<sub>2</sub> with enhanced photocatalytic activity for bleaching methylene orange (MO) aqueous under UV light illumination, and the improvement of photocatalytic performance was ascribed to the reoriented crystal facet exposure dominated by (001) due to the Nb-doping. Sengele et al. 121 presented that the Ta-doped TiO<sub>2</sub> photocatalyst eliminated diethyl sulfide, used as a simulant of chemical warfare agent, under the irradiation of UV-A. However, the effect of Nb or Ta-doping on the reduction of the band gap is limited (Figure 1.12 a), which is primarily due to the upper /similar energy level between Nb 4d/Ta 5d and Ti 3d orbitals. 122-124 Although the yellow-color Nb-doped TiO2 responding to visible light has been also reported, 125 it should be noted that the visible response is attributed to the defect states (Ti<sup>3+</sup> and surface peroxo) rather than the energy states of Nb itself (Figure 1.12 b).

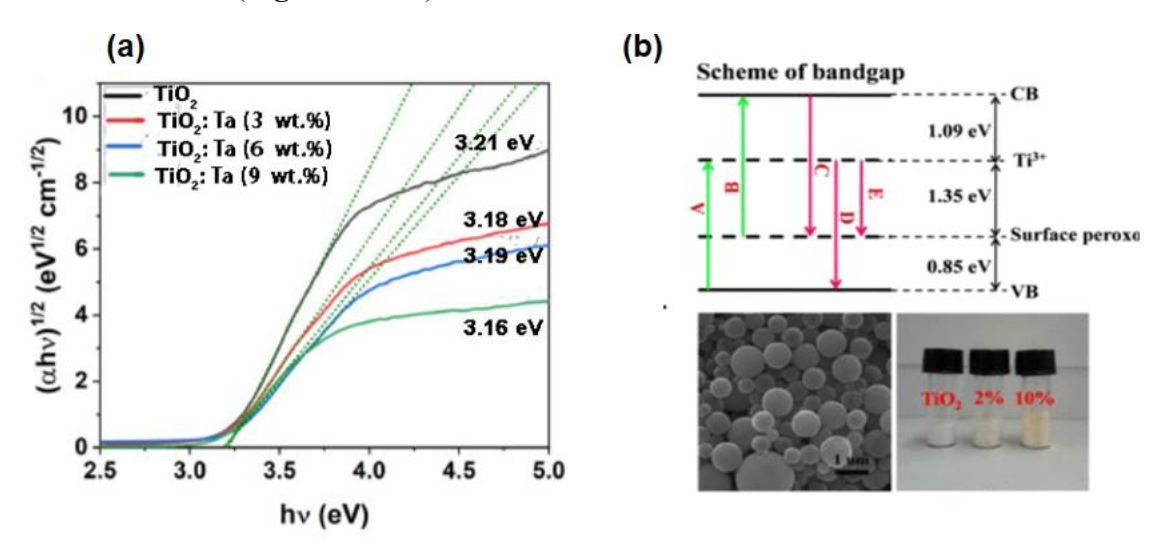


**Figure 1.12:** (a) Band gap of Ta-doped TiO<sub>2</sub> samples.<sup>124</sup> (b) scheme of band gap, SEM image and optical image for the visible response of Nb-doped TiO<sub>2</sub>.<sup>125</sup>

Compared to doping with Nb or Ta, doping with W is more useful in improving the visible absorption of TiO<sub>2</sub>. For example, by using the density functional theory method, Gong *et al.*<sup>126</sup> demonstrated the hybridization of Ti 3d and W 5d due to W doping could shift the absorption spectra of W-doped TiO<sub>2</sub> to visible light region, and the theoretical calculation is in good accord with their experimental characterization of UV-vis spectra (**Figure 1.13 a**).

Lorret *et al.*<sup>127</sup> reported a W-doped TiO<sub>2</sub> synthesized via sol-gel method which can be activated by both UV and visible light for the reaction of photodegradation of methylene blue (MB). In addition to the slight downward shift of the conduction band of the W-doped TiO<sub>2</sub>, multiple oxidations of W (usually from W<sup>4+</sup> to W<sup>6+</sup>) were indicated in several studies (**Figure 1.13 b**). <sup>128,129</sup>

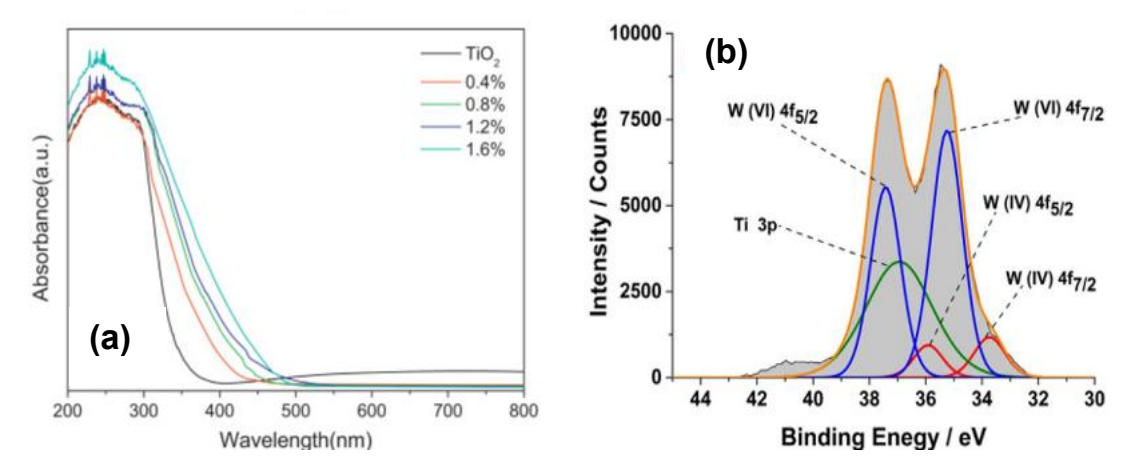


**Figure 1.13:** (a) The diffuse reflectance UV–vis DRS spectra of pure TiO<sub>2</sub> and W-doped TiO<sub>2</sub> samples. (b) The W 4f XPS peaks for the W-doped TiO<sub>2</sub> (W: 4.47 at.%) grown via aerosol-assisted chemical vapor deposition. (130)

## 4.2 Anion-doping

The research on anion-doped  $TiO_2$  was pioneered by Asahi and his coworkers in 2001, in which the prepared N-doped  $TiO_2$  showed activity in the gas phase for degradation of MB and acetaldehyde under visible irradiation ( $\lambda$ =500 nm). Since then, doping  $TiO_2$  with other anions, such as C,  $^{132}$  P,  $^{133}$  S,  $^{134}$  has been reported. The main motivation for conducting anion-doping is to introduce acceptor states of the p orbitals of the anion above the VBT of  $TiO_2$ . Consequently, the photo-response of the anion-doped materials can be extended toward the visible light region.

Among various options of anion, N-doped TiO<sub>2</sub> materials are still the most widely researched in the field. One important reason for the preference of N is that N 2p orbitals are promising to be efficiently mixed with O 2p, leading to a narrower band gap by upshifting the VBT. On the contrary, doping with C and P may introduce deep localized states in the band gap, since the p orbitals of C and P are much higher than O 2p (**Figure 1.14**). <sup>131,135</sup> These localized energy states may result in a difficulty of charge transfer and a significant decrease in the oxidation power of the photogenerated holes. Although doping with S is expected to result in a similar band-narrowing effect as that of N, its bigger ion radius requires a high formation energy of S dopants in the lattice of TiO<sub>2</sub>. <sup>136</sup> Consequently, the solubility of S is low, and the localized energy states may be introduced in the band gap, limiting charge carrier mobility. <sup>137</sup>

Compared to the cation dopants, the existence of the doped N in  $TiO_2$  lattice is more complex. Apart from substituted N (N<sub>s</sub>), <sup>131,138</sup> formed by replacing O<sup>2-</sup> with N<sup>3-</sup>, N dopants

can also be present in the interstitial positions (N<sub>i</sub>)<sup>139,140</sup> of TiO<sub>6</sub> octahedra or exist in the form of NO<sub>x</sub> complexes (NO or NO<sub>2</sub>).<sup>141,142</sup> It is demonstrated that the N species present in a specific N-doped TiO<sub>2</sub> sample is greatly influenced by the condition of nitridation. Asahi *et. al.* reported that the formation of N<sub>s</sub> is favored under a reduced condition while N<sub>i</sub> and NO<sub>x</sub> are more stabilized in an O-rich environment.<sup>143</sup> On the other hand, there is a point under debate concerning the energy states caused by the doped N species. Some researchers claimed that the narrowed band gap originated from the upshift of VBT due to the hybridization of N 2p and O 2p,<sup>144,145</sup> while others ascribed the visible response to the localized defect states in the band gap above the VBT.<sup>146,147</sup> The density of states (DOS) work indicated an important role of the amount, as well as the type of N sites involved on the resulting electronic structure of the resultant N-doped TiO<sub>2</sub>.<sup>142,148</sup>

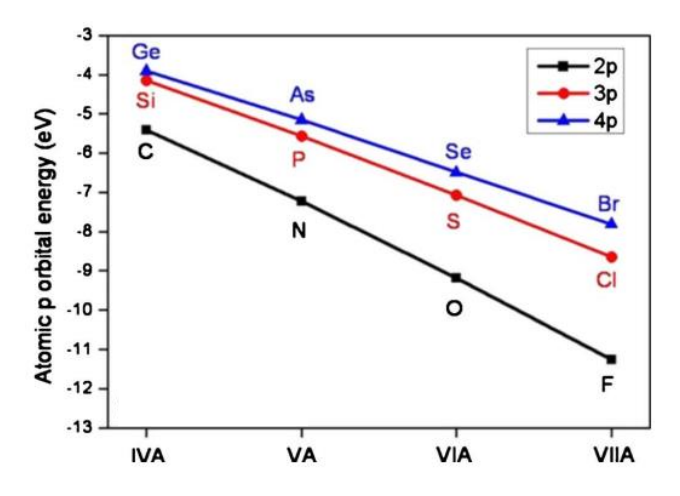


Figure 1.14: Atomic p orbital energy of selected non-metal elements. 149

Although the N-doped TiO<sub>2</sub> materials exhibit visible-light-activated performance, these mono-doped catalysts suffer from the weakness of inefficient internal charge transport. Photo-152 Romualdo Torres *et al.* 150 reported that the incident photo-to-current efficiency (IPCE) of the N-doped TiO<sub>2</sub> was lower than that of undoped TiO<sub>2</sub> under illumination in the UV region. The decrease of charge carrier dynamic is further confirmed by time-resolved studies. 153,154 It is shown that the charge separation efficiency under visible-light excitation was only one-third of that under UV excitation in the N-doped TiO<sub>2</sub>. It is explained by the generation of oxygen vacancy (Vo<sup>+</sup>) associated with the N doping, which could act as carrier traps. 155 Besides, The oxidative power of the photogenerated holes exited by the visible illumination was fund diminished compared to those generated by UV light. 147,156 Tachikawa *et al.* 156 reported the direct photocatalytic oxidation of ethylene glycol (C<sub>2</sub>H<sub>6</sub>O<sub>2</sub>) was only achieved under the irradiation of 355 nm UV laser but not by using 460 nm visible laser.

# 4.3 Cation-anion co-doping

As discussed above, conducting mono-doping with cation or anion could introduce localized energy states (electron donors for cation-doping; electron acceptors for anion-doping) in the band gap of TiO<sub>2</sub>, the observed visible absorption is primarily related to the

transition involving these energy states. However, these localized energy states possibly function as deep charge carrier traps limiting the mobility of the photogenerated charge carriers. Besides, in the case of mono-doping, defects such as  $V_0^+$  and  $Ti^{3+}$  could be generated to neutralize the additional charge brought by the dopants. These defects may act as charge recombination centers, reducing the photocatalytic activity although they contribute to visible light absorption.

To overcome the disadvantages of mono-doping, another approach has been developed. It involves introducing both cation and anion (co-doping) in the lattice of TiO<sub>2</sub>, in which Ti<sup>4+</sup> and O<sup>2-</sup> are substituted by the cation and anion respectively. With the charge compensation effect between the cation and anion, fewer defects are expected. In the last few years, both theoretical and experimental studies have demonstrated the potential of co-doped TiO<sub>2</sub>. Therefore, the following part is a short review of the previous studies.

#### 4.3.1 Theoretical study

#### 4.3.1.1 Ideal model of co-doping

At the beginning of the 2010's several *ab initio* calculations<sup>157</sup> have proposed charge-balanced co-doping as an approach to deeply modify the TiO<sub>2</sub> optoelectronic structure by introducing stoichiometric quantities of cation (M<sup>n+</sup>) and anion (A<sup>p-</sup>). That was after described by Brancho and Bartlett:<sup>158</sup>

$$Ti_{(1-x)}^{4+}M_x^{(4+n)+}O_{(2-\frac{n}{p}x)}^{2-}A_{\frac{n}{p}x}^{(2+p)-}$$
 (eq. 1.12)

Thanks to the charge compensation between cation and anion, the defects acting as charge recombination centers could be limited. Another advantage of co-doping is that it allows the insertion of a larger amount of doping species compared to mono-doping. This could favor the formation of a special type of co-doped TiO<sub>2</sub>, which is known as co-alloyed TiO<sub>2</sub>. As shown in **Figure 1.15**, when the doping concentration is low, the energy levels introduced by the cation (donor) and anion (acceptor) do not overlap completely with the band of TiO<sub>2</sub>. Thus, these energy levels are still localized to some degree, limiting the charge mobility in the co-doped TiO<sub>2</sub> material. In the case of co-alloyed TiO<sub>2</sub>, due to the increase of doping concentration, sufficient hybridization between the energy levels of dopants and the ones of TiO<sub>2</sub> could be achieved, creating a continuum of energy levels, overlapping with the VBT and CBB of TiO<sub>2</sub>. This situation is expected to be more favorable for the generation of mobile charge carriers under visible light than localized energy states that are formed by mono-doping. <sup>158,159</sup>

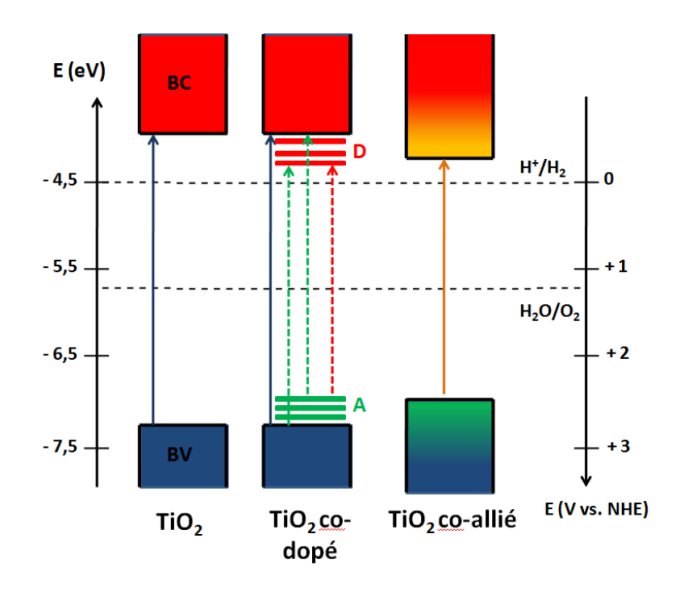
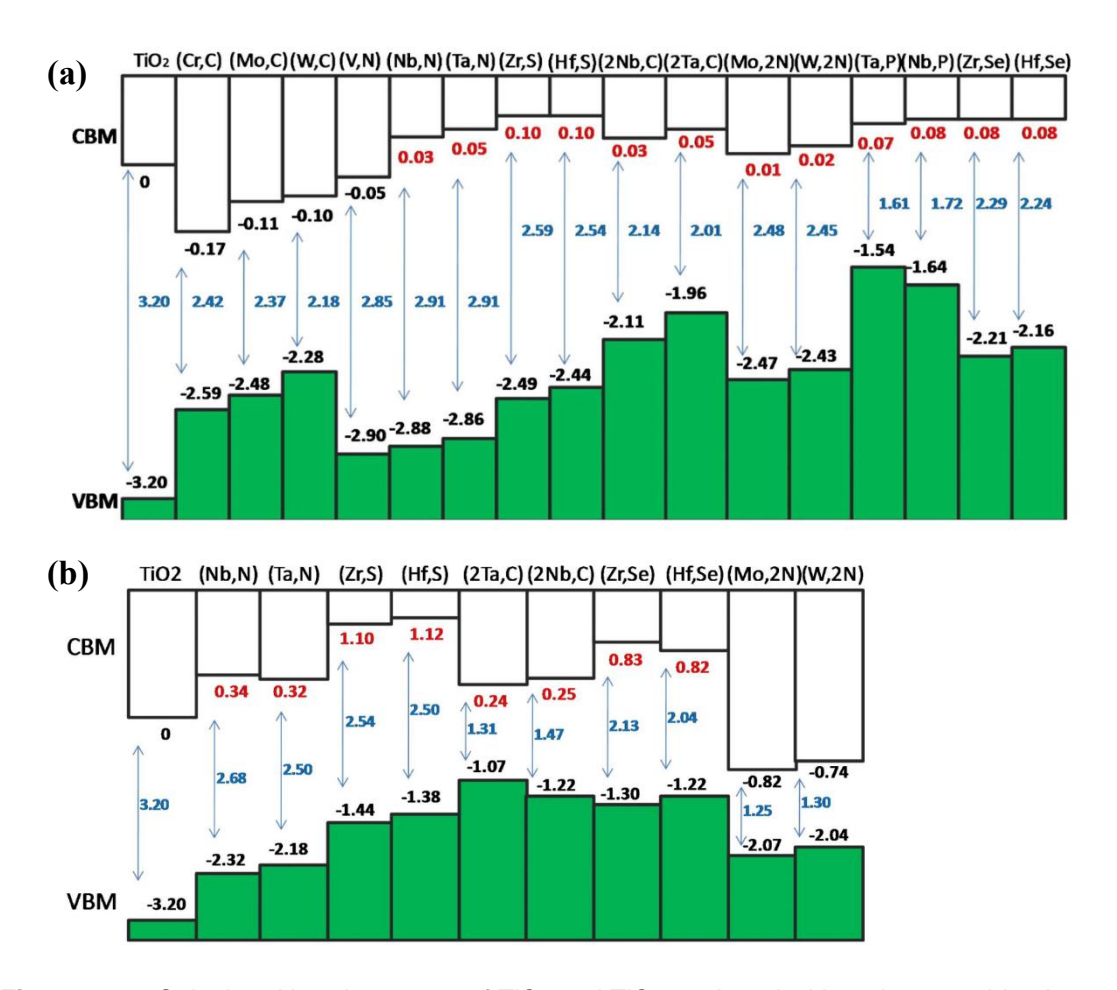


Figure 1.15: Band structures of TiO<sub>2</sub>, co-doped TiO<sub>2</sub> and co-alloyed TiO<sub>2</sub>.<sup>160</sup>

#### 4.3.1.2 Selection of cation-anion combination

When applying co-alloyed/co-doped TiO<sub>2</sub> materials in photocatalysis, one that needs to be considered is the cation-anion combination. Considering the huge number of possible combinations, it is impossible to try all of them. Luckily, the theoretical study has guided the selection of cation-anion combinations, targeting different types of photocatalytic reactions.

Based on a DFT study, Yin et al. have made efforts to identify potential candidates among the co-doped anatase TiO<sub>2</sub> for the application of water splitting. <sup>149</sup> The band structure resulting from the introduction of different cation-anion combinations into anatase structure was analyzed. They concluded that the band gap value and the band position of the co-doped TiO<sub>2</sub> were influenced by both the type of cation-anion combination and the doping concentration. Under low concentration (Figure 1.16 a), (Mo,2N) and (W,2N) are predicted to be the best cation-anion combinations. Mo<sup>6+</sup> and W<sup>6+</sup> allow more nitrogen to be inserted into the TiO<sub>2</sub> lattice compared to Nb<sup>5+</sup>, Ta<sup>5+</sup> and V<sup>5+</sup>, reducing the band gap to 2.48 eV and 2.45 eV. Besides, the conduction bands of TiO<sub>2</sub> modified by (Mo,2N) and (W,2N) co-doping remain higher than that of TiO2, which is important to keep the reducing power of photogenerated electrons. On the other hand, under a higher doping concentration (Figure 1.16 b), (Ta-N) and (Nb-N) co-doping are the best choices to obtain the best performance for water splitting. The band gap of the resultant materials are reduced to 2.68 eV and 2.50 eV, respectively, and their CBB is located more than 0.3 eV higher than that of TiO<sub>2</sub>. As for (Mo,2N) and (W,2N) co-doped TiO<sub>2</sub>, an undesirable downward shift of CBB is observed, which could limit the HER.



**Figure 1.16:** Calculated band structure of TiO<sub>2</sub> and TiO<sub>2</sub> co-doped with various combinations of cation and anion under low (a) and high doping concentration (b) (The CBM of pure TiO<sub>2</sub> is set to zero as the reference and the band gap is corrected using a scissor operator) <sup>149</sup>

In another study published Wang *et al.* made a prediction of the photocatalytic activities of TiO<sub>2</sub> (anatase) co-doped with different cation-anion combinations for an application of organic pollutant degradation.<sup>137</sup> The band gap value and band position were calculated using a DFT+U method. According to their results, (Ta,N) co-doping is expected to be the best choice, which not only broadens the range for visible absorption but also raises the reducing power of the photogenerated electrons by upward shifting the CB. Consequently, more superoxide acid and superoxide radicals can be generated during the catalytic reaction.

It is noteworthy that both authors pointed out the important influence of the ion radius of the dopants on the activity of the resultant co-doped TiO<sub>2</sub> materials. S, P and Se are considered to be not suitable for the co-doped or co-alloyed TiO<sub>2</sub>. Due to the large size mismatch between these dopants and oxygen, limited solubility of dopants was predicted. As a result, localized acceptor energy states could be introduced above the VBT, limiting the mobility of charge carriers.

#### 4.3.1.3 Difference between ideal model and realistic material

Although numerous computational studies carried out on the co-doped system have predicted a charge compensation effect between the cation and anion dopants  $^{149,161-163}$ , it should be noted that these studies were based on the prerequisite that the host  $TiO_2$  is a perfect crystal. However, in reality, it is almost impossible to have a perfect stoichiometric ratio between different elements in the compounds. In the case of  $TiO_2$ , a n-type semiconductor feature is commonly observed, for which the crystal is constructed in a Ti-rich/O-poor environment. Therefore, the aforementioned studies did not take into account the possible intrinsic defects, such as  $V_O^+$  or titanium vacancies ( $V_{Ti}$ ), which may also influence the physicochemical properties of the co-doped  $TiO_2$  system.

Williams *et al.*  $^{164}$  analyzed the evolution of the charge compensation scheme in (Nb,N) and (Ta,N) co-doped anatase structure with temperature through a DFT calculation, with the presence of intrinsic defects. The authors demonstrated that the ideal model of co-doping is unachievable. The calculation was conducted under both n-type (Ti-rich/O-poor) and p-type (Ti-poor/O-rich) conditions, where  $V_{\rm O}^+$  and  $V_{\rm Ti}$  are dominant intrinsic defects respectively.

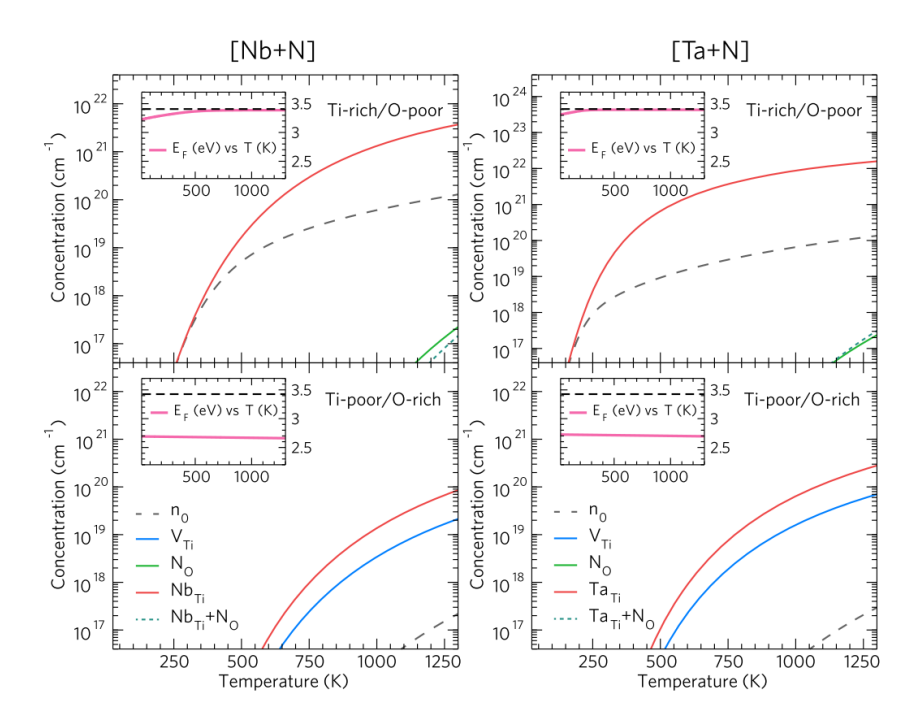


**Figure 1.17**: Equilibrium concentrations of metal dopants  $M_{Ti}$  (red line, where M = Nb or Ta), titanium vacancies ( $V_{Ti}$ , blue line), substitutional N on O sites ( $N_O$ , green line), complexes of substitutional nitrogen and metal dopants ( $M_{Ti} + N_O$ , dotted teal line, where M = Nb or Ta) and electron carriers ( $n_O$ , dashed orange line) calculated as a function of temperature. The left panel gives the concentrations for Nb doping, the right for Ta doping. The upper and lower panels correspond to Ti-rich/O-poor and Ti-poor/O-rich conditions, respectively. The insets show the self-consistent Fermi level ( $E_F$ , magenta line) as a function of temperature, with the zero of the energy scale set equal to the VBT and the dashed line indicating the position of the CBB.

As shown in **Figure 1.17**. Their results show that under both conditions, the substitution of Ti by Nb (Nb<sub>Ti</sub>) or Ta (Ta<sub>Ti</sub>) is favorable due to the low formation energy. However, introducing nitrogen into the lattice by replacing oxygen relatively requires a higher formation energy, no matter in the form of single dopants (N<sub>O</sub>) or the complex with the cation (Nb<sub>Ti</sub>+N<sub>O</sub>, Ta<sub>Ti</sub>+N<sub>O</sub>). Consequently, the concentration of nitrogen was considered significantly lower than that of Nb or Ta across all values of temperature. Instead, under the n-type condition, the positive charge brought by the cation dopants is predominantly compensated by electron carriers (n<sub>O</sub>), resulting in an  $E_F$  close to the CBB. On the other hand, under the p-type condition, V<sub>Ti</sub> is the main defect for charge compensation. In conclusion, they pointed out that nitrogen may only exist in the form of complex such as NH<sub>4</sub><sup>-</sup> with a very low concentration in the (Nb,N) and (Ta,N) co-doped anatase structure. In other words, achieving an ideal charge-balanced doping in a non-stoichiometric TiO<sub>2</sub> is impossible according to their calculations. Considering the complexity of the chemical composition of the realistic substance, future studies combining theoretical calculation and experiment are needed.

#### 4.3.2 Experimental study

Following the promising catalytic properties predicted by the theoretical studies, research efforts experimentally have focused on co-doped/co-alloyed TiO<sub>2</sub> materials. Among numerous cation-anion combinations, the groups of transition metals (in particular 3d, 4d and 5d blocks) and nitrogen are the most widely researched. Thus in the following part, we will introduce the corresponding synthesis and application of some representative co-doped TiO<sub>2</sub> materials reported in recent studies.

### 4.3.2.1 Co-doping with 3d metal and N

R. Raiswal *et al.* prepared (V, N) co-doped TiO<sub>2</sub> via a sol-gel method, in which Triethylamine and ammonia metavanadate were used as precursors to introduce V and N, respectively. The synthesized co-doped catalyst exhibited an enhanced visible light photocatalytic activity for rhodamine B (RhB) degradation, compared to the undoped TiO<sub>2</sub> and N or V mono-doped TiO<sub>2</sub>. The authors proposed a synergy effect between V dopants and N dopants increasing visible light absorption and efficiency of charge carrier separation (**Figure 1.18**). The visible light absorption originated from the excitation involving the energy states of V 3d and N 2p in the band gap. Due to the strong V-N bond, the interaction between V 3d and N 2p orbitals lowers the energy levels of N 2p, and thereby increases the mixing of N 2p and O 2p states, which is favorable for the trap of photogenerated holes. On the other hand, the localized V 3d states could act as electron traps, diminishing the possibility of charge carrier recombination. In addition, they observed that the V dopants presented two oxidation states (V<sup>4+</sup> and V<sup>5+</sup>), and a partial of V<sup>5+</sup> existed in the form of V<sub>2</sub>O<sub>5</sub> on the sample surface, facilitating the electron injection into the V<sup>5+</sup> species.

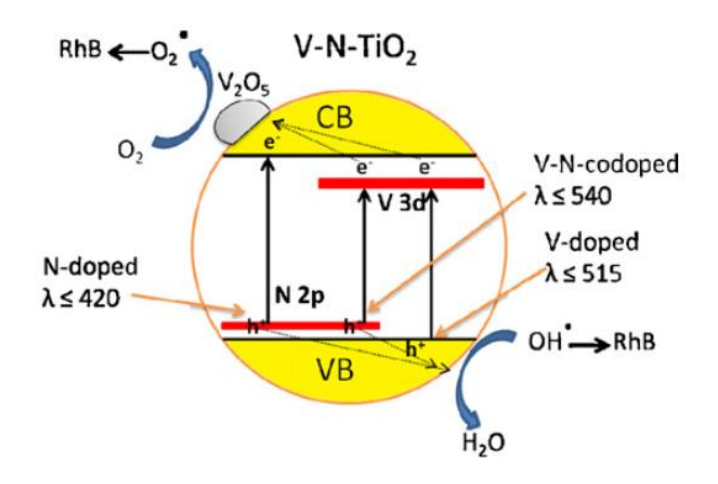


**Figure 1.18:** Schematic diagram for photocatalytic degradation of RhB dye over(V,N) co-doped TiO<sub>2</sub> under the illumination of visible light. <sup>165</sup>

(Fe,N) co-doped TiO<sub>2</sub> catalysts were synthesized by a sol-gel method followed by annealing in ammonia.<sup>166</sup> A higher degree of crystallization and pronounced mesoporosity with narrow pore-size distribution were observed on the prepared co-doped materials. Under visible illumination, the (Fe,N) co-doped TiO<sub>2</sub> showed enhanced activity for the degradation of MO compared to the mono-doped counterparts and commercial P25 (increase by 137%). In another study published by, Naik *et al.*, the (Fe,N) co-doped TiO<sub>2</sub> was applied to photodegradation of phenol.<sup>167</sup> The enhanced visible light activity was attributed to the effective reduction of the band gap due to the co-doping of Fe and N. Besides the mixing between Fe 3d and Ti 3d states, the authors also proposed that the Fe t<sub>2g</sub> levels may mixed with O 2p and N 2p states, leading to an upward shift of the VBT. Considering that both the introduction of Fe and N contribute to decreasing the positive charge in the co-doped system, other defects with positively charged centers might play an important role in the case of (Fe,N) co-doping.

#### 4.3.2.2 Co-doping with 4d metal and N

Breault *et. al* prepared anatase-structured TiO<sub>2</sub> co-doped with Nb and N by a sol-gel process (Nb doping) followed by calcination under ammonia flow (N doping). The prepared (Nb,N) co-doped TiO<sub>2</sub> nanoparticles had an onset of optical absorption of about 580 nm, indicating an effective reduction of band gap from 3.2 eV (pure TiO<sub>2</sub>) to 2.0 eV. The Nb, N co-doped sample presents the best activity for MB degradation under the irradiation of simulated solar light (AM1.5). In their follow-up work, a series of (Nb,N) co-doped TiO<sub>2</sub> with varying mole percentages of niobium substituting for titanium (1-30 mol%) were prepared via the same method and used for exploring the composition-dependence of the photocatalytic activity. The best photocatalytic activity was observed on the (Nb,N) co-doped sample comprising 25 mol% Nb with a narrowed band gap of 2.21 eV. Furthermore, this optimum photocatalyst was then decorated with RuO<sub>2</sub> as a co-catalyst using a chemical impregnation technique and applied for visible-light-activated water oxidation. The

In the previous work on our team, anodization of titanium foils in the presence of an ammonium fluoroniobate salt ((NH<sub>4</sub>)<sub>5</sub>[(NbOF<sub>4</sub>)(NbF<sub>7</sub>)<sub>2</sub>]) followed by calcination at 500°C for 2 h under ammonia was implemented for the preparation of aligned (Nb, N) co-doped TiO<sub>2</sub> nanotube arrays (NTs).<sup>171</sup> In the synthesis, the fluoroniobate complex provides simultaneously the source of Nb dopants and fluoride ions that are required for the formation of nanotubes. The co-doped material exhibits enhanced photoelectrochemical conversion efficiency in the visible light range when compared to Nb- or N-doped TiO<sub>2</sub>-NTs (Figure 1.19 a). By further adjusting the content of Nb in the (Nb,N) co-doped structure, the optimized sample (0.50 Nb/TiO<sub>2</sub>-NTs d.NH<sub>3</sub> in Figure 1.19 b) showed a light conversion yield which is more than 2 times and 5 times greater than that of N-doped TiO<sub>2</sub>-NTs in the visible region ( $\lambda$ >400 nm) and the UV region, respectively. However, it is noticed that the conversion efficiency of the (Nb,N) co-doped TiO<sub>2</sub>-NTs is lower than the undoped TiO<sub>2</sub> in the UV region, indicating a certain decrease of charge carrier mobility after the co-doping process. Similar efficiency loss in the UV region was also reported by Favet et al.. 172 This may suggest the existence of the localized energy states in the band gap. In other words, the ideal co-alloyed model with a fully hybridized energy band may not achieved in our case of (Nb,N) co-doping.

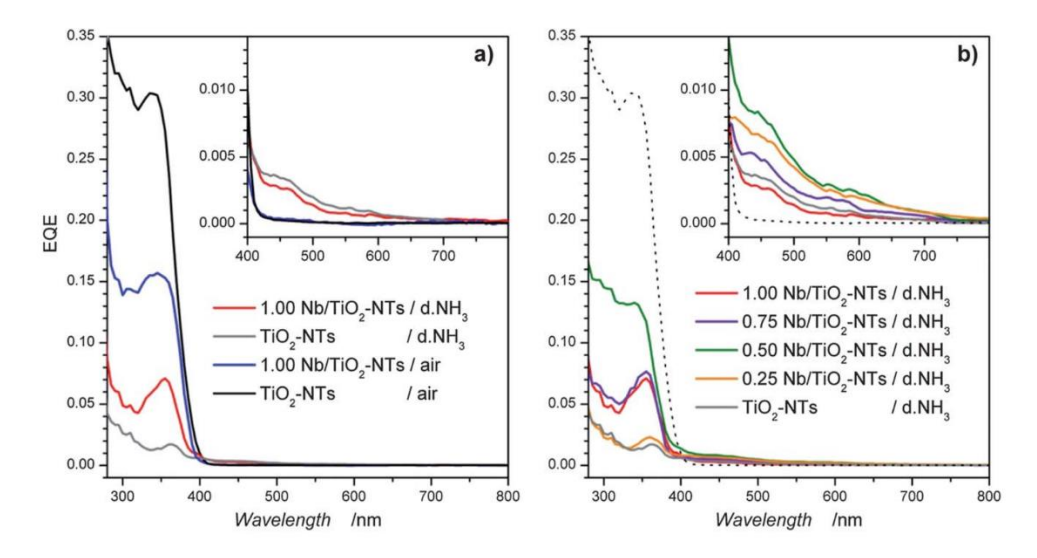


**Figure 1.19**: External Quantum Efficiency (EQE) in 0.1 mol L<sup>-1</sup> H<sub>2</sub>SO<sub>4</sub> and applied potential of +0.2 V vs. MSE for (a) TiO<sub>2</sub>-NTs, N-, Nb- and (Nb,N)-co-doped TiO<sub>2</sub>-NTs. Inset is an enlargement of the EQE in the visible spectral region. (b) EQE for (Nb,N) co-doped TiO<sub>2</sub>-NTs with different content of niobium annealed in NH<sub>3</sub>. The dotted line corresponds to the TiO<sub>2</sub>-NTs sample annealed in air. <sup>171</sup>

Gao et al.<sup>173</sup> prepared (Zr,N) co-doped TiO<sub>2</sub> nanoparticles using a sol-gel method combined with a hydrothermal method. In the sol-gel process, zirconium butoxide was mixed with titanium butoxide to introduce Zr first. Then, the obtained sol was subjected to a post-hydrothermal reaction with the presence of ammonia water to produce the (Zr,N) co-doped TiO<sub>2</sub>. The co-doped material exhibited an enhanced photocatalytic activity for the degradation of acid red 88 and benzene degradation under visible light irradiation, compared to the undoped TiO<sub>2</sub> and N-doped TiO<sub>2</sub>. XPS and DRS studies revealed that the N dopants were mainly located on the surface layer of the catalyst and induced a surface state close to

VBT. On the other hand, lattice Ti<sup>4+</sup> ions were substituted by Zr<sup>4+</sup> ions, resulting in an upward shift of CBB of the co-doped material, thereby promoting the reduction of oxygen into active oxygen radicals. It should be noted that Zr<sup>4+</sup> can not bring addictional positive charge compared to Ti<sup>4+</sup>, thus it may not contribute to increase the amount of N-dopants according to eq. 1.12.

### 4.3.2.3 Co-doping with 5d metal and N

Hoang *et. al* prepared (Ta,N) co-doped rutile TiO<sub>2</sub> nanowire arrays (NWs) on fluorine-doped tin oxide (FTO) coated glass substrates through a solvothermal method followed by nitridation under ammonia.<sup>174</sup>. The color of (Ta,N) co-doped samples varied from yellow to green with the increase of Ta doping concentration (0.11 to 3.47 atomic %). The synthesized (Ta,N) co-doped material was used as a photoanode for photoelectrochemical water oxidation reaction. The (Ta,N) co-doped TiO<sub>2</sub> NWs with the optimum Ta concentration (0.29 atomic %) demonstrated significant improvement in photoelectrochemical performance with the photocurrent reaching 0.52 and 0.18 mA/cm<sup>2</sup> under AM 1.5 G and visible light (>420 nm) illumination, respectively, compared with 0.26 and 0.13 mA/cm<sup>2</sup> for N-doped TiO<sub>2</sub> NWs (**Figure 1.20**). It is interesting to note that an amorphous layer was observed only on the surface of the N-doped TiO<sub>2</sub> NWs but not on the surface of (Ta,N) co-doped samples The authors proposed that this amorphous could act as charge recombination centers. Thus, conducting (Ta,N) co-doping not only extended visible light response but also improved hole extraction and PEC performance.

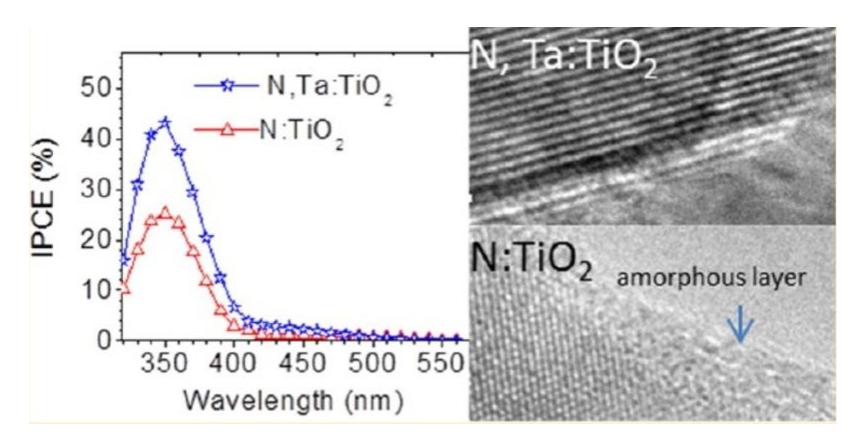


**Figure 1.20:** incident photon conversion efficiency (IPCE) spectrum measured at 1.23 V<sub>RHE</sub> (left) and the TEM images of N-doped TiO<sub>2</sub> NWs and (Ta,N) co-doped TiO<sub>2</sub> NWs.

Gupta et. al<sup>175</sup> applied the (Ta,N) co-doped TiO<sub>2</sub> nanoparticles to photocatalytic advanced oxidation reactions, including organic dye degradation and sterilization. The co-doped materials were synthesized by a sol-gel method followed by annealing under ammonia. The doping concentration of Ta was adjusted from 3 to 30 mol%. It was shown that the band gap of the co-doped samples decreased with the increase of Ta concentration, in the range of 3 to 20 mol% (2.20 eV at 20 mol%). However, with a further increase of Ta concentration, the band gap enlarged instead. The XRD result showed that phase segregation in the form of Ta<sub>2</sub>O<sub>5</sub> occurred at a higher Ta doping concentration. The photocatalytic of the series of co-doped samples was evaluated first by degradation of MB solution (pH=7) under sunlight

irradiation (4.14 kWh.m²), and the one with Ta concentration of 20 mol% was determined as the optimized catalyst (denoted as  $20\text{-Ta/N-TiO}_2$ ). Then, the photocatalytic activity of  $20\text{-Ta/N-TiO}_2$  was explored by employing disc-diffusion method against *E. coli*, *S. aureus*, and *Bacillus* under visible light irradiation (80 W) at ambient temperature  $37 \pm 2^{\circ}\text{C}$  for 24 h. According to the scale of bacteria inhibition zone (dash circle in **Figure 1.21**), they concluded that the (Ta,N) co-doped TiO<sub>2</sub> catalyst can be used as an antimicrobial material, and the sterilization effect was observed to be more significant for *E. coli*. Unfortunately, the authors did not provide a detailed analysis of the mechanism of visible light photocatalytic sterilization.

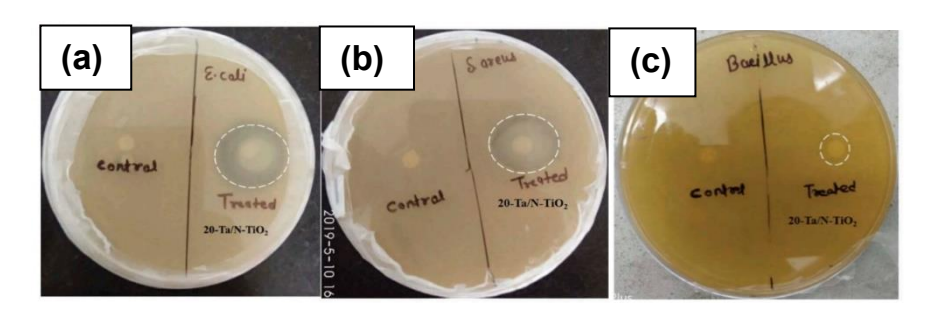


**Figure 1.21:** Bacteria inhibition zone around 20-Ta/N-TiO<sub>2</sub> in (a) E. coli, (b) S. aureus and (c) Bacillus. 175

Besides, W is another popular choice in the 5d blocks. So far, to the best of our knowledge, the application of (W,N) co-doped materials is mainly focused on photocatalytic advanced oxidation reactions. Chen et. al prepared (W,N) co-doped TiO<sub>2</sub> nanobelts via hydrothermal reaction in which tungstic acid and urea were utilized as the source of W and N. 176 The photocatalytic performance of the optimum (W, N) co-doped TiO<sub>2</sub> sample (3 mol%) W) for RhB degradation under visible light was enhanced to 4.8 times that of unmodified TiO<sub>2</sub>. Besides, conducting photocatalytic degradation of MB, <sup>177</sup> and phenol, <sup>178</sup> using (W,N) co-doped TiO<sub>2</sub> as photocatalysts have been also reported. Another interesting study was reported by Kubacka et al. in which the (W,N) co-doped TiO2 and W-doped TiO2 were synthesized by a microemulsion preparation method followed by a nitridation treatment in a mixture gas of ammonia and nitrogen, and the photocatalysts were used for partial oxidation of toluene and styrene under simulated sunlight.<sup>179</sup> They found that the selectivity of oxidation products highly depends on the N-doping process. Before nitridation, the W-doped samples tended to completely oxidize toluene and styrene into CO<sub>2</sub>. For the (W,N) co-doped materials, the insertion of nitrogen resulted in a dominant product of benzaldehyde due to the partial oxidation reaction. In the case of styrene, styrene oxide was also observed. The XPS results indicated a decreased concentration of W on the surface of the co-doped samples, which were supposed to be relate to the change in product selectivity.

### 4.3.2.4 Challenges in the research field

As mentioned, aiming at preparing charge-balanced co-alloyed TiO<sub>2</sub> material, different synthetic strategies and cation-anion combinations have been studied over the past decade. Although numerous examples showed superior photocatalytic activities of the co-

doped TiO<sub>2</sub> compared to the mono-doped counterparts, there are still challenges that remain in the field.

Firstly, synthetic preparation for co-doped TiO<sub>2</sub> with a homogeneous distribution of dopants remains difficult. For most of two-step synthetic methods, the co-doped TiO<sub>2</sub> was produced by introducing anion into a cation-doped TiO<sub>2</sub> structure through heat treatment in in a reactive atmosphere. However, heterogeneous reactions may mainly occur on the sample surface, due to the limit of gas diffusion. Consequently, improving the overall amount of anion dopants is difficult. In most N-doped TiO<sub>2</sub> and (cation, N) co-doped TiO<sub>2</sub>, the molar concentration of N is estimated in the range of 2% to 7%. <sup>158</sup> Besides, from the perspective of light absorption, if co-doping is only achieved on the surface, the band structure of the bulk part will not be modified. Thus, the visible light absorption is not likely to be efficient. The inhomogeneous distribution of cations has been observed by our team based on the (Nb,N) and (Ta,N) co-doped TiO<sub>2</sub>-NTs synthesized in an anodization process (**Figure 1.22**). <sup>172</sup> This could be due to an non-homogeneous distribution of the cation in the alloys used for synthesis. The inhomogeneity of dopants discussed above increases the complexity of the chemical composition of co-doped materials. As a result, the charge compensation scheme may vary in different sampling areas of the same material.

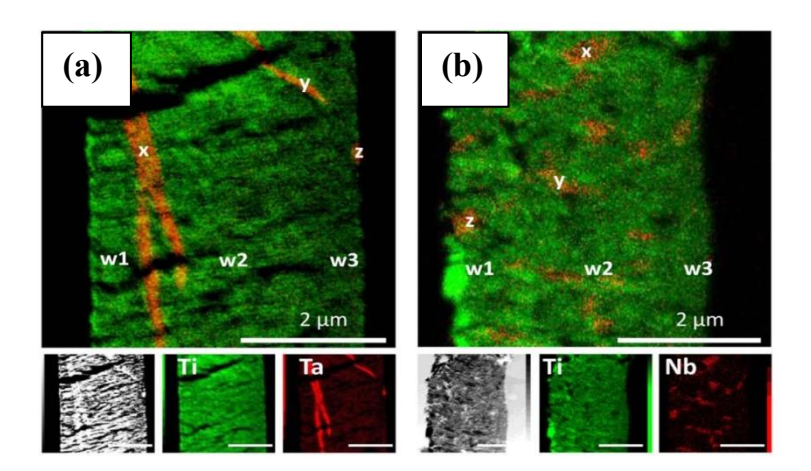


**Figure 1.22:** STEM mapping of Ta-doped TiO<sub>2</sub> (a) and Nb-doped TiO<sub>2</sub> (b). The green and red illustrate the distribution of Ti and Ta/Nb. 172

Secondly, determining the chemical composition of the prepared co-doped material remains difficult. Since the charge compensation scheme in a specific co-doped TiO<sub>2</sub> material significantly depends on the quantities of dopants, great efforts have been taken to figure out the ratio between the cation and anion. So far, in most studies, the quantification was conducted by energy-dispersive X-ray spectroscopy (EDX) and X-ray photoelectron spectroscopy (XPS). However, these two techniques cannot provide a precise chemical composition representing the overall material. EDX analysis is more favorable for the determination of the cation dopants. It is not suitable for light elements such as C and N due to the overlapping lines on the spectrum with Ti and ease of contamination. On the other hand, XPS is a well-known surface-sensitive technique, for which the analysis depth is limited to 5 nm near the sample surface. Thus, the XPS result cannot tell the bulk

composition. In addition, C and N species from the air or synthesis may be also adsorbed on the material surface, further interfering with the quantification of anion dopants. An example can be the study published by Sun *et. al*, <sup>180</sup> in which the authors claimed a defect-pair effect for sufficient charge compensation in the (Nb,N) co-doped TiO<sub>2</sub>. The XPS result indicated that the atomic concentrations of Nb<sup>5+</sup> and N<sup>3-</sup> are 5.3% and 5.6% respectively. (based on the XPS spectra of *N-equal* sample in **Figure 1.23**), which is the one closest to the ideal charge-balanced co-doping, as far as we know. However, it is worth noting that on the XPS spectra of the N 1s region (**Figure 1.23 b**), the peak at ~396 eV corresponding to the N dopants replacing O atoms is absent. Considering nitric acid was used as the source of nitrogen in the solvothermal synthetic process, the N peaks (N<sub>1</sub> and N<sub>2</sub>) can originate from nitrogen species from the synthesis that remains on the sample surface.

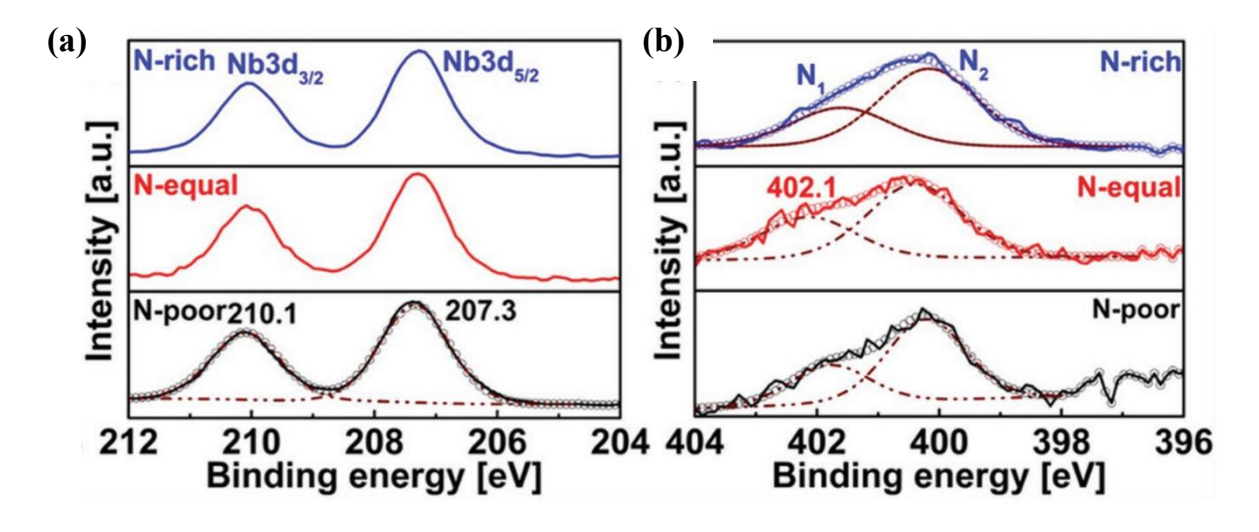


**Figure 1.23 :** XPS specra of N-poor (5.4 at% Nb<sup>5+</sup> + 3.7 at% N³<sup>-</sup>), N-equal (5.3 at% Nb<sup>5+</sup> + 5.6 at% N³<sup>-</sup>), and N-rich (5.6 at% Nb<sup>5+</sup> + 7.5 at% N³<sup>-</sup>) co-doped TiO<sub>2</sub> nanocrystals. <sup>180</sup>

Instead of directly determining the quantification of dopants, another idea is to infer the charge compensation status by characterizing defects in the material. If the cation and anion are well balanced, fewer defects are expected. Otherwise, more defects such as  ${\rm Ti}^{3+}$ ,  ${\rm V_O}^+$  and cation vacancies may be generated to neutralize the additional charge. Unfortunately, due to the limit of characterization methods, our understanding of the defects is also insufficient. Photoluminescence (PL) spectroscopy is a standard technique to evaluate charge carrier lifetime. It can provide us with information on charge transportation and recombination affected by the defects. On the other hand, electron paramagnetic resonance (EPR) analysis is only useful for defects with unpaired electrons, but the identification of other defects remains difficult.

Thirdly, it is difficult to compare the experimental results published by different research groups due to differences in morphology, synthetic methods, dopant concentration without mentioning an extreme variability in the experimental conditions of the targeted photocatalytic reactions. Thus, a general conclusion to guide future synthesis and application of the co-doped TiO<sub>2</sub> materials is still missing. Aiming at enhancing the photocatalytic activity of the co-doped materials in a specific type of photocatalytic reaction, optimizing

the choice of cation-anion combination is important. However, so far, most studies only focused on a specific cation-anion combination selected empirically. Even among the studies in which the same cation-anion combination was selected, the difference in doping concentration, synthetic method and photocatalytic test condition may result in a biased conclusion. Therefore, it is hard to know how far the prediction made by theoretical studies is from the realistic situation. Systemic comparative studies are needed to determine the individual influence of cation and anion in different combinations and the impact of the synthesis method for different photocatalytic reactions.

Our group has demonstrated a certain experience in the field of co-doped TiO<sub>2</sub> by being the first to realize (Nb,N) co-doped TiO<sub>2</sub> nanotubes using modified anodization methods. <sup>171,172</sup> If the obtained photoelectrodes presented improved OER activity in particular after the deposition of a co-catalyst, <sup>181</sup> we still believe that some improvement can be done by a better control of the crystal structure of the photocatalyst. Nevertheless, the morphology of the sample imposes restrictions in terms of material characterizations. The metallic substrate made difficult the UV visible spectroscopy analysis and prevented EPR measurements, the low amount of material is not appropriate for extensive TGA or BET analysis and the strong orientation of the nanotubes complicates the XRD analysis. For these reasons we aimed to investigate (M,N) co-doped TiO<sub>2</sub> on the form of nanoparticles that could be a good complement to understand the properties brought by this approach.

# 5. Outline and scope of this thesis

This thesis is structured around the synthesis, characterization, and photocatalytic performance of TiO<sub>2</sub> co-doped with transition metal (M=Nb, Ta or W) and nitrogen for the application of degradation of organic dye (methylene blue MB) aqueous solution and water splitting (half reaction for hydrogen production or water oxidation). It has been organized into 3 following chapters:

Chapter 2 presents a sol-gel method followed by a post-thermal nitridation in ammonia for the synthesis of (Nb,N) co-doped TiO<sub>2</sub>. The photocatalytic activities of the co-doped materials are evaluated by conducting photocatalytic degradation of MB and compared with undoped TiO<sub>2</sub>, Nb-doped TiO<sub>2</sub> and N-doped TiO<sub>2</sub>. The structure, composition, and electronic structure of the prepared materials are discussed in detail. In particular, the effect of thermal conditions for the nitridation process on the photocatalytic activity of the co-doped materials is emphasized. Two different types of N-doping processes that depended on the nitridation conditions are thoroughly analyzed.

Following the study in Chapter 2, in Chapter 3, we changed the cation-anion combination for the co-doped system. Using a similar sol-gel method, Ta and W-doped TiO<sub>2</sub>, (Ta,N) and (W,N) co-doped TiO<sub>2</sub> materials are prepared. The emphasis is placed on the role of cation in determining the physicochemical properties of the M-doped and (M,N) co-doped TiO<sub>2</sub> (M= Nb, Ta or W). The effect of both doping concentration and type of cation on materials' crystal structure and light absorption behavior is analyzed. Based on the

characterization, the N-doping process as well as the associated defects for each (M,N) codoped TiO<sub>2</sub> family are discussed.

Chapter 4 presents the photocatalytic performances of the materials synthesized in Chapter 3. Three types of photocatalytic reactions are tested: (i) Photocatalytic degradation of MB. (ii) photocatalytic hydrogen production (iii) photocatalytic water oxidation. For the MB degradation reaction, in addition to the nature of the material itself, the effect of experimental conditions on the resultant degradation kinetics is also discussed. By comparing the photocatalytic results of the (Nb,N) co-doped samples obtained in Chapter 3 and Chapter 2 respectively, we have pointed out the importance of controlling the initial MB concentration. For the water-splitting reactions, the effect of different types of doping and co-doping on the co-catalyst deposition is analyzed. Besides, a method of dual co-catalyst (Pt and RuO<sub>x</sub>) deposition is developed to further improve the photocatalytic performance of TiO<sub>2</sub> materials.

# 6. References

- (1) Wrigley, E. A. Energy and the English Industrial Revolution. *Philosophical Transactions of the Royal Society A: Mathematical, Physical and Engineering Sciences* **2013**, *371* (1986), 20110568. https://doi.org/10.1098/rsta.2011.0568.
- (2) Albritton Jonsson, F. The Industrial Revolution in the Anthropocene. *The Journal of Modern History* **2012**, *84* (3), 679–696. https://doi.org/10.1086/666049.
- (3) Climate Change: Global Temperature | NOAA Climate.gov. http://www.climate.gov/news-features/understanding-climate/climate-change-global-temperature (accessed 2023-07-06).
- (4) Yearly Carbon Dioxide Peak | Climate Central. https://www.climatecentral.org/climatematters/yearly-carbon-dioxide-peak (accessed 2023-07-06).
- (5) Stott, P. How Climate Change Affects Extreme Weather Events. *Science* **2016**, *352* (6293), 1517–1518. https://doi.org/10.1126/science.aaf7271.
- (6) Sario, M. D.; Katsouyanni, K.; Michelozzi, P. Climate Change, Extreme Weather Events, Air Pollution and Respiratory Health in Europe. *European Respiratory Journal* **2013**, *42* (3), 826–843. https://doi.org/10.1183/09031936.00074712.
- (7) Rao, C.; Yan, B. Study on the Interactive Influence between Economic Growth and Environmental Pollution. *Environ Sci Pollut Res* **2020**, *27* (31), 39442–39465. https://doi.org/10.1007/s11356-020-10017-6.
- (8) Briggs, D. Environmental Pollution and the Global Burden of Disease. *British Medical Bulletin* **2003**, 68 (1), 1–24. https://doi.org/10.1093/bmb/ldg019.
- (9) Schwarzenbach, R. P.; Egli, T.; Hofstetter, T. B.; von Gunten, U.; Wehrli, B. Global Water Pollution and Human Health. *Annual Review of Environment and Resources* **2010**, *35* (1), 109–136. https://doi.org/10.1146/annurev-environ-100809-125342.
- (10) Thomas Cottineau. Ingénierie de Nanostructures 1D de TiO<sub>2</sub> Hiérarchisées Pour Des Applications Photoélectrochimiques; Habilitation à Diriger des Recherches.
- (11) Forecasts and scenarios for global energy supply | en:former. https://www.enformer.com/en/forecasts-scenarios-global-energy-supply/ (accessed 2023-06-13).
- (12) Nath, U. kumar; Sen, R. A Comparative Review on Renewable Energy Application, Difficulties and Future Prospect. In *2021 Innovations in Energy Management and Renewable Resources*(52042); 2021; pp 1–5. https://doi.org/10.1109/IEMRE52042.2021.9386520.
- (13) Li, C.; Yao, Y.; Zhao, R.; Xie, K. Optimization Model for Time-Varying Settlement of Renewable Energy Consumption Considering Accommodation Difficulty and Supply–Demand Interaction. *International Journal of Electrical Power & Energy Systems* **2021**, *125*, 106469. https://doi.org/10.1016/j.ijepes.2020.106469.
- (14) Horowitz, C. A. Paris Agreement. *International Legal Materials* **2016**, *55* (4), 740–755. https://doi.org/10.1017/S0020782900004253.
- (15) Ritchie, H.; Roser, M.; Rosado, P. Energy. Our World in Data 2022.
- (16) Perez, M.; Perez, R. Update 2022 A Fundamental Look at Supply Side Energy Reserves for the Planet. *Solar Energy Advances* **2022**, *2*, 100014. https://doi.org/10.1016/j.seja.2022.100014.
- (17) Weijermars, R.; Taylor, P.; Bahn, O.; Das, S. R.; Wei, Y.-M. Review of Models and Actors in Energy Mix Optimization Can Leader Visions and Decisions Align with Optimum Model Strategies for Our Future Energy Systems? *Energy Strategy Reviews* **2012**, *I* (1), 5–18. https://doi.org/10.1016/j.esr.2011.10.001.

- (18) Liu, H.; Wang, C.; Wang, G. Photocatalytic Advanced Oxidation Processes for Water Treatment: Recent Advances and Perspective. *Chem. Asian J.* **2020**, *15* (20), 3239–3253. https://doi.org/10.1002/asia.202000895.
- (19) Sharma, S.; Kumar, R.; Raizada, P.; Ahamad, T.; Alshehri, S. M.; Nguyen, V.-H.; Thakur, S.; Nguyen, C. C.; Kim, S. Y.; Le, Q. V.; Singh, P. An Overview on Recent Progress in Photocatalytic Air Purification: Metal-Based and Metal-Free Photocatalysis. *Environmental Research* **2022**, *214*, 113995. https://doi.org/10.1016/j.envres.2022.113995.
- (20) Li, J.; Wu, N. Semiconductor-Based Photocatalysts and Photoelectrochemical Cells for Solar Fuel Generation: A Review. *Catal. Sci. Technol.* **2015**, *5* (3), 1360–1384. https://doi.org/10.1039/C4CY00974F.
- (21) Chen, X.; Shen, S.; Guo, L.; Mao, S. S. Semiconductor-Based Photocatalytic Hydrogen Generation. *Chem. Rev.* **2010**, *110* (11), 6503–6570. https://doi.org/10.1021/cr1001645.
- (22) Guo, Q.; Zhou, C.; Ma, Z.; Yang, X. Fundamentals of TiO<sub>2</sub> Photocatalysis: Concepts, Mechanisms, and Challenges. *Adv. Mater.* **2019**, *31* (50), 1901997. https://doi.org/10.1002/adma.201901997.
- (23) Linsebigler, A. L.; Lu, G.; Yates, J. T. Photocatalysis on TiO<sub>2</sub> Surfaces: Principles, Mechanisms, and Selected Results. *Chem. Rev.* **1995**, *95* (3), 735–758. https://doi.org/10.1021/cr00035a013.
- (24) Ren, G.; Han, H.; Wang, Y.; Liu, S.; Zhao, J.; Meng, X.; Li, Z. Recent Advances of Photocatalytic Application in Water Treatment: A Review. *Nanomaterials* **2021**, *11* (7), 1804. https://doi.org/10.3390/nano11071804.
- (25) Bahnemann, D.; Robertson, P.; Wang, C.; Choi, W.; Daly, H.; Danish, M.; Lasa, H. de; Escobedo, S.; Hardacre, C.; Jeon, T. H.; Kim, B.; Kisch, H.; Li, W.; Long, M.; Muneer, M.; Skillen, N.; Zhang, J. 2023 Roadmap on Photocatalytic Water Splitting. *J. Phys. Energy* **2023**, *5* (1), 012004. https://doi.org/10.1088/2515-7655/aca9fd.
- (26) Tahir, M.; Pan, L.; Idrees, F.; Zhang, X.; Wang, L.; Zou, J.-J.; Wang, Z. L. Electrocatalytic Oxygen Evolution Reaction for Energy Conversion and Storage: A Comprehensive Review. *Nano Energy* **2017**, *37*, 136–157. https://doi.org/10.1016/j.nanoen.2017.05.022.
- (27) Duan, L.; Bozoglian, F.; Mandal, S.; Stewart, B.; Privalov, T.; Llobet, A.; Sun, L. A Molecular Ruthenium Catalyst with Water-Oxidation Activity Comparable to That of Photosystem II. *Nat Chem* **2012**, *4* (5), 418–423. https://doi.org/10.1038/nchem.1301.
- (28) Khan, K.; Tao, X.; Zhao, Y.; Zeng, B.; Shi, M.; Ta, N.; Li, J.; Jin, X.; Li, R.; Li, C. Spatial Separation of Dual-Cocatalysts on One-Dimensional Semiconductors for Photocatalytic Hydrogen Production. *J. Mater. Chem. A* **2019**, 7 (26), 15607–15614. https://doi.org/10.1039/C9TA03090E.
- Zheng, M.; Cao, X.; Ding, Y.; Tian, T.; Lin, J. Boosting Photocatalytic Water Oxidation Achieved by BiVO<sub>4</sub> Coupled with Iron-Containing Polyoxometalate: Analysis the True Catalyst. *Journal of Catalysis* **2018**, *363*, 109–116. https://doi.org/10.1016/j.jcat.2018.04.022.
- (30) Tsuji, K.; Tomita, O.; Higashi, M.; Abe, R. Manganese-Substituted Polyoxometalate as an Effective Shuttle Redox Mediator in Z-Scheme Water Splitting under Visible Light. *ChemSusChem* **2016**, *9* (16), 2201–2208. https://doi.org/10.1002/cssc.201600563.
- (31) Wang, W.; Chen, J.; Li, C.; Tian, W. Achieving Solar Overall Water Splitting with Hybrid Photosystems of Photosystem II and Artificial Photocatalysts. *Nat Commun* **2014**, *5* (1), 4647. https://doi.org/10.1038/ncomms5647.
- (32) Sasaki, Y.; Kato, H.; Kudo, A.  $[Co(Bpy)_3]^{3+/2+}$  and  $[Co(Phen)_3]^{3+/2+}$  Electron Mediators for Overall Water Splitting under Sunlight Irradiation Using Z-Scheme Photocatalyst System. *J. Am. Chem. Soc.* **2013**, 135 (14), 5441–5449. https://doi.org/10.1021/ja400238r.
- (33) Sayama, K.; Arakawa, H. Effect of Carbonate Salt Addition on the Photocatalytic Decomposition of Liquid Water over Pt–TiO<sub>2</sub> Catalyst. *Journal of the Chemical Society, Faraday Transactions* **1997**, *93* (8), 1647–1654. https://doi.org/10.1039/A607662I.

- (34) Tabata, S.; Nishida, H.; Masaki, Y.; Tabata, K. Stoichiometric Photocatalytic Decomposition of Pure Water in Pt/TiO<sub>2</sub> Aqueous Suspension System. *Catal Lett* **1995**, *34* (1), 245–249. https://doi.org/10.1007/BF00808339.
- (35) Lehn, J. M.; Sauvage, J. P.; Zlessel, R.; Hilaire, L. Water Photolysis by UV Irradiation of Rhodium Loaded Strontium Titanate Catalysts. Relation between Catalytic Activity and Nature of the Deposit from Combined Photolysis and ESCA Studies. *Israel Journal of Chemistry* **1982**, *22* (2), 168–172. https://doi.org/10.1002/ijch.198200032.
- (36) Ikeda, S.; Fubuki, M.; Takahara, Y. K.; Matsumura, M. Photocatalytic Activity of Hydrothermally Synthesized Tantalate Pyrochlores for Overall Water Splitting. *Applied Catalysis A: General* **2006**, *300* (2), 186–190. https://doi.org/10.1016/j.apcata.2005.11.007.
- (37) Layered Perovskite Oxychloride Bi<sub>4</sub>NbO<sub>8</sub>Cl: A Stable Visible Light Responsive Photocatalyst for Water Splitting | Journal of the American Chemical Society. https://pubs.acs.org/doi/10.1021/jacs.5b11191 (accessed 2023-05-25).
- (38) Wang, Q.; Hisatomi, T.; Ma, S. S. K.; Li, Y.; Domen, K. Core/Shell Structured La- and Rh-Codoped SrTiO<sub>3</sub> as a Hydrogen Evolution Photocatalyst in Z-Scheme Overall Water Splitting under Visible Light Irradiation. *Chem. Mater.* **2014**, *26* (14), 4144–4150. https://doi.org/10.1021/cm5011983.
- (39) Kim, J.; Hwang, D. W.; Kim, H. G.; Bae, S. W.; Lee, J. S.; Li, W.; Oh, S. H. Highly Efficient Overall Water Splitting Through Optimization of Preparation and Operation Conditions of Layered Perovskite Photocatalysts. *Top Catal* **2005**, *35* (3), 295–303. https://doi.org/10.1007/s11244-005-3837-x.
- (40) Inoue, Y.; Kubokawa, T.; Sato, K. Photocatalytic activity of alkali-metal titanates combined with ruthenium in the decomposition of water. ACS Publications. https://doi.org/10.1021/j100163a032.
- (41) Ogura, S.; Kohno, M.; Sato, K.; Inoue, Y. Photocatalytic Activity for Water Decomposition of RuO<sub>2</sub>-Combined M<sub>2</sub>Ti<sub>6</sub>O<sub>13</sub> (M = Na, K, Rb, Cs). *Applied Surface Science* **1997**, *121–122*, 521–524. https://doi.org/10.1016/S0169-4332(97)00358-9.
- (42) Xing, J.; Fang, W. Q.; Zhao, H. J.; Yang, H. G. Inorganic Photocatalysts for Overall Water Splitting. *Chemistry An Asian Journal* **2012**, *7* (4), 642–657. https://doi.org/10.1002/asia.201100772.
- (43) Maeda, K.; Higashi, M.; Lu, D.; Abe, R.; Domen, K. Efficient Nonsacrificial Water Splitting through Two-Step Photoexcitation by Visible Light Using a Modified Oxynitride as a Hydrogen Evolution Photocatalyst. *J. Am. Chem. Soc.* **2010**, *132* (16), 5858–5868. https://doi.org/10.1021/ja1009025.
- (44) Escobedo, S.; de Lasa, H. Synthesis and Performance of Photocatalysts for Photocatalytic Hydrogen Production: Future Perspectives. *Catalysts* **2021**, *11* (12), 1505. https://doi.org/10.3390/catal11121505.
- (45) Qi, K.; Cheng, B.; Yu, J.; Ho, W. Review on the Improvement of the Photocatalytic and Antibacterial Activities of ZnO. *Journal of Alloys and Compounds* **2017**, 727, 792–820. https://doi.org/10.1016/j.jallcom.2017.08.142.
- (46) Xu, M.; Girish, Y. R.; Rakesh, K. P.; Wu, P.; Manukumar, H. M.; Byrappa, S. M.; Udayabhanu; Byrappa, K. Recent Advances and Challenges in Silicon Carbide (SiC) Ceramic Nanoarchitectures and Their Applications. *Materials Today Communications* **2021**, 28, 102533. https://doi.org/10.1016/j.mtcomm.2021.102533.
- (47) Boyle, C.; Skillen, N.; Gunaratne, H. Q. N.; Sharma, P. K.; Byrne, J. A.; Robertson, P. K. J. The Use of Titanium Dioxide Nanotubes as Photoanodes for Chloride Oxidation. *Materials Science in Semiconductor Processing* **2020**, *109*, 104930. https://doi.org/10.1016/j.mssp.2020.104930.
- (48) Maeda, K. Photocatalytic Water Splitting Using Semiconductor Particles: History and Recent Developments. *Journal of Photochemistry and Photobiology C: Photochemistry Reviews* **2011**, *12* (4), 237–268. https://doi.org/10.1016/j.jphotochemrev.2011.07.001.

- (49) Kapilashrami, M.; Zhang, Y.; Liu, Y.-S.; Hagfeldt, A.; Guo, J. Probing the Optical Property and Electronic Structure of TiO<sub>2</sub> Nanomaterials for Renewable Energy Applications. *Chem. Rev.* **2014**, *114* (19), 9662–9707. https://doi.org/10.1021/cr5000893.
- (50) Schneider, J.; Matsuoka, M.; Takeuchi, M.; Zhang, J.; Horiuchi, Y.; Anpo, M.; Bahnemann, D. W. Understanding TiO<sub>2</sub> Photocatalysis: Mechanisms and Materials. *Chem Rev* **2014**, *114* (19), 9919–9986. https://doi.org/10.1021/cr5001892.
- (51) Yamada, Y.; Kanemitsu, Y. Determination of Electron and Hole Lifetimes of Rutile and Anatase TiO<sub>2</sub> Single Crystals. *Applied Physics Letters* **2012**, *101* (13), 133907. https://doi.org/10.1063/1.4754831.
- (52) Qian, J. X.; Chen, T. W.; Enakonda, L. R.; Liu, D. B.; Basset, J.-M.; Zhou, L. Methane Decomposition to Pure Hydrogen and Carbon Nano Materials: State-of-the-Art and Future Perspectives. *International Journal of Hydrogen Energy* **2020**, *45* (32), 15721–15743. https://doi.org/10.1016/j.ijhydene.2020.04.100.
- (53) Zhu, S.; Lei, J.; Zhang, L.; He, J. CoO/NF Nanowires Promote Hydrogen and Oxygen Production for Overall Water Splitting in Alkaline Media. *International Journal of Hydrogen Energy* **2020**, *45* (15), 8031–8040. https://doi.org/10.1016/j.ijhydene.2020.01.085.
- (54) Liu, X.; Hou, Y.; Tang, M.; Wang, L. Atom Elimination Strategy for MoS<sub>2</sub> Nanosheets to Enhance Photocatalytic Hydrogen Evolution. *Chinese Chemical Letters* **2023**, *34* (3), 107489. https://doi.org/10.1016/j.cclet.2022.05.003.
- (55) Parra-Ortiz, E.; Caselli, L.; Agnoletti, M.; A. Skoda, M. W.; Li, X.; Zhao, D.; Malmsten, M. Mesoporous Silica as a Matrix for Photocatalytic Titanium Dioxide Nanoparticles: Lipid Membrane Interactions. *Nanoscale* **2022**, *14* (34), 12297–12312. https://doi.org/10.1039/D2NR01958B.
- (56) Liu, T.; Zhao, Q.; Li, C.; Lyu, Y.; Dupuis, M. Photocatalytic Facet Selectivity in BiVO<sub>4</sub> Nanoparticles: Polaron Electronic Structure and Thermodynamic Stability Considerations for Photocatalysis. *J. Phys. Chem. C* **2019**, *123* (33), 20142–20151. https://doi.org/10.1021/acs.jpcc.9b05929.
- (57) Huang, M. H.; Madasu, M. Facet-Dependent and Interfacial Plane-Related Photocatalytic Behaviors of Semiconductor Nanocrystals and Heterostructures. *Nano Today* **2019**, *28*, 100768. https://doi.org/10.1016/j.nantod.2019.100768.
- (58) Zhu, J.; Fan, F.; Chen, R.; An, H.; Feng, Z.; Li, C. Direct Imaging of Highly Anisotropic Photogenerated Charge Separations on Different Facets of a Single BiVO<sub>4</sub> Photocatalyst. *Angewandte Chemie* **2015**, *127* (31), 9239–9242. https://doi.org/10.1002/ange.201504135.
- (59) Tachikawa, T.; Yamashita, S.; Majima, T. Evidence for Crystal-Face-Dependent TiO<sub>2</sub> Photocatalysis from Single-Molecule Imaging and Kinetic Analysis. *J. Am. Chem. Soc.* **2011**, *133* (18), 7197–7204. https://doi.org/10.1021/ja201415j.
- (60) Murakami, N.; Kurihara, Y.; Tsubota, T.; Ohno, T. Shape-Controlled Anatase Titanium(IV) Oxide Particles Prepared by Hydrothermal Treatment of Peroxo Titanic Acid in the Presence of Polyvinyl Alcohol. *J. Phys. Chem. C* **2009**, *113* (8), 3062–3069. https://doi.org/10.1021/jp809104t.
- (61) Yadav, A.; Bagotia, N.; Sharma, A. K.; Kumar, S. Simultaneous Adsorptive Removal of Conventional and Emerging Contaminants in Multi-Component Systems for Wastewater Remediation: A Critical Review. *Science of The Total Environment* **2021**, *799*, 149500. https://doi.org/10.1016/j.scitotenv.2021.149500.
- (62) Zuo, W.; Yu, Y.; Huang, H. Making Waves: Microbe-Photocatalyst Hybrids May Provide New Opportunities for Treating Heavy Metal Polluted Wastewater. *Water Research* **2021**, *195*, 116984. https://doi.org/10.1016/j.watres.2021.116984.
- (63) Hu, H.; Yang, M.; Dang, J. Treatment of Strong Acid Dye Wastewater by Solvent Extraction. *Separation and Purification Technology* **2005**, *42* (2), 129–136. https://doi.org/10.1016/j.seppur.2004.07.002.
- (64) Khatun, S.; Pal, S.; Sinha, N.; Das, C.; Ahmed, T.; Roy, P. New Age Chloride Shielding Strategies for Corrosion Resistant Direct Seawater Splitting. *Chem. Commun.* **2023**, *59* (31), 4578–4599. https://doi.org/10.1039/D3CC00416C.

- (65) Photocorrosion Inhibition of Semiconductor-Based Photocatalysts: Basic Principle, Current Development, and Future Perspective | ACS Catalysis. https://pubs.acs.org/doi/abs/10.1021/acscatal.9b00313 (accessed 2023-06-04).
- (66) Meissner, D.; Memming, R.; Shuben, L.; Yesodharan, S.; Grätzel, M. Photocorrosion by Oxygen Uptake in Aqueous Cadmium Sulphide Suspensions. *Berichte der Bunsengesellschaft für physikalische Chemie* **1985**, *89* (2), 121–124. https://doi.org/10.1002/bbpc.19850890208.
- (67) Meissner, D.; Memming, R.; Kastening, B.; Bahnemann, D. Fundamental Problems of Water Splitting at Cadmium Sulfide. *Chemical Physics Letters* **1986**, *127* (5), 419–423. https://doi.org/10.1016/0009-2614(86)80583-8.
- (68) Toe, C. Y.; Scott, J.; Amal, R.; Ng, Y. H. Recent Advances in Suppressing the Photocorrosion of Cuprous Oxide for Photocatalytic and Photoelectrochemical Energy Conversion. *Journal of Photochemistry and Photobiology C: Photochemistry Reviews* **2019**, 40, 191–211. https://doi.org/10.1016/j.jphotochemrev.2018.10.001.
- (69) Morales-Guio, C. G.; Liardet, L.; Mayer, M. T.; Tilley, S. D.; Grätzel, M.; Hu, X. Photoelectrochemical Hydrogen Production in Alkaline Solutions Using Cu<sub>2</sub>O Coated with Earth-Abundant Hydrogen Evolution Catalysts. *Angewandte Chemie International Edition* **2015**, *54* (2), 664–667. https://doi.org/10.1002/anie.201410569.
- (70) Kouser, S.; Lingampalli, S. R.; Chithaiah, P.; Roy, A.; Saha, S.; Waghmare, U. V.; Rao, C. N. R. Extraordinary Changes in the Electronic Structure and Properties of CdS and ZnS by Anionic Substitution: Cosubstitution of P and Cl in Place of S. *Angewandte Chemie* **2015**, *127* (28), 8267–8271. https://doi.org/10.1002/ange.201501532.
- (71) Lee, G.-J.; Anandan, S.; Masten, S. J.; Wu, J. J. Photocatalytic Hydrogen Evolution from Water Splitting Using Cu Doped ZnS Microspheres under Visible Light Irradiation. *Renewable Energy* **2016**, *89*, 18–26. https://doi.org/10.1016/j.renene.2015.11.083.
- (72) Dong, B.; Cui, J.; Gao, Y.; Qi, Y.; Zhang, F.; Li, C. Heterostructure of 1D Ta<sub>3</sub>N<sub>5</sub> Nanorod/BaTaO<sub>2</sub>N Nanoparticle Fabricated by a One-Step Ammonia Thermal Route for Remarkably Promoted Solar Hydrogen Production. *Advanced Materials* **2019**, *31* (15), 1808185. https://doi.org/10.1002/adma.201808185.
- (73) Wang, X.; Liu, G.; Wang, L.; Chen, Z.-G.; Lu, G. Q. (Max); Cheng, H.-M. ZnO–CdS@Cd Heterostructure for Effective Photocatalytic Hydrogen Generation. *Advanced Energy Materials* **2012**, *2* (1), 42–46. https://doi.org/10.1002/aenm.201100528.
- (74) Fujishima, A.; Honda, K. Electrochemical Photolysis of Water at a Semiconductor Electrode. *Nature* **1972**, *238* (5358), 37–38. https://doi.org/10.1038/238037a0.
- (75) Dambournet, D.; Belharouak, I.; Amine, K. Tailored Preparation Methods of TiO<sub>2</sub> Anatase, Rutile, Brookite: Mechanism of Formation and Electrochemical Properties. *Chem. Mater.* **2010**, *22* (3), 1173–1179. https://doi.org/10.1021/cm902613h.
- (76) Nosheen, S.; Galasso, F. S.; Suib, S. L. Role of Ti–O Bonds in Phase Transitions of TiO<sub>2</sub>. *Langmuir* **2009**, *25* (13), 7623–7630. https://doi.org/10.1021/la9002719.
- (77) Diebold, U. The Surface Science of Titanium Dioxide. *Surface Science Reports* **2003**, *48* (5), 53–229. https://doi.org/10.1016/S0167-5729(02)00100-0.
- (78) Pang, C. L. Strain and Stress Effects on Single Crystal-Supported Titania and Related Nanostructures. *Semicond. Sci. Technol.* **2020**, *35* (11), 113001. https://doi.org/10.1088/1361-6641/ab9faa.
- (79) Koparde, V. N.; Cummings, P. T. Phase Transformations during Sintering of Titania Nanoparticles. *ACS Nano* **2008**, *2* (8), 1620–1624. https://doi.org/10.1021/nn800092m.
- (80) Zhang, H.; Banfield, J. F. Understanding Polymorphic Phase Transformation Behavior during Growth of Nanocrystalline Aggregates: Insights from TiO<sub>2</sub>. *J. Phys. Chem. B* **2000**, *104* (15), 3481–3487. https://doi.org/10.1021/jp000499j.

- (81) Hummer, D. R.; Kubicki, J. D.; Kent, P. R. C.; Post, J. E.; Heaney, P. J. Origin of Nanoscale Phase Stability Reversals in Titanium Oxide Polymorphs. *J. Phys. Chem. C* **2009**, *113* (11), 4240–4245. https://doi.org/10.1021/jp811332w.
- (82) Zhang, J.; Li, M.; Feng, Z.; Chen, J.; Li, C. UV Raman Spectroscopic Study on TiO<sub>2</sub>. I. Phase Transformation at the Surface and in the Bulk. *J. Phys. Chem. B* **2006**, *110* (2), 927–935. https://doi.org/10.1021/jp0552473.
- (83) Mohamad, M.; Ul Haq, B.; Ahmed, R.; Shaari, A.; Ali, N.; Hussain, R. A Density Functional Study of Structural, Electronic and Optical Properties of Titanium Dioxide: Characterization of Rutile, Anatase and Brookite Polymorphs. *Materials Science in Semiconductor Processing* **2015**, *31*, 405–414. https://doi.org/10.1016/j.mssp.2014.12.027.
- (84) Marchand, R.; Brohan, L.; Tournoux, M. TiO<sub>2</sub>(B) a New Form of Titanium Dioxide and the Potassium Octatitanate K2Ti8O17. *Materials Research Bulletin* **1980**, *15* (8), 1129–1133. https://doi.org/10.1016/0025-5408(80)90076-8.
- (85) Reyes-Coronado, D.; Rodríguez-Gattorno, G.; Espinosa-Pesqueira, M. E.; Cab, C.; Coss, R. de; Oskam, G. Phase-Pure TiO<sub>2</sub> Nanoparticles: Anatase, Brookite and Rutile. *Nanotechnology* **2008**, *19* (14), 145605. https://doi.org/10.1088/0957-4484/19/14/145605.
- (86) Cromer, D. T.; Herrington, K. The Structures of Anatase and Rutile. *J. Am. Chem. Soc.* **1955**, 77 (18), 4708–4709. https://doi.org/10.1021/ja01623a004.
- (87) Thompson, T. L.; Yates, J. T. Surface Science Studies of the Photoactivation of TiO<sub>2</sub> New Photochemical Processes. *Chem. Rev.* **2006**, *106* (10), 4428–4453. https://doi.org/10.1021/cr050172k.
- (88) Liu, G.; Wang, L.; Yang, H. G.; Cheng, H.-M.; Lu, G. Q. (Max). Titania-Based Photocatalysts Crystal Growth, Doping and Heterostructuring. *J. Mater. Chem.* **2010**, 20 (5), 831–843. https://doi.org/10.1039/B909930A.
- (89) Pelaez, M.; Nolan, N. T.; Pillai, S. C.; Seery, M. K.; Falaras, P.; Kontos, A. G.; Dunlop, P. S. M.; Hamilton, J. W. J.; Byrne, J. A.; O'Shea, K.; Entezari, M. H.; Dionysiou, D. D. A Review on the Visible Light Active Titanium Dioxide Photocatalysts for Environmental Applications. *Applied Catalysis B: Environmental* **2012**, *125*, 331–349. https://doi.org/10.1016/j.apcatb.2012.05.036.
- (90) Landmann, M.; Rauls, E.; Schmidt, W. G. The Electronic Structure and Optical Response of Rutile, Anatase and Brookite TiO<sub>2</sub>. *J. Phys.: Condens. Matter* **2012**, *24* (19), 195503. https://doi.org/10.1088/0953-8984/24/19/195503.
- (91) Madhusudan Reddy, K.; Manorama, S. V.; Ramachandra Reddy, A. Bandgap Studies on Anatase Titanium Dioxide Nanoparticles. *Materials Chemistry and Physics* **2003**, 78 (1), 239–245. https://doi.org/10.1016/S0254-0584(02)00343-7.
- (92) Zhang, J.; Zhou, P.; Liu, J.; Yu, J. New Understanding of the Difference of Photocatalytic Activity among Anatase, Rutile and Brookite TiO<sub>2</sub>. *Phys. Chem. Chem. Phys.* **2014**, *16* (38), 20382–20386. https://doi.org/10.1039/C4CP02201G.
- (93) Pan, X.; Cai, Q.; Chen, W.; Zhuang, G.; Li, X.; Wang, J. A DFT Study of Gas Molecules Adsorption on the Anatase (001) Nanotube Arrays. *Computational Materials Science* **2013**, *67*, 174–181. https://doi.org/10.1016/j.commatsci.2012.09.006.
- (94) Asahi, R.; Taga, Y.; Mannstadt, W.; Freeman, A. J. Electronic and Optical Properties of Anatase TiO<sub>2</sub>. *Phys. Rev. B* **2000**, *61* (11), 7459–7465. https://doi.org/10.1103/PhysRevB.61.7459.
- (95) Wang, Z.; Wen, B.; Hao, Q.; Liu, L.-M.; Zhou, C.; Mao, X.; Lang, X.; Yin, W.-J.; Dai, D.; Selloni, A.; Yang, X. Localized Excitation of Ti<sup>3+</sup> Ions in the Photoabsorption and Photocatalytic Activity of Reduced Rutile TiO<sub>2</sub>. *J. Am. Chem. Soc.* **2015**, *137* (28), 9146–9152. https://doi.org/10.1021/jacs.5b04483.

- (96) Wen, B.; Hao, Q.; Yin, W.-J.; Zhang, L.; Wang, Z.; Wang, T.; Zhou, C.; Selloni, A.; Yang, X.; Liu, L.-M. Electronic Structure and Photoabsorption of Ti<sup>3+</sup> Ions in Reduced Anatase and Rutile TiO<sub>2</sub>. *Phys. Chem. Phys.* **2018**, *20* (26), 17658–17665. https://doi.org/10.1039/C8CP02648C.
- (97) Setvin, M.; Franchini, C.; Hao, X.; Schmid, M.; Janotti, A.; Kaltak, M.; Van de Walle, C. G.; Kresse, G.; Diebold, U. Direct View at Excess Electrons in TiO<sub>2</sub> Rutile and Anatase. *Phys. Rev. Lett.* **2014**, *113* (8), 086402. https://doi.org/10.1103/PhysRevLett.113.086402.
- (98) Yu, J.-H.; Nam, S.-H.; Lee, J. W.; Kim, D. I.; Boo, J.-H. Oxidation State and Structural Studies of Vanadium-Doped Titania Particles for the Visible Light-Driven Photocatalytic Activity. *Applied Surface Science* **2019**, 472, 46–53. https://doi.org/10.1016/j.apsusc.2018.04.125.
- (99) Zhou, W.; Liu, Q.; Zhu, Z.; Zhang, J. Preparation and Properties of Vanadium-Doped TiO<sub>2</sub> Photocatalysts. *J. Phys. D: Appl. Phys.* **2010**, *43* (3), 035301. https://doi.org/10.1088/0022-3727/43/3/035301.
- (100) Das, K.; Sharma, S. N.; Kumar, M.; De, S. K. Morphology Dependent Luminescence Properties of Co Doped TiO<sub>2</sub> Nanostructures. *J. Phys. Chem. C* **2009**, *113* (33), 14783–14792. https://doi.org/10.1021/jp9048956.
- (101) Barakat, M. A.; Schaeffer, H.; Hayes, G.; Ismat-Shah, S. Photocatalytic Degradation of 2-Chlorophenol by Co-Doped TiO<sub>2</sub> Nanoparticles. *Applied Catalysis B: Environmental* **2005**, *57* (1), 23–30. https://doi.org/10.1016/j.apcatb.2004.10.001.
- (102) Sadanandam, G.; Lalitha, K.; Kumari, V. D.; Shankar, M. V.; Subrahmanyam, M. Cobalt Doped TiO<sub>2</sub>: A Stable and Efficient Photocatalyst for Continuous Hydrogen Production from Glycerol: Water Mixtures under Solar Light Irradiation. *International Journal of Hydrogen Energy* **2013**, *38* (23), 9655–9664. https://doi.org/10.1016/j.ijhydene.2013.05.116.
- (103) Wu, Q.; Yang, C.-C.; van de Krol, R. A Dopant-Mediated Recombination Mechanism in Fe-Doped TiO<sub>2</sub> Nanoparticles for the Photocatalytic Decomposition of Nitric Oxide. *Catalysis Today* **2014**, *225*, 96–101. https://doi.org/10.1016/j.cattod.2013.09.026.
- (104) Xin, B.; Ren, Z.; Wang, P.; Liu, J.; Jing, L.; Fu, H. Study on the Mechanisms of Photoinduced Carriers Separation and Recombination for Fe<sup>3+</sup>–TiO<sub>2</sub> Photocatalysts. *Applied Surface Science* **2007**, *253* (9), 4390–4395. https://doi.org/10.1016/j.apsusc.2006.09.049.
- (105) Khan, H.; Swati, I. K. Fe3+-Doped Anatase TiO<sub>2</sub> with d-d Transition, Oxygen Vacancies and Ti<sup>3+</sup> Centers: Synthesis, Characterization, UV-Vis Photocatalytic and Mechanistic Studies. *Ind. Eng. Chem. Res.* **2016**, *55* (23), 6619–6633. https://doi.org/10.1021/acs.iecr.6b01104.
- (106) Zhang, J.; Chen, X.; Shen, Y.; Li, Y.; Hu, Z.; Chu, J. Synthesis, Surface Morphology, and Photoluminescence Properties of Anatase Iron-Doped Titanium Dioxide Nano-Crystalline Films. *Phys. Chem. Chem. Phys.* **2011**, *13* (28), 13096–13105. https://doi.org/10.1039/C0CP02924F.
- (107) Shannon, R. D. Revised Effective Ionic Radii and Systematic Studies of Interatomic Distances in Halides and Chalcogenides. *Acta Cryst A* **1976**, *32* (5), 751–767. https://doi.org/10.1107/S0567739476001551.
- (108) Yamada, N.; Shibata, T.; Taira, K.; Hirose, Y.; Nakao, S.; Hoang, N. L. H.; Hitosugi, T.; Shimada, T.; Sasaki, T.; Hasegawa, T. Enhanced Carrier Transport in Uniaxially (001)-Oriented Anatase Ti<sub>0.94</sub>Nb<sub>0.06</sub>O<sub>2</sub> Films Grown on Nanosheet Seed Layers. *Appl. Phys. Express* **2011**, *4* (4), 045801. https://doi.org/10.1143/APEX.4.045801.
- (109) Mazzolini, P.; Gondoni, P.; Russo, V.; Chrastina, D.; Casari, C. S.; Li Bassi, A. Tuning of Electrical and Optical Properties of Highly Conducting and Transparent Ta-Doped TiO<sub>2</sub> Polycrystalline Films. *J. Phys. Chem. C* **2015**, *119* (13), 6988–6997. https://doi.org/10.1021/jp5126156.
- (110) Emeline, A. V.; Furubayashi, Y.; Zhang, X.; Jin, M.; Murakami, T.; Fujishima, A. Photoelectrochemical Behavior of Nb-Doped TiO<sub>2</sub> Electrodes. *J. Phys. Chem. B* **2005**, *109* (51), 24441–24444. https://doi.org/10.1021/jp055090e.

- (111) Altomare, M.; Lee, K.; Killian, M. S.; Selli, E.; Schmuki, P. Ta-Doped TiO<sub>2</sub> Nanotubes for Enhanced Solar-Light Photoelectrochemical Water Splitting. *Chemistry A European Journal* **2013**, *19* (19), 5841–5844. https://doi.org/10.1002/chem.201203544.
- (112) Lira-Cantu, M.; Khoda Siddiki, M.; Muñoz-Rojas, D.; Amade, R.; González-Pech, N. I. Nb-TiO<sub>2</sub>/Polymer Hybrid Solar Cells with Photovoltaic Response under Inert Atmosphere Conditions. *Solar Energy Materials and Solar Cells* **2010**, *94* (7), 1227–1234. https://doi.org/10.1016/j.solmat.2010.03.011.
- (113) Lü, X.; Mou, X.; Wu, J.; Zhang, D.; Zhang, L.; Huang, F.; Xu, F.; Huang, S. Improved-Performance Dye-Sensitized Solar Cells Using Nb-Doped TiO<sub>2</sub> Electrodes: Efficient Electron Injection and Transfer. *Advanced Functional Materials* **2010**, *20* (3), 509–515. https://doi.org/10.1002/adfm.200901292.
- (114) Liu, J.; Yang, H.; Tan, W.; Zhou, X.; Lin, Y. Photovoltaic Performance Improvement of Dye-Sensitized Solar Cells Based on Tantalum-Doped TiO<sub>2</sub> Thin Films. *Electrochimica Acta* **2010**, *56* (1), 396–400. https://doi.org/10.1016/j.electacta.2010.08.063.
- (115) Fehse, M.; Cavaliere, S.; Lippens, P. E.; Savych, I.; Iadecola, A.; Monconduit, L.; Jones, D. J.; Rozière, J.; Fischer, F.; Tessier, C.; Stievano, L. Nb-Doped TiO<sub>2</sub> Nanofibers for Lithium Ion Batteries. *J. Phys. Chem. C* **2013**, *117* (27), 13827–13835. https://doi.org/10.1021/jp402498p.
- (116) Su, D.; Liu, L.; Liu, Z.; Dai, J.; Wen, J.; Yang, M.; Jamil, S.; Deng, H.; Cao, G.; Wang, X. Electrospun Ta-Doped TiO<sub>2</sub>/C Nanofibers as a High-Capacity and Long-Cycling Anode Material for Li-Ion and K-Ion Batteries. *J. Mater. Chem. A* **2020**, *8* (39), 20666–20676. https://doi.org/10.1039/D0TA06327D.
- (117) Joshi, B. N.; Yoon, H.; van Hest, M. F. A. M.; Yoon, S. S. Niobium-Doped Titania Photocatalyst Film Prepared via a Nonaqueous Sol-Gel Method. *Journal of the American Ceramic Society* **2013**, *96* (8), 2623–2627. https://doi.org/10.1111/jace.12336.
- (118) Hirano, M.; Matsushima, K. Photoactive and Adsorptive Niobium-Doped Anatase (TiO<sub>2</sub>) Nanoparticles: Influence of Hydrothermal Conditions on Their Morphology, Structure, and Properties. *Journal of the American Ceramic Society* **2006**, *89* (1), 110–117. https://doi.org/10.1111/j.1551-2916.2005.00648.x.
- (119) Qian, X.; Yang, W.; Gao, S.; Xiao, J.; Basu, S.; Yoshimura, A.; Shi, Y.; Meunier, V.; Li, Q. Highly Selective, Defect-Induced Photocatalytic CO<sub>2</sub> Reduction to Acetaldehyde by the Nb-Doped TiO<sub>2</sub> Nanotube Array under Simulated Solar Illumination. *ACS Appl. Mater. Interfaces* **2020**, *12* (50), 55982–55993. https://doi.org/10.1021/acsami.0c17174.
- (120) Zhang, C.; Uchikoshi, T.; Ishigaki, T. Effect of Crystalline Orientation on Photocatalytic Performance for Nb-Doped TiO<sub>2</sub> Nanoparticles. *Advanced Powder Technology* **2021**, *32* (11), 4149–4154. https://doi.org/10.1016/j.apt.2021.09.019.
- (121) Sengele, A.; Robert, D.; Keller, N.; Keller, V.; Herissan, A.; Colbeau-Justin, C. Ta-Doped TiO<sub>2</sub> as Photocatalyst for UV-A Activated Elimination of Chemical Warfare Agent Simulant. *Journal of Catalysis* **2016**, *334*, 129–141. https://doi.org/10.1016/j.jcat.2015.11.004.
- (122) Biedrzycki, J.; Livraghi, S.; Giamello, E.; Agnoli, S.; Granozzi, G. Fluorine- and Niobium-Doped TiO<sub>2</sub>: Chemical and Spectroscopic Properties of Polycrystalline n-Type-Doped Anatase. *J. Phys. Chem. C* **2014**, *118* (16), 8462–8473. https://doi.org/10.1021/jp501203h.
- (123) Hitosugi, T.; Kamisaka, H.; Yamashita, K.; Nogawa, H.; Furubayashi, Y.; Nakao, S.; Yamada, N.; Chikamatsu, A.; Kumigashira, H.; Oshima, M.; Hirose, Y.; Shimada, T.; Hasegawa, T. Electronic Band Structure of Transparent Conductor: Nb-Doped Anatase TiO<sub>2</sub>. *Appl. Phys. Express* **2008**, *1* (11), 111203. https://doi.org/10.1143/APEX.1.111203.
- (124) Paul, R.; K., K.; S., P. Tantalum Doped Titanium Dioxide Nanoparticles for Efficient Photocatalytic Degradation of Dyes. *Journal of Molecular Structure* **2023**, *1277*, 134869. https://doi.org/10.1016/j.molstruc.2022.134869.

- (125) Kong, L.; Wang, C.; Zheng, H.; Zhang, X.; Liu, Y. Defect-Induced Yellow Color in Nb-Doped TiO<sub>2</sub> and Its Impact on Visible-Light Photocatalysis. *J. Phys. Chem. C* **2015**, *119* (29), 16623–16632. https://doi.org/10.1021/acs.jpcc.5b03448.
- (126) Gong, C. wei; Jiao, J. rong; Wang, J. heng; Shao, W. Structural, Optical and Magnetic Properties of W-Doped TiO<sub>2</sub>: Theory and Experiment. *Physica B: Condensed Matter* **2015**, *457*, 140–143. https://doi.org/10.1016/j.physb.2014.09.045.
- (127) Lorret, O.; Francová, D.; Waldner, G.; Stelzer, N. W-Doped Titania Nanoparticles for UV and Visible-Light Photocatalytic Reactions. *Applied Catalysis B: Environmental* **2009**, *91* (1), 39–46. https://doi.org/10.1016/j.apcatb.2009.05.005.
- (128) Sathasivam, S.; Bhachu, D. S.; Lu, Y.; Chadwick, N.; Althabaiti, S. A.; Alyoubi, A. O.; Basahel, S. N.; Carmalt, C. J.; Parkin, I. P. Tungsten Doped TiO<sub>2</sub> with Enhanced Photocatalytic and Optoelectrical Properties via Aerosol Assisted Chemical Vapor Deposition. *Sci Rep* **2015**, *5* (1), 10952. https://doi.org/10.1038/srep10952.
- (129) Liu, S.; Guo, E.; Yin, L. Tailored Visible-Light Driven Anatase TiO<sub>2</sub> Photocatalysts Based on Controllable Metal Ion Doping and Ordered Mesoporous Structure. *J. Mater. Chem.* **2012**, *22* (11), 5031–5041. https://doi.org/10.1039/C2JM15965A.
- (130) Chen, H.; Wang, L.; Guan, L.; Ren, H.; Zhang, Y.; Tao, J. Tungsten and Nitrogen Co-Doped TiO<sub>2</sub> Nanobelts with Significant Visible Light Photoactivity. *Surf Interface Anal* **2018**, *50* (2), 146–153. https://doi.org/10.1002/sia.6351.
- (131) Asahi, R.; Morikawa, T.; Ohwaki, T.; Aoki, K.; Taga, Y. Visible-Light Photocatalysis in Nitrogen-Doped Titanium Oxides. *Science* **2001**, *293* (5528), 269–271. https://doi.org/10.1126/science.1061051.
- (132) Cheng, C.; Sun, Y. Carbon Doped TiO<sub>2</sub> Nanowire Arrays with Improved Photoelectrochemical Water Splitting Performance. *Applied Surface Science* **2012**, *263*, 273–276. https://doi.org/10.1016/j.apsusc.2012.09.042.
- (133) Gopal, N. O.; Lo, H.-H.; Ke, T.-F.; Lee, C.-H.; Chou, C.-C.; Wu, J.-D.; Sheu, S.-C.; Ke, S.-C. Visible Light Active Phosphorus-Doped TiO<sub>2</sub> Nanoparticles: An EPR Evidence for the Enhanced Charge Separation. *J. Phys. Chem. C* **2012**, *116* (30), 16191–16197. https://doi.org/10.1021/jp212346f.
- (134) Xu, P.; Xu, T.; Lu, J.; Gao, S.; Hosmane, N. S.; Huang, B.; Dai, Y.; Wang, Y. Visible-Light-Driven Photocatalytic S- and C- Codoped Meso/Nanoporous TiO<sub>2</sub>. *Energy Environ. Sci.* **2010**, *3* (8), 1128–1134. https://doi.org/10.1039/C001940M.
- (135) Piątkowska, A.; Janus, M.; Szymański, K.; Mozia, S. C-,N- and S-Doped TiO<sub>2</sub> Photocatalysts: A Review. *Catalysts* **2021**, *11* (1), 144. https://doi.org/10.3390/catal11010144.
- (136) Tian; Liu. DFT Description on Electronic Structure and Optical Absorption Properties of Anionic S-Doped Anatase TiO<sub>2</sub>. *J. Phys. Chem. B* **2006**, *110* (36), 17866–17871. https://doi.org/10.1021/jp0635462.
- (137) A passivated codoping approach to tailor the band edges of TiO<sub>2</sub> for efficient photocatalytic degradation of organic pollutants | *Applied Physics Letters* | *AIP Publishing*. https://pubs.aip.org/aip/apl/article/95/1/012106/337861/A-passivated-codoping-approach-to-tailor-the-band (accessed 2023-08-30).
- (138) Morikawa, T.; Asahi, R.; Ohwaki, T.; Aoki, K.; Taga, Y. Band-Gap Narrowing of Titanium Dioxide by Nitrogen Doping. *Jpn. J. Appl. Phys.* **2001**, *40* (6A), L561. https://doi.org/10.1143/JJAP.40.L561.
- (139) Ananpattarachai, J.; Kajitvichyanukul, P.; Seraphin, S. Visible Light Absorption Ability and Photocatalytic Oxidation Activity of Various Interstitial N-Doped TiO<sub>2</sub> Prepared from Different Nitrogen Dopants. *Journal of Hazardous Materials* **2009**, *168* (1), 253–261. https://doi.org/10.1016/j.jhazmat.2009.02.036.

- (140) Zeng, L.; Song, W.; Li, M.; Jie, X.; Zeng, D.; Xie, C. Comparative Study on the Visible Light Driven Photocatalytic Activity between Substitutional Nitrogen Doped and Interstitial Nitrogen Doped TiO<sub>2</sub>. *Applied Catalysis A: General* **2014**, *488*, 239–247. https://doi.org/10.1016/j.apcata.2014.09.041.
- (141) Sato, S. Photocatalytic Activity of NOx-Doped TiO<sub>2</sub> in the Visible Light Region. *Chemical Physics Letters* **1986**, *123* (1), 126–128. https://doi.org/10.1016/0009-2614(86)87026-9.
- (142) Di Valentin, C.; Pacchioni, G.; Selloni, A.; Livraghi, S.; Giamello, E. Characterization of Paramagnetic Species in N-Doped TiO<sub>2</sub> Powders by EPR Spectroscopy and DFT Calculations. *J. Phys. Chem. B* **2005**, *109* (23), 11414–11419. https://doi.org/10.1021/jp051756t.
- (143) Asahi, R.; Morikawa, T. Nitrogen Complex Species and Its Chemical Nature in TiO<sub>2</sub> for Visible-Light Sensitized Photocatalysis. *Chemical Physics* **2007**, *339* (1), 57–63. https://doi.org/10.1016/j.chemphys.2007.07.041.
- (144) Diwald, O.; Thompson, T. L.; Zubkov, T.; Walck, S. D.; Yates, J. T. Photochemical Activity of Nitrogen-Doped Rutile TiO<sub>2</sub> (110) in Visible Light. *J. Phys. Chem. B* **2004**, *108* (19), 6004–6008. https://doi.org/10.1021/jp031267y.
- (145) Yin, S.; Zhang, Q.; Saito, F.; Sato, T. Preparation of Visible Light-Activated Titania Photocatalyst by Mechanochemical Method. *Chem. Lett.* **2003**, *32* (4), 358–359. https://doi.org/10.1246/cl.2003.358.
- (146) Lee, J.-Y.; Park, J.; Cho, J.-H. Electronic Properties of N- and C-Doped TiO<sub>2</sub>. *Applied Physics Letters* **2005**, 87 (1), 011904. https://doi.org/10.1063/1.1991982.
- (147) Nakamura, R.; Tanaka, T.; Nakato, Y. Mechanism for Visible Light Responses in Anodic Photocurrents at N-Doped TiO<sub>2</sub> Film Electrodes. *J. Phys. Chem. B* **2004**, *108* (30), 10617–10620. https://doi.org/10.1021/jp048112q.
- (148) Irie, H.; Washizuka, S.; Watanabe, Y.; Kako, T.; Hashimoto, K. Photoinduced Hydrophilic and Electrochemical Properties of Nitrogen-Doped TiO<sub>2</sub> Films. *J. Electrochem. Soc.* **2005**, *152* (11), E351. https://doi.org/10.1149/1.2048227.
- (149) Yin, W.-J.; Tang, H.; Wei, S.-H.; Al-Jassim, M. M.; Turner, J.; Yan, Y. Band Structure Engineering of Semiconductors for Enhanced Photoelectrochemical Water Splitting: The Case of TiO<sub>2</sub>. *Phys. Rev. B* **2010**, *82* (4), 045106. https://doi.org/10.1103/PhysRevB.82.045106.
- (150) Lindgren, T.; Lu, J.; Hoel, A.; Granqvist, C.-G.; Torres, G. R.; Lindquist, S.-E. Photoelectrochemical Study of Sputtered Nitrogen-Doped Titanium Dioxide Thin Films in Aqueous Electrolyte. *Solar Energy Materials and Solar Cells* **2004**, *84* (1), 145–157. https://doi.org/10.1016/j.solmat.2004.02.044.
- (151) Pomoni, K.; Vomvas, A.; Trapalis, Chr. Dark Conductivity and Transient Photoconductivity of Nanocrystalline Undoped and N-Doped TiO<sub>2</sub> Sol-Gel Thin Films. *Thin Solid Films* **2008**, *516* (6), 1271–1278. https://doi.org/10.1016/j.tsf.2007.05.040.
- (152) Photoelectrochemical Study of Nitrogen-Doped Titanium Dioxide for Water Oxidation | *The Journal of Physical Chemistry B*. https://pubs.acs.org/doi/abs/10.1021/jp037477s (accessed 2023-06-12).
- (153) Yamanaka, K.; Ohwaki, T.; Morikawa, T. Charge-Carrier Dynamics in Cu- or Fe-Loaded Nitrogen-Doped TiO<sub>2</sub> Powder Studied by Femtosecond Diffuse Reflectance Spectroscopy. *J. Phys. Chem. C* **2013**, *117* (32), 16448–16456. https://doi.org/10.1021/jp404431z.
- (154) Yamanaka, K.; Morikawa, T. Charge-Carrier Dynamics in Nitrogen-Doped TiO<sub>2</sub> Powder Studied by Femtosecond Time-Resolved Diffuse Reflectance Spectroscopy. *J. Phys. Chem. C* **2012**, *116* (1), 1286–1292. https://doi.org/10.1021/jp209210u.
- (155) Deep-level optical spectroscopy investigation of N-doped TiO<sub>2</sub> films | *Applied Physics Letters* | *AIP Publishing*. https://pubs.aip.org/aip/apl/article/86/13/132104/329704/Deep-level-optical-spectroscopy-investigation-of-N (accessed 2023-06-12).

- (156) Tachikawa, T.; Takai, Y.; Tojo, S.; Fujitsuka, M.; Irie, H.; Hashimoto, K.; Majima, T. Visible Light-Induced Degradation of Ethylene Glycol on Nitrogen-Doped TiO<sub>2</sub> Powders. *J. Phys. Chem. B* **2006**, *110* (26), 13158–13165. https://doi.org/10.1021/jp0620217.
- (157) Gai, Y.; Li, J.; Li, S.-S.; Xia, J.-B.; Wei, S.-H. Design of Narrow-Gap TiO<sub>2</sub>: A Passivated Codoping Approach for Enhanced Photoelectrochemical Activity. *Phys. Rev. Lett.* **2009**, *102* (3), 036402. https://doi.org/10.1103/PhysRevLett.102.036402.
- (158) Brancho, J. J.; Bartlett, B. M. Challenges in Co-Alloyed Titanium Oxynitrides, a Promising Class of Photochemically Active Materials. *Chem. Mater.* **2015**, *27* (21), 7207–7217. https://doi.org/10.1021/acs.chemmater.5b02357.
- (159) Serpone, N. Is the Band Gap of Pristine TiO<sub>2</sub> Narrowed by Anion- and Cation-Doping of Titanium Dioxide in Second-Generation Photocatalysts? *J. Phys. Chem. B* **2006**, *110* (48), 24287–24293. https://doi.org/10.1021/jp065659r.
- (160) Favet, T. Conversion de l'énergie solaire en carburant H<sub>2</sub> par photoélectrolyse de l'eau sur des matériaux nanohybrides à base de TiO<sub>2</sub>/nanoparticules. phdthesis, Université de Strasbourg; Institut national de la recherche scientifique (Québec, province), 2019. https://theses.hal.science/tel-03186944 (accessed 2023-08-30).
- (161) Tailoring the electronic structure of anatase TiO<sub>2</sub>(001) surface through W and N codoping: a DFT calculation | SpringerLink. https://link.springer.com/article/10.3938/jkps.70.286 (accessed 2023-08-30).
- (162) Choi, H.; Shin, D.; Yeo, B. C.; Song, T.; Han, S. S.; Park, N.; Kim, S. Simultaneously Controllable Doping Sites and the Activity of a W–N Codoped TiO<sub>2</sub> Photocatalyst. *ACS Catal.* **2016**, *6* (5), 2745–2753. https://doi.org/10.1021/acscatal.6b00104.
- (163) Huang, J.; Wen, S.; Liu, J.; He, G. Band Gap Narrowing of TiO<sub>2</sub> by Compensated Codoping for Enhanced Photocatalytic Activity. *Journal of Natural Gas Chemistry* **2012**, *21* (3), 302–307. https://doi.org/10.1016/S1003-9953(11)60368-X.
- (164) Williamson, B. A. D.; Buckeridge, J.; Chadwick, N. P.; Sathasivam, S.; Carmalt, C. J.; Parkin, I. P.; Scanlon, D. O. Dispelling the Myth of Passivated Codoping in TiO<sub>2</sub>. *Chem. Mater.* **2019**, *31* (7), 2577–2589. https://doi.org/10.1021/acs.chemmater.9b00257.
- (165) Jaiswal, R.; Patel, N.; Kothari, D. C.; Miotello, A. Improved Visible Light Photocatalytic Activity of TiO<sub>2</sub> Co-Doped with Vanadium and Nitrogen. *Applied Catalysis B: Environmental* **2012**, *126*, 47–54. https://doi.org/10.1016/j.apcatb.2012.06.030.
- (166) Shen, X.-Z.; Guo, J.; Liu, Z.-C.; Xie, S.-M. Visible-Light-Driven Titania Photocatalyst Co-Doped with Nitrogen and Ferrum. *Applied Surface Science* **2008**, *254* (15), 4726–4731. https://doi.org/10.1016/j.apsusc.2008.01.086.
- (167) Solar Light Active Photodegradation of Phenol over a  $Fe_xTi_{1-x}O_{2-y}N_y$  Nanophotocatalyst. https://doi.org/10.1021/ie100889m.
- (168) Breault, T. M.; Bartlett, B. M. Lowering the Band Gap of Anatase-Structured TiO<sub>2</sub> by Coalloying with Nb and N: Electronic Structure and Photocatalytic Degradation of Methylene Blue Dye. *J. Phys. Chem. C* **2012**, *116* (10), 5986–5994. https://doi.org/10.1021/jp2078456.
- (169) Breault, T. M.; Bartlett, B. M. Composition Dependence of TiO<sub>2</sub>:(Nb,N)- x Compounds on the Rate of Photocatalytic Methylene Blue Dye Degradation. J. Phys. Chem. C **2013**, 117 (17), 8611–8618. https://doi.org/10.1021/jp312199t.
- (170) Breault, T. M.; Brancho, J. J.; Guo, P.; Bartlett, B. M. Visible Light Water Oxidation Using a Co-Catalyst Loaded Anatase-Structured Ti  $_{1-(5x/4)}$  Nb $_x$ O  $_{2-y-\delta}$  N $_y$  Compound. *Inorg. Chem.* **2013**, *52* (16), 9363–9368. https://doi.org/10.1021/ic400932m.
- (171) Cottineau, T.; Béalu, N.; Gross, P.-A.; Pronkin, S. N.; Keller, N.; Savinova, E. R.; Keller, V. One Step Synthesis of Niobium Doped Titania Nanotube Arrays to Form (N,Nb) Co-Doped TiO<sub>2</sub> with High Visible Light

- Photoelectrochemical Activity. *J. Mater. Chem. A* **2013**, *I* (6), 2151–2160. https://doi.org/10.1039/C2TA00922F.
- (172) Favet, T.; Ihiawakrim, D.; Keller, V.; Cottineau, T. Anions and Cations Distribution in M<sup>5+</sup>/N<sup>3-</sup> Co-Alloyed TiO<sub>2</sub> Nanotubular Structures for Photo-Electrochemical Water Splitting. *Materials Science in Semiconductor Processing* **2018**, *73*, 22–29. https://doi.org/10.1016/j.mssp.2017.05.018.
- (173) Gao, B.; Luo, X.; Fu, H.; Lin, B.; Chen, Y.; Gu, Z. Visible-Light-Driven Photocatalytic Performance of Nitrogen-Doped Ti<sub>1-x</sub>Zr<sub>x</sub>O<sub>2</sub> Solid Solution. *Materials Research Bulletin* **2013**, *48* (2), 587–594. https://doi.org/10.1016/j.materresbull.2012.11.044.
- (174) Hoang, S. Coincorporation of N and Ta into TiO<sub>2</sub> Nanowires for Visible Light Driven Photoelectrochemical Water Oxidation. *J. Phys. Chem. C* **2012**, *116* (44), 23283–23290. https://doi.org/10.1021/jp309743u.
- (175) Gupta, K.; Kumar, J.; Singh, R. P.; Pandey, A.; Rai, P.; Pandey, A. Standardised Nanostructured Ta/N-TiO<sub>2</sub> For Environmental Contaminants: An Efficient Visible Light Induced Photochemical Quencher for Dyes. *Materials Technology* **2019**, *34* (13), 765–775. https://doi.org/10.1080/10667857.2019.1628331.
- (176) Chen, H.; Wang, L.; Guan, L.; Ren, H.; Zhang, Y.; Tao, J. Tungsten and Nitrogen Co-Doped TiO<sub>2</sub> Nanobelts with Significant Visible Light Photoactivity. *Surface and Interface Analysis* **2018**, *50* (2), 146–153. https://doi.org/10.1002/sia.6351.
- (177) Shen, Y.; Xiong, T.; Li, T.; Yang, K. Tungsten and Nitrogen Co-Doped TiO<sub>2</sub> Nano-Powders with Strong Visible Light Response. *Applied Catalysis B: Environmental* **2008**, *83* (3), 177–185. https://doi.org/10.1016/j.apcatb.2008.01.037.
- (178) Li, J.; Xu, J.; Dai, W.-L.; Li, H.; Fan, K. One-Pot Synthesis of Twist-like Helix Tungsten–Nitrogen-Codoped Titania Photocatalysts with Highly Improved Visible Light Activity in the Abatement of Phenol. *Applied Catalysis B: Environmental* **2008**, *82* (3), 233–243. https://doi.org/10.1016/j.apcatb.2008.01.022.
- (179) Kubacka, A.; Colón, G.; Fernández-García, M. N- and/or W-(Co)Doped TiO<sub>2</sub>-Anatase Catalysts: Effect of the Calcination Treatment on Photoactivity. *Applied Catalysis B: Environmental* **2010**, *95* (3), 238–244. https://doi.org/10.1016/j.apcatb.2009.12.028.
- (180) Sun, Q.; Cortie, D.; Zhang, S.; Frankcombe, T. J.; She, G.; Gao, J.; Sheppard, L. R.; Hu, W.; Chen, H.; Zhuo, S.; Chen, D.; Withers, R. L.; McIntyre, G.; Yu, D.; Shi, W.; Liu, Y. The Formation of Defect-Pairs for Highly Efficient Visible-Light Catalysts. *Adv. Mater.* **2017**, *29* (11), 1605123. https://doi.org/10.1002/adma.201605123.
- (181) Favet, T.; Sharna, S.; Keller, V.; El Khakani, M. A.; Cottineau, T. (M,N) Codoping (M = Nb or Ta) and CoO Nanoparticle Decoration of TiO<sub>2</sub> Nanotubes: Synergistic Enhancement of Visible Photoelectrochemical Water Splitting. *Materials Today Energy* **2023**, *37*, 101376. https://doi.org/10.1016/j.mtener.2023.101376.

Chapter- 2 Influence of nitridation parameters on photocatalytic properties of (Nb,N) co-doped TiO<sub>2</sub> for methylene blue degradation

## Summary:

1. Introduction	. 51
2. Material preparation.	. 52
2.1 Synthesis of TiO <sub>2</sub> and Nb-doped sample	. 52
2.1.1 Sol-gel synthesis procedure	. 52
2.1.2 Determination of annealing conditions	. 53
2.2 Synthesis of N-doped and (Nb,N) co-doped samples	. 55
3. Material characterization	. 56
3.1 Crystal structure analyzed by XRD	. 56
3.2 Study of the morphology	. 58
3.2.1 SEM and TEM	. 58
3.2.2 Specific surface area	. 59
3.3 UV-vis spectroscopy	. 60
3.4 X-ray photoelectron spectroscopy	. 61
3.5 Electron paramagnetic resonance spectroscopy	. 65
3.6 Discussion on the charge compensation mechanism	. 66
3.7 Reversed double-beam photoacoustic spectroscopy	. 67
3.7.1 Experimental setup	. 68
3.7.2 Result and discussion	. 69
3.7.3 Proposed electronic band structure	. 71
3.8 X-ray absorption and emission spectroscopy with synchrotron irradiatio	n72
3.8.1 Principle of X-ray Absorption and Emission Spectroscopy (XAS & X	KES)
	. 72
3.8.2 Experimental parameters	. 74
3.8.3 Experimental results	. 74
3.8.4 Conclusion on synchrotron measurement.	. 77
4. Photocatalytic activity for methylene blue degradation	. 78
4.1 Experimental conditions	. 78
4.2 Photocatalytic activity measurements	. 79
4.2.1 Control experiments	. 79
4.2.2 Result discussion	. 80
5. Conclusion	. 82
6. References	. 85

#### 1. Introduction

In Chapter-1 the co-doping strategy was presented as a possible approach to deeply modify the TiO<sub>2</sub> optoelectronic structure by replacing both Ti<sup>4+</sup> and O<sup>2-</sup> in the lattice with cation and anion. An ideal charge compensation between the doped cation and anion was proposed by *ab initio* calculations, in which fewer intrinsic defects acting as charge recombination center is predicted. <sup>1,2</sup> Among a variety of cation and anion combinations for the synthesis of co-doped TiO<sub>2</sub>, Nb and N co-doping has attracted extensive research interest. It is proved both computationally and experimentally that (Nb,N) co-doping could effectively reduce the band gap of TiO<sub>2</sub> and thus improve its absorption in the visible region. In most previous studies, the successful introduction of Nb and N was examined by EDX and XPS, and the synthesized co-doped materials were tested in photocatalytic or photoelectrochemical conversion and demonstrated improved visible light activity. <sup>3-6</sup> These previous works generally ascribed the enhancements of activity to the increase in visible light absorption due to the co-doping of Nb and N.

However, quantifying the level of charge compensation between doping cation and anion remains a major difficulty. Most previous studies used EDX and XPS to determine the chemical composition of the co-doped TiO<sub>2</sub> and calculate the molar ratio between Nb and N dopants. If EDX could produce reliable results for cation, its ability to quantify light elements such as N is poor, especially when Ti is present. XPS can provide more reliable quantification for both types of dopants, but it is a surface-sensitive analysis that may not be representative of the whole material. So far, when reported, no experimental study demonstrated a complete charge balance, and a deficiency of anionic dopant was often observed.

It should be noted that, in opposition to seminal *ab initio* studies, recent theoretical work has predicted the impossibility of achieving balanced co-alloying in  $TiO_2$  because thermodynamically, intrinsic defects of  $TiO_2$  acting as electron donors have a dominating effect on the charge compensation.<sup>7</sup> These conflicting predictions need to be tested experimentally. Unfortunately, there has been little research into the influence of the doping sites or defects that may have been generated during the synthesis. Although defects such as  $Ti^{3+}$  and oxygen vacancy  $(O_v^+)$  have been identified in a recent study,<sup>4</sup> the relation between doping sites, defects and the resultant photocatalytic activity needs more in-depth study. In our opinion, the effect of defects on the properties of the co-doped materials should not be ignored. Theoretically, the generation of defects associated with the doping process is inevitable in the case where perfect charge-balanced (M,N) co-doping is not confidently achieved. We believe that the identification of these defects and their nature could help to understand the mechanism of charge compensation in co-doped  $TiO_2$  as well as how it affects the photocatalytic activity of the co-doped materials.

Therefore, in this chapter, we report the synthesis of TiO<sub>2</sub> co-doped with Nb and N via a sol-gel method followed by thermal nitridation in ammonia atmosphere. This pair of anion-cation is one of the most promising in terms of activity and also one of the most studied which is interesting for comparison of our work and other teams. By controlling the calcination process of TiO<sub>2</sub> and Nb-doped TiO<sub>2</sub> materials, we were able to keep other parameters of the

materials comparable in terms of morphology (size, specific surface area) and TiO<sub>2</sub> crystal phase. This helps us to highlight the effect of (Nb,N) co-doping on the resultant properties and photocatalytic activities for the synthesized materials. One important objective of this chapter was to study the influence of the nitridation conditions on the doping sites in the (Nb,N) co-doped TiO<sub>2</sub> materials, an aspect that was largely ignored so far by the scientific community. In order to research different charge compensation mechanisms in the (Nb,N) co-doped TiO<sub>2</sub> with different nitrogen concentrations, two sets of thermal conditions of nitridation were carried out.

A combination of characterization methods (UV-vis and XPS, EPR, RDB-PAS) was used to identify the defects created in the (Nb,N) co-doped TiO<sub>2</sub> samples and to further understand their impact on the charge compensation mechanisms. In addition to nitrogen doping, these analyses highlighted the role of oxygen vacancies and Ti<sup>3+</sup> induced by the thermal nitridation conditions. In particular, reversed double-beam photoacoustic spectroscopy (RDB-PAS) provides a direct representation of the electronic states distribution within the bandgap of modified TiO<sub>2</sub> and this helps us to outline the electronic band structure of the synthesized materials. Furthermore, synchrotron X-ray spectroscopy was used to reveal the coordination of the dopants. Finally, the photocatalytic activity of the synthesized materials was evaluated by conducting photo-degradation of methylene blue (MB). Emphasis was placed on the influence of the thermal condition of nitridation on the photocatalytic activity of the resultant TiO<sub>2</sub>-based photocatalysts. Particularly, the defects associated with nitrogen insertion on the specific material were studied in detail.

## 2. Material preparation

## 2.1 Synthesis of TiO<sub>2</sub> and Nb-doped sample

## 2.1.1 Sol-gel synthesis procedure

The sol-gel method is widely used to produce metal oxide nanoparticles of high purity with uniform nanostructure. The precursors of the target metal oxides are dissolved into the solvent to form a low-viscosity solution, which opens up a wide range of possibilities for doping other elements. This liquid-phase reaction stage can facilitate the homogeneous distribution of the components at the molecular level in a short time.<sup>8,9</sup> In the case of Nb-doping into the TiO<sub>2</sub> lattice, there is a wide range of niobium precursors, such as NbCl<sub>5</sub>, NbF<sub>5</sub> and niobium ethoxide, which can be easily dissolved in alcohols at room temperature and sufficiently mixed with the titanium precursor. Therefore, the sol-gel method was used in our experiment to prepare TiO<sub>2</sub> and Nb-doped TiO<sub>2</sub> materials.

The detailed synthesis process is shown in **Figure 2.1**. For TiO<sub>2</sub>, 5 mL of titanium butoxide (99%; Acros) was dissolved into 20 mL of absolute ethanol (99.9%; Carlo Erba), and the solution was stirred for 1h at 40°C. Then a mixture of 0.9 mL HNO<sub>3</sub> (70%; Merck), 5 mL of deionized water, and 5 mL of ethanol was added drop-wise to the former solution. The gel was formed after stirring for 2h at 40°C. The gel of Nb-doped TiO<sub>2</sub> was obtained with a similar procedure but adding 990.35 mg of NbCl<sub>5</sub> (99.8%; Merck) to the titanium butoxide solution to achieve a molar ratio Nb/Ti = 0.25 (*i.e.* 20% of Ti substitution, denoted as 0.25NbTi). In this

case, the precursor solution needed to be heated up to 80°C for 2h to form the gel, and this is probably due to the inhibition of the gel formation caused by the addition of Nb. Then, the formed gels were further dried at 80°C for 48h in a box oven to obtain the dried gel samples.

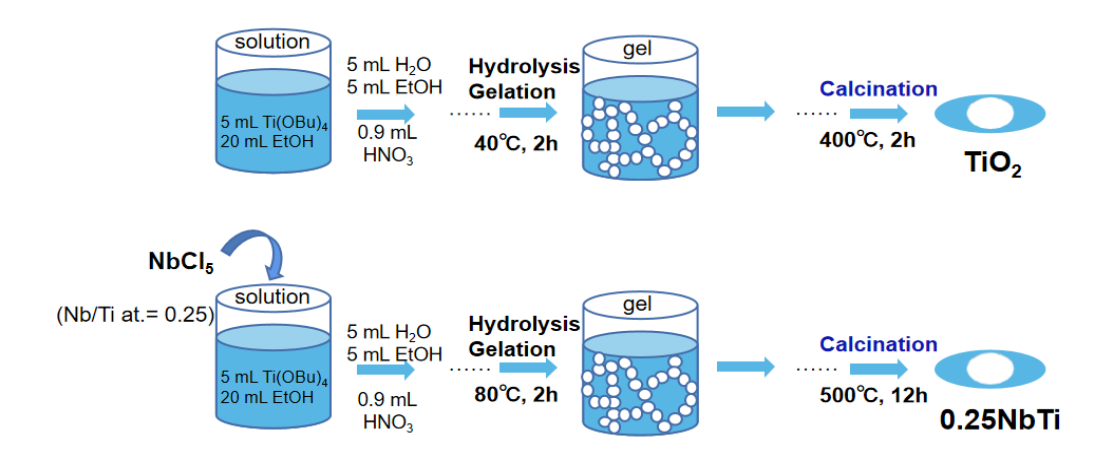


Figure 2.1: Synthesis of TiO<sub>2</sub> and Nb-doped TiO<sub>2</sub> via sol-gel method

#### 2.1.2 Determination of annealing conditions

#### 2.1.2.1 Analysis of carbon residual elimination temperature

In order to remove the carbon residual from the titanium butoxide and ethanol that used in synthesis and to obtain the crystallized TiO<sub>2</sub> materials, the dried gels were annealed in a tube furnace under air flow (100 mL.min<sup>-1</sup>) with a heating ramp of 4°C.min<sup>-1</sup>. Since the temperature required for the removal of organic residual in different samples may differ with the doping, thermogravimetric analysis (TGA) of the synthesized dried gel of TiO<sub>2</sub> and 0.25NbTi was conducted to determine the proper calcination temperature.

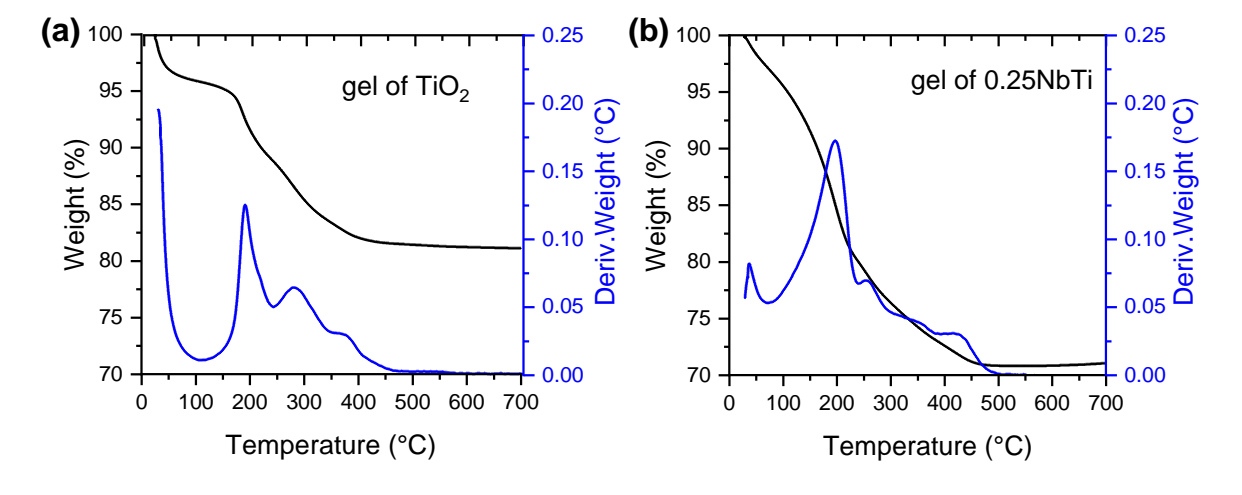


Figure 2.2: Thermogravimetric analysis of (a) gel of TiO<sub>2</sub> and (b) 0.25NbTi.

The analysis was performed on Q5000 IR Thermogravimetric Analyzer from TA Instruments. About 2 mg of the dried gel sample was heated from room temperature to 700°C

under air flow (25 mL.min<sup>-1</sup>) with a ramp of 4°C.min<sup>-1</sup>. As shown in **Figure 2.2 a**, the mass of TiO<sub>2</sub> gel stops decreasing at ~450°C with a total mass loss of ~18%, indicating sufficient combustion of the carbon residual. The temperature required to eliminate carbon residual for the Nb-doped sample is increased to ~460°C, and a larger mass loss of ~29% is observed, which could be due to the removal of chlorine ions from the niobium precursor (NbCl<sub>5</sub>) (**Figure 2.2 b**). Thus, to ensure the removal of carbon residual from the synthesis, annealing of the dried 0.25NbTi gel was carried out at 500°C for 12h while it can be limited to 400°C for 2h for TiO<sub>2</sub>.

#### 2.1.2.2 Determination of the TiO<sub>2</sub> phases

These temperatures were also chosen to limit  $TiO_2$  rutile phase formation, and thus to achieve a comparable crystalline structure (anatase) and surface area between the 0.25NbTi and  $TiO_2$  samples. This should allow us to emphasize the effect of doping and the associated defects alone on the photocatalytic performance of  $TiO_2$  materials. To analyze which allotrope of  $TiO_2$  is present, X-Ray diffraction (XRD) analysis was conducted on  $TiO_2$  annealed at  $400^{\circ}C$  for 2h ( $TiO_2$ ) or  $500^{\circ}C$  for 12h ( $TiO_2$ -2) and 0.25NbTi (at  $500^{\circ}C$  for 12h). The measurements were performed on a Bruker D8 Advance equipped with a LynxEye detector with a step size of  $0.02^{\circ}$  in the range of  $2\theta = 10$ -80°. The X-ray source is a copper anticathode, with main lines of  $K\alpha_1$  ( $\lambda$ =1.5406 Å) and  $K\alpha_2$  ( $\lambda$ =1.5445 Å).

The results are presented in **Figure 2.3** and it can be seen that the proportion between the different phases of TiO<sub>2</sub> changes significantly for the different samples. TiO<sub>2</sub> mainly crystallized in anatase, with a small trace of rutile and brookite. This phase characteristic is close to that of 0.25NbTi, which presents a pure anatase phase. For TiO<sub>2</sub>-2, the rutile phase is observed to increase obviously. Therefore, annealing TiO<sub>2</sub> at 400°C for 2h is proper to produce TiO<sub>2</sub> with a similar crystal structure as the Nb-doped TiO<sub>2</sub>.

Considering these results of TGA and XRD, we decided for future experiments to do the annealing of Nb-doped TiO<sub>2</sub> gel at 500°C for 12h in order to remove all carbonaceous contamination from the sol-gel precursor, while for TiO<sub>2</sub> gel, this annealing will be done at only 400°C during 2h to limit the formation of rutile.

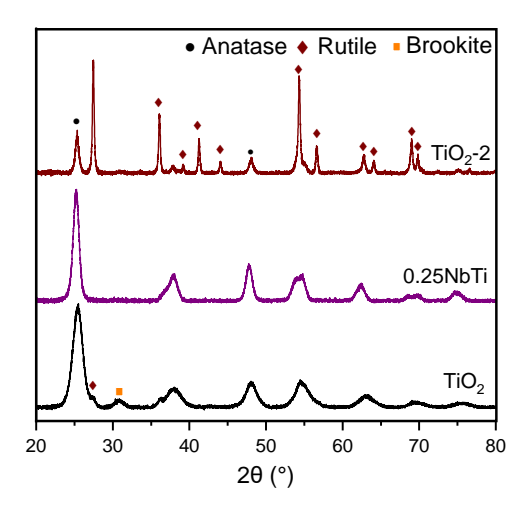


**Figure 2.3:** XRD patterns of TiO<sub>2</sub> (calcined at 400°C for 2h in air), 0.25NbTi (calcined at 500°C for 12h in air) and TiO<sub>2</sub> -2 (calcined at 500°C for 12h in air).

## 2.2 Synthesis of N-doped and (Nb,N) co-doped samples

N-doped and (Nb,N) co-doped samples were produced by annealing TiO<sub>2</sub> and 0.25NbTi under ammonia flow (100 mL.min<sup>-1</sup>; > 99.96%, Air Liquide) in an Annealsys AS1 furnace following the thermal program described in Figure 2.4. The heating and cooling steps were done with a rate of 4°C.min<sup>-1</sup> under nitrogen flow (100 mL.min<sup>-1</sup>). In order to study the Influence of nitridation parameters on the properties and photocatalytic activities of the resultant samples, two different sets of thermal conditions (mild and harsh) for the nitridation process were carried out on both (Nb,N) co-doped samples and N-doped samples. In the case of (Nb,N) co-doped TiO<sub>2</sub>, the samples subjected to mild nitridation (350°C for 12h) and harsh nitridation (450°C for 1h) are designated as 0.25NbNTi-m and 0.25NbNTi-h, respectively. In the case of TiO<sub>2</sub>, as detailed later, these conditions do not ensure significant N doping, then the mild and harsh nitridations were conducted at 450°C for 1h and 450°C for 12h to produce NTim and NTi-h, respectively. These thermal conditions were determined based on a trial-error process, in which a series of parameters were applied to produce the N-doped and (Nb,N) codoped materials. It is observed that increasing the nitridation temperature or extending the nitridation duration could promote the evolution of sample color from yellow to dark. By the technique of UV-vis spectroscopy, two different types of absorption spectra corresponding yellow or dark color were revealed (detailed later in 3.3). According to the UV-vis measurements, for each sample family, the mild condition was determined as the parameter that gives yellow color with the maximum absorption, while the harsh condition refers to the parameter that leads to the appearance of dark color.

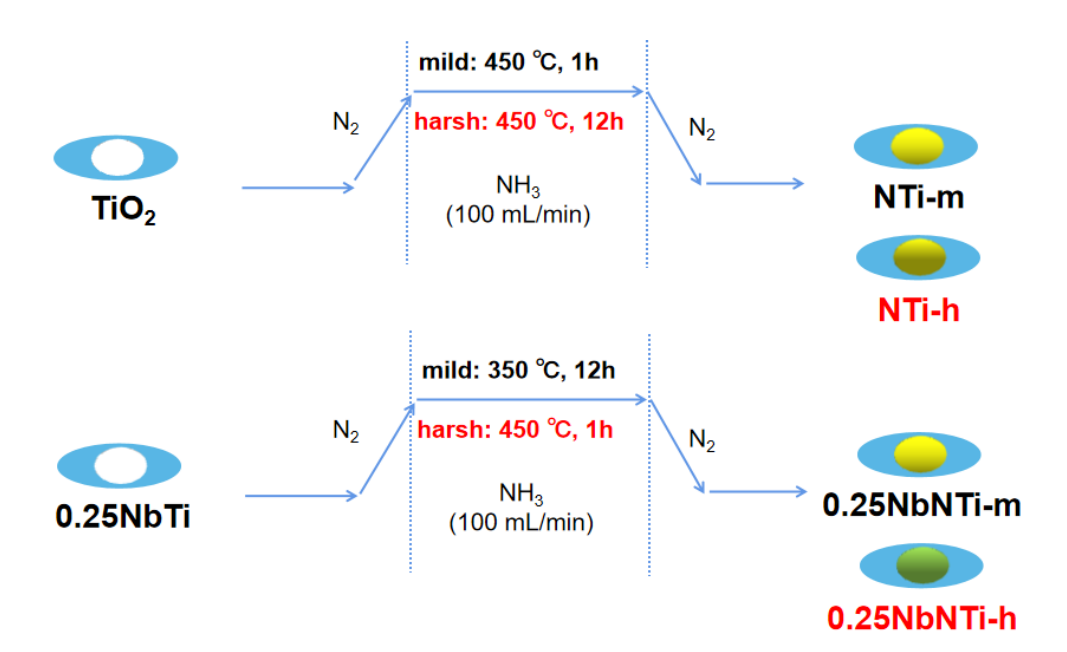


Figure 2.4: Synthesis of N-doped and co-doped samples through thermal nitridation in ammonia.

#### 3. Material characterization

#### 3.1 Crystal structure analyzed by XRD

The crystalline structure of the prepared materials were characterized by XRD. Rietveld analysis (Collaboration with Marc Lenertz, IPCMS UMR7504) based on the obtained XRD patterns was carried out using Fullprof software to extract information on lattice parameters and crystalline size.

The XRD patterns of the different samples are presented in Figure 2.5 a and the crystallite size  $\tau$ , lattice parameters a and c of anatase TiO<sub>2</sub>, and the cell volume increase as determined by Rietveld refinement for each sample are gathered in Table 2.1. After annealing the gel in air at 400°C, TiO<sub>2</sub> particles crystallized mainly in the anatase phase and have a measured crystallite size of 5.034 nm. Small contributions of rutile (ca. 5%) and brookite (ca. 32%) allotropes are also identified by their main peaks at 27.477° and 30.832°, respectively. The N-doped samples also exhibit multiple phases composition with an increase of the rutile proportion (ca. 9% and 14% for NTi-m and NTi-h) and an increase of the crystalline size of anatase along with the duration of the nitridation treatment. This indicates a growth of anatase as well as a phase transition from anatase to rutile during the thermal nitridation. Besides, it is noted that the characteristic peaks of rutile are sharper than those of anatase, suggesting a larger crystallite size of the formed rutile phase compared to the anatase phase. To further figure out the effect of nitridation on the observed phase transition, we compared the XRD patterns of NTi-m (NH<sub>3</sub>; 450°C, 1h) and NTi-h (NH<sub>3</sub>; 450°C, 12h) with their counterparts annealed in air under the same thermal condition (Figure 2.6). The ratio between rutile and anatase (R/A) for each sample is calculated using the area of the peak of anatase (101) and rutile (110). It is shown that the samples annealed in ammonia exhibit an increased rutile proportion. This indicates the facilitation of phase transition from anatase to rutile during the nitridation.

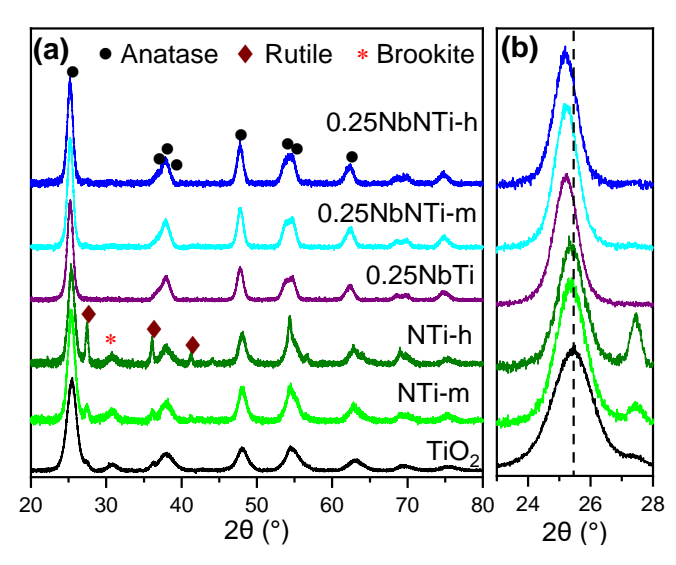


**Figure 2.5:** XRD patterns of as-prepared TiO<sub>2</sub>, N-doped, Nb-doped and (Nb,N) co-doped TiO<sub>2</sub> (a) full range and (b) magnification on anatase (101) and rutile (110) peaks.

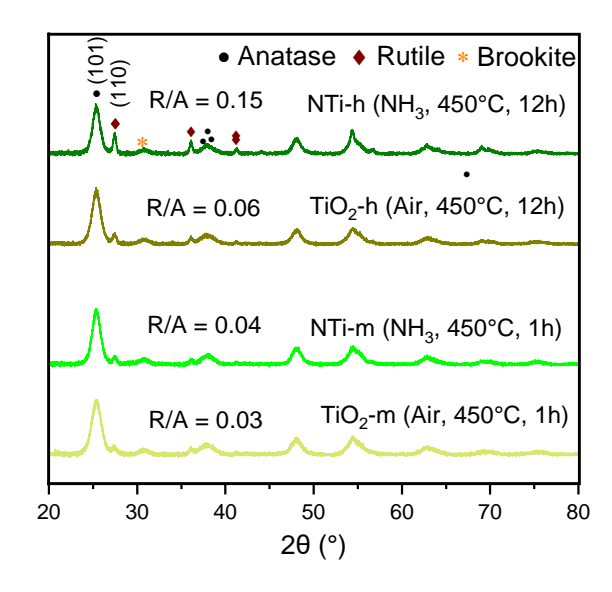


Figure 2.6: XRD patterns of TiO<sub>2</sub>-m, NTi-m, TiO<sub>2</sub>-h and NTi-h.

On the opposite, for the Nb-doped and (Nb,N) co-doped samples, only anatase TiO<sub>2</sub> is observed and no peaks corresponding to any niobium oxide, oxynitride or nitride phases were detected in **Figure 2.5**, suggesting that no segregation of niobium occurred under current experimental conditions. The crystallite size for 0.25NbTi (7.391 nm) is larger than pristine TiO<sub>2</sub>, which could be explained by the higher temperature of the initial annealing in air needed for the removal of all organic contamination.

It can also be noted that the characteristic diffraction peaks of anatase are shifted to lower  $2\theta$  angles for the Nb-doped and (Nb,N) co-doped samples compared to  $TiO_2$  and N-doped samples (**Figure 2.5 b**). A slight extension of the lattice parameters a and c is observed in the case of the N-doped samples, resulting in a cell volume increase of +0.15% compared to  $TiO_2$  (**Table 2.1**). For the Nb-containing samples, the lattice volume extends more significantly with an average of 1.764% which is a first indication of the successful insertion of Nb<sup>5+</sup> in the  $TiO_2$  crystalline structure, Nb<sup>5+</sup> having a slightly larger ionic radius than  $Ti^{4+}$ . This value is in good agreement with the observation made by Breault  $et\ al..^{10}$ 

**Table 2.1:** Crystallite size ( $\tau$ ), lattice parameters 'a' and 'c' and change of lattice volume  $\Delta V$  %, for the different samples.

Sample	$TiO_2$	NTi-m	NTi-h	0.25NbTi	0.25NbNTi-m	0.25NbNTi-h
$\tau / nm$	5.034	6.078	6.790	7.391	7.531	7.503
$(\pm X.X)$	(0.003)	(0.003)	(0.002)	(0.005)	(0.007)	(0.004)
a/Å	3.7895	3.7902	3.7904	3.8096	3.8099	3.8119
$(\pm X.X)$	(0.0005)	(0.0003)	(0.0003)	(0.0002)	(0.0002)	(0.0002)
c / Å	9.478	9.485	9.488	9.5366	9.5376	9.5438
$(\pm X.X)$	(0.002)	(0.009)	(0.001)	(0.0007)	(0.0006)	(0.0006)
$\Delta V \%$	-	0.111	0.153	1.688	1.715	1.888

## 3.2 Study of the morphology

#### 3.2.1 SEM and TEM

Scanning electron microscopy (SEM) and transmission electron microscopy (TEM) were used to observe the morphology of the synthesized materials. The SEM images were recorded with a Zeiss Gemini 500 SEM microscope equipped with a field effect gun (FEG) energy-dispersive X-ray spectroscopy (EDX) and the TEM images were recorded on a JEOL 2100 operated at 200 kV.

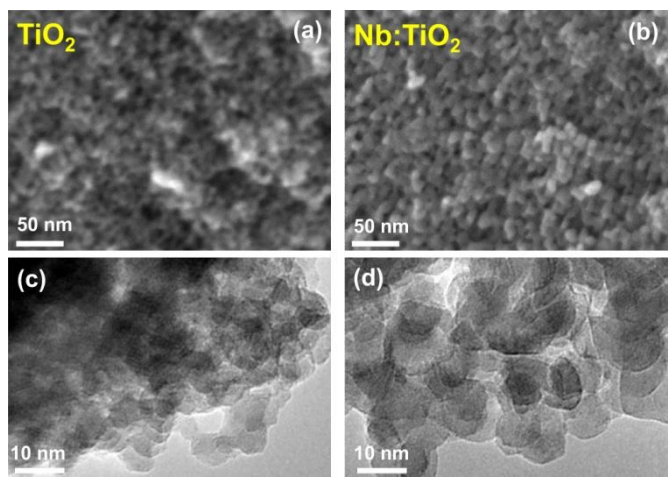


**Figure 2.7:** SEM (top line) and HRTEM (bottom line) images of  $TiO_2$  (a and c) and 0.25NbTi (b and d).

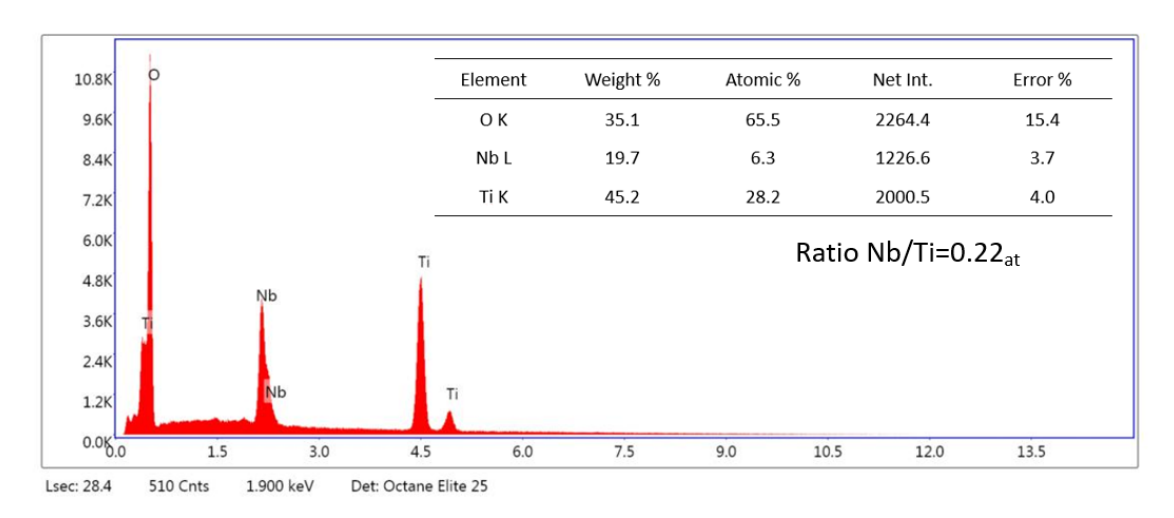


Figure 2.8: SEM-EDX spectrum for 0.25NbTi.

The synthesized nanoparticles of TiO<sub>2</sub> and 0.25NbTi present a uniform spherical morphology as observed by SEM and TEM (shown in **Figure 2.7**). SEM-EDX result (shown in **Fig. 2.8**) indicates a ratio Nb/Ti =  $0.22_{at.}$  close to the one expected from the synthesis (Nb/Ti =  $0.25_{at.}$ ). High-resolution transmission electron microscopy (HRTEM) gave complementary and consistent results on the morphology of the synthesized TiO<sub>2</sub> (**Fig. 2.7 c**) and 0.25NbTi materials (**Fig. 2.7 d**). The particle size of TiO<sub>2</sub> and 0.25NbTi measured by TEM are 6.1 and  $7.9 \pm 2.0$  nm respectively (average on 12 particles), in good agreement with the crystallite size

calculated from XRD data, indicating that each elemental particle is constituted of a single crystallite.

#### 3.2.2 Specific surface area

In addition, to analyze the specific surface area as well as the pore structure of the prepared sample, BET surface areas (BET $_{\rm SSA}$ ) were measured by conducting N $_2$  adsorption at 77 K using an ASAP2010 (Micromeritics Tristar). Before measurements, all samples were subject to degassing at 250 °C under a vacuum for 6 hours.

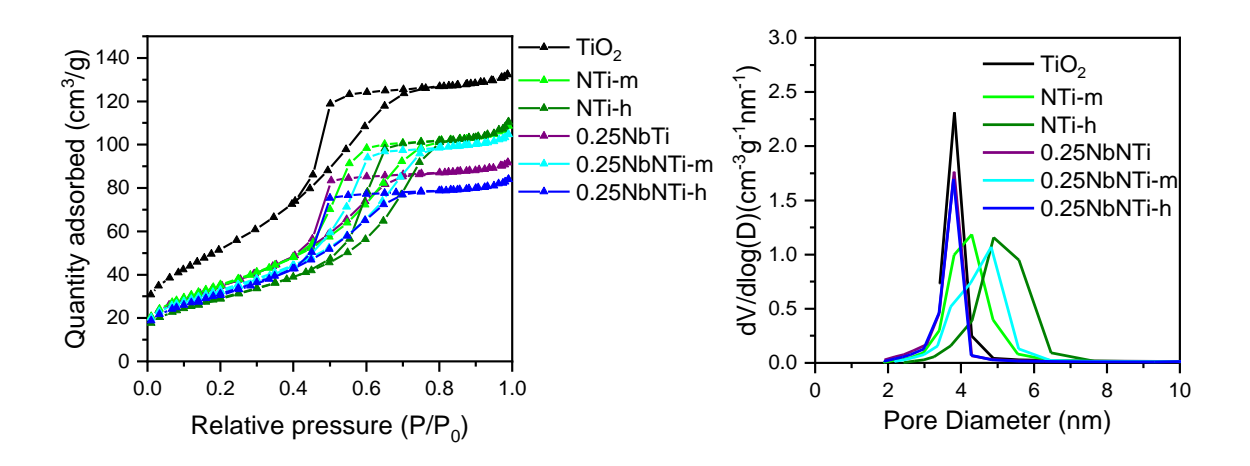


**Figure 2.9**: (a) N<sub>2</sub> sorption isotherms and (b) distribution of pore diameter for TiO<sub>2</sub>, N-doped, Nb-doped and (Nb,N) co-doped TiO<sub>2</sub>.

**Figure 2.9** presents the N<sub>2</sub> adsorption-desorption isotherms and pore size distributions for the different samples. All the samples present a type IV isotherm with a hysteresis of type H2 appearing in the relative pressure range between 0.4 to 0.8, indicating a typical mesoporous structure of the synthesized materials. Besides, the pore sizes of all the samples were distributed in the range of 3 to 6 nm, and a slight increase of the pore size is observed on the N-doped samples and 0.25NbNTi-m.

The BET<sub>SSA</sub> of each sample is reported in **Table 2.2** The specific surface area of TiO<sub>2</sub> (191 m<sup>2</sup>.g<sup>-1</sup>) is larger than that of the doped and co-doped samples (between 110-130 m<sup>2</sup>.g<sup>-1</sup>), which is in accord with the reduced particle and crystalline size measured for TiO<sub>2</sub>. The difference between TiO<sub>2</sub> and 0.25NbTi in terms of particle size and specific surface area could be explained by the fact that the initial annealing temperature under air for TiO<sub>2</sub> was limited at 400°C to limit the formation of rutile while it was 500°C for 0.25NbTi. From the results in **Table 2.2**, we can also observe a decrease in specific surface area with the nitridation process. In the case of TiO<sub>2</sub> samples, the decrease of specific surface area under ammonia annealing is 44% (TiO<sub>2</sub>, NTi-m, NTi-h), while for Nb-containing TiO<sub>2</sub> samples (0.25NbTi, 0.25NbNTi-m, 0.25NbNTi-h) this decrease is limited to 10%. The more significant decrease in specific surface area for TiO<sub>2</sub> samples could be ascribed to the increase of the rutile proportion after the nitridation since the formed rutile has a larger crystallite size than that of anatase as already

discussed from XRD (Figure 2.5).

Sample	$TiO_2$	NTi-m	NTi-h	0.25NbTi	0.25NbNTi-m	0.25NbNTi-h
DET / 2 1 / 0.0)	101	120	107	120	120	114

**Table 2.2:** BET surface area (BET<sub>ssa</sub>) for the different samples.

The above results indicate that all the synthesized materials possess similar morphology, which is important to ensure that the differences in photocatalytic activity discussed later are mainly related to electronic band structure modification due to the doping and/or the generated defects.

## 3.3 UV-vis spectroscopy

It is expected that the thermal nitridation can promote nitrogen insertion into the TiO<sub>2</sub> lattice and thus modify its electronic band structure. The color of the sample powders was noted to be altered due to the Nb-doping and/or the nitridation treatment. In particular, the N-doped and (Nb,N) co-doped samples exhibit a color ranging from yellow to dark green (**Figure 2.10** a). These color differences are the first indication that the light absorption of the TiO<sub>2</sub> materials could be shifted into the visible region through the annealing in ammonia. Thus, we characterized the light absorption properties of as-prepared samples by conducting UV-visible spectroscopy.

The measurements were carried out on a Perkin Elmer Lambda 950 spectrophotometer equipped with a 100 nm integrating sphere in the wavelength range of 300 to 800 nm. The original spectra were recorded in diffuse reflection mode. Then the absorption spectrum was calculated from the reflection spectra using the Kubelka-Munk equation (eq. 2.1).<sup>12</sup>

$$F(R) = \frac{K}{S} = \frac{(1-R)^2}{2R}$$
 (eq. 2.1)

where K is the absorption coefficient, S is the diffusion coefficient, and R is the reflectance. According to the obtained absorption spectra, the Tauc equation (eq. 2.2) was used to determine the band gap value of the sample.

$$(F(R) * h\nu)^n = a(h\nu - Eg)$$
 (eq. 2.2)

Where F(R) is the K-M function, h is the Planck constant, v is the photon frequency; n is a coefficient that depends on the nature of the bandgap transition (½ in the case of an indirect band gap such as  $TiO_2$  anatase), and  $E_g$  is the band gap value. By plotting  $(F(R)hv)^{1/2}$  as a function of photon energy, we can obtain the Tauc curves. Then the energy of the band gap corresponds to the intersection between the abscissa axis and the tangent line at the curve's inflection point.

The absorption spectra calculated by the Kubelka Munk function and the corresponding Tauc plots are presented in Figure 2.10 b and Figure 2.10 c respectively. It is shown that TiO<sub>2</sub>

has a band gap of  $3.06 \pm 0.05$  eV as expected and the band gap of 0.25NbTi is in the same range at  $3.08 \pm 0.05$  eV, but a small absorption between 400 and 500 nm gives a slight yellow color to this powder compared to the white TiO<sub>2</sub>. Similar observations were also reported in other works, and they were attributed to the local distortion of TiO<sub>2</sub> anatase lattice due to the introduction of Nb, resulting in new states with slightly lower energy than the CBB. <sup>13,14</sup>

The absorption spectra of (Nb,N) co-doped and N-doped samples depend on the thermal nitridation conditions: 0.25NbNTi-m and NTi-m samples subjected to mild nitridation show an increase of light absorption starting around 550 nm associated with a yellow/orange color. They have a shorter band gap of 2.44eV and  $2.47 \pm 0.05$  eV, respectively. In the case of NTi-m a second bandgap at 3.16 eV is also observed, a value which is closer to undoped anatase. Samples enduring harsh thermal nitridation also present this shorter absorption edge ( $E_g = 2.49$  and 2.39 eV for 0.25NbNTi-h and NTi-h respectively), but in addition, absorption at a longer wavelength ( $\lambda > 550$  nm) is observed for these samples resulting in darker colors compared to 0.25NbNTi-m and NTi-m (shown in **Figure 2.10 a**). This suggests a transition involving deep defect levels in the bandgap of TiO<sub>2</sub>. It is also noticeable that for similar thermal conditions of nitridation, co-doped samples have a more pronounced light absorption in the visible compared to their N-doped counterparts. This improved visible light absorption might be due to the facilitation of N incorporation when niobium is already present in the lattice of TiO<sub>2</sub>.

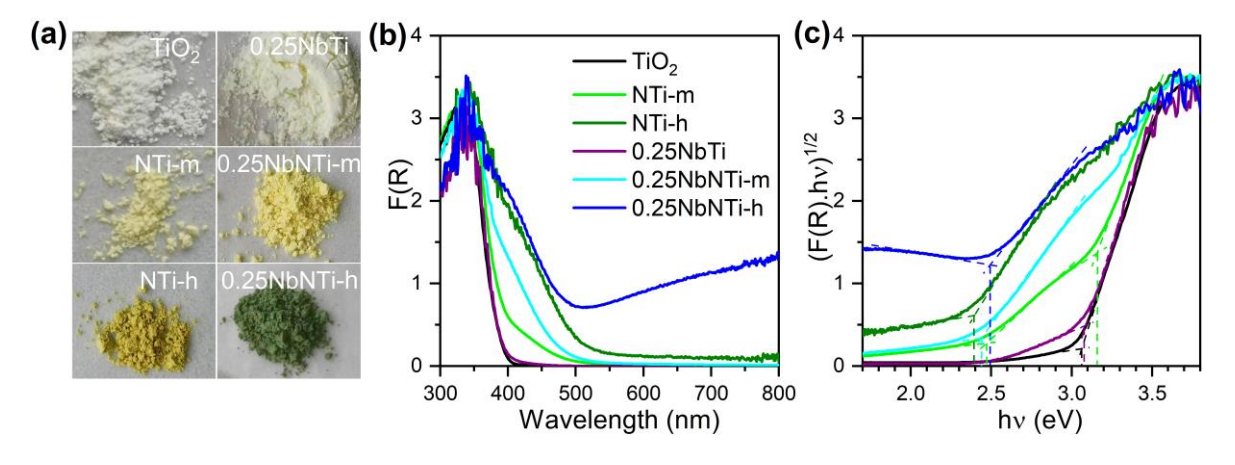


**Figure 2.10:** (a) Optical images of TiO<sub>2</sub>, N-doped, Nb-doped and (Nb,N) co-doped TiO<sub>2</sub> samples. (b) UV–visible absorption spectra of each sample. (c) Tauc plots of (F(R).hv)<sup>1/2</sup> vs (hv) for estimating the indirect band gap of each sample.

## 3.4 X-ray photoelectron spectroscopy

X-ray photoelectron spectroscopy (XPS) was utilized to analyze the surface chemical composition of the synthesized samples. The measurements were carried out by a Thermo-VG Scientific spectrometer equipped with a CLAM4 (MCD) hemispherical electron analyzer. For each sample, the Al  $K_{\alpha}$  line (1486.6 eV) and Mg  $K_{\alpha}$  line (1254 eV) anode X-ray sources were used as incident radiation for the measurements. The spectra of Nb 3d and N 1s, as well as O 1s, C 1s and Ti 2p were recorded to identify the doping species in this study. All data were processed with CasaXPS. (The survey spectra for different samples are shown in **Figure S2.1**, **Page 187**. The peak fitting details are summarized in **Table S2.1**, **Page 188**).

Three contributions are observed in the region of C 1s for all the samples (shown in **Figure S2.2, Page 187,** with an example of  $TiO_2$ ). The first peak C 1s A, with a binding energy of 285.0 eV, corresponds to the C-C and C-H bonds. This signal comes mainly from the residual carbonaceous organic pollution and was used as a reference peak to calibrate other XPS spectra. The second peak C 1s B at 286.5  $\pm$ 0.1 eV is attributed to the C-O bonds and the last peak C 1s C located at 289.  $\pm$ 0.2 eV is assigned to the C=O bonds (carbonyl). 15

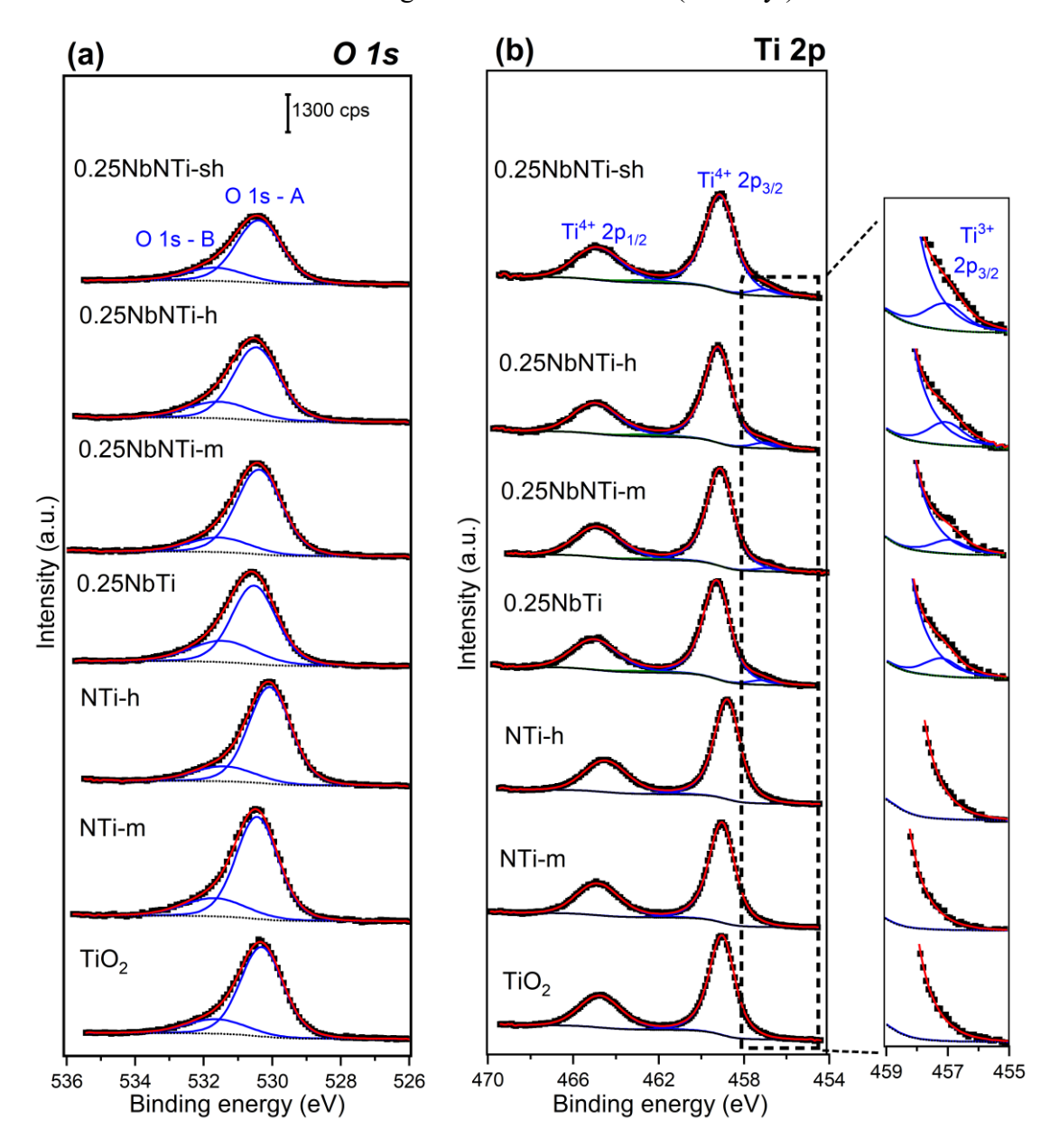


**Figure 2.11:** (a) XPS spectra of O 1s region for the different samples. (b) XPS spectra of Ti 2p region for the different samples. The zoom-in area of the dashed box exhibits the contribution of Ti<sup>3+</sup>. (Black points are the experiment data, black, blue and red lines are the baseline, the individual peak contributions, and the fitted signals).

In the O 1s region (**Figure 2.11 a**), all the samples present the spectra with two main contributions. The first peak O 1s A, located at  $530.4 \pm 0.1$ eV, is attributed to the lattice oxygen forming the chemical bond with Ti or the cation in the lattice. The second peak O 1s B, located

at 531.6  $\pm$  0.1 eV, is a composite peak attributed to surface oxygen species such as hydroxyl and carboxyl groups. <sup>16</sup>

The XPS spectra of Ti 2p for all samples (**Figure 2.11 b**) display two main peaks at  $459.1 \pm 0.2$  eV and  $465.0 \pm 0.2$  eV, consistent with the doublet of Ti 2p, the energy split between the two peaks is typical of Ti<sup>4+</sup>. Two additional peaks with a binding energy of  $457.1 \pm 0.2$  eV and  $462.9 \pm 0.2$  eV, characteristic of Ti<sup>3+</sup>,<sup>17</sup> can be observed on Nb-containing samples (zoom in **Figure 2.11 b**). To complete our observation of the Ti<sup>3+</sup> amount evolution, besides mild and harsh nitridation conditions, an (Nb,N) co-doped TiO<sub>2</sub> sample is synthesized under "super harsh" conditions (550°C for 1h in NH<sub>3</sub>) (0.25NbNTi-sh). The atomic proportion of Ti<sup>3+</sup> to the total Ti for 0.25NbTi, 0.25NbNTi-m, 0.25NbNTi-h, and 0.25NbNTi-sh is 4.0%, 3.2%, 5.2%, and 6.1%, respectively. These results suggest the facilitation of Ti<sup>3+</sup> generation by the introduction of niobium, as well as nitridation in ammonia. Nevertheless, a possible reduction of titanium, facilitated by Nb, during the XPS analysis under vacuum and X-ray irradiation, cannot be ruled out.<sup>18</sup>

**Figure 2.12 a** shows the Nb 3d XPS spectra of the Nb-doped and (Nb,N) co-doped samples with the peaks located at 207.7 and  $210.5 \pm 0.2$  eV typical of Nb  $3d_{5/2}$  and  $3d_{3/2}$  for Nb<sup>5+</sup>. <sup>14</sup> The atomic ratio between Nb and Ti for 0.25NbTi, 0.25NbNTi-m, 0.25NbNTi-h and 0.25NbNTi-sh is 0.34, 0.35, 0.36, and 0.31 respectively. These values are higher than the theoretical one (0.25) expected from the synthesis, which may be due to an enrichment of Nb-dopants on the sample surface. An additional contribution characteristic of Nb<sup>4+</sup> is needed to fit Nb 3d area for 0.25NbNTi-sh, suggesting the partial reduction of Nb<sup>5+</sup> after the super harsh nitridation.

Figure 2.12 b shows the N 1s spectral regions measured by Al anode for all samples. All Nb-containing TiO<sub>2</sub> powders present a broad peak at 395.0 ± 0.4 eV (Nb<sub>sat</sub>) which is a satellite of Nb 3p. <sup>19</sup> All samples present a common peak at  $400.6 \pm 0.3$  eV (N 1s-A), which is usually assigned to surface chemisorbed nitrogen or nitrogen in the interstitial position in the lattice. 20,21 After the mild thermal nitridation, the contribution of N 1s-A for NTi-m and 0.25NbNTi-m increases by 2.5 and 3.5 times respectively in comparison with their counterparts annealed in air. This result indicates the better insertion of N in the interstitial position when Nb is already present in the TiO2 lattice. While no significant change is observed for the intensity of N 1s-A between mild and harsh nitridation conditions, a new contribution located at 396.5  $\pm$  0.3 eV (N 1s-B) appears for samples subjected to harsh nitridation. This last contribution is usually attributed to nitrogen in substitution of oxygen in the lattice.<sup>22,23</sup> This contribution is multiplied by a factor of 5 when the temperature of nitridation is raised from 450°C (0.25NbNTi-h) to 550°C (0.25NbNTi-sh), while N 1s-A intensity decreases. The comparison between NTi-m and 0.25NbNTi-h samples, which have the same thermal history, confirms a greater amount of nitrogen for 0.25NbNTi-h due to both an increase of N 1s-A and the appearance of N 1s-B peak for the niobium doped sample. This is another observation that suggests a lower formation energy of nitrogen species in the (Nb,N) co-doped TiO<sub>2</sub> crystalline structure compared to the N single-doped TiO2.24 The atomic ratio between N and Nb for 0.25NbNTi-m, 0.25NbNTi-h and 0.25NbNTi-sh are 0.12, 0.18 and 0.44, indicating that the ideal balanced co-doping is not achieved with our synthetic conditions.

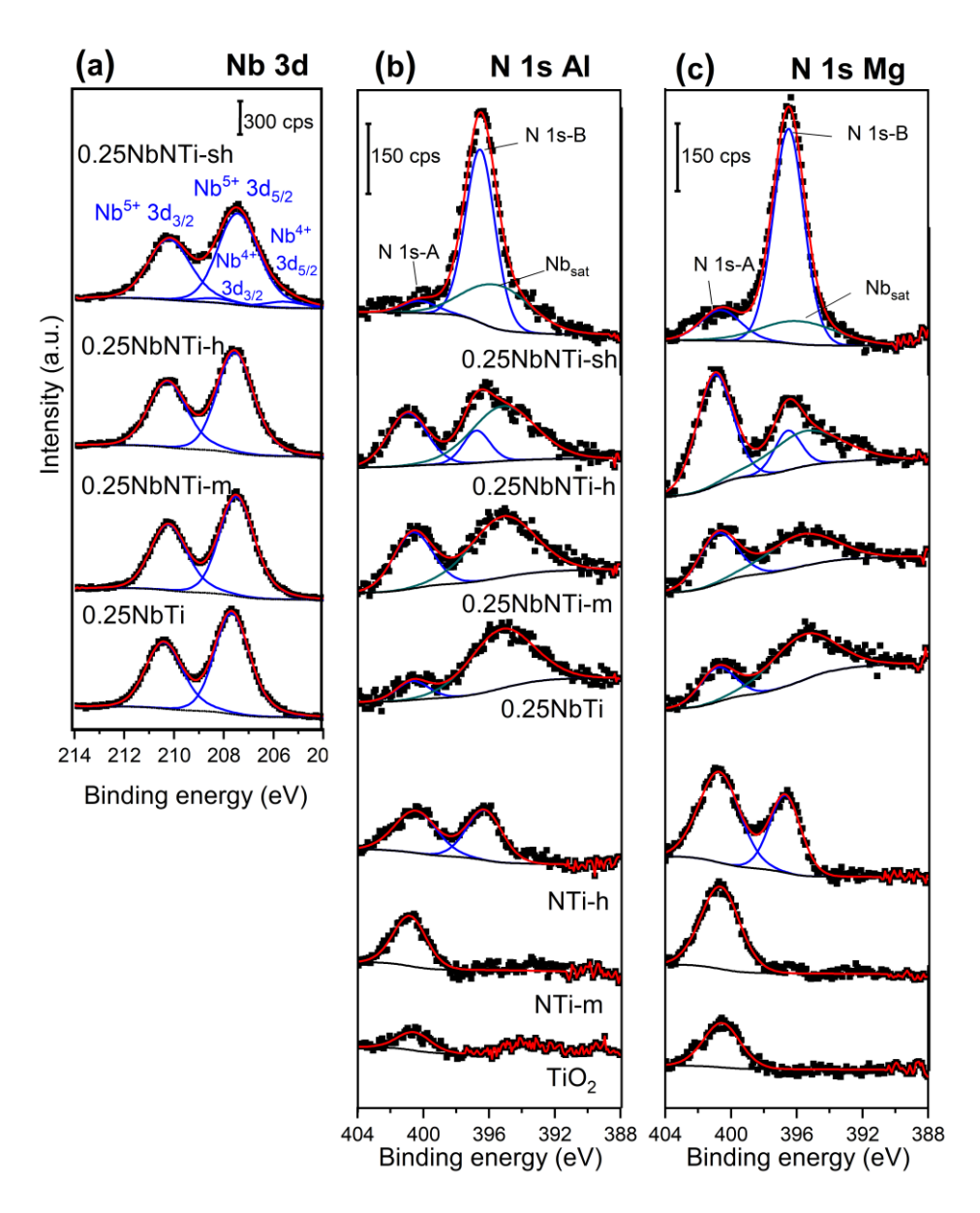


Figure 2.12: (a) XPS spectra of Nb 3d region for Nb-doped TiO<sub>2</sub> and (Nb,N) co-doped TiO<sub>2</sub> samples. (b) and (c) shows XPS spectra of N 1s region for the different samples with Al and Mg X-ray sources, respectively. (Black points are the experiment data, black, blue, green, and red lines are the baseline, the individual N 1s contributions, the Nb<sub>sat</sub> peak green, and the fitted signals)

To estimate whether these nitrogen species are located on the surface or in the core of the nanoparticles, the N 1s spectra measured with the Mg anode (**Figure 2.12 c**) was compared with those recorded by using the Al anode (**Figure 2.12 b**). In the case of Mg anode, incident X-ray with lower energy penetrates less in the sample than when using the Al anode, and consequently, species located preferentially at the surface will have a higher signal when measured with an Mg X-ray source. The ratio between N 1s peak intensities measured by Mg anode and Al anode ( $R_{N ls-x} = N ls-x^{(Mg)}/N ls-x^{(Al)}$ ) was calculated for each sample. Before nitridation, TiO<sub>2</sub> and 0.25NbTi show similar  $R_{N ls-A}$  values (~2.0), which indicates that the nitrogen species associated with this peak originated from the surface and is probably coming from adsorbed nitrogen species. After nitridation, while we observe an increase of N 1s-A

intensity for Mg and Al X-ray source,  $R_{N \, 1s\text{-}A}$  is slightly reduced (~1.8). On the other hand, The  $R_{N \, 1s\text{-}B}$  of NTi-h, 0.25NbNTi-h and 0.25NbNTi-sh is lower (~1.2), indicating a more homogeneous distribution of the substitutional nitrogen in the particles. The analysis comparing XPS signal from Mg and Al X-rays sources was also conducted on the other elements. In the case of Nb 3d peaks, the measured ratio of ~1.1 indicates no significant surface enrichment in niobium in the particles.

#### 3.5 Electron paramagnetic resonance spectroscopy

Complementary to XPS, Electron paramagnetic resonance (EPR) measurements were conducted to investigate the defects with a paramagnetic signature that were generated during the synthesis for the specific sample (Collaboration with Bertrand Vileno and Nolwenn Le Breton, Institut de Chimie UMR7177). The measurements were performed at 100 K on an X-band EMX-plus spectrometer (Bruker Biospin GmbH) equipped with a high sensitivity resonator (ER4119HSW, Bruker) and a variable temperature unit ER4131VT, Bruker). The g factor was calibrated using the Bruker strong pitch (g =2.0028). Between 20 and 50 mg of sample were placed in a quartz tube and degassed with He. EPR intensity was obtained by double integration of the EPR spectra.

As shown in **Figure 2.13**, 3 types of EPR active centers are identified for  $TiO_2$ . The triplet at 336, 332.5 and 330.0 mT (\*) is assigned to the NO species captured at the surface of the porous  $TiO_2$  already identified by the N 1s-A peak of XPS spectra. At g=2.00 (332 mT; indicated by  $\Delta$ ), another visible signal is the signature of an unpaired electron trapped on an oxygen vacancy  $V_0^+$ , a common defect created in various metal oxides. Finally the weak signal indicated by I, which is attributed to paramagnetic nitrogen species is  $N^{2-}$  in a  $[O-Ti^{4+}-N^{2-}-Ti^{4+}]$  unit. The latter signal is not observed for the Nb-containing samples and could result from N of the nitric acid used during the sol-gel synthesis not being completely removed due to the lower annealing temperature used for pure  $TiO_2$ . However, as observed in raw data normalized by the mass of the sample (**Figure 2.13 a**), the EPR signal remains low for  $TiO_2$  and 0.25NbTi. On the opposite, for the  $TiO_2$  sample after mild nitridation (NTi-m), an intense fine signal related to oxygen vacancies  $V_0^+$  as well as the small signal associated with  $N^{2-}$  can be observed. With the intensification of the nitridation condition (NTi-h), alongside  $V_0^+$ , new contributions (•, •) characteristic of  $Ti^{3+}$  in different sites appears (see high resolution normalized spectra in **Figure 2.13 b**).

 ${
m Ti}^{3+}$  signal is also observed for all Nb-containing samples but with an important difference in the signal intensity. 0.25NbTi shows similar signals as  ${
m TiO}_2$ , with the signal associated with surface-adsorbed NO groups and a small contribution of  ${
m Ti}^{3+}$ . For 0.25NbNTim, the signals of  ${
m V_0}^+$  and  ${
m Ti}^{3+}$  are observed, but as can be observed on the non-normalized data, in comparison with NTi-m, the  ${
m V_0}^+$  remains significantly lower, confirming the improved defects passivation by (Nb,N) co-doping through the mild nitridation. Similar spectral features are observed on 0.25NbNTi-h but the intensity of the signal attributed to  ${
m Ti}^{3+}$  and  ${
m V_0}^+$  is significantly higher. Furthermore, on the large field spectra, we can observe a broad contribution that originates from a collection of surface  ${
m Ti}^{3+}$  centers with different local coordination. We hypothesize that these  ${
m Ti}^{3+}$  centers are mainly located at a disordered layer at

the surface of the particles, slightly more rich in Nb as suggested by XPS measurements.

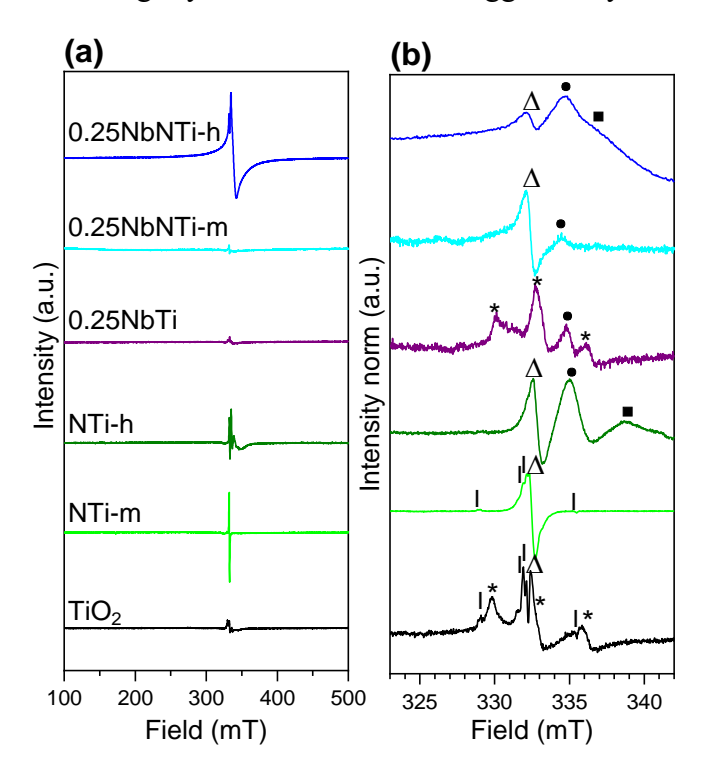


**Figure 2.13:** EPR spectra for different samples: (a) large filed spectra normalized with sample mass and (b) high-resolution spectra with peak-to-peak normalization.

## 3.6 Discussion on the charge compensation mechanism

Our results of EDX and XPS confirm that Nb can be successfully introduced into the lattice of  $TiO_2$  via the sol-gel method, and the XPS result also shows an effective nitrogen insertion by the nitridation treatment under the current experimental conditions. Based on the characterization of EPR, we found that the intrinsic defects present in the prepared  $TiO_2$  materials are mainly  $V_O^+$  and  $Ti^{3+}$  centers,  $^{32}$  depending on the initial presence of Nb as well as the specific thermal condition of nitridation. Different charge compensation mechanisms occur in the different samples to maintain the overall electrical neutrality of the material.

For the samples without nitridation,  $V_O^+$  centers were identified by EPR in our undoped TiO<sub>2</sub>, but not on the 0.25NbTi sample. This suggests that the presence of niobium, due to its additional positive charge, must reduce the natural concentration of  $V_O^+$  in TiO<sub>2</sub>, and on the opposite favors defects that add a negative charge to the structure such as interstitial oxygen  $O_i^{2-}$ , Ti vacancies, or  $Ti^{3+}$ .<sup>4</sup> A signal of  $Ti^{3+}$  was observed on EPR and XPS for the 0.25NbTi sample and could be a possible mechanism to compensate for the excessive positive charge introduced by  $Nb^{5+}$ .<sup>33,34</sup> Nevertheless considering Nb/Ti=0.25, 25% of the  $Ti^{4+}$  should be reduced in  $Ti^{3+}$  while the measured XPS value is only 4%. Consequently, either the  $Ti^{3+}$  dominantly exists in the deeper bulk or a mechanism involving  $O_i^{2-}$  or Ti vacancies cannot be ruled out since these two defects would be EPR silent and would not provide any discernible XPS signal.

Under mild nitridation conditions, NTi-m exhibits a strong  $V_{\rm O}^+$  signal in EPR, and an increased signal of interstitial nitrogen (N<sub>i</sub>) in XPS compared to TiO<sub>2</sub> suggesting that the additional negative charges brought by nitrogen atoms are compensated by a  $V_{\rm O}^+$  occupied by a lone electron according to:

$$Ti^{4+}O^{2-}_{(2-2x)}N_x^{3-}V_{0(-x)}^+$$
 (eq. 2.3)

In the case of 0.25NbNTi-m, a different charge compensation mechanism may occur: besides a higher amount of  $N_i$  observed by XPS, the main difference is that the EPR signal associated with  $V_O^+$  is significantly lower than for NTi-m. In that case, a possible explanation is that  $N_i$  may replace the aforementioned  $O_i^{2-}$  in the lattice to balance the positive charge brought by  $Nb^{5+}$ :

$$Ti_{(1-x)}^{4+} Nb_x^{5+} O_{(2-x)}^{2-} N_x^{3-}$$
 (eq. 2.4)

It should be noted that the amount of nitrogen is almost only one tenth of that of niobium, as discussed in **3.4** based on the XPS results, indicating that the negative charge brought by N<sup>3</sup>-cannot completely compensate the positive charge brought by Nb<sup>5+</sup>. Thus, the above equations represent only one of the charge compensation mechanisms identified by the current characterization techniques (XPS and EPR). The existence of other mechanisms that add negative charges to the system is highly possible. However, further characterization to reveal the defects, such as O<sub>i</sub><sup>2-</sup>, cation vacancies is needed, since these defects are not detectable by XPS or EPR.

Under harsh nitridation conditions, another doping mechanism seems to happen for both 0.25NbNTi-h and NTi-h. According to the XPS result, both samples present substitutional nitrogen ( $N_s$ ), suggesting that the formation of  $N_s$  requires an increased energy input compared to that of interstitial nitrogen ( $N_i$ ). The EPR result indicates that when the nitridation is harsh, the charge compensation is related to both  $V_O^+$  and  $Ti^{3+}$ . These two defects might be promoted by the decomposition of  $NH_3$  at high temperatures that produce  $H_2$ ,  $^{29,35}$  and can facilitate the insertion of  $N_s$ . As observed by XPS, this second mechanism seems predominant at a higher temperature, since the intensity of the N 1s-B peak, associated with  $N_s$  increases with the temperature while the one (N 1s-A) of  $N_i$  does not evolve. Additionally, the quantity of  $Ti^{3+}$  measured by XPS for co-doped samples increases with the temperature, and in the case of 0.25NbNTiO2-sh, treated at 550°C, the charge compensation also involves the partial reduction of  $Nb^{5+}$  to  $Nb^{4+}$ .

## 3.7 Reversed double-beam photoacoustic spectroscopy

Based on the aforementioned characterization, we identified the doping species of niobium and nitrogen and associated defects of  $V_0^+$  and  $Ti^{3+}$ . All of them may modify the electronic structure of the specific sample by introducing new energy states. Therefore, to determine the effect of these different states on the electronic structure of the different samples, the energy-resolved distribution of electron traps (ERDT) was measured by photoacoustic spectroscopy (PAS) and reversed double-beam photoacoustic spectroscopy (RDB-PAS) (Collaboration with Mai Takashima and Bunsho Othani, Hokkaido University). These

methods provide the spectral dependence (between 650 and 300 nm) of photoacoustic signal related to the filling of electron traps (ETs) by photoexcitation of valence-band electrons while photogenerated holes are captured by methanol.

#### 3.7.1 Experimental setup

Both PAS and RDB-PAS measurements were carried out using a laboratory-made PAS cell equipped with a MEMS (micro-electro-mechanical system) microphone module (SparkFun MEMS Microphone Breakout, INMP401 (ADMP401)) and a quartz window on the upper part, as illustrated in **Figure 2.14 a**. Firstly, conventional PAS measurements were performed to estimate the bandgap, *i.e.* conduction-band bottom (CBB) energy in reference to valence-band top (VBT), of samples under  $N_2$  atmosphere. A beam of monochromatic light from a monochromator (Spectral Products CM110) with an Eagle Engineering R300-3J Xenon lamp was modulated at 80 Hz and wavelength scanned from 550 nm to 300 nm with a step of 1 nm to record photoacoustic (PA) signal intensity. The resultant PA signal was detected by a digital lock-in amplifier (NF Corporation LI5630) and calibrated using the spectral response of a graphite sample as a reference (**Figure S2.3, Page 189,** presents PA spectra for different samples). The position of the CBB was estimated according to the onset wavelength ( $\lambda_{bg}$ ) of the PA spectrum.

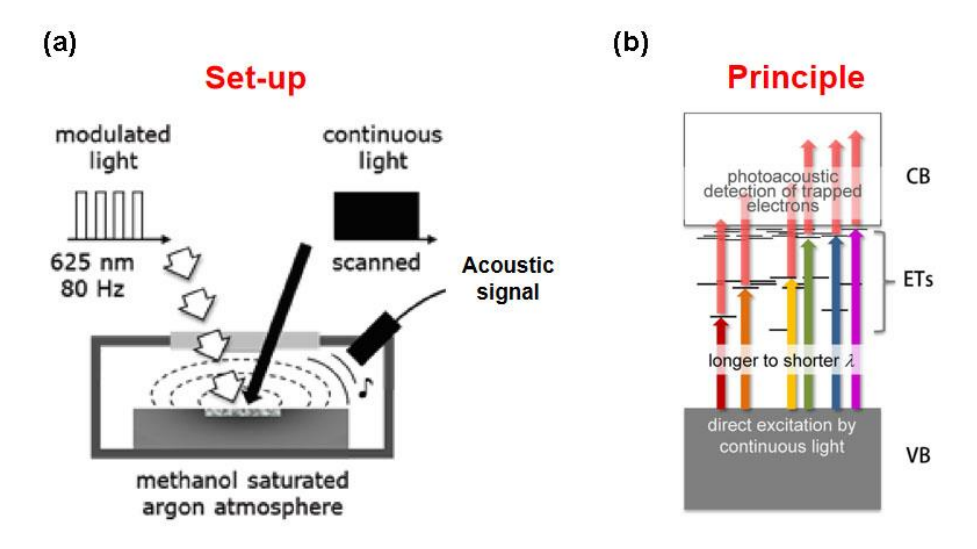


**Figure 2.14:** The set-up (a) and working principle (b) of photoacoustic spectroscopy (PAS) and reversed double-beam photoacoustic spectroscopy (RDB-PAS) measurement.

Then, RDB-PAS measurements were conducted to estimate the density of ETs. The powder sample was set in the PAS cell under the flow of argon saturated with methanol vapor. The purpose of methanol is to trap the holes and avoid charge recombination during the subsequent measurement. A beam from a 625-nm LED (Luxeon LXHL-ND98) light intensity modulated at 35 Hz was used to generate the resultant PA signal. Simultaneously, the other beam of wavelength-scanned continuous monochromatic light (650 to 300 nm with a step of 5 nm) was mixed with the mentioned 625-nm modulated beam by a UV quartz combiner light guide (Moritex MWS5-1000S-UV3) and irradiated from the upper side of the sample cell.

During the scanning by the continuous monochromatic light, the electrons can be exited from the valence band and further trapped by ETs (**Figure 2.14 b**), resulting in the generation of PA signal. The intensity of the recorded PA signal was plotted against the energy of continuous light in reference to VBT in the form of the RDB-PA spectrum (**Figure S2.4**, **Page 189**, presents the RDB-PA spectra for different samples), and then the obtained spectrum was converted into ETs density in the unit of µmol g<sup>-1</sup> by conducting differentiation from the lower energy side to higher energy side. <sup>36,37</sup>

#### 3.7.2 Result and discussion

It is worth noting that Ti<sup>3+</sup> states cannot be detected by this method, since they are already electron-filled energy states lying below the Fermi level. Figure 2.15 shows the ERDT/CBB patterns for different TiO2 samples, in which the horizontal dashed lines represent the conduction-band bottom energy (in reference to VBT) as determined by PAS measurements, the histogram represents the energy distribution of ETs relative to VBT and the values <XX> denote the total density of ETs in the unit of µmol.g<sup>-1</sup>. The estimated band gaps of TiO<sub>2</sub> and 0.25NbTi are ca. 3.0 eV, in agreement with UV-vis spectroscopy results (3.06 and 3.08 eV respectively). ETs in TiO<sub>2</sub> and 0.25NbTi are distributed predominately near the CBB, and could be mainly assigned to some intrinsic ETs, such as V<sub>0</sub><sup>+</sup>. The increased density of ETs that is observed on 0.25NbTi may be due to the addition of empty 4d orbital states of Nb in the vicinity of the CB. While ETs are expected to be in the bandgap (i.e., below the conduction band bottom CBB) their distributions extend inside the CB. This can be explained by at least two phenomenon:<sup>36</sup> (i) the electron trap position is represented relative to the VBT but the density of states (DOS) in the valence band is not homogeneous and could be low around the VBT, the ERDT would then also reflect the DOS of the VB, i.e., the energy is overestimated and (ii) most of ETs may be located on the surface of the particles<sup>36</sup> and present a different structure and energy position than bulk ETs.

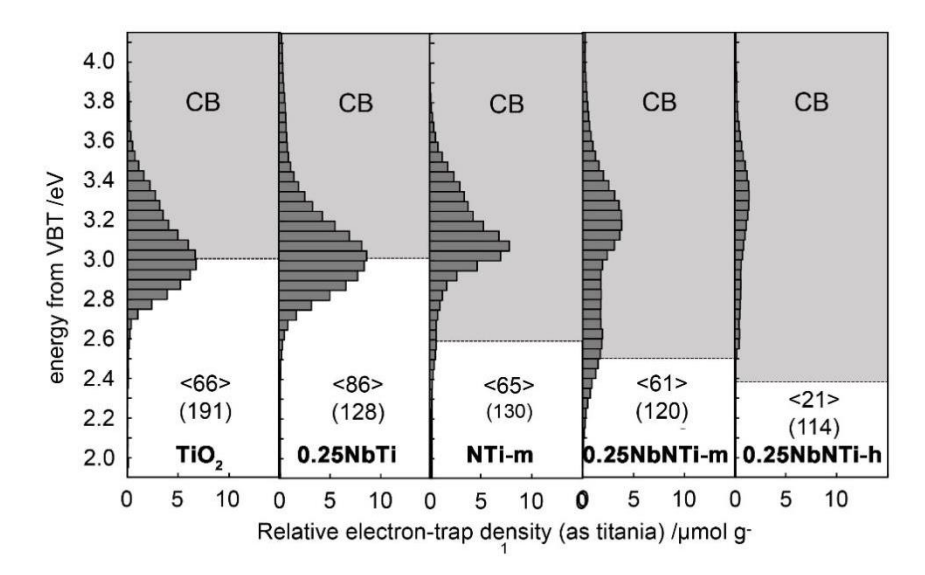


**Figure 2.15:** ERDT/CBB patterns of TiO<sub>2</sub>, NTi-m, 0.25NbTi, 0.25NbNTi-m and 0.25NbNTi-h. Values <XX> denote the total density of ETs in μmol.g<sup>-1</sup>. The specific surface area in m<sup>2</sup>.g<sup>-1</sup> is indicated by (YY). The ordinate represents the energy states of ETs counting from the valence band top (VBT). The length of the bars represents the relative electron-trap density.

In the case of NTi-m, the ERDT has a sharper distribution centered on 3.1 eV that extends to lower energy until 2.4 eV. The band gap measured by PAS for this sample is 2.6 eV while the Tauc plot revealed two transitions at 2.47 and 3.16 eV. This case illustrates that most of the photo-trapped electron originates from the VBT of TiO2 with a small contribution possibly from N 1s states above the VB. For 0.25NbNTi-m and 0.25NbNTi-h, the ETs are observed to distribute more homogenously on a broad range of energy between 3.8 and 2.4 eV with a maximum of ERDT around 3.2 eV revealing strong changes in the electronic band structure. When compared with NTi-m, 0.25NbNTi-m presents a more intense ERDT between 2.4 and 3.0 eV which suggests a higher density of states induced by nitrogen above the VB. A possible explanation is that a higher amount of nitrogen doping increases the density of electron-filled states above the VBT and excitation from these states can fill up ETs, which requires lower energy. 0.25NbNTi-h present the same distribution of ETs as 0.25NbNTi-m but the total ETs density is 3 times lower. This observation suggests that for this sample more photogenerated electron-hole pairs recombine before their transfer to ETs (for e<sup>-</sup>) or to the surface for methanol oxidation (for h<sup>+</sup>). A possible explanation for this lower availability of charge carriers is a strong binding of the exciton with the lattice in the presence of Ti<sup>3+</sup> center and/or substitutional nitrogen.

To verify this hypothesis, the sample 0.25NbNTi-h was exposed to ozone to undergo an oxidation treatment, and the RDB-PAS measurement was conducted again after the oxidation treatment. As shown in **Figure 2.16**, the ERDT patterns and ETs density of the treated sample (0.25NbNTi-h-O<sub>3</sub>/O<sub>2</sub>) tend to become closer to the one of 0.25NbNTi-m. It is observed that the ETs below 2.4 eV appear again after the treatment, and the total intensity of ETs is increased to twice that of 0.25NbNTi-h. This suggests that the Ti<sup>4+</sup> might be reduced into Ti<sup>3+</sup> during the harsh thermal nitridation, *i.e.*, filling electrons in ETs. The generated Ti<sup>3+</sup> may act as the photogenerated charge recombination center, resulting in a significant decrease in the detectable PA signals. This reduction process can be reversed with ozone treatment thus allowing more electrons to be excited to the ETs. Consequently, the ERDT patterns of the sample after oxidation treatment present similarity to that of the sample after mild nitridation.

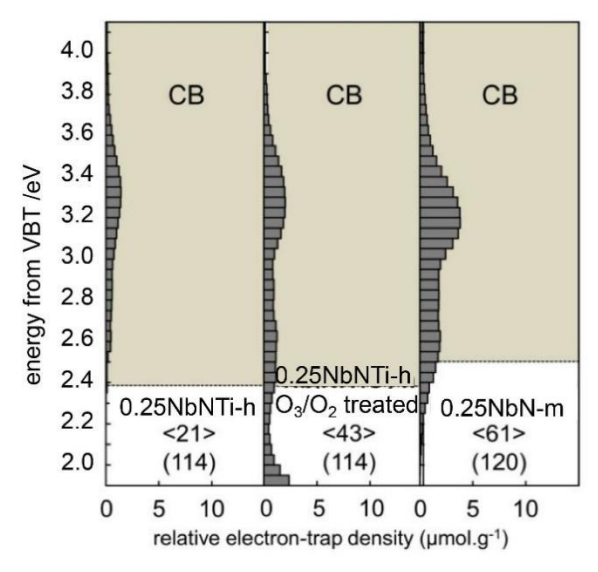


**Figure 2.16:** ERDT/CBB patterns of 0.25NbNTi-h before and after O<sub>3</sub>/O<sub>2</sub> treatment compared to 0.25NbNTi-m.

#### 3.7.3 Proposed electronic band structure

Based on the discussion of the above characterization results, a schematic diagram illustrating the possible band electronic structure for the different samples is proposed in Figure 2.17. TiO<sub>2</sub> is believed to have its typical electronic structure with a band gap of 3.06 eV and some intrinsic defect states, that are considered mainly to be V<sub>0</sub><sup>+</sup>, distributed near the CBB. Nb incorporation produced the hybridization between the d orbits of Nb and Ti inside the CBB since no narrowing of the band gap was observed. Due to the low concentration of Ti<sup>3+</sup>, we hypothesize that the charge compensation could be partially achieved by cation vacancy or interstitial oxygen. For NTi-m, according to XPS results (see Table S2.1), 0.4 %at, of nitrogen was incorporated by conducting mild thermal nitridation, forming N 2p states above the VBT and reducing the optical bandgap to 2.47 eV. This additional nitrogen is accompanied by an increase of V<sub>O</sub><sup>+</sup> density as revealed by EPR. For 0.25NbNTi-m, the nitrogen quantity is almost doubled (0.8 %at.), ensuring a higher DOS above the VB of TiO2 and a more intense light absorption associated with a band gap of 2.44 eV. In addition, the EPR signal of V<sub>O</sub><sup>+</sup> signal remains low for this sample, indicating that under mild thermal nitridation, the charge compensation mechanism involves Nb<sup>5+</sup> and N<sub>i</sub><sup>3-</sup> which insertion is facilitated by the Nb-doping of TiO<sub>2</sub>. For the samples annealed under harsh conditions, both NTi-h and 0.25NbNTi-h present a similar increase of nitrogen (~1.3 %<sub>at.</sub>) associated with the appearance of substitutional nitrogen but no significant change of bandgap when compared to mild conditions. These samples have a significant signal increase of V<sub>O</sub><sup>+</sup> but also of Ti<sup>3+</sup>, the latter being responsible for the absorption at long wavelengths ( $\lambda > 500$  nm) that is observed for these samples.

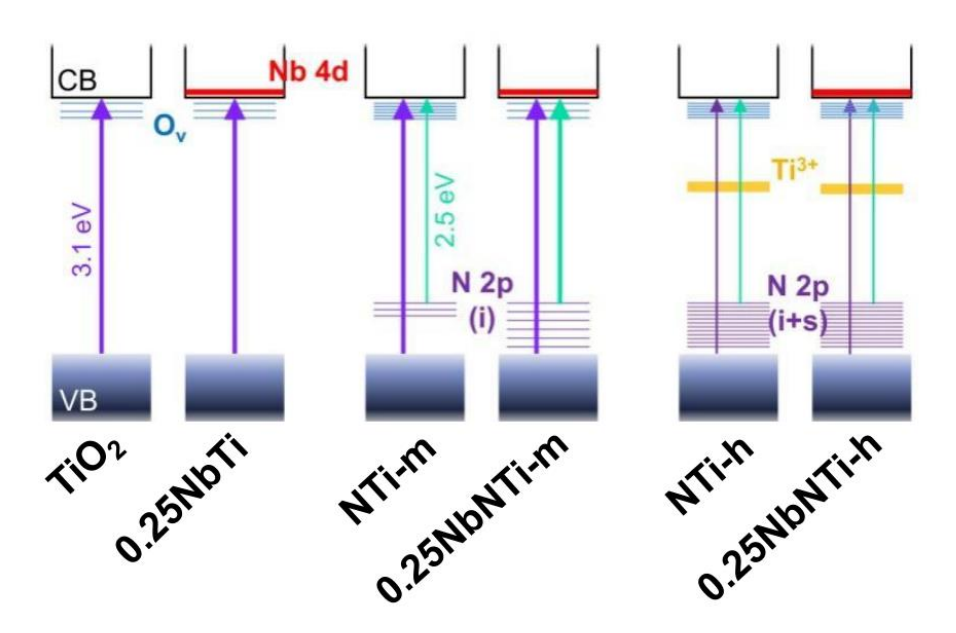


**Figure 2.17:** Proposed electronic band structures and defects position for TiO<sub>2</sub>, 0.25NbTi annealed under air, and treated with mild and harsh nitridation in NH<sub>3</sub>. (i and s for N 2p states correspond to interstitial and substitutional nitrogen)

# 3.8 X-ray absorption and emission spectroscopy with synchrotron irradiation

Based on the previous characterizations, we have outlined the electronic structure of the synthesized (Nb,N) co-doped TiO<sub>2</sub> materials. However, these characterization results mainly revealed the overall properties of the material and allowed us to identify two clear behaviors associated with different types of defects but the location of these defects in the anatase lattice remains unclear. Cationic doping sites have been identified as Nb<sup>5+</sup> in substitution of Ti<sup>4+</sup> in the TiO<sub>2</sub> lattice. But in the case of N doping sites, although *ab initio* DFT calculation predicted that the M-N pair is the most thermodynamically stable configuration, <sup>38</sup> no conclusive experimental evidence is available and this aspect is hardly discussed in the field while it seems to play a key role in the photocatalytic properties.

The main issue here is the lack of methods that can provide this information. For instance, XRD or EXAFS can indicate an enlargement of the cell but does not discriminate N from O due to their close atomic weight. TEM allows observing the position of Nb in the lattice but again it is not possible to distinguish N from O. XPS and EPR have provided useful information, but are not sensitive to the location of these sites. XPS has allowed us to identify at least two types of N environments depending on the nitridation process, and by EPR we were able to probe paramagnetic defects, but these analyses do not provide crystallographic information on the doping sites.

## 3.8.1 Principle of X-ray Absorption and Emission Spectroscopy (XAS & XES)

X-ray spectroscopic methods provide an opportunity to probe the electronic and geometric structure of a specific element in the material. They can provide a detailed experimental map of the molecular orbitals, giving insight into the oxidation state and ligand environment around a specific absorbing atom. Several studies of dopants in TiO<sub>2</sub> nanostructures based on the X-ray spectroscopic methods have been reported. For instance, Stewart *et al.* found Ti in fivefold coordination for the N-doped TiO<sub>2</sub> by studying the XANES spectra of Ti. <sup>39</sup> Garcia-Tecedor *et al.* demonstrated the substitution site of Nb in the Nb-doped TiO<sub>2</sub> and they found the reduction of Nb<sup>5+</sup> to Nb<sup>4+</sup> under the electrochemical reaction conditions. <sup>40</sup>

X-ray Absorption Spectroscopy (XAS) involves the excitation of core-level electrons of a given atom by absorption of a photon of energy hv. Depending on the energy of the incident photon, the photoelectron is excited to different empty levels and involved in various physical processes leading to different structures on the X-ray absorption spectrum. The electronic states involved are illustrated in **Figure 2.18 a** and an example of the resulting spectra is shown in **Figure 2.18 b**. The spectrum can be divided into several regions: the EXAFS region (Extended X-ray Absorption Fine Structure) is observed when the energy of the photoelectron is enough to reach the continuum and extract the electron from its atom. EXAFS can provide structural information on the first neighboring atoms, but will not be discussed in detail here since it does

not allow distinguishing N from O ligand. The threshold structures or XANES (X-ray Absorption Near Edge Structure) are obtained for lower energy and can be divided into two regions. The pre-edge is related to the transition from the core level to empty orbitals of the absorbing atom. In the case of Ti K-edge, the pre-edge peaks can be ascribed to the transition from the 1s orbital to the partially occupied 3d orbitals, and the empty 4p orbitals. When the energy of the photon increases until it reaches the continuum, there is a sudden rise in the X-ray absorption coefficient which is the threshold. The XANES contains both electronic and stereochemical information about the absorbing atom.

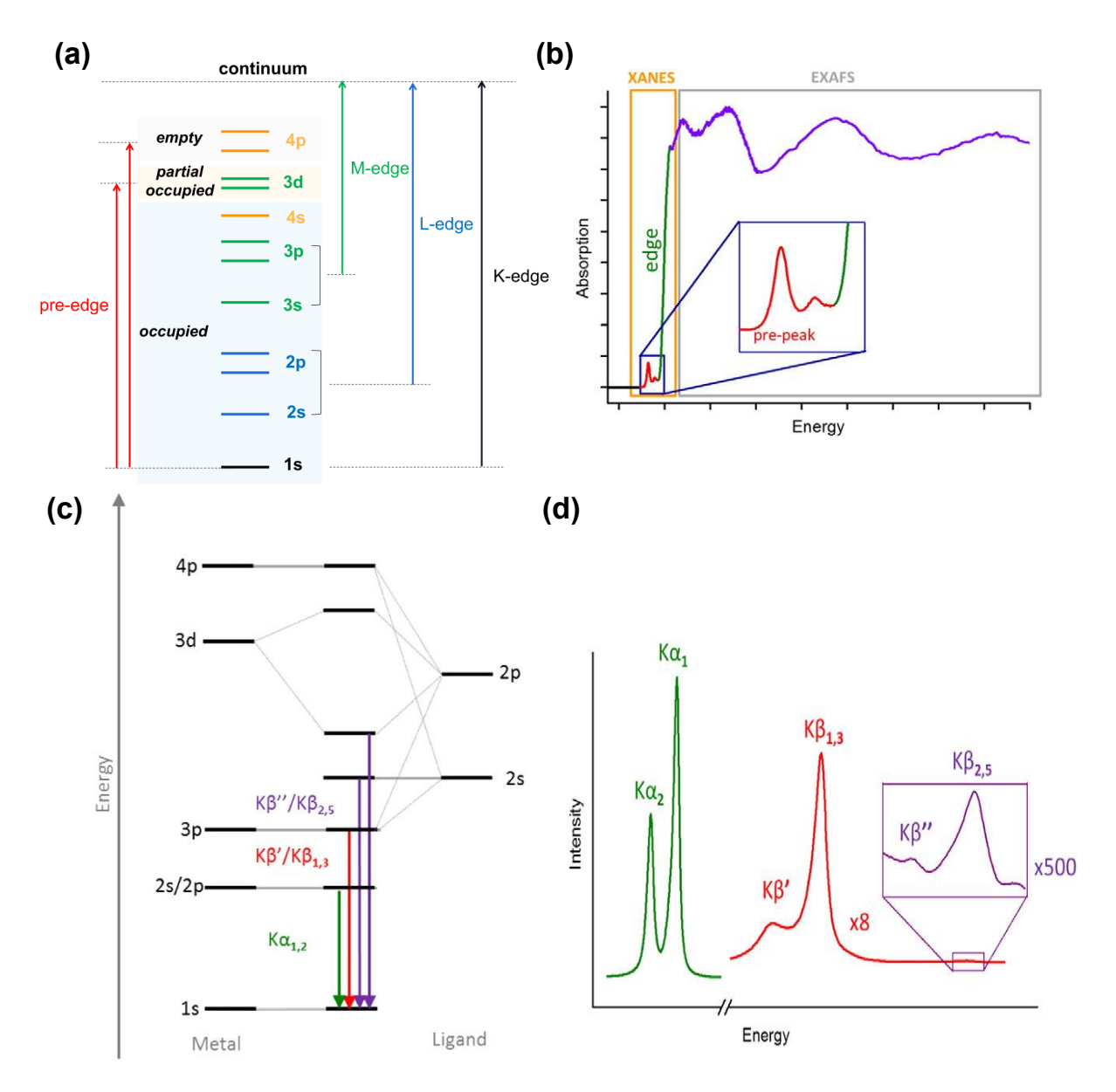


**Figure 2.18:** (a) Energy diagram showing the origin of the K, L, M-edge and K pre-peak features in the X-ray absorption spectrum (example of Ti). (b) Example of resulting XAS spectrum. (c) Energy level diagram for K emission lines in the X-Ray emission spectrum. (d) K emission spectrum fine structure for K-line of 3d atoms.

During the X-ray absorption process, the excitation of the core electron creates a core hole. Then, this hole is filled by an electron from a higher level, resulting in the emission of an

X-ray photon. This is the origin of X-ray Emission Spectroscopy (XES) which can provide useful information when spectrally resolved. The most studied emission lines are K lines, which originate from the filling of 1s core hole (**Figure 2.18 c** and **2.18 d**). When the filling electron is from 2s/2p (L shell), the emissions are K $\alpha$  lines, while the electron from higher orbital results in K $\beta$  lines. In addition, for d transition metal the emission lines K $\beta$ " and K $\beta_{2,5}$ , are related to transitions involving 2s or 2p orbitals of the ligand to the 1s core level of the absorbing atom. These are collectively referred to as the valence-to-core region (VTC-XES), the VTC region provides a sensitive probe of ligand identity by the energy position of these peaks. These transitions have a low probability (~1000 times less likely than the K $\alpha$  emission) but are detectable thanks to the progress in synchrotron radiation sources. This approach was used to probe the ligand coordinating transition metal atoms in the case of Co<sup>42</sup>, Ti<sup>43,44</sup> and Nb<sup>45</sup> for instance.

#### 3.8.2 Experimental parameters

In our experiment, both XAS and XES spectra at the K-edge of Ti ( $\approx$  5 keV) and Nb ( $\approx$ 19 keV) were characterized for different samples. These experiments were done on the beamline ID26 of the ESRF (European Synchrotron Research Facility). This beamline was chosen for its high energy which is necessary to work at the Nb K-edge and its high X-ray flux. As in XPS analysis, the samples subjected to super harsh nitridation (550°C; 1h; NTi-sh and 0.25NbNTi-sh) were also characterized to amplify the concentration of N dopants in coordination with the cations. For the measurement based on Ti K-edge, commercial materials of TiN (99.9%, Merck), Ti<sub>2</sub>O<sub>3</sub> (99.9%, Merck) and anatase UV100 were used as references. TiN and Ti<sub>2</sub>O<sub>3</sub> can provide the typical characteristics of Ti-N and Ti<sup>3+</sup>-O bond. UV100 is used to confirm the common characteristics from anatase structure. For the measurement based on Nb k-edge, the reference compounds are Nb<sub>2</sub>O<sub>5</sub>, NbN and NbON. Among them, Nb<sub>2</sub>O<sub>5</sub> (99.9%, Merck) and NbN (99.9%, Merck) are commercial products, which are used to provide information on Nb-O and Nb-N bond, respectively. NbON was synthesized using a similar solgel method as that for 0.25NbTi-sh. The difference is that Ti was absent and the nitridation was conducted directly based on the formed gel without air calcination. We expected to reach a higher doping concentration of nitrogen, thus make a better comparison.

The XAS spectra were recorded by irradiating the sample with X-ray energy ranging from 4.95 to 5.10 keV for Ti K-edge and from 18.94 to 19.20 keV for Nb K-edge. The signal was recorded by monitoring the total fluorescence of the element.

The VTC XES was recorded by irradiating the sample at a fixed wavelength higher than the K-edge (5.1 and 19.2 keV for Ti and Nb respectively). Then the fluorescence signal was diffracted on a crystal (Si 006) and sent to a spectral analyzer. The K $\beta$  emission spectra with high resolution were recorded from 4.90 to 4.99 keV for Ti and 18.90 to 19.05 keV for Nb.

#### 3.8.3 Experimental results

#### 3.8.3.1 Ti K-edge

Figure 2.19 a exhibits the XANES spectral region of the Ti K-edge for the different

samples and the reference materials (TiN, Ti<sub>2</sub>O<sub>3</sub> and anatase UV100). Four main pre-edge features (labeled as A, B, C and D) can be observed on all synthesized samples and UV100. Features A and B correspond to the transition of the core election to the hybridization of the empty 4p and 3d states. <sup>46–48</sup> The relative intensity of these peaks is related to the symmetry of the polyhedron, and the coordination of the titanium. Feature C corresponds to the transition to the states that are hybridized by Ti 4p and Ti 2s orbitals, <sup>49</sup> and feature D is assigned to the transition to the states hybridized by Ti 4p and O 2p orbitals. <sup>50</sup>

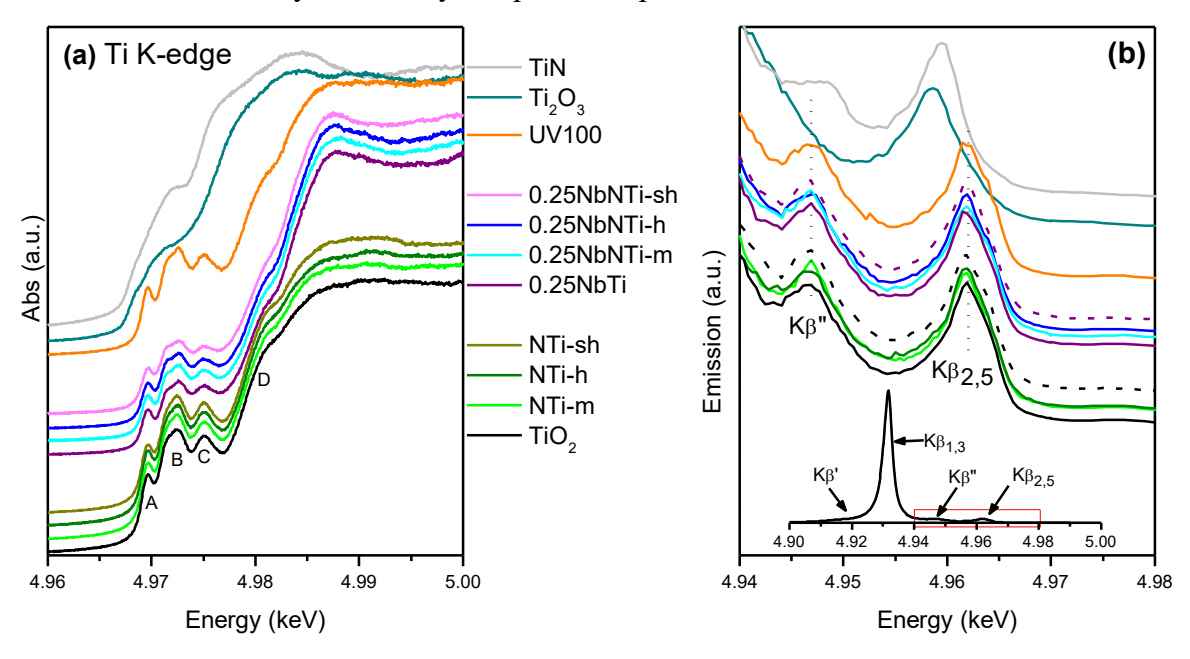


**Figure 2.19:** (a) XANES spectra at the Ti K-edge for the synthesized materials, TiN, Ti<sub>2</sub>O<sub>3</sub> and UV100. (b) X-ray emission spectra (presenting the emission lines of Kβ" and Kβ<sub>2,5</sub>) The inset represents the whole Kβ emission region.

As references, both TiN and Ti<sub>2</sub>O<sub>3</sub> show a different absorption edge which is strongly shifted significantly towards lower energy, which corresponds to the lower oxidation state of Ti<sup>3+</sup>. A high similarity of the spectral feature is observed on the spectra of TiO<sub>2</sub>, N-doped TiO<sub>2</sub> samples and UV100, indicating a dominant anatase character of these samples. We can also observe a slight decrease in the relative intensity of feature A on NTi-h and NTi-sh, which could be attributed to the increase of rutile proportion observed by XRD.<sup>51</sup> On the other hand, the same four pre-edge features also appear on Nb-containing samples but with a decreased intensity. We supposed that the higher calcination temperature for 0.25NbTi (500°C 12h) compared to TiO<sub>2</sub> (400°C 2h) may increase the crystallinity and thus decrease the distortion of the octahedral structure in Nb-containing samples, resulting in a weaker intensity of pre-edge features. A similar change in the pre-edge was also published by Paula C. Angelome et al. by comparing the XANES spectra of amorphous TiO<sub>2</sub> and TiO<sub>2</sub> calcined at different temperatures. 46 A slight peak at the edge top can be noticed for Nb-containing samples. In this region, the photoelectron has a long lifetime and can be diffused several times by the neighboring atoms and the presence of Niobium in large quantities can thus explain this change. Nevertheless, we did not observe any significant change in the pre-edge energy that can indicate a change of coordination or the reduction of Ti for these samples.

Figure 2.19 b presents VTC-XES spectra of Ti for all synthesized samples, together with the references. All synthesized samples exhibit identical spectral features to those of UV100, where the contribution of K $\beta$ " and K $\beta$ 2,5 are observed at the same energy. The former can be attributed to the electron-filling of the core level from O 2s states of the ligand whereas the latter is mainly due to the transition from the hybridized orbitals involving O 2p to the 1s core level of Ti.

For  $Ti_2O_3$ , only  $K\beta_{2,5}$  is observed with a shift to lower energy, in agreement with the results from Mandić *et al.*<sup>43</sup> Amongst all the other samples, only TiN presents an obvious decrease in energy split between  $K\beta$ " and  $K\beta_{2,5}$  which indicates the presence of nitrogen in the coordination sphere. This change is mainly due to the difference in the electron-filling transitions originating from the states of the N ligand compared to the mentioned O orbitals. Consequently, the above XAS and VTC-XES results at Ti K edge show that the insertion of nitrogen has no detectable effect on the coordination of the Ti atom in the  $TiO_2$  lattice.

#### 3.8.3.2 Nb K-edge

**Figure 2.20 a** shows the Nb K-edge XANES spectra of the Nb-containing samples and the reference compounds Nb<sub>2</sub>O<sub>5</sub>, NbN and NbON. The absorption edge of all synthesized samples and Nb<sub>2</sub>O<sub>5</sub> are almost identical confirming the Nb<sup>5+</sup> oxidation state observed by XPS for all Nb-containing samples, whereas the absorption edge of NbN (Nb<sup>3+</sup> oxidation state) is shifted to lower energy. Besides, the pre-edge feature originates from the transition from 1s to 4d <sup>52</sup> and verifies the substitution of Nb for Ti in octahedral sites. In addition, the relative intensity ratio between feature B and feature C is observed to change for the synthesized Nb-containing samples compared to Nb<sub>2</sub>O<sub>5</sub>. This could be due to the modified chemical environment around Nb in TiO<sub>2</sub> lattice compared to pure Nb<sub>2</sub>O<sub>5</sub>.

The XES spectra for the corresponding samples are shown in **Figure 2.20 b.** The peaks of  $K\beta_2$ ,  $K\beta_4$  and  $K\beta$ " are present in all samples, even if the latter is significantly less intense for NbN sample.  $K\beta_2$  and  $K\beta_4$  are assigned to the transition from 4p and 4d orbitals of Nb to the 1s core state, and the  $K\beta$ " emission line is related to the transition from the 2s orbital of the ligand. 45

All the Nb-containing samples share mostly the same characteristics of  $K\beta_2$  and  $K\beta_4$  with Nb<sub>2</sub>O<sub>5</sub>, suggesting an oxidation state of Nb<sup>5+</sup> and an octahedral configuration for the Nb in the lattice of TiO<sub>2</sub>. The emission signals were fitted with Lorentzian function (the inset of **Figure 2.20 b** shows an example for 0.25NbTi, and the fitting results of other samples are shown in **Figure S2.5**, **Page 190**). The energy position and area of the emission peaks for each spectrum are summarized in **Table 2.3** as well as the energy splitting  $\Delta E(K\beta''-K\beta_2)$  and  $\Delta E(K\beta_4-K\beta'')$  and area ratio  $A(K\beta'')/A(K\beta_2)$ . For Nb<sub>2</sub>O<sub>5</sub> and 0.25NbTi samples, the  $K\beta''-K\beta_2$  energy split is 15.0 and 15.2 ± 0.2 eV. For the NbN reference, this value increases up to 17.1 eV, which is comprised between the values for Nb<sub>2</sub>O<sub>5</sub> (15.3 eV) and NbC (19.8 eV) observed by Ravel *et al.* <sup>45</sup> Additionally and the intensities of  $K\beta_4$  and mainly  $K\beta''$  are reduced compared to the oxide references. The energy split between  $K\beta_4$  and  $K\beta''$  and the intensity of  $K\beta''$  normalized by the one of  $K\beta_2$  can provide useful information that depends on the ligand. The  $\Delta E(K\beta_4-K\beta'')$  decreases from 14.2 to 13.7 eV with the increase of nitridation temperature. This value remains

far from the 9.4 eV measured for the NbN sample, but such a shift was not observed for the Ti K $\beta$  emission. Furthermore, the intensity of K $\beta$ " is slightly reduced for the sample with the lowest  $\Delta E(K\beta_4-K\beta)$ ". It should be noted that such an effect was not observed for the 0.25NbTim sample that does not contains substitutional nitrogen according to our XPS results.

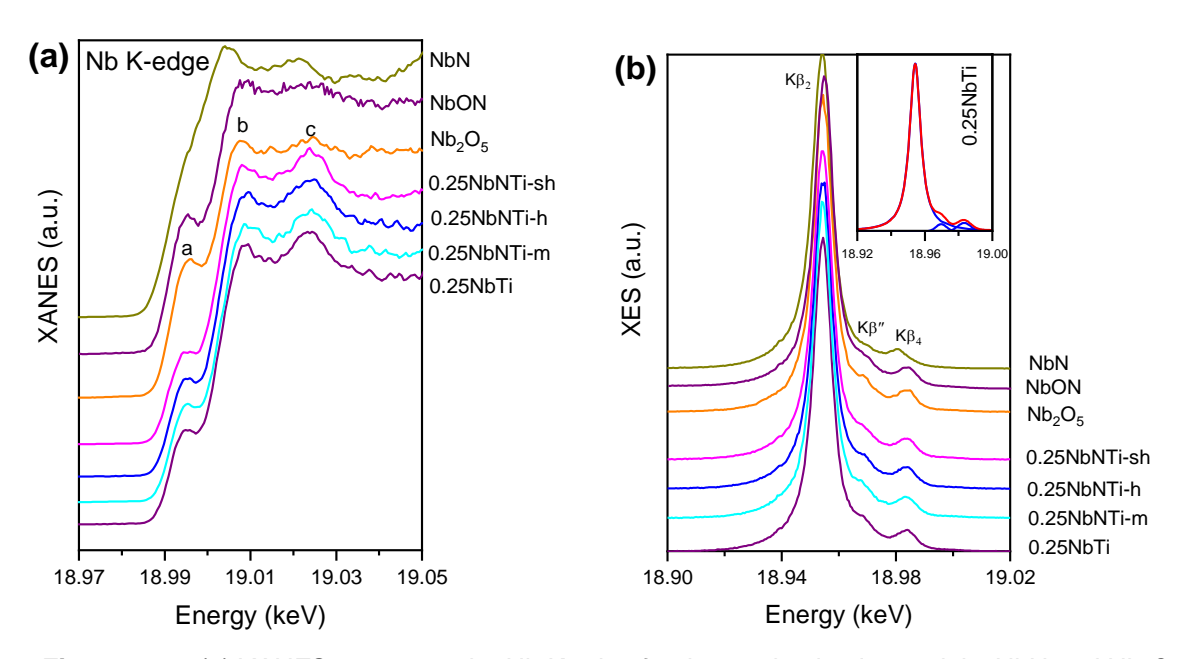


**Figure 2.20:** (a) XANES spectra at the Nb K-edge for the synthesized materials, NbN and Nb<sub>2</sub>O<sub>5</sub>. (b) X-ray emission spectra (presenting the emission lines of  $Kβ_2$ , Kβ" and  $Kβ_4$ ). The inset shows the fit to 0.25NbTi. The three fitted peaks represent  $Kβ_2$ , Kβ" and  $Kβ_4$ .

		Nb <sub>2</sub> O <sub>5</sub>	0.25NbTi	0.25NbTi-	0.25NbTi-	0.25NbTi-	NbON	NbN
				m	h	sh		
$K\beta_2$	Pos. (keV)	18.9545	18.9543	18.9543	18.9543	18.9543	18.9545	18.9540
	A (a.u.)	4.80e-4	4.80e-4	4.75e-4	4.82e-4	4.81e-4	4.83e-4	4.99e-4
Κβ"	Pos. (keV)	18.9694	18.9695	18.9693	18.9697	18.9698	18.9699	18.9712
	A (a.u.)	1.44e-5	1.46e-5	1.62e-5	1.27e-5	1.39e-5	1.25e-5	2.36e-6
$K\beta_4$	Pos. (keV)	18.9835	18.9835	18.9835	18.9834	18.9835	18.9834	18.9806
	A (a.u.)	2.37e-5	2.27e-5	2.23e-5	2.37e-5	2.21e-5	2.09e-5	1.66e-5
ΔΕ(Κβ'	'-Kβ <sub>2</sub> ) (eV)	15.0	15.2	15.0	15.4	15.5	15.4	17.1
$\Delta E(K\beta_4)$	<sub>ι</sub> -Kβ") (eV)	14.1	14.0	14.2	13.8	13.7	13.5	9.4
A(Kβ	")/A(Kβ <sub>2</sub> )	0.0311	0.0306	0.0342	0.0264	0.0288	0.0258	0.0047

Table 2.3: Peak fitting for XES of Nb related to Figure S2.5

#### 3.8.4 Conclusion on synchrotron measurement.

XAS and VTC-XES methods have been tested to reveal the local coordination of the Ti and Nb atoms in the lattice of (Nb,N) co-doped TiO<sub>2</sub>. According to the result of the Ti K-edge spectra, we have confirmed the dominant anatase structure of all the synthesized samples but no change of signal that can be assigned to the N-ligand was observed on the XES spectra at the Ti K-edge for the (Nb,N) co-doped samples or N doped samples. The result from the Nb K-

edge spectra confirms the dominant  $Nb^{5+}$  oxidation states in the co-doped samples. Furthermore, the evolution of the ligand-dependent emission  $K\beta$ " with the increasing nitridation temperature was observed on the co-doped samples with substitutional N. However, this effect remains small since both oxygen and nitrogen are in the coordination of the cations. Nevertheless, since the signal change was observed only on Nb emission peaks our results suggest that this substitutional nitrogen preferentially interacts with the  $Nb^{5+}$  creating the Nb-N defect pairs.

## 4. Photocatalytic activity for methylene blue degradation

The utilization of the photocatalytic degradation of methylene blue (MB) as the model reaction for estimating the photocatalytic activities of the photocatalysts is a common practice in the field of photocatalysis. As an aniline-based dye, MB has good solubility in water. The UV-Vis spectrum of MB aqueous solution presents a maximum absorbance peak at ~664nm. Therefore, it is convenient to monitor the evolution of MB solution concentration during the photocatalytic reaction by UV-vis spectroscopy. During the photocatalytic reaction, the free radicals generated by semiconductor photocatalysts can destroy the molecular structure of MB, leading to a decolorization of the tested solution and a decrease of the mentioned absorbance peak or the degradation can occur by a direct hole transfer from the SC to adsorbed MB at its surface.

In this study, the photocatalytic activities of the prepared samples were evaluated by conducting the photodegradation of MB under UV light (365 nm) and visible light (450 nm) using LED and also under simulated solar light (Xe arc lamp with AM 1.5G filter, 100 mW.cm<sup>2</sup>). In addition, methylene blue was chosen to exclude the possibility of photodegradation via photosensitization of the photocatalyst pathway at the two illumination wavelengths from the LED.<sup>54</sup>

## 4.1 Experimental conditions

Photodegradation under UV or visible light was conducted at 30°C and monitored with an immersion probe connected to the spectrometer by an optical fiber (set-up described in **Figure 2.21 a and 2.21 b**): The scanning light (800 nm to 510 nm) was generated from the light source of the spectrometer and then transmitted in the inlet optical fiber. After passing through the suspension, the light was reflected into the outlet fiber, which finally transmitted the light to the detector of the UV-visible spectrophotometer. Throughout the whole experiment, the reactor was covered by a black box to avoid any interference from external light.

For each experiment, 30 mg of photocatalyst powder was dispersed into 135 mL deionized water, and the suspension was stirred at 650 rpm for 30 min before recording the baseline. Then 5 mL of MB solution was added into the suspension (ie) the initial MB concentration is 14.3  $\mu$ mol.L<sup>-1</sup>) and kept in the dark for 30 min before illuminating to reach absorption–desorption equilibrium. The UV-visible spectra were recorded every 5 min and the evolution of MB concentration was evaluated by monitoring the characteristic absorption peak at 664 nm.

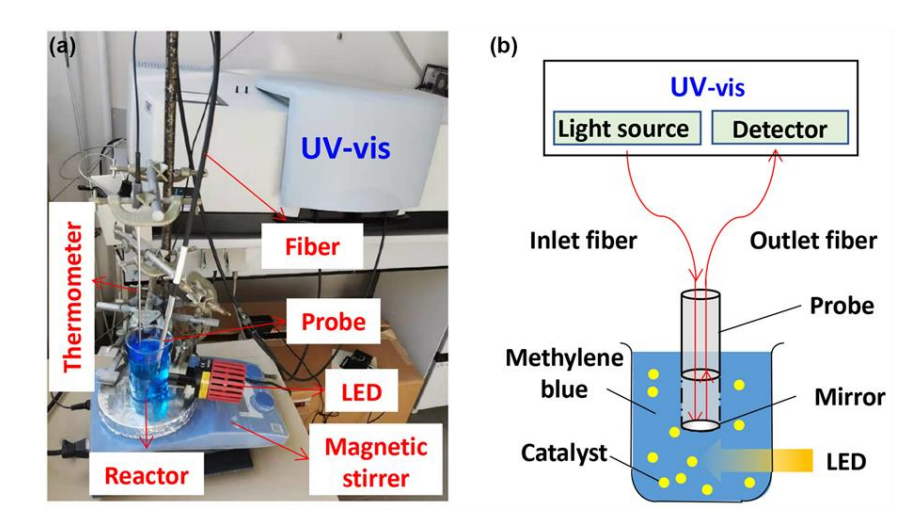


**Figure 2.21:** (a) Image of the experimental setup. (b) Schematic diagram of the probe for measurement of photo-degradation.

The linear relationship between MB concentration and the absorbance at 664 nm was calibrated by measuring standard MB solutions with known concentrations (**Figure 2.22 a and 2.22 b**). When using simulated solar light, the immersion probe cannot be used due to visible light interferences, then 1 mL of the solution was taken manually every 30 min, and the absorbance spectra of the supernatant were recorded to monitor the degradation.

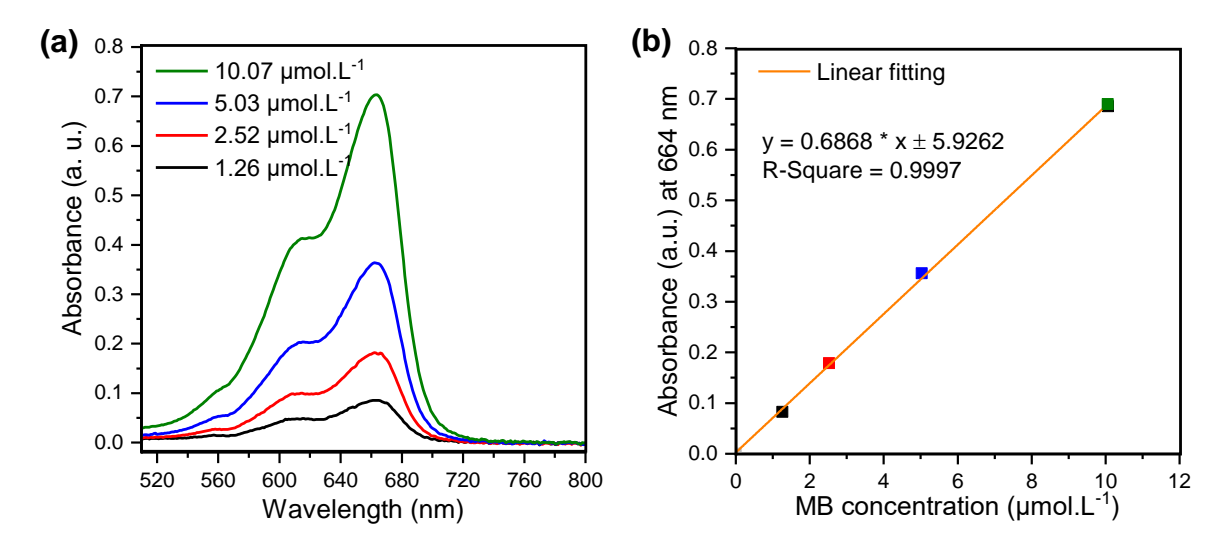


**Figure 2.22:** (a) Spectra of MB solution with different concentrations used for calibration. (b) Calibration curve of MB absorbance at 664 nm.

## 4.2 Photocatalytic activity measurements

#### 4.2.1 Control experiments

Before using the synthesized samples as photocatalysts, the absence of degradation of MB under UV light without photocatalyst was checked (**Figure 2.23 a**). This ensures that the observed photocatalytic degradation of MB (detailed later) is promoted by the s photocatalysts.

Furthermore, the dark equilibrium adsorptions of MB for different samples are shown in **Figure 2.23 b.** It is observed that the Nb-containing samples have a slightly improved adsorption capacity for MB, which could be attributed to the change of surface charge due to Nb doping.

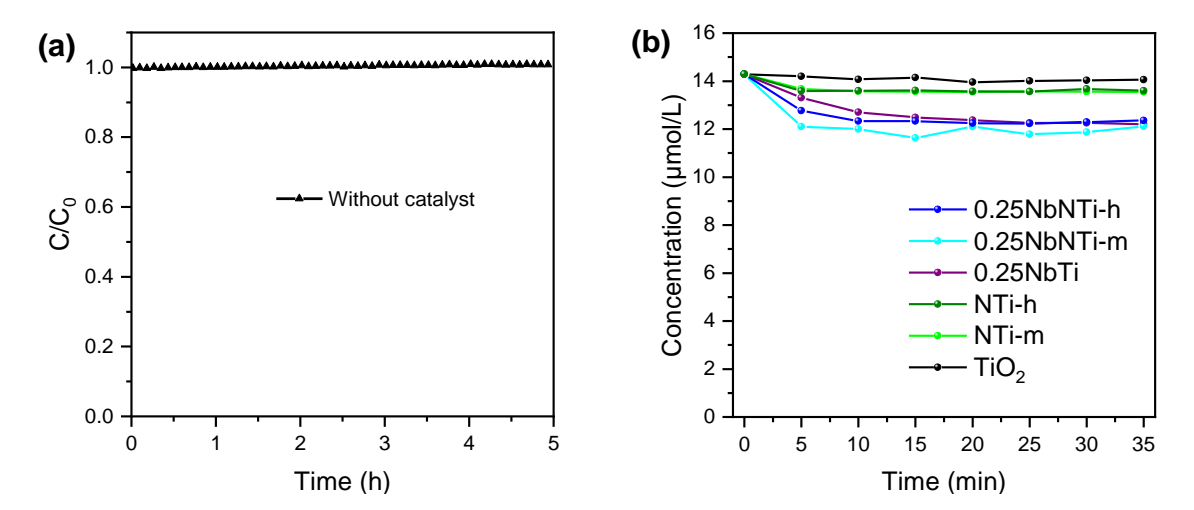


**Figure 2.23:** (a) MB concentration evolution under UV LED (365 nm) irradiation without catalyst. (b) Dark equilibrium adsorption isotherms of MB for TiO<sub>2</sub>, N-doped TiO<sub>2</sub>, Nb-doped TiO<sub>2</sub> and (Nb,N) co-doped TiO<sub>2</sub> samples.

#### 4.2.2 Result discussion

The degradation rate for the reaction was described as pseudo-first-order kinetics:

$$ln\left(\frac{c_0}{c_t}\right) = k.t \tag{eq.2.5}$$

where  $C_t$  is the concentration of MB at time t, and  $C_\theta$  is the concentration of MB when the illumination is started. The degradation profiles and associated kinetic for the different samples are shown in **Figure 2.24 a** and **2.24 b** (UV), **2.24 c** and **2.24 d** (visible) and the calculated k are presented in **Table 2.4**.

Under UV light irradiation, the excitation from VBT to CBB can be theoretically achieved for all samples. Therefore, the photocatalytic activity should mainly be determined by the efficiency of the separation and transfer of photogenerated charge carriers. Benefiting from its small crystalline size and large surface area, the synthesized TiO<sub>2</sub>, used as a reference, was able to fully degrade the MB within 120 min, with a kinetic constant  $k = 2.6124 \, h^{-1}$ . NTi-m and 0.25NbNTi-m exhibit similar k for photo-degradation of MB as TiO<sub>2</sub>. Considering the low quantity of  $V_0^+$  in 0.25NbNTi-m, whereas it was higher in NTi-m, we suppose that  $V_0^+$  does not influence significantly the degradation kinetic. 0.25NbTi shows an enhanced photocatalytic activity ( $k = 3.5100 \, h^{-1}$ ) in comparison with TiO<sub>2</sub>, which could be ascribed to the improvement of adsorption for MB molecular (**Figure 2.23 b**) as well as an enhancement of charge carrier mobility resulting from the introduction of Nb.<sup>55,56</sup> However, a significant decrease in photocatalytic activity can be observed on NTi-h ( $k = 0.6198 \, h^{-1}$ ) and 0.25NbNTi-h ( $k = 0.4908 \, h^{-1}$ ), which could be due to the generation of Ti<sup>3+</sup> and/or substitutional nitrogen that may act as charge recombination centers.

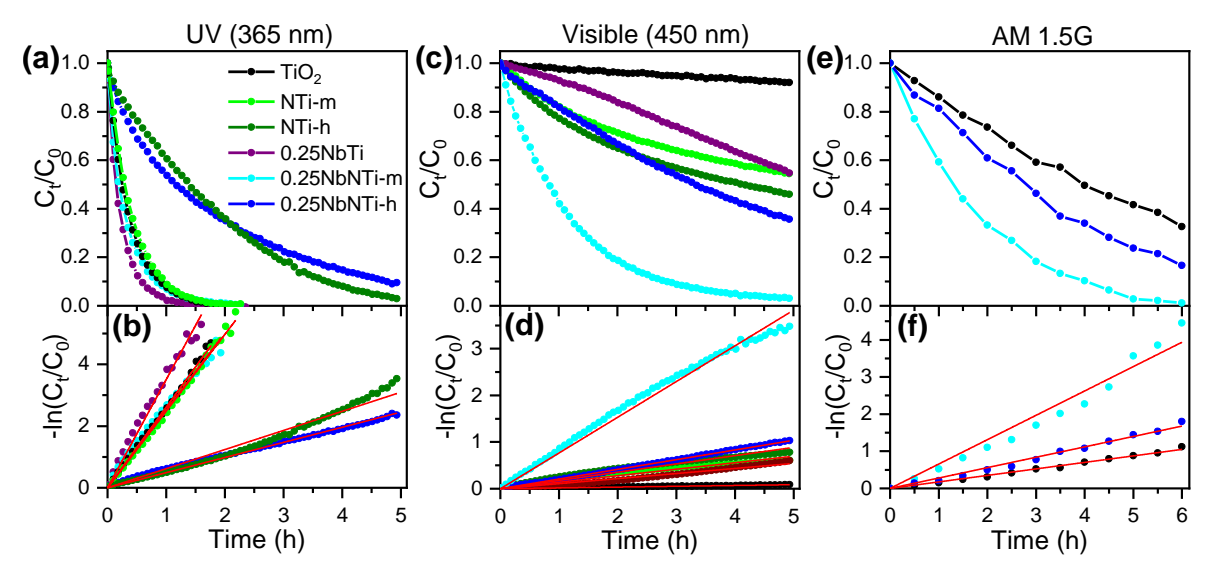


Figure 2.24: Photocatalytic activities of MB degradation kinetics for the different samples under the irradiation using UV LED (365 nm) (a and b), visible LED (450 nm) (c and d) and AM 1.5G simulated solar light (e and f).

**Table 2.4:** Pseudo-first-order kinetic constant of photo-degradation for the different (Nb,N) codoped TiO₂ photocatalysts under UV and visible irradiation.

Sample	<i>k</i> -UV / h <sup>-1</sup>	<i>k</i> -visible / h <sup>-1</sup>
TiO <sub>2</sub>	2.6124	0.0174
NTi-m	2.4870	0.1392
NTi-h	0.6198	0.1770
0.25NbTi	3.5100	0.1086
0.25NbNTi-m	2.5128	0.7656
0.25NbNTi-h	0.4908	0.2076

With visible light illumination at 450 nm, the photon absorption depends on the sample. As shown in Figures 2.24 c and 2.24 d, TiO<sub>2</sub> limited by its wide band gap (3.06 eV), achieves negligible photodegradation of MB ( $k = 0.0174 \text{ h}^{-1}$ ). All other samples have enhanced photocatalytic activity for the degradation of MB, which could be ascribed to the increase of photon absorption due to Nb and/or N doping. 0.25NbNTi-m shows the highest degradation speed with  $k = 0.7656 \text{ h}^{-1}$ . In comparison, even though 0.25NbNTi-h has the best light absorption at 450 nm among all samples, its photocatalytic activity is divided by almost 4 (k =0.2076 h<sup>-1</sup>). NTi-h has only slightly higher photocatalytic activity than NTi-m while the last one presents a lower absorption in the visible at 450 nm. Consequently, while increased visible absorption in the range of 365 nm to 550 nm may effectively enhance the photocatalytic efficiency, the samples submitted to harsh nitridation conditions with absorption at longer wavelengths caused by Ti<sup>3+</sup> states are less efficient for MB degradation. These two types of absorption, which give contradictory results, are ascribed to different types of defect and doping centers identified by EPR and XPS and the photocatalytic results confirm that substitutional nitrogen and/or Ti<sup>3+</sup> centers, induced by harsh nitridation, may act as charge-carriers recombination centers.

Finally, the (Nb,N) co-doped samples that present the best activity in the visible regions were tested in a photo-degradation experiment under AM1.5G simulated solar light and compared to TiO<sub>2</sub> (**Figure 2.24 e and 2.24 f**). 0.25NbNTi-m confirms its superior photocatalytic activity compared to TiO<sub>2</sub> and 0.25NbNTi-h, which can be explained by its activity in the visible region. For 0.25NbNTi-h, it can be noticed that while it shows lower activity than TiO<sub>2</sub> and 0.25NbNTi-m under UV illumination, its photocatalytic activity under AM1.5G remains higher than TiO<sub>2</sub> thanks to its absorption and photoconversion in the visible range (between 400 and 550 nm), a spectral region of the solar spectrum that contains more energy than the UV region.

### 5. Conclusion

 $TiO_2$  and Nb-doped  $TiO_2$  photocatalysts were successfully prepared via a sol-gel method. By controlling the calcination temperature and duration (400°C, 2h for  $TiO_2$ , 500°C, 12h for 0.25NbTi), we ensured as much as possible comparable crystal structures and specific surface areas between the different samples. According to the XRD result, it is found that the Nb-doping favors the stabilization of the anatase phase. Then, N-doped and (Nb,N) co-doped materials were prepared by conducting thermal nitridation in ammonia based on  $TiO_2$  and Nb-doped  $TiO_2$ . While the nitridation process was found to facilitate the increase of rutile proportion in the N-doped samples, the (Nb,N) co-doped samples still crystallized in pure anatase phase due to the presence of Nb in the crystalline, with a small particle size (< 10 nm) and consequently a large specific surface area ( $\sim$ 120 m<sup>2</sup>g<sup>-1</sup>).

The results of UV-vis spectroscopy show that the nitridation treatment effectively induces light absorption of the N-doped and (Nb,N) co-doped samples in the visible region. Furthermore, the thermal condition of nitridation was found to have a great influence on the absorption properties of the materials. Samples subjected to mild nitridation conditions (NTi-m and 0.25NbNTi-m) present a yellow color. When the nitridation conditions are harsher, the samples took a dark coloration with visible light absorption at  $\lambda > 550$  nm.

The synthesized materials were characterized by XPS and EPR to identify the doping species and associated defects that could be responsible for the aforementioned UV-vis spectral characteristics. It is shown that the two sets of nitridation conditions are related to different doping and charge compensation mechanisms. When the nitridation conditions are mild, the nitrogen species are inserted in the interstitial position in the lattice of NTi-m and 0.25NbNTi-m. In addition, it turns out that the presence of Nb in the TiO<sub>2</sub> improves the insertion of nitrogen when compared to pure TiO<sub>2</sub>, leading to more intense light absorption in the visible range (400-550 nm) observed on 0.25NbNTi-m. For this sample, the additional negative charge brought by the N³- is compensated by Nb⁵+, even if the ideal cationic-anionic charge compensation predicted for the co-doping approach could not be reached. For NTi-m, the compensation mechanism involves the creation of oxygen vacancies Vo⁴-. Under more harsh nitridation conditions, in addition to interstitial nitrogen, substitutional nitrogen was also introduced into the lattice of TiO<sub>2</sub> materials. The EPR result indicates that both Vo⁴- and Ti³+ centers associated with the substitutional nitrogen are involved in the charge compensation mechanism.

Electronic band structures of the synthesized materials were proposed based on RDB-PAS data, which provides information on the energy distribution of electron traps in the bandgap of the modified photocatalyst. For 0.25NbNTi-m, a broader distribution of states, which we attributed to N 2p states above the VBT, was observed when compared to NTi-m and  $TiO_2$  reference. We believe that this specific electronic state distribution is responsible for the reduction of the bandgap and the improved photocatalytic properties. For the 0.25NbNTi-h sample, which was submitted to more harsh nitridation, the decrease of the PAS signal is possibly due to charge carrier recombination related to  $Ti^{3+}$  and/or substitutional nitrogen centers. Moreover, the coordination of Ti and Nb in the lattice of (Nb,N) co-doped samples was investigated by XANES and VTC-XES measurements. The result confirms the dominant anatase phase and the presence of Nb<sup>5+</sup> in octahedral configuration. On the other hand, the Nb K-edge XES spectra show some evolution of the ligand-dependent peak (K $\beta$ ") with the increasing nitridation temperature which was not observed on Ti K edge. We suppose that this might be evidence for the existence of Nb-N defect pairs that are created in harsh conditions when substitutional nitrogen is present.

Photo-degradation of MB was conducted in different spectral regions (UV, visible and AM 1.5G simulated solar light) to evaluate the photocatalytic properties of the as-prepared photocatalysts. 0.25NbNTi-m exhibits the best activity, especially under visible light and simulated solar light illumination for which the kinetic of the photodegradation is almost 4 times faster than TiO<sub>2</sub>. The results support previous reports, in which the enhanced photocatalytic activity was generally ascribed to the band gap narrowing due to Nb and N codoping of TiO<sub>2</sub>. Furthermore, in the present work, we reveal the importance of tuning the thermal condition of nitridation to produce the specific co-doped sample with enhanced activity. The samples submitted to harsh nitridation conditions (0.25NbNTi-h) have their photocatalytic activities reduced in the UV region, but also in the visible region compared to 0.25NbNTi-m, even though they present an improved optical light absorption in the visible region. We suppose that the higher concentration of Ti<sup>3+</sup>acting as charge recombination centers leads to this deterioration of photocatalytic activity.

From these results, it appears that the accurate adjustment of nitridation parameters is primordial to control the charge compensation mechanism in co-doped TiO<sub>2</sub> photocatalysts. If the optical bandgap is reduced by annealing in ammonia and the co-doping approach favors the introduction of nitrogen atoms in the TiO<sub>2</sub> structure, the photocatalytic efficiency depends on the type of defects created in the material. Under similar synthesis conditions, we identified two N doping mechanisms, depending on the annealing temperature, associated with two different light absorption regions. We have made efforts to investigate the configuration of the niobium and nitrogen dopants, and the result confirms the substitution by Nb<sup>5+</sup> without changing the anatase structure of the original TiO<sub>2</sub>. However, quantitative analysis of nitrogen in bulk remains elusive due to the lack of effective means of characterization. On the other hand, the configuration of N still requires further investigation, even though we found traces of the existence of Nb-N defect pairs by XES. Considering the very low concentration of N dopants, these results need to be confirmed by supplementary experiments focusing on ascertaining the configuration and distribution of nitrogen in the (Nb,N) co-doped TiO<sub>2</sub> structure. This would

help us better understand the relationship between material structure and photocatalytic performance. Finally, we should point out that this study only focused on the (Nb,N) co-doped TiO<sub>2</sub>. The applicability of the conclusions obtained in this chapter to other co-doped systems is unknown. That is why the next chapter is dedicated to (Ta,N) and (W,N) co-doped TiO<sub>2</sub> that will be compared with (Nb,N) co-doped TiO<sub>2</sub>, with an emphasis on the effect of cation on the properties of the co-doped material.

## 6. References

- (1) Gai, Y.; Li, J.; Li, S.-S.; Xia, J.-B.; Wei, S.-H. Design of Narrow-Gap TiO<sub>2</sub>: A Passivated Codoping Approach for Enhanced Photoelectrochemical Activity. *Phys. Rev. Lett.* **2009**, *102* (3), 036402. https://doi.org/10.1103/PhysRevLett.102.036402.
- (2) Yin, W.-J.; Tang, H.; Wei, S.-H.; Al-Jassim, M. M.; Turner, J.; Yan, Y. Band Structure Engineering of Semiconductors for Enhanced Photoelectrochemical Water Splitting: The Case of TiO<sub>2</sub>. *Phys. Rev. B* **2010**, *82* (4), 045106. https://doi.org/10.1103/PhysRevB.82.045106.
- (3) Cottineau, T.; Béalu, N.; Gross, P.-A.; Pronkin, S. N.; Keller, N.; Savinova, E. R.; Keller, V. One Step Synthesis of Niobium Doped Titania Nanotube Arrays to Form (N,Nb) Co-Doped TiO<sub>2</sub> with High Visible Light Photoelectrochemical Activity. *J. Mater. Chem. A* **2013**, *I* (6), 2151–2160. https://doi.org/10.1039/C2TA00922F.
- (4) Breault, T. M.; Bartlett, B. M. Lowering the Band Gap of Anatase-Structured TiO<sub>2</sub> by Coalloying with Nb and N: Electronic Structure and Photocatalytic Degradation of Methylene Blue Dye. *J. Phys. Chem. C* **2012**, *116* (10), 5986–5994. https://doi.org/10.1021/jp2078456.
- (5) Favet, T.; Ihiawakrim, D.; Keller, V.; Cottineau, T. Anions and Cations Distribution in M <sup>5+</sup> /N <sup>3-</sup> Co-Alloyed TiO<sub>2</sub> Nanotubular Structures for Photo-Electrochemical Water Splitting. *Materials Science in Semiconductor Processing* **2018**, *73*, 22–29. https://doi.org/10.1016/j.mssp.2017.05.018.
- (6) Marchiori, C.; Di Liberto, G.; Soliveri, G.; Loconte, L.; Lo Presti, L.; Meroni, D.; Ceotto, M.; Oliva, C.; Cappelli, S.; Cappelletti, G.; Aieta, C.; Ardizzone, S. Unraveling the Cooperative Mechanism of Visible-Light Absorption in Bulk N,Nb Codoped TiO<sub>2</sub> Powders of Nanomaterials. *J. Phys. Chem. C* **2014**, *118* (41), 24152–24164. https://doi.org/10.1021/jp507143z.
- (7) Williamson, B. A. D.; Buckeridge, J.; Chadwick, N. P.; Sathasivam, S.; Carmalt, C. J.; Parkin, I. P.; Scanlon, D. O. Dispelling the Myth of Passivated Codoping in TiO<sub>2</sub>. *Chem. Mater.* **2019**, *31* (7), 2577–2589. https://doi.org/10.1021/acs.chemmater.9b00257.
- (8) Parashar, M.; Shukla, V. K.; Singh, R. Metal Oxides Nanoparticles via Sol–Gel Method: A Review on Synthesis, Characterization and Applications. *J Mater Sci: Mater Electron* **2020**, *31* (5), 3729–3749. https://doi.org/10.1007/s10854-020-02994-8.
- (9) Akpan, U. G.; Hameed, B. H. The Advancements in Sol–Gel Method of Doped-TiO<sub>2</sub> Photocatalysts. *Applied Catalysis A: General* **2010**, *375* (1), 1–11. https://doi.org/10.1016/j.apcata.2009.12.023.
- (10) Breault, T. M.; Bartlett, B. M. Composition Dependence of TiO<sub>2</sub>:(Nb,N)- *x* Compounds on the Rate of Photocatalytic Methylene Blue Dye Degradation. *The Journal of Physical Chemistry C* **2013**, *117* (17), 8611–8618. https://doi.org/10.1021/jp312199t.
- (11) Buttersack, C. Modeling of Type IV and V Sigmoidal Adsorption Isotherms. *Physical Chemistry Chemical Physics* **2019**, *21* (10), 5614–5626. https://doi.org/10.1039/C8CP07751G.
- (12) Makuła, P.; Pacia, M.; Macyk, W. How To Correctly Determine the Band Gap Energy of Modified Semiconductor Photocatalysts Based on UV–Vis Spectra. *J. Phys. Chem. Lett.* **2018**, *9* (23), 6814–6817. https://doi.org/10.1021/acs.jpclett.8b02892.
- (13) Znad, H.; Ang, M. H.; Tade, M. O. Ta/Ti-and Nb/Ti-Mixed Oxides as Efficient Solar Photocatalysts: Preparation, Characterization, and Photocatalytic Activity. *International Journal of Photoenergy* **2012**, *2012*, 1–9. https://doi.org/10.1155/2012/548158.
- (14) Kubacka, A.; Colón, G.; Fernández-García, M. Cationic (V, Mo, Nb, W) Doping of TiO<sub>2</sub>—Anatase: A Real Alternative for Visible Light-Driven Photocatalysts. *Catalysis Today* **2009**, *143* (3–4), 286–292. https://doi.org/10.1016/j.cattod.2008.09.028.
- (15) Determination of the concentration of surface hydroxyl groups on metal oxide films by a quantitative XPS method McCafferty 1998 Surface and Interface Analysis Wiley Online Library. https://doi.org/10.1002/(SICI)1096 9918(199807)26:8<549::AID-SIA396>3.0.CO;2-Q

- (16) Cheng, X.; Yu, X.; Xing, Z. Characterization and Mechanism Analysis of Mo–N-Co-Doped TiO<sub>2</sub> Nano-Photocatalyst and Its Enhanced Visible Activity. *Journal of Colloid and Interface Science* **2012**, *372* (1), 1–5. https://doi.org/10.1016/j.jcis.2011.11.071.
- (17) Yue, J.; Suchomski, C.; Voepel, P.; Ellinghaus, R.; Rohnke, M.; Leichtweiss, T.; Elm, M. T.; Smarsly, B. M. Mesoporous Niobium-Doped Titanium Dioxide Films from the Assembly of Crystalline Nanoparticles: Study on the Relationship between the Band Structure, Conductivity and Charge Storage Mechanism. *J. Mater. Chem. A* **2017**, *5* (5), 1978–1988. https://doi.org/10.1039/C6TA06840E.
- (18) Dong, G.; Wang, X.; Chen, Z.; Lu, Z. Enhanced Photocatalytic Activity of Vacuum-Activated TiO<sub>2</sub> Induced by Oxygen Vacancies. *Photochemistry and Photobiology* **2018**, *94* (3), 472–483. https://doi.org/10.1111/php.12874.
- (19) Sen, S. K.; Riga, J.; Verbist, J. 2s and 2p X-Ray Photoelectron Spectra of Ti<sup>4+</sup> Ion in TiO<sub>2</sub>. *Chemical Physics Letters* **1976**, *39* (3), 560–564. https://doi.org/10.1016/0009-2614(76)80329-6.
- (20) Asahi, R.; Morikawa, T.; Ohwaki, T.; Aoki, K.; Taga, Y. Visible-Light Photocatalysis in Nitrogen-Doped Titanium Oxides. *Science* **2001**, *293* (5528), 269–271. https://doi.org/10.1126/science.1061051.
- (21) Zeng, L.; Song, W.; Li, M.; Jie, X.; Zeng, D.; Xie, C. Comparative Study on the Visible Light Driven Photocatalytic Activity between Substitutional Nitrogen Doped and Interstitial Nitrogen Doped TiO<sub>2</sub>. *Applied Catalysis A: General* **2014**, *488*, 239–247. https://doi.org/10.1016/j.apcata.2014.09.041.
- (22) Yuan, B.; Wang, Y.; Bian, H.; Shen, T.; Wu, Y.; Chen, Z. Nitrogen Doped TiO<sub>2</sub> Nanotube Arrays with High Photoelectrochemical Activity for Photocatalytic Applications. *Applied Surface Science* **2013**, *280*, 523–529. https://doi.org/10.1016/j.apsusc.2013.05.021.
- (23) Saha, N. C.; Tompkins, H. G. Titanium Nitride Oxidation Chemistry: An X-ray Photoelectron Spectroscopy Study. *Journal of Applied Physics* **1992**, 72 (7), 3072–3079. https://doi.org/10.1063/1.351465.
- (24) Long, R.; English, N. J. Band Gap Engineering of (N,Ta)-Codoped TiO<sub>2</sub>: A First-Principles Calculation. *Chemical Physics Letters* **2009**, *478* (4–6), 175–179. https://doi.org/10.1016/j.cplett.2009.07.084.
- (25) Kong, L.; Wang, C.; Zheng, H.; Zhang, X.; Liu, Y. Defect-Induced Yellow Color in Nb-Doped TiO<sub>2</sub> and Its Impact on Visible-Light Photocatalysis. *J. Phys. Chem. C* **2015**, *119* (29), 16623–16632. https://doi.org/10.1021/acs.jpcc.5b03448.
- (26) Livraghi, S.; Chierotti, M. R.; Giamello, E.; Magnacca, G.; Paganini, M. C.; Cappelletti, G.; Bianchi, C. L. Nitrogen-Doped Titanium Dioxide Active in Photocatalytic Reactions with Visible Light: A Multi-Technique Characterization of Differently Prepared Materials. *J. Phys. Chem. C* **2008**, *112* (44), 17244–17252. https://doi.org/10.1021/jp803806s.
- (27) Hensling, F. V. E.; Xu, C.; Gunkel, F.; Dittmann, R. Unraveling the Enhanced Oxygen Vacancy Formation in Complex Oxides during Annealing and Growth. *Sci Rep* **2017**, *7* (1), 39953. https://doi.org/10.1038/srep39953.
- (28) Deml, A. M.; Holder, A. M.; O'Hayre, R. P.; Musgrave, C. B.; Stevanović, V. Intrinsic Material Properties Dictating Oxygen Vacancy Formation Energetics in Metal Oxides. *J. Phys. Chem. Lett.* **2015**, *6* (10), 1948–1953. https://doi.org/10.1021/acs.jpclett.5b00710.
- (29) Kuznetsov, V. N.; Serpone, N. On the Origin of the Spectral Bands in the Visible Absorption Spectra of Visible-Light-Active TiO<sub>2</sub> Specimens Analysis and Assignments. *J. Phys. Chem. C* **2009**, *113* (34), 15110–15123. https://doi.org/10.1021/jp901034t.
- (30) Zhang, Z.; Long, J.; Xie, X.; Lin, H.; Zhou, Y.; Yuan, R.; Dai, W.; Ding, Z.; Wang, X.; Fu, X. Probing the Electronic Structure and Photoactivation Process of Nitrogen-Doped TiO<sub>2</sub> Using DRS, PL, and EPR. *ChemPhysChem* **2012**, *13* (6), 1542–1550. https://doi.org/10.1002/cphc.201100991.
- (31) Wu, T.; Niu, P.; Yang, Y.; Yin, L.-C.; Tan, J.; Zhu, H.; Irvine, J. T. S.; Wang, L.; Liu, G.; Cheng, H.-M. Homogeneous Doping of Substitutional Nitrogen/Carbon in TiO<sub>2</sub> Plates for Visible Light Photocatalytic Water Oxidation. *Adv. Funct. Mater.* **2019**, 7.

- (32) Serpone, N. Is the Band Gap of Pristine TiO<sub>2</sub> Narrowed by Anion- and Cation-Doping of Titanium Dioxide in Second-Generation Photocatalysts? *J. Phys. Chem. B* **2006**, *110* (48), 24287–24293. https://doi.org/10.1021/jp065659r.
- (33) Biedrzycki, J.; Livraghi, S.; Giamello, E.; Agnoli, S.; Granozzi, G. Fluorine- and Niobium-Doped TiO<sub>2</sub>: Chemical and Spectroscopic Properties of Polycrystalline n-Type-Doped Anatase. *J. Phys. Chem. C* **2014**, *118* (16), 8462–8473. https://doi.org/10.1021/jp501203h.
- (34) De Trizio, L.; Buonsanti, R.; Schimpf, A. M.; Llordes, A.; Gamelin, D. R.; Simonutti, R.; Milliron, D. J. Nb-Doped Colloidal TiO<sub>2</sub> Nanocrystals with Tunable Infrared Absorption. *Chem. Mater.* **2013**, *25* (16), 3383–3390. https://doi.org/10.1021/cm402396c.
- (35) Kosowska, B.; Mozia, S.; Morawski, A. W.; Grzmil, B.; Janus, M.; Kałucki, K. The Preparation of TiO<sub>2</sub>–Nitrogen Doped by Calcination of TiO<sub>2</sub>·xH<sub>2</sub>O under Ammonia Atmosphere for Visible Light Photocatalysis. *Solar Energy Materials and Solar Cells* **2005**, *88* (3), 269–280. https://doi.org/10.1016/j.solmat.2004.11.001.
- (36) Nitta, A.; Takase, M.; Takashima, M.; Murakami, N.; Ohtani, B. A Fingerprint of Metal-Oxide Powders: Energy-Resolved Distribution of Electron Traps. *Chem. Commun.* **2016**, *52* (81), 12096–12099. https://doi.org/10.1039/C6CC04999K.
- (37) Nitta, A.; Takashima, M.; Murakami, N.; Takase, M.; Ohtani, B. Reversed Double-Beam Photoacoustic Spectroscopy of Metal-Oxide Powders for Estimation of Their Energy-Resolved Distribution of Electron Traps and Electronic-Band Structure. *Electrochimica Acta* **2018**, *264*, 83–90. https://doi.org/10.1016/j.electacta.2017.12.160.
- (38) Sun, Q.; Cortie, D.; Zhang, S.; Frankcombe, T. J.; She, G.; Gao, J.; Sheppard, L. R.; Hu, W.; Chen, H.; Zhuo, S.; Chen, D.; Withers, R. L.; McIntyre, G.; Yu, D.; Shi, W.; Liu, Y. The Formation of Defect-Pairs for Highly Efficient Visible-Light Catalysts. *Adv. Mater.* **2017**, *29* (11), 1605123. https://doi.org/10.1002/adma.201605123.
- (39) Stewart, S. J.; Fernández-García, M.; Belver, C.; Mun, B. S.; Requejo, F. G. Influence of N-Doping on the Structure and Electronic Properties of Titania Nanoparticle Photocatalysts. *J. Phys. Chem. B* **2006**, *110* (33), 16482–16486. https://doi.org/10.1021/jp0624451.
- (40) García-Tecedor, M.; Gorni, G.; Oropeza, F.; Gómez, L.; Liras, M.; O'Shea, V. A. de la P.; Barawi, M. Unravelling Nanostructured Nb-Doped TiO<sub>2</sub> Dual Band Behaviour in Smart Windows by in Situ Spectroscopies. *Journal of Materials Chemistry A* **2022**, *10* (37), 19994–20004. https://doi.org/10.1039/D2TA03239B.
- (41) Kowalska, J.; DeBeer, S. The Role of X-Ray Spectroscopy in Understanding the Geometric and Electronic Structure of Nitrogenase. *Biochimica et Biophysica Acta (BBA) Molecular Cell Research* **2015**, *1853* (6), 1406–1415. https://doi.org/10.1016/j.bbamcr.2014.11.027.
- (42) Kühn, T.-J.; Hormes, J.; Matoussevitch, N.; Bönnemann, H.; Glatzel, P. Site-Selective High-Resolution X-Ray Absorption Spectroscopy and High-Resolution X-Ray Emission Spectroscopy of Cobalt Nanoparticles. *Inorg. Chem.* **2014**, *53* (16), 8367–8375. https://doi.org/10.1021/ic5000183.
- (43) Mandić, L.; Fazinić, S.; Jakšić, M. Chemical Effects on the K $\beta$ " and K $\beta$ <sub>2,5</sub> X-Ray Lines of Titanium and Its Compounds. *Phys. Rev. A* **2009**, *80* (4), 042519. https://doi.org/10.1103/PhysRevA.80.042519.
- (44) Miaja-Avila, L.; O'Neil, G. C.; Joe, Y. I.; Morgan, K. M.; Fowler, J. W.; Doriese, W. B.; Ganly, B.; Lu, D.; Ravel, B.; Swetz, D. S.; Ullom, J. N. Valence-to-Core X-Ray Emission Spectroscopy of Titanium Compounds Using Energy Dispersive Detectors. *X-Ray Spectrometry* **2021**, *50* (1), 9–20. https://doi.org/10.1002/xrs.3183.
- (45) Ravel, B.; Kropf, A. J.; Yang, D.; Wang, M.; Topsakal, M.; Lu, D.; Stennett, M. C.; Hyatt, N. C. Nonresonant Valence-to-Core x-Ray Emission Spectroscopy of Niobium. *Physical Review B* **2018**, *97* (12).
- (46) Angelomé, P. C.; Andrini, L.; Calvo, M. E.; Requejo, F. G.; Bilmes, S. A.; Soler-Illia, G. J. A. A. Mesoporous Anatase TiO<sub>2</sub> Films: Use of Ti K XANES for the Quantification of the Nanocrystalline Character and Substrate Effects in the Photocatalysis Behavior. *J. Phys. Chem. C* **2007**, *111* (29), 10886–10893. https://doi.org/10.1021/jp069020z.

- (47) AN INTRODUCTION TO TRANSITION-METAL CHEMISTRY Ligand-Field Theory par Leslie E. Orgel: Hardcover (1963) First Edition; Fourth Printing. | Rare Book Cellar. https://www.abebooks.fr/edition-originale/INTRODUCTION-TRANSITION-METAL-CHEMISTRY-Ligand-Field-Theory-Leslie/31013666908/bd (accessed 2023-05-18).
- (48) Farges, F.; Brown, G. E.; Rehr, J. J. Ti K-Edge XANES Studies of Ti Coordination and Disorder in Oxide Compounds: Comparison between Theory and Experiment. *Phys. Rev. B* **1997**, *56* (4), 1809–1819. https://doi.org/10.1103/PhysRevB.56.1809.
- (49) Otal, E. H.; Angelomé, P. C.; Bilmes, S. A.; Soler-Illia, G. J. a. A. Functionalized Mesoporous Hybrid Thin Films as Selective Membranes. *Advanced Materials* **2006**, *18* (7), 934–938. https://doi.org/10.1002/adma.200502215.
- (50) Brydson, R.; Sauer, H.; Engel, W.; Thomass, J. M.; Zeitler, E.; Kosugi, N.; Kuroda, H. Electron Energy Loss and X-Ray Absorption Spectroscopy of Rutile and Anatase: A Test of Structural Sensitivity. *J. Phys.: Condens. Matter* **1989**, *I* (4), 797. https://doi.org/10.1088/0953-8984/1/4/012.
- (51) Masai, H.; Sakurai, H.; Koreeda, A.; Fujii, Y.; Ohkubo, T.; Miyazaki, T.; Akai, T. Photocatalytic Hydrogen Generation of Monolithic Porous Titanium Oxide-Based Glass-Ceramics. *Sci Rep* **2020**, *10* (1), 11615. https://doi.org/10.1038/s41598-020-68410-7.
- (52) Antonio, R. Coordination and Valence of Niobium in TiO<sub>2</sub>-NbO<sub>2</sub> Solid Solutions through X-Ray Absorption Spectroscopy.
- (53) Din, M. I.; Khalid, R.; Najeeb, J.; Hussain, Z. Fundamentals and Photocatalysis of Methylene Blue Dye Using Various Nanocatalytic Assemblies- a Critical Review. *Journal of Cleaner Production* **2021**, *298*, 126567. https://doi.org/10.1016/j.jclepro.2021.126567.
- (54) Vinodgopal, K.; Wynkoop, D. E.; Kamat, P. V. Environmental Photochemistry on Semiconductor Surfaces: Photosensitized Degradation of a Textile Azo Dye, Acid Orange 7, on TiO<sub>2</sub> Particles Using Visible Light. *Environ. Sci. Technol.* **1996**, *30* (5), 1660–1666. https://doi.org/10.1021/es950655d.
- (55) Bhachu, D. S.; Sathasivam, S.; Sankar, G.; Scanlon, D. O.; Cibin, G.; Carmalt, C. J.; Parkin, I. P.; Watson, G. W.; Bawaked, S. M.; Obaid, A. Y.; Al-Thabaiti, S.; Basahel, S. N. Solution Processing Route to Multifunctional Titania Thin Films: Highly Conductive and Photcatalytically Active Nb:TiO<sub>2</sub>. *Advanced Functional Materials* **2014**, *24* (32), 5075–5085. https://doi.org/10.1002/adfm.201400338.
- (56) Dabney, M. S.; van Hest, M. F. A. M.; Teplin, C. W.; Arenkiel, S. P.; Perkins, J. D.; Ginley, D. S. Pulsed Laser Deposited Nb Doped TiO<sub>2</sub> as a Transparent Conducting Oxide. *Thin Solid Films* **2008**, *516* (12), 4133–4138. https://doi.org/10.1016/j.tsf.2007.10.093.

Chapter-3 Characterizations of M-doped  $TiO_2$  and (M,N) co-doped  $TiO_2$  (M=Nb, Ta, W) materials

## Summary

1. Introduction.	92
2. Material preparation	93
2.1 Preparation of M-doped TiO <sub>2</sub> materials	93
2.1.1 Sol-gel synthesis	93
2.1.2 Determination of calcination condition	94
2.2 Preparation of co-doped TiO <sub>2</sub> materials	95
3. Material characterization	95
3.1 Characterization of M-doped TiO <sub>2</sub>	95
3.1.1 XRD analysis	95
3.1.2 in-situ temperature-dependent XRD analysis	97
3.1.3 Morphology study:	102
3.1.4 Optical property	103
3.1.5 Surface chemical composition by XPS	104
3.1.6 Identification of defects in M-doped samples by EPR	106
3.2 Conclusion on the M-doped TiO <sub>2</sub>	107
3.3 Characterizations of the (M,N) co-doped samples	108
3.3.1 Crystal structure by XRD	108
3.3.2 Morphology study	110
3.3.3 Optical properties	111
3.3.4 Surface chemical composition by XPS	116
3.3.5 Defects identification in the (M,N) co-doped TiO <sub>2</sub> samples	119
3.4 Conclusion on the (M,N) co-doped samples	121
4. In-situ characterization of UV-visible properties during the thermal tr	
4.1 Experimental section	122
4.1.1 Apparatus	122
4.1.2 Calibration of temperature	123
4.1.3 Data treatment	124
4.2 Results and discussion	124
4.2.1 Cleaning pre-treatment	124
4.2.2 In-situ observation of nitridation process	126
4.2.3 In-situ observation of the oxidation process	131

4.3 Conclusion on the in-situ UV-visible.	133
5. Conclusion	134
6. References	136

#### 1. Introduction

As described in Chapter 1, the strategy of cation-anion co-doping is considered an effective approach to reduce the band gap of TiO2, while limiting the problems of low stability and high charge recombination of N-doped TiO2. 1-3 Even considering only transition metal cations, there is a wide range of possible combinations in terms of cation, anion, and doping concentration. For this reason, most of the previous studies in the field of (M,A) co-doped TiO<sub>2</sub> photocatalysts focus on a specific anion-cation couple, intending to explore the influence of the anion and/or cation concentration on the visible light absorption and the resulting photocatalytic activity. <sup>4,5</sup>To the best of our knowledge, except the seminal DFT studies, 6,7 no experimental study has compared the photocatalytic activity of co-doped TiO<sub>2</sub> material with different (M,A) pairs obtained in similar conditions. Therefore, due to the experimental differences between the publications of each group in terms of material composition, doping concentration, and synthesis but also regarding the photocatalytic experiments, it is difficult to understand the role of cations in the (M,A) co-doped TiO<sub>2</sub> materials. Even for (M,N) compositions, which are by far the most studied, only one review article gathered the results of different groups, 8 and it remains difficult to make comparisons and draw some conclusions on the photocatalytic efficiency as a function of the cation used for co-doping of TiO<sub>2</sub>.

In Chapter 2, we studied (Nb,N) co-doped  $TiO_2$ , which is the most described in the literature. Our results confirmed a reduction of the band gap to 2.5 eV. However, we demonstrated that the photocatalytic activity of the co-doped  $TiO_2$  is significantly influenced by the thermal conditions of the nitridation process. The harsh nitridation has been shown to introduce  $Ti^{3+}$  and  $V_O^+$ , which act as charge recombination centers, resulting in a deterioration of the photocatalytic activity. In the literature, examples of  $TiO_2$  co-doping with 5d cations (Ta, W) and N have also been confirmed to be effective in reducing the band gap of  $TiO_2$ , resulting in an enhanced photoresponse to visible light. This includes various photocatalytic reactions, such as photocatalytic degradation and water oxidation. <sup>5,9–13</sup>

Therefore, in this chapter, we aimed to change the doping cation of (M,N) co-doped TiO<sub>2</sub>. By following the same synthetic strategy, we prepared (Nb,N), (Ta,N) and (W,N) co-doped TiO<sub>2</sub> photocatalysts. The energy of the d orbital for a specific cation may change the band structure of the resulting co-doped material: the CB of the (M,N) TiO<sub>2</sub> is formed by the hybridization of Ti 3d and the specific M d orbital, the type of cation may influence the CB position and other properties of the (M,N) co-doped TiO<sub>2</sub>. DFT studies have shown that the energy levels of Nb 4d and W 5d are theoretically close to that of Ti 3d, while Ta 5d is located at a higher energy level (**Figure 3.1**).<sup>6</sup> Nb and Ta are elements of the same column of the periodic table, so we expect to obtain the (M,N) co-doped TiO<sub>2</sub> materials with similar physicochemical properties. By comparing the (W,N) co-doping with the (Nb,N) and (Ta,N) co-doped TiO<sub>2</sub>, we expect to figure out how the positive charge brought by the cation influence N-doping and defect generation for the (M,N) co-doped TiO<sub>2</sub> materials. W<sup>6+</sup> can introduce an additional positive charge compared to Nb<sup>5+</sup> and Ta<sup>5+</sup>, and according to the

ideal charge-balanced of co-doped TiO<sub>2</sub> (eq. **1.12**), the amount of N should be doubled compared to the case of Nb and Ta.

Therefore in this chapter, the combination of several characterization methods was used to determine the influence of the cation on the formation of the (M,N) co-doped TiO<sub>2</sub> and its properties. In particular, we tried to determine how the cation affects the insertion of nitrogen and if the two behaviors observed in Chapter 2 for (Nb,N) TiO<sub>2</sub> are observed in the case of Ta and W. The optoelectronic properties of each (M,N)-TiO<sub>2</sub> and the defects associated with the nitrogen insertion were also analyzed.

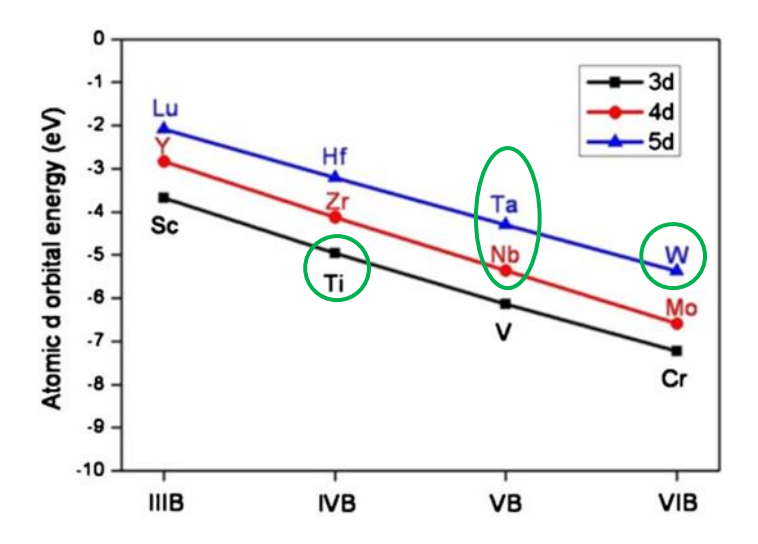


Figure 3.1: Atomic d orbital energy of different 3d, 4d, 5d transition metals.6

## 2. Material preparation

## 2.1 Preparation of M-doped TiO<sub>2</sub> materials

## 2.1.1 Sol-gel synthesis

The M-doped  $TiO_2$  (M = Nb, Ta or W) was synthesized using the sol-gel method described in Chapter 2. Two doping concentrations were achieved by adjusting the addition of the cation precursor (NbCl<sub>5</sub>: 99.8%; Merck, TaCl<sub>5</sub>: 99.8%, Fisher, and WCl<sub>6</sub>: 99.8%; Merck). The samples with high doping concentration (molar ratio M/Ti = 0.25) are denoted as 0.25NbTi, 0.25TaTi and 0.25WTi. The ones with low doping concentration, (molar ratio M/Ti = 0.1) are labeled as 0.1NbTi, 0.1TaTi and 0.1WTi. It should be noted that the sample 0.25NbTi, as well as the undoped  $TiO_2$ , are the same as that discussed in Chapter 2.

The only difference was the temperature required for the transition from sol to gel which was influenced by the type of cation. For the synthesis of Nb or Ta-doped TiO<sub>2</sub> gels, the precursor solutions were heated up to 80°C and held at this temperature for 2h to form the gel, while for undoped TiO<sub>2</sub> the gel is formed at 40°C within 1 hour. For W-doped TiO<sub>2</sub> gels, heating at 60°C for 2h is sufficient to promote the gel formation. In addition, for the

sample doped with a specific cation, we observed that the gelification took a longer time for high doping concentration. After formation, all gels were dried at 80°C for 48h.

#### 2.1.2 Determination of calcination condition

TGA analysis of all the M-doped materials was conducted (**Figure S3.1**, **Page 191**) to determine the calcination temperature for each sample. As shown in Chapter 2, Nb-doping increases the temperature required to remove carbon residue from the sol-gel synthesis. It is supposed that Ta or W-doping may have a similar effect. The derivative of mass loss for each sample are compared with reference TiO<sub>2</sub> in **Figure 3.2**.

The common weight loss observed on all the samples below 100°C is assigned to the dehydration of water. <sup>14</sup> The weight loss after 100°C is mainly attributed to the combustion of carbon species, accompanied by the crystallization of TiO<sub>2</sub>. <sup>15</sup> Three main peaks are observed for TiO<sub>2</sub>, located at 146°C, 238°C and 331°C, respectively, corresponding to different stages of the carbon compound decomposition. For all the M-doped samples, the main peaks are shifted to higher temperatures. On the other hand, an absence of any derivative peak indicates a complete removal of carbon residual. For TiO<sub>2</sub>, 0.1TaTi and 0.1WTi, the sample mass stopped decreasing at ~450°C. For 0.1NbTi, 0.25NbTi, 0.25TaTi and 0.25WTi, this temperature is increased to ~500°C.

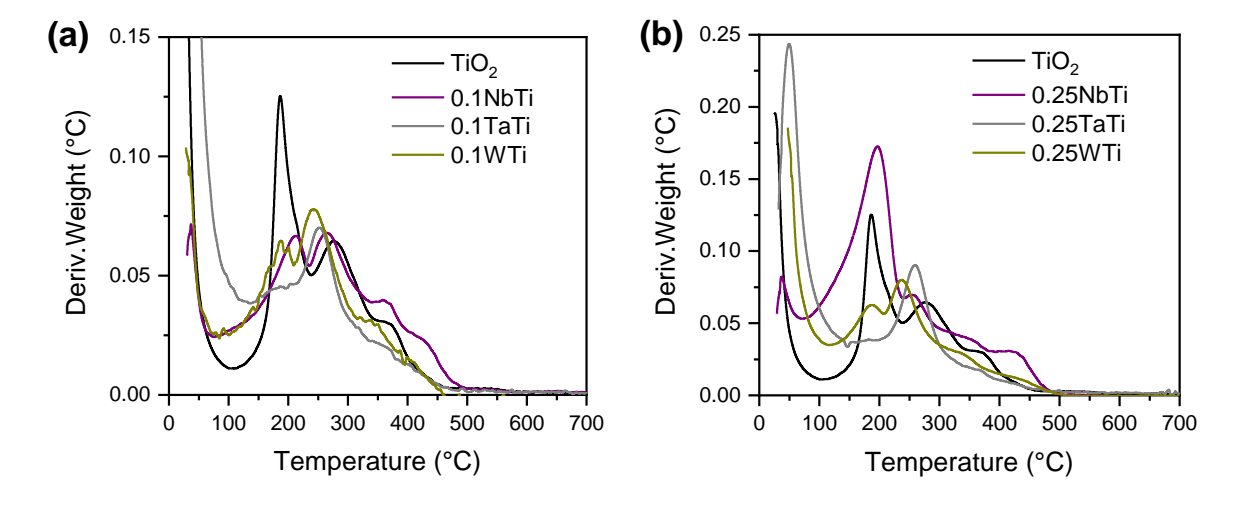


**Figure 3.2:** Derivative curve of the mass loss for the prepared  $TiO_2$  and the M-doped  $TiO_2$ : (a) 0.1MTi samples. (b) 0.25MTi samples.

The results confirm that doping with cation increased the required calcination temperature. In particular, Nb-doping, even a low doping concentration, can raise the required temperature to 500 C. Thus, the annealing of the gels of all the M-doped samples to form the crystalline photocatalysts was conducted at 500°C for 12h, under airflow (100 mL.min<sup>-1</sup>) with a heating rate of 4°C.min<sup>-1</sup>, while for TiO<sub>2</sub> we kept 400°C during 2h in order to limit the rutile formation.

## 2.2 Preparation of co-doped TiO<sub>2</sub> materials

(M,N) co-doped TiO<sub>2</sub> were obtained by performing a thermal nitridation in ammonia flow (100 mL.min<sup>-1</sup>) of the related M-doped samples. As concluded in Chapter 2, we found that the thermal conditions for the nitridation process significantly influence the properties and the photocatalytic activity of the (Nb,N) co-doped photocatalysts. Therefore, the nitridation conditions for the synthesis of the (Ta,N) co-doped TiO<sub>2</sub> and (W,N) co-doped TiO<sub>2</sub> were also adjusted to obtain "mild" and "harsh" samples. The detailed parameters of the nitridation step for each sample are summarized in **Table 3.1**. The resultant co-doped samples are denoted with the specific thermal condition for the nitridation process, where "m" means "mild" and "h" means "harsh".

Sample	Nitridation conditions	
0.1NbNTi & 0.25NbNTi	mild	350°C, 12h
	harsh	450°C, 1h
0.1TaNTi & 0.25TaNTi	mild	450°C, 1h
	harsh	450°C, 12h
0.1WNTi & 0.25WNTi	mild	250°C, 12h
	harsh	350°C, 12h

**Table 3.1:** Thermal conditions of nitridation process for the (M,N) co-doped TiO<sub>2</sub> samples.

The thermal conditions in **Table 3.1** were determined by a trial-error process and by analyzing the UV visible spectra of each sample (detailed discussion in **3.3.3**). In our experiment, we have tried a series of thermal conditions based on each M-doped material. Mild conditions correspond to the highest temperature/longer duration for which only the yellow contribution, identified in Chapter 2 for 0.25NbNTi-m, was observed. For harsh conditions, the sample presents a darker color, with absorption at a longer wavelength (> 550 nm), that was related to the generation of Ti<sup>3+</sup> in the case of (Nb,N) co-doped TiO<sub>2</sub>.

## 3. Material characterization

## 3.1 Characterization of M-doped TiO<sub>2</sub>

#### 3.1.1 XRD analysis

The crystal structures of the synthesized M-doped samples were characterized by XRD (same experimental parameters as in Chapter 2, **2.1.2.2**) and compared with the undoped TiO<sub>2</sub> (**Figure 3.3**). As already mentioned, TiO<sub>2</sub> mainly crystallized in anatase (*ca.* 63%), with a certain amount of rutile (*ca.* 5%) and brookite (*ca.* 32%). When the cation was introduced into the TiO<sub>2</sub> materials, a reduction or disappearance of the rutile and brookite phases can be observed (**Figure 3.3 a**). At low cation substitution (0.1 M/Ti), 0.1NbTi and 0.1TaTi samples still present the coexistence of anatase, rutile and brookite, but the

proportion of rutile (*ca.* 1% for both 0.1NbTi and 0.1TaTi) and brookite (*ca.* 13% and 22% for 0.1NbTi and 0.1TaTi, respectively) are diminished compared to  $TiO_2$ . Besides, it can be noted that only anatase is observed on 0.1WTi. All M-doped samples with 0.25M/Ti present only the anatase phase. These results indicate that cation doping inhibits the anatase to rutile transition, with a more pronounced effect for W than for Nb or Ta but also for higher doping concentration. In addition, we do not observe any peaks corresponding to the cationic oxides or oxynitride phases for any of the M-doped samples. This indicates that, even with a doping concentration of M/Ti = 0.25, the doping cations mainly remain in the lattice of  $TiO_2$  anatase, as already observed in Chapter 2 for 0.25NbTi. **Figure 3.3 b** exhibits a magnification of the anatase (101) peak of all samples. A shift to the lower  $2\theta$  angles can be noticed for all M-doped samples, indicating an expansion of the interplanar spacing of the anatase (101) due to the introduction of the cation.

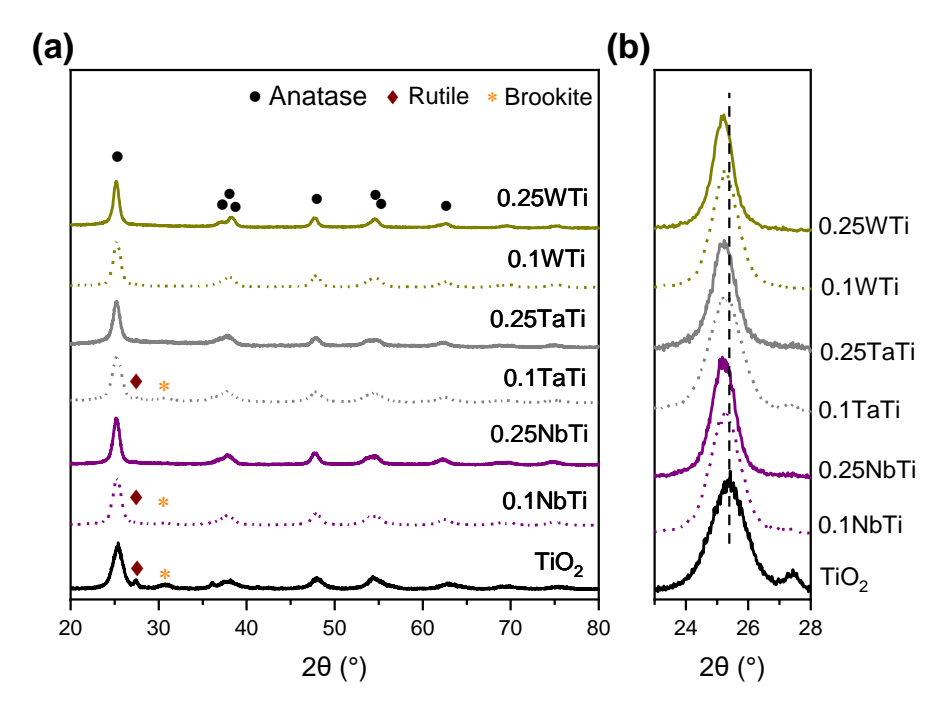


**Figure 3.3:** XRD patterns of TiO<sub>2</sub> and M-doped samples: (a) full range and (b) magnification on anatase (101).

The crystalline size  $\tau$  and anatase lattice parameters a and c of the different samples were determined by conducting Rietveld refinement, and the results are gathered in **Table 3.2.** All M-doped samples exhibit larger crystalline sizes than undoped TiO<sub>2</sub> (5.3 nm). This could be attributed to the higher calcination temperature for the M-doped samples (500 °C) compared to that of TiO<sub>2</sub> (400 °C). The increased heat provided during calcination could promote the growth of the crystalline of the M-doped samples. In addition, the doping concentration of the cation also contributes to increasing the crystalline size as observed by the slightly larger  $\tau$  values for the 0.25MTi samples compared to their 0.1MTi counterparts. Generally, the lattice parameters a and c of the M-doped TiO<sub>2</sub> increase with the doping concentration of the cation, resulting in an enlarged lattice volume. It is noted that the effect of Nb-doping and Ta-doping on the lattice extension is more significant than that of W-

doping. This could be explained by the larger ionic radius of Nb (0.64 Å) and Ta (0.64 Å) compared to that of W (0.60 Å). <sup>16</sup> The result is in good accord with the previously mentioned observation for the shift of anatase (101), further confirming the existence of the cation in the lattice of the M-doped  $TiO_2$  materials.

		•	•	
Sample ID	τ / nm (± X.X)	a / Å (± X.X)	c / Å (± X.X)	ΔV %
TiO <sub>2</sub>	5.034 (0.003)	3.7895 (0.0005)	9.478 (0.002)	-
0.1NbTi	6.154 (0.005)	3.7987 (0.0003)	9.5306 (0.0009)	1.044
0.25NbTi	7.391 (0.005)	3.8096 (0.0002)	9.5366 (0.0007)	1.688
0.1TaTi	5.383 (0.005)	3.7962 (0.0004)	9.537 (0.001)	0.979
0.25TaTi	6.115 (0.005)	3.7985 (0.0005)	9.545 (0.001)	1.186
0.1WTi	6.921 (0.004)	3.7981 (0.0002)	9.4895 (0.007)	0.576
0.25WTi	8.110 (0.005)	3.8083 (0.0003)	9.4307 (0.0009)	0.491

**Table 3.2:** Crystallite size  $(\tau)$ , lattice parameters 'a' and 'c' and increase of lattice volume  $\Delta V$  % for  $TiO_2$  and the M-doped samples

## 3.1.2 in-situ temperature-dependent XRD analysis

The crystal structure of TiO<sub>2</sub> catalysts is influenced by the temperature of the anatase to rutile phase transition.<sup>17</sup> A previous study also reported an increased phase transition temperature due to Nb doping, <sup>18</sup> and the above results suggest a similar behavior in the case of Ta and W. So far the annealing of the samples was conducted at a fixed temperature, which was determined by the TGA results. In order to determine more quantitatively the role of the doping cations and their concentration impact on the crystallinity of the TiO<sub>2</sub> nanocrystals with temperature, we performed *in-situ* temperature-dependent XRD (TDXRD) measurements in collaboration with Marc Lenertz (IPCMS UMR7504).

### 3.1.2.1 Experimental part

The measurements were performed on a Bruker D8 Advance equipped with a Lynxeye energy-dispersive 1D detector. The X-ray source is a monochromated copper anticathode ( $K\alpha_1 \lambda=1.5406 \text{ Å}$ ). Each scan was performed in the range of  $2\theta=20\text{-}80^\circ$ , with a step size of  $0.02^\circ$ . The analyses were conducted on the gel of  $TiO_2$  and the M-doped  $TiO_2$  under airflow (20 ml.min<sup>-1</sup>) in an Anton-Paar HTK 1200 temperature chamber.

The detailed experimental steps are as follows: The sample of dried gel was placed in a corundum sample holder equipped with a controlled heating plate. Then temperature of the sample holder was raised to the maximum calcination temperature  $(T_m)$  under the control of the program shown in **Figure 3.4 a**. Based on the XRD results in **3.1.1**, the  $T_m$  for the

measurement of TiO<sub>2</sub> was determined at 700°C to sufficiently promote the phase transition from anatase to rutile. For the M-doped samples, the value of  $T_m$  was raised to 900°C, since we have already observed the inhibition of rutile formation. The heating rate was 20°C.min<sup>-1</sup>, (which is faster than our synthesis condition 4°C.min<sup>-1</sup>). At each XRD recording step, the temperature was held for 30 minutes to ensure thermal stabilization of the sample. The first two scans were recorded at 30°C and 50°C respectively, and the subsequent scans were recorded every 25°C until reaching  $T_m$ .

It should be noted that, during the experiment, with the temperature increase, the bottom of the sample holder was gradually exposed (Figure 3.4 b and 3.4 c), increasing the corundum signal. Thus, the XRD pattern of the sample holder was also recorded as a reference (Figure S3.2, Page 192). After the *in-situ* TDXRD measurement, the XRD pattern of each sample was recorded at room temperature on a classical glass holder (Figure S3.3, Page 192). This allows us to determine the final crystal structure of each sample without any interference of peaks from the corundum sample holder.

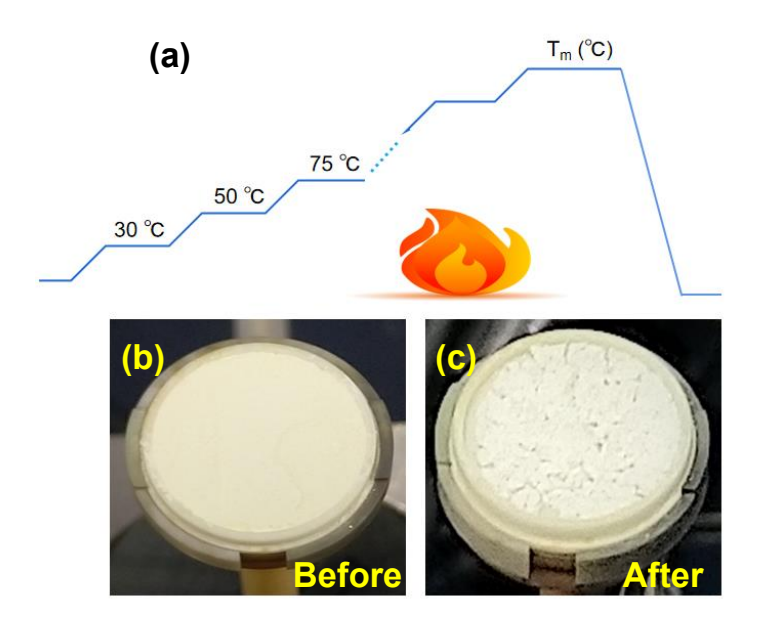


**Figure 3.4:** (a) Heating program for the TDXRD measurements. Optical images of TiO<sub>2</sub> gel sample before (b) and after (c) the measurement.

#### 3.1.2.2 Experimental results

The obtained *in-situ* TDXRD patterns are presented in the form of a two-dimensional XRD image ( $2\theta$  vs T; **Figure 3.5 and Figure 3.6**), with a color scale representing the intensity of the XRD peaks (stacked raw data available in **Figure S3.4**, **Page 193-194**). The XRD pattern of the first (at 30°C) and the last scan (at  $T_m$ ) are shown at the bottom and top of each figure, respectively.

The in-situ TDXRD patterns of TiO<sub>2</sub> gel (**Figure 3.5**) present its crystallization and phase transition process during the heating process. At 30°C, the main characteristic peaks assigned to anatase are present but broader than for the calcined TiO<sub>2</sub> presented in **Figure** 

**3.3** ((FWHM for (101) = 1.477 for  $TiO_2$  and 1.864 for the gel). In addition, the low signal-to-noise ratio of this scan indicates a low crystallinity of the dried gel sample without calcination. Moreover, we note the presence of a small amount of brookite with a weak peak at  $30.8^{\circ}$ . This indicates that the brookite is formed during the sol-gel synthesis before any annealing processes.

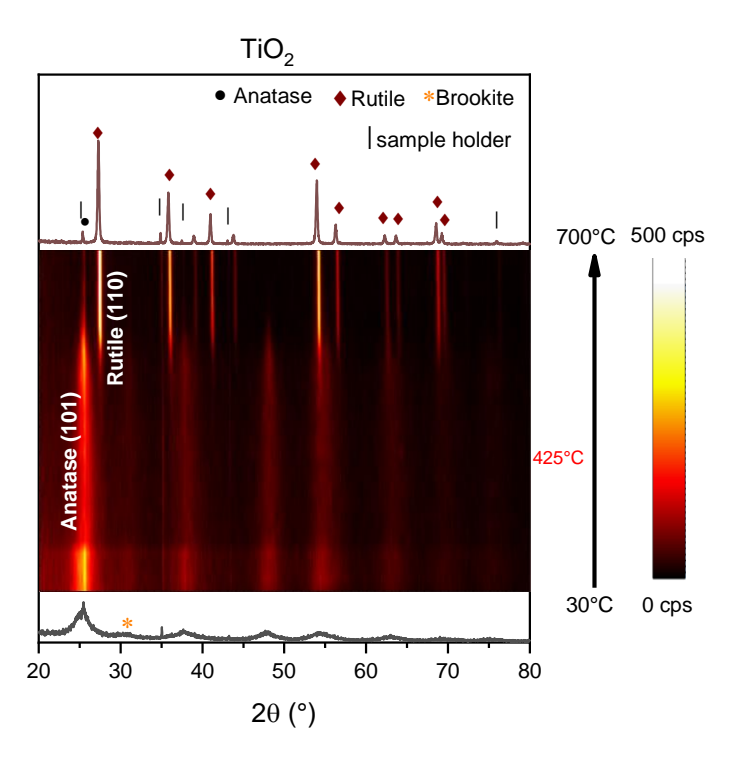


**Figure 3.5:** The TDXRD pattern of  $TiO_2$ . The two-dimensional XRD image is shown in the middle of the figure. The XRD pattern of the first (at 30°C) and the last scan (at  $T_m$ =700°C) are shown at the bottom and top of the figure, respectively.

Then, during the heating, we observed that the peak intensity of anatase (101) increases with temperature, while its width decreases, suggesting a larger crystalline size of anatase. The temperature for the phase transition ( $T_{PT}$ ) from anatase to rutile (indicated in red on the right of the figure) is determined by the first appearance of the characteristic peak of rutile (110) (the values of  $T_{PT}$  are also shown on the raw data in **Figure S3.4**, **Page 193-194**). For TiO<sub>2</sub>, the phase transition appears at 425°C, a value that is higher than the annealing temperature for the undoped TiO<sub>2</sub> (400°C). This deviation could be attributed to the difference in the ramp and calcination duration between the TDXRD heating program and the synthesis conditions. A slower heating ramp and longer calcination duration, by bringing more heat to the sample, could increase the thermally activated formation of rutile. The XRD pattern measured at room temperature after the *in-situ* measurement (**Figure S3.3**, **Page 192**), confirms a complete transition of anatase to rutile by heating up to 700°C, and the phase transition from anatase to rutile is irreversible as anatase is a metastable phase.

**Figures 3.6 a and 3.6 b** present the TDXRD patterns of the Nb-doped samples. Compared to the undoped TiO<sub>2</sub>, the temperature of transition from anatase to rutile phase is observed to be increased to 575°C and 775°C for 0.1NbTi and 0.25NbTi, respectively. This

confirms the inhibition of the phase transition observed in Chapter 2 caused by Nb doping. Furthermore, we found that at high temperatures, a portion of the Nb segregates from the lattice in the form of TiNb<sub>2</sub>O<sub>7</sub> (JCPDS 70-2009). The temperature for the phase segregation (*T*<sub>PS</sub>) changes with the Nb concentration, with values of 825°C and 750°C for 0.1NbTi and 0.25NbTi, respectively. The values of *T*<sub>PT</sub> and *T*<sub>PS</sub> for all samples are gathered in **Table 3.3**. Similarly, the *T*<sub>PT</sub> of Ta-doped samples are observed to increase with the doping concentration (625°C for 0.1TaTi and 850°C for 0.25TaTi). With the increase in temperature, the segregation of Ta<sub>2</sub>O<sub>5</sub> (JCPDS 25-0922) occurred on 0.1TaTi and 0.25TaTi at 850°C and 775°C, respectively (shown in **Figure 3.6 c** and **3.6 d**). For the W-doped samples (**Figure 3.6 e** and **3.6 f**), phase segregation in the form of WO<sub>3</sub> (JCPDS 43-1035) was initiated at 750°C (0.1WTi) and 650°C (0.25WTi). Furthermore, the phase transition from anatase to rutile is only observed on 0.1WTi at 825°C, but not on 0.25WTi. This suggests a highly stable anatase structure for the 0.25WTi up to 900°C.

**Table 3.3:** Temperature of phase transition and phase segregation during the TDXRD measurements for TiO<sub>2</sub> and M-doped samples.

Sample	T <sub>PT</sub> (°C)	T <sub>PS</sub> (°C)
TiO <sub>2</sub>	425	-
0.25NbTi	775	750
0.1NbTi	575	825
0.25TaTi	850	775
0.1TaTi	625	850
0.25WTi	-	650
0.1WTi	825	750

The above results confirm the inhibition of rutile formation by the introduction of Nb, Ta or W. According to the  $T_{PT}$ , for the samples doped with different cations but the same doping concentrations, the effect follows the order: W>Ta>Nb. The increase of M/Ti from 0.1 to 0.25 rise up the  $T_{PT}$  of approximately 200°C, and in the case of 0.25WTi the  $T_{PT}$  is expected to be higher than 900°C. Phase segregation in the form of corresponding oxides (TiNb<sub>2</sub>O<sub>7</sub>, Ta<sub>2</sub>O<sub>5</sub> or WO<sub>3</sub>) is observed for all the M-doped samples with similar values for Nb and Ta doped samples but lower values in the case of W ( $T_{PS}$  = 650 and 750°C for 0.25WTi and 0.1WTi respectively). Furthermore, the  $T_{PS}$  increases for lower doping concentrations. This suggests a limited solubility of the cation in the TiO<sub>2</sub> lattice, which is observed to decrease with temperature and probably occurs due to the metastable nature of the anatase phase. The phase segregation that occurred on the Nb-doped and Ta-doped TiO<sub>2</sub> has been reported in a previous study, and it was reported that the addition of Zr (about 1 wt%) was found to sufficiently suppress such phase segregation.<sup>19</sup>

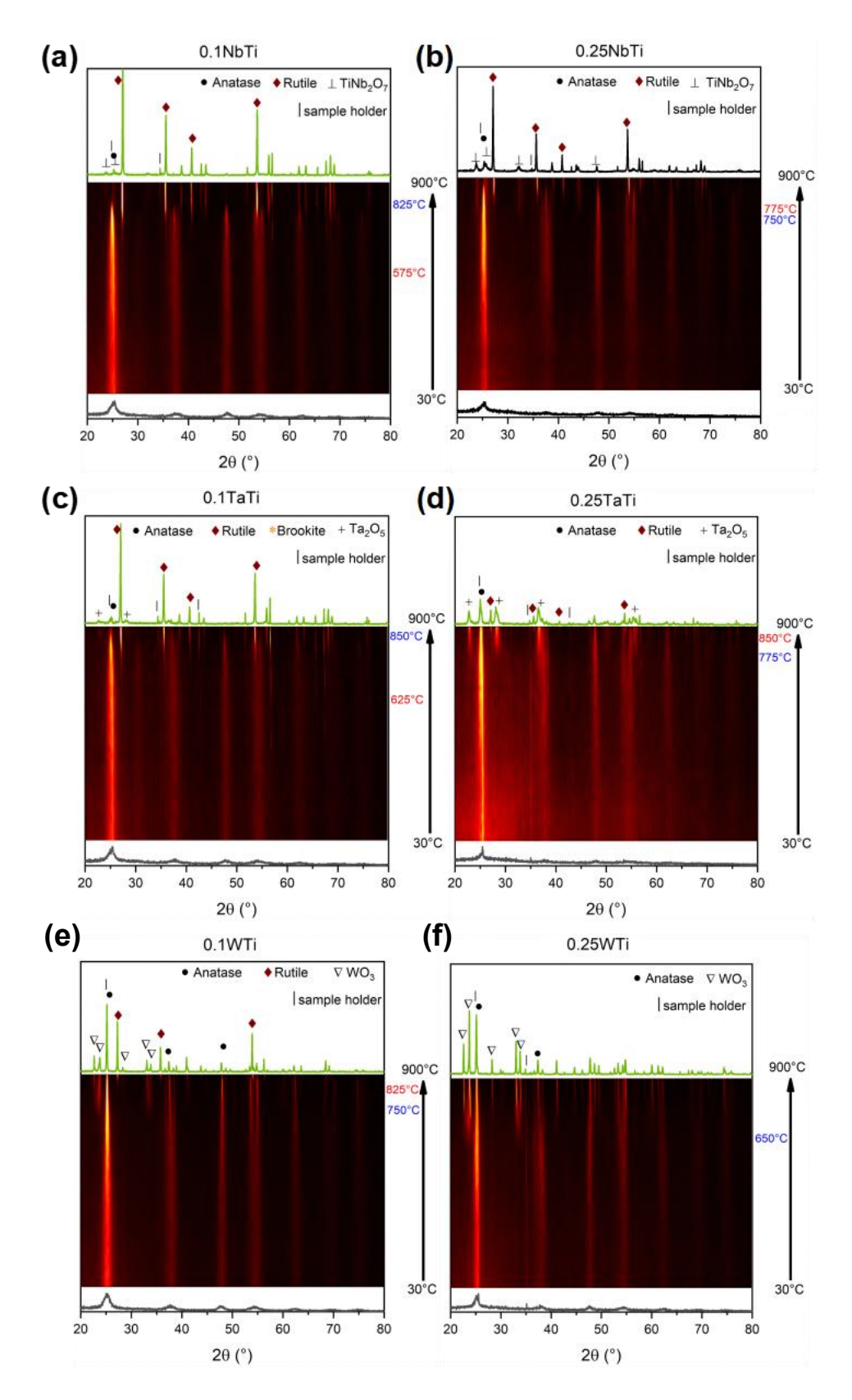


**Figure 3.6:** The TDXRD patterns of the M-doped samples. (a) and (b) for the Nb-doped  $TiO_2$ ; (c) and (d) for the Ta-doped  $TiO_2$ ; (e) and (f) for the W-doped  $TiO_2$ . The two-dimensional XRD image is shown in the middle of each figure. The XRD pattern of the first (at 30°C) and the last scan (at  $T_m=900$ °C) are shown at the bottom and top of each figure, respectively.)

In summary, this study confirmed that for all M-doped samples, the  $T_{PT}$  and  $T_{PS}$  are always above the temperature of the initial annealing in air (500°C) that is used to prepare our photocatalyst. Thus, the prepared M-doped samples should be mainly with the anatase phase. Besides, the results could guide the optimization of calcination conditions for synthesizing  $TiO_2$  materials with specific chemical compositions and phase structures. On the other hand, it is important to note that the current measurement condition may not ensure a complete phase transition or segregation at a specific temperature during the heating program, since each temperature was only kept for 30 min. Consequently, the above values of  $T_{PT}$  and  $T_{PS}$  may be overestimated to some extent.

#### 3.1.3 Morphology study:

As shown in **Figure 3.7**, all the M-doped samples present a uniform spherical morphology. The particle size of the M-doped samples is observed to be larger than that of TiO<sub>2</sub> and also increased with the doping concentration. The particle sizes of 0.25NbTi, 0.25TaTi and 0.25WTi are measured as  $10.0 \pm 2.0$  nm,  $7.9 \pm 1.2$  nm and  $7.2 \pm 2.8$  nm, respectively (average on 15 particles).

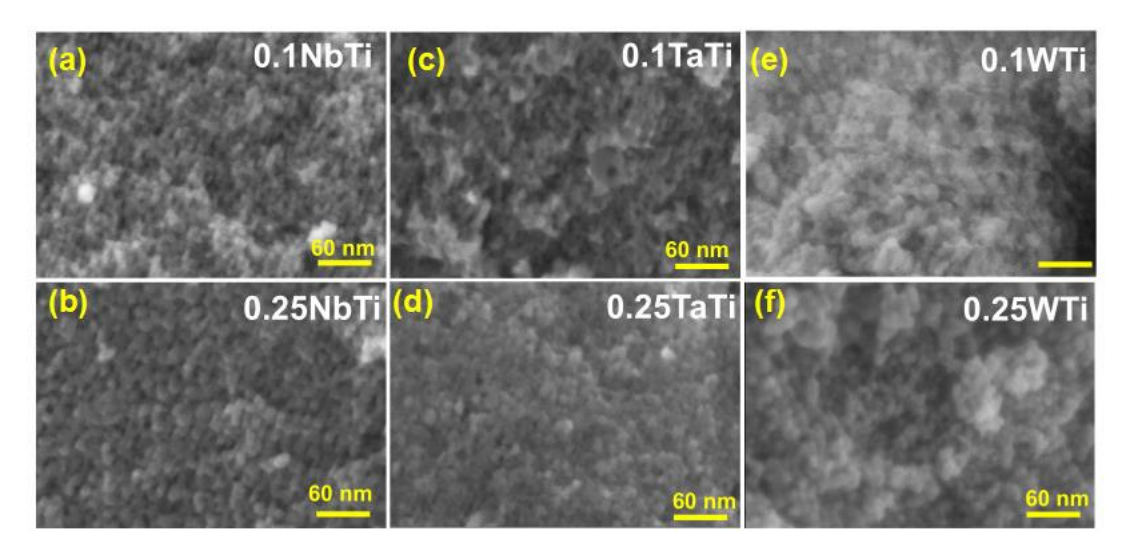


**Figure 3.7:** SEM images of the M-doped TiO<sub>2</sub>: (a) and (b) for the M-doped samples; (c) and (d) for the M-doped samples.

To obtain the molar ratio of M/Ti, SEM-EDX was performed based on a large area in the SEM image of each sample. The result (**Table 3.4** and **Table S3.1**, **Page 194**) indicates that the molar ratio of Nb/Ti, Ta/Ti and W/Ti for the specific M-doped sample is close to the value that we expected from the synthesis (0.25 or 0.1).

**Figure 3.8 a** presents the N<sub>2</sub> adsorption-desorption isotherms and pore size distributions for TiO<sub>2</sub> and the M-doped samples. All samples present a type IV isotherm,<sup>20</sup> with a hysteresis of type H2 <sup>21</sup> appearing in the relative pressure range between 0.4 to 0.8. This confirms a common mesoporous structure of all the M-doped TiO<sub>2</sub>. In addition, as shown in **Figure 3.8 b**, the pore sizes of all the M-doped TiO<sub>2</sub> are between 3 nm and 5 nm, which is highly similar to that of the TiO<sub>2</sub>. Thus, with the presence of cation, the higher calcination temperature (500°C 12h) does not influence the pore size of the M-doped

samples. On the other hand, it is observed that the specific BET surface areas of all the M-doped samples are smaller than that of TiO<sub>2</sub>, and also decrease with the doping concentration. This could be due to the increase in the particle size of the M-doped samples. In Chapter 2, the difference between TiO<sub>2</sub> and 0.25NbTi in terms of particle size and BET<sub>SSA</sub> are ascribed to their different initial annealing conditions (400°C 2h for TiO<sub>2</sub> and 500°C 12h for 0.25NbTi). Here, by comparing the results between 0.1MTi and 0.25MTi, we can conclude that the M-doping itself also contributes to increasing(decreasing) the particle size (BET<sub>SSA</sub>).

	_		
Sample ID	M/Ti (SEM-EDX)	$BET_{SSA} / m^2.g^{-1} (\pm 8.0)$	$E_{g}\left( eV\right)$
TiO <sub>2</sub>		191	3.06
0.1NbTi	0.10	168	3.04
0.25NbTi	0.22	128	3.08
0.1TaTi	0.09	171	3.02
0.25TaTi	0.20	143	3.03
0.1WTi	0.09	148	2.97
0.25WTi	0.22	144	2.92

**Table 3.4:** The molar ratio of M/Ti determined by SEM-EDX, BET specific surface area (BET<sub>SSA</sub>), and bandgap of the M-doped TiO<sub>2</sub>

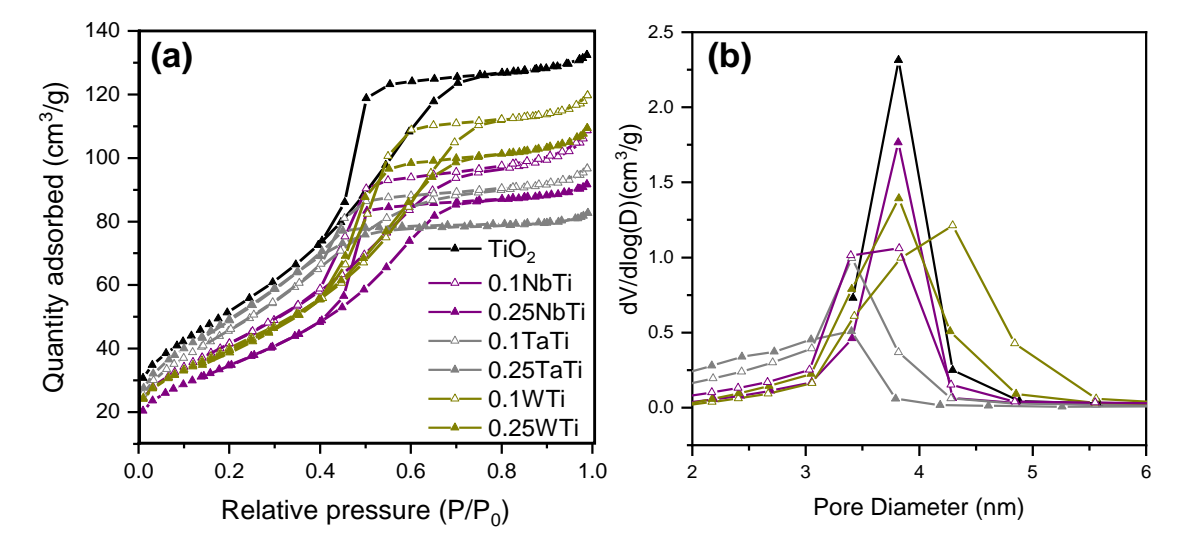


Figure 3.8: N<sub>2</sub> sorption isotherms (a) and pore size distribution(b) for TiO<sub>2</sub> and M-doped TiO<sub>2</sub>.

#### 3.1.4 Optical property

The UV-vis spectra of each M-doped sample were recorded by the same procedure as described in Chapter 2 and are presented in **Figure 3.9 a** using the Kubleka-Munk equation. Their bandgap energy  $(E_g)$  evaluated based on the Tauc plots (**Figure 3.9 b**) are summarized in **Table 3.4**.

Slight shifts of the absorption edge are observed on the M-doped samples, depending on the type and doping concentration of the cation. The differences in  $E_g$  value of the Nb-

doped and Ta-doped samples with that of  $TiO_2$  are less than 0.04 eV, indicating a non-significative modification of the band gap structure due to Nb or Ta-doping. The absorption edge of the W-doped samples is more clearly shifted to the longer wavelength, and the  $E_g$  values of 0.1WTi and 0.25WTi are determined as 2.97 eV and 2.92 eV, respectively. This reduction of the band gap due to the W-doping, may be attributed to a lower CB formed by the hybridization of W 5d and Ti 3d orbitals.

Besides the band gap absorption, a slight absorption between 400 nm and 500 nm is observed on the Nb-doped and W-doped samples, and the absorption intensity increases with the doping concentration. As discussed in Chapter 2, this absorption was ascribed to energy states below CBB due to the lattice distortion caused by the cation-doping. However, the same type of absorption does not appear on the Ta-doped samples, although it has a lattice expansion similar to the Nb-doped samples and larger than W-doped samples according to the XRD results. A hypothesis could be that these energy levels inducing a small visible absorption are determined by the energy level of the cation d orbital. Theoretically, Ta 5d is located at a higher energy level than Nb 4d and W 5d. Thus, the energy levels due to the Ta-doping may be above the CBB for the Ta-doped TiO<sub>2</sub>.

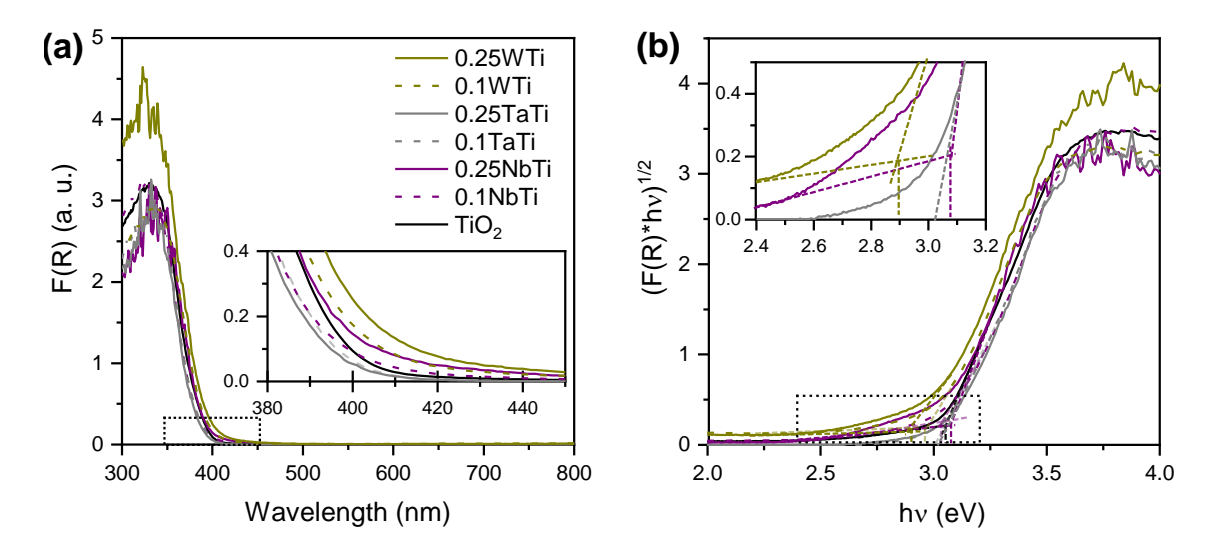


**Figure 3.9:** (a) UV–visible absorption spectra of  $TiO_2$  and the M-doped samples (300 to 800 nm). (b) Tauc plots of  $(F(R).hv)^{1/2}$  vs (hv) for estimating the indirect band gap of each sample. (The inset shows a zoom-in view of the area enclosed by the dashed box. For readability purposes, the inset in (b) only shows the band gap determination of 0.25MTi samples)

#### 3.1.5 Surface chemical composition by XPS

The surface chemical composition of the M-doped samples was analyzed by XPS and compared to that of TiO<sub>2</sub>. The signals of C 1s, O 1s, and Ti 2p can be easily identified on the survey spectra for all the samples (**Figure S3.5**, **Page 195**). All the peaks are calibrated with the peak C 1s A (285 eV). The signals of Nb 3d, Ta 4d, and W 4d are also visible on the samples doped with the specific cation. However, it is difficult to observe the signal from N on the survey spectra due to its low concentration and low sensitivity.

In the O 1s spectral region (**Figure S3.6 a, Page 195**), all the M-doped TiO<sub>2</sub> present the same characteristic peaks as TiO<sub>2</sub>, which are assigned to lattice oxygen (O 1s A) and surface oxygen species (O 1s B), respectively. **Figure S 3.6 b** (**Page 195**) presents the Ti 2p region of the M-doped samples and TiO<sub>2</sub>. For all the samples, a doublet with the binding energies of  $459.0 \pm 0.1$  eV and  $464.8 \pm 0.1$  eV is observed, which corresponds to the Ti  $2p_{3/2}$  and Ti  $2p_{1/2}$  of Ti<sup>4+</sup>.<sup>24</sup> This suggests that when Nb, Ta or W is introduced into the TiO<sub>2</sub> lattice, the chemical environment of titanium remains the same as that of TiO<sub>2</sub>. However, in Chapter 2, a small signal corresponding to Ti<sup>3+</sup> has been observed on 0.25NbTi, as reminded in the magnification on Ti 2p in **Figure S3.7**, **Page 196**. This small amount of Ti<sup>3+</sup> could be produced during the XPS analysis in the vacuum environment. Previous studies have also reported the appearance of Ti<sup>3+</sup> after vacuum treatment.<sup>25,26</sup> Interestingly, the signal of Ti<sup>3+</sup> was not observed on TiO<sub>2</sub>, 0.25TaTi and 0.25WTi, for which the data points completely coincided with the fitted curve using only Ti<sup>4+</sup> contribution. We hypothesize that the hybridization between Nb 4d and Ti 3d orbitals may facilitate the transfer of electrons to Ti sites, reducing Ti<sup>4+</sup> into Ti<sup>3+</sup>.

A doublet in the Nb 3d region (**Figure 3.10 a**) is identified for 0.25NbTi, with a binding energy of 207.7 eV and 210.8 eV. These peaks are assigned to Nb  $3d_{5/2}$  and Nb  $3d_{3/2}$  for Nb<sup>5+</sup>.<sup>27</sup> The Ta 4d region (**Figure 3.10 b**) of 0.25TaTi exhibits a doublet at 230.3 eV and 241.8 eV, corresponding to Ta  $4d_{5/2}$  and Ta  $4d_{3/2}$  of Ta<sup>5+</sup> species.<sup>28</sup> **Figure 3.10 c** shows the W 4d region of 0.25WTi, in which the doublet at 247.6 and 260.4 eV is observed. These two characteristic peaks are assigned to W  $4d_{5/2}$  and W  $4d_{3/2}$  of W<sup>6+</sup> species.<sup>29</sup> The results indicate that the oxidation states of Nb, Ta and W do not change during the doping process compared to the cation precursors (NbCl<sub>5</sub>, TaCl<sub>5</sub> and WCl<sub>6</sub>) used for synthesis.

**Figure 3.10 d** shows the N 1s spectral regions. A common peak at  $400.5 \pm 0.2$  eV (N 1s A), which can be attributed to surface chemisorbed nitrogen or nitrogen in the interstitial position (N<sub>i</sub>), is observed for all the samples.<sup>30,31</sup> For the spectrum of 0.25NbTi An additional broad peak at 395.2 eV is observed, and this peak is attributed to the satellite peak of Nb 3p.<sup>32</sup> Besides, a broad peak is also present in the N 1s spectral region of 0.25TaTi, with a binding energy at 404.7 eV. This peak is not attributed to any N species but to the contribution of Ta 4p,<sup>33</sup> which appears in the same binding energy range as N 1s. The atomic concentration of N for TiO<sub>2</sub>, 0.25NbTi, 0.25TaTi and 0.25WTi is calculated as 0.2%, 0.2%, 0.5% and 0.9%, respectively. It is noteworthy that the intensity of the N1s A peak of the 0.25WTi is higher than that of the other samples. This might be due to that the surface of the 0.25WTi is more favorable for the adsorption of nitrogen impurities, or some N species from the nitric acid used for the synthesis remain in the W-doped sample.

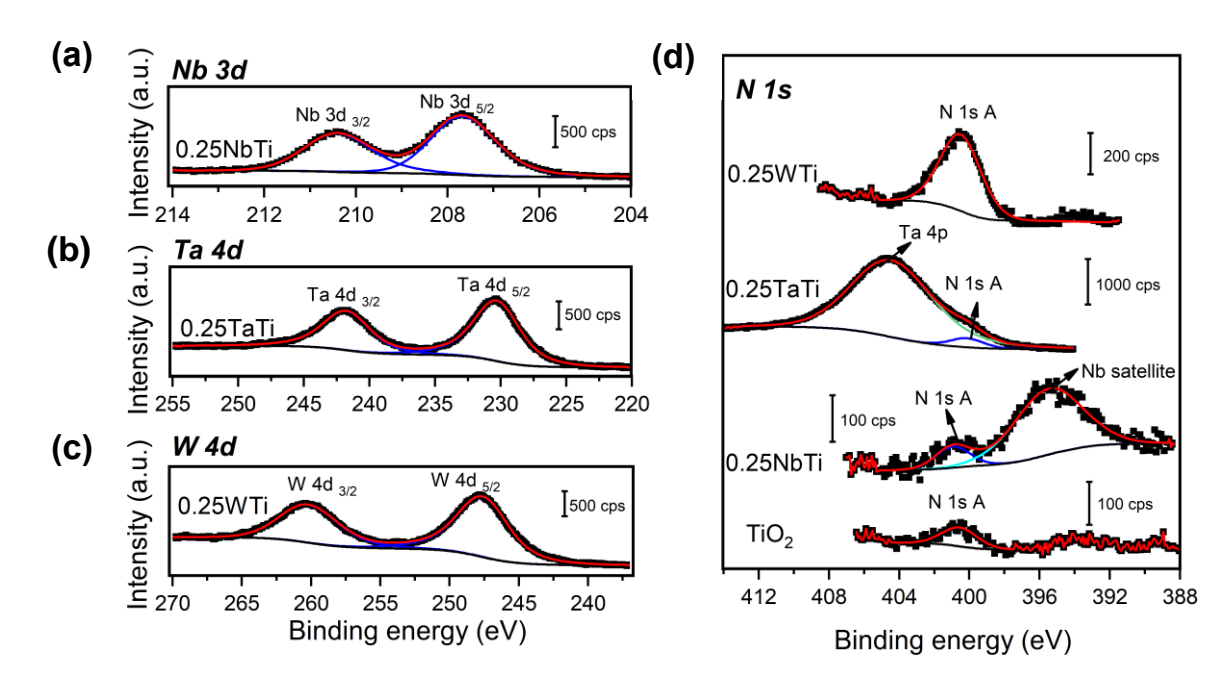


**Figure 3.10:** XPS spectra of Nb 3d region for 0.25NbTi (a); Ta 4d region for 0.25TaTi (b); W 4d region for 0.25WTi (c); N 1s region for TiO<sub>2</sub> and M-doped samples (d). (Black points are the experiment data, red lines are the fitted signals, blue, green, and cyan lines are different contributions).

#### 3.1.6 Identification of defects in M-doped samples by EPR

To investigate the possible defects introduced by the cation doping, EPR spectra of the 0.25MTi samples were recorded at 100K, as shown in Figure 3.11. The high-resolution spectra obtained by peak-to-peak normalization are presented in Figure 3.11 b. As already discussed in Chapter 2, the undoped TiO<sub>2</sub> presents 3 types of broad signals, corresponding to NO species captured at the surface (indicated by \*), 34,35 oxygen vacancy V<sub>O</sub><sup>+</sup> (sharp signal indicated by  $\Delta$ ),  $^{36,37}$  and the N species in a [O-Ti<sup>4+</sup>-N<sup>2-</sup>-Ti<sup>4+</sup>] unit (indicated by | ).<sup>38</sup> For 0.25NbTi, a small contribution of Ti<sup>3+</sup> is observed, which confirms the XPS result. On the other hand, the signal of  $V_0^+$  is not observed. The evolution of  $T_i^{3+}$  and  $V_0^+$  favors balancing the additional positive charge brought by Nb<sup>5+</sup>. For 0.25TaTi and 0.25WTi, no signal of Ti<sup>3+</sup> is observed, and the contribution of NO species is noted to increase and almost hide the signal of V<sub>O</sub><sup>+</sup> compared to that of TiO<sub>2</sub> indicating a decreased V<sub>O</sub><sup>+</sup> concentration for these cation-doped samples. Besides, The results are consistent with the XPS results, where a higher atomic proportion of N is determined for 0.25TaTi and 0.25WTi. In addition, signals with the g value of 1.80 and 1.64 (indicated by +) are observed on 0.25WTi (Figure 3.11 a), which could be attributed to the W<sup>5+</sup>. <sup>39,40</sup> Since W<sup>5+</sup> was not detected by XPS, we suppose that the amount of W<sup>5+</sup> is extremely low, or it is located mainly in the bulk.

According to the EPR results, we can conclude that doping with cation reduces the concentration of  ${\rm V_O}^+$  in the M-doped TiO<sub>2</sub> materials. Depending on the cation type, other defects, such as Ti<sup>3+</sup> (0.25NbTi), NO species (0.25TaTi and 0.25WTi), and W<sup>5+</sup> (0.25WTi), could be also involved in the charge compensation scheme for the M-doped TiO<sub>2</sub>.

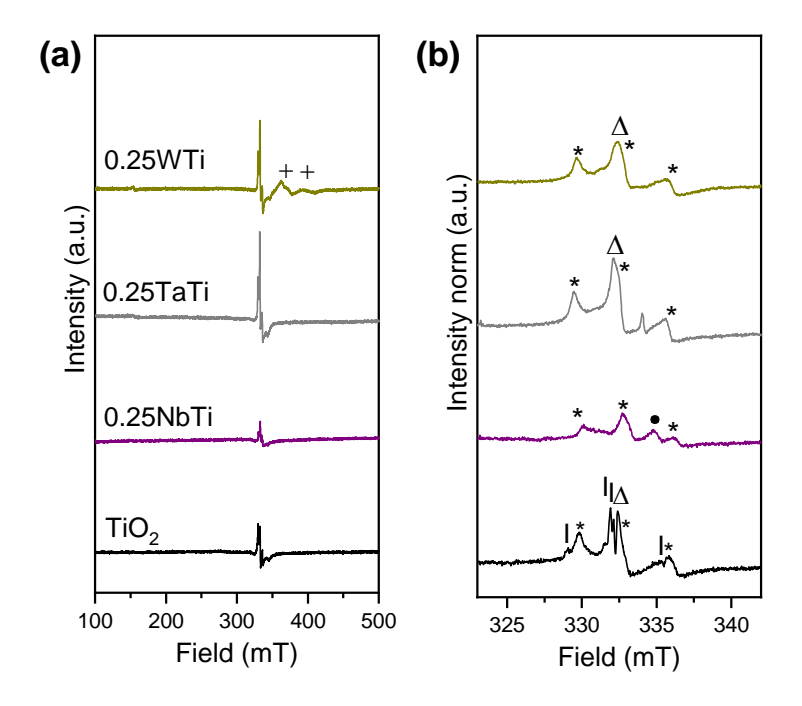


**Figure 3.11:** EPR spectra for TiO<sub>2</sub> and M-doped TiO<sub>2</sub> samples: (a) large range spectra and (b) high-resolution spectra with peak-to-peak normalization.

## 3.2 Conclusion on the M-doped TiO<sub>2</sub>

Following the sol-gel synthesis method described in Chapter 2, the M-doped TiO<sub>2</sub> materials were successfully synthesized with Nb, Ta, and W. The influence of the cation type and doping concentration on the properties of the resultant M-doped samples was systematically studied. Generally speaking, all the M-doped TiO<sub>2</sub> present a uniform spherical morphology similar to that of TiO<sub>2</sub>. It is observed that the particle size of TiO<sub>2</sub> nanoparticles for a specific M-doped sample increases with cation doping concentration, leading to a slight decrease in the BET specific surface area.

The XRD results confirm the inhibition of the rutile phase formation due to the introduction of cation. This inhibition effect is observed to be more significant on the W-doped TiO<sub>2</sub>, and it is also enhanced with increasing cation doping concentration. Besides, a technique of *in-situ* TDXRD analysis was developed for better understanding the evolution of the crystal structure for the specific M-doped samples as a function of temperature. It is shown that all the M-doped TiO<sub>2</sub> present a higher phase transition temperature compared to TiO<sub>2</sub>. For the M-doped TiO<sub>2</sub> with the same doping concentration, the values of  $T_{PT}$  follow the order: W>Ta>Nb. On the other hand, the observed phase segregation indicates a limited solubility of cations in the TiO<sub>2</sub> lattice at high temperatures. Although the current *in-situ* TDXRD may overestimate the value of  $T_{PT}$  and  $T_{PS}$  due to the limited time at each temperature step, the results could be used to optimize the calcination conditions for the synthesis of TiO<sub>2</sub> materials.

According to the UV-vis spectra results, doping with Nb or Ta has hardly an impact on the band gap structure of the resultant  $TiO_2$  materials. On the contrary, the band gap of the W-doped  $TiO_2$  was reduced to 2.79 eV (0.1WTi) and 2.72 eV (0.25WTi). Besides, a slight absorption between 400 to 500 nm is observed on the Nb-doped and W-doped samples but not on the Ta-doped samples. It is hypothesized that these new energy states are located above the CBB for the Ta-doped  $TiO_2$ . The EPR results suggest a decrease of the  $V_0^+$  in all the M-doped  $TiO_2$ , which is favored by the compensation of the additional positive charge brought by the cation dopants.

#### 3.3 Characterizations of the (M,N) co-doped samples

The (M,N) co-doped samples were prepared by conducting a nitridation process on the M-doped sample and according to the parameters in **Table 3.1** to obtain mild and harsh conditions. In Chapter 2, it is found that the initial presence of Nb influences significantly the nitridation process and results in properties different from that of undoped TiO<sub>2</sub>. In this part, to highlight the role of cation type in determining the properties of the resultant (M,N) co-doped TiO<sub>2</sub> material, we mainly focused on the characterizations of the samples with high cation concentration (M/Ti=0.25), while the samples 0.1NbNTi, 0.1TaNTi and 0.1WNTi are mainly discussed in terms of optical properties.

#### 3.3.1 Crystal structure by XRD

The crystal structures of the (M.N) co-doped materials were studied by XRD (**Figure 3.12**). There is no significant difference between the diffractograms of the co-doped samples and their counterparts before nitridation. All the co-doped samples still present the characteristic peaks corresponding to anatase. As shown in Chapter 2, 3.1, the XRD results of the N-doped TiO<sub>2</sub> proved that doping with nitrogen could facilitate the phase transition from anatase to rutile. Therefore, the effect of M cation and nitrogen are antagonistic to each other. Our result confirms that for all the (M,N) co-doped TiO<sub>2</sub> samples, the anatase to rutile phase transition does not occur during the nitridation process. This indicates the effect of cation prevails over the one of nitrogen under the current experimental conditions and that the presence of the cation in the lattice of TiO<sub>2</sub> is essential to limit the phase transition from anatase to rutile in the (M.N) co-doped TiO<sub>2</sub> materials.

The crystallite sizes  $\tau$  and the interplanar spacing of the anatase (101) of all the samples were calculated using the Debye-Sherrer formula (eq. 3.1) and the Bragg formula (eq. 3.2), respectively. The results are summarized in Table 3.5

$$\tau = \frac{K\lambda}{B\cos(\theta)} \tag{eq 3.1}$$

$$d = \frac{\lambda}{\sin(\theta)} \tag{eq 3.2}$$

Here K is a correction factor (K = 0.89 for the spherical particles);  $\lambda$  is the X-ray wavelength (Cu K $_{\alpha}$  X-rays source,  $\lambda$  = 0.15418 nm); B is the peak full width at half maximum (FWHM) and  $\theta$  is the angle of the diffraction peak considered.

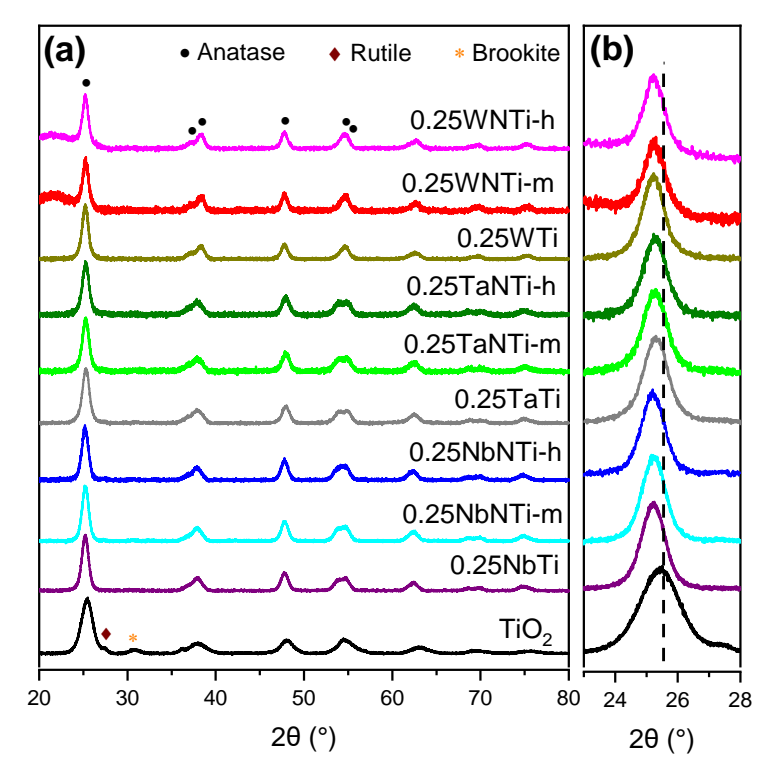


**Figure 3.12:** XRD patterns of TiO<sub>2</sub>, M-doped and co-doped samples: (a) full range and (b) magnification on anatase (101) peak.

**Table 3.5:** Crystallite size (D) determined by Debye-Sherrer equation, interplanar spacing of anatase (101)( $d_{101}$ ) determined by Bragg formula and BET specific surface area for the different (M,N) co-doped TiO<sub>2</sub> samples.

Sample	D (nm) (± 0.1)	$d_{101}$ (Å) (± 0.005)	BET $(m^2.g^{-1})$ $(\pm 8.0)$
TiO <sub>2</sub>	5.3	3.499	191
0.25NbTi	8.4	3.528	128
0.25NbNTi-m	9.2	3.523	120
0.25NbNTi-h	9.3	3.530	114
0.25TaTi	8.8	3.520	143
0.25TaNTi-m	8.6	3.518	127
0.25TaNTi-h	9.2	3.520	115
0.25WTi	9.9	3.527	144
0.25WNTi-m	11.2	3.527	137
0.25WNTi-h	11.3	3.528	133

The crystallite sizes of TiO<sub>2</sub> and the M-doped TiO<sub>2</sub> determined by the Debye-Sherrer equation (**Table 3.5**) are slightly larger than those determined by Rietveld refinement (**Table 3.2**). This is probably because the XRD patterns shown in **Figure 3.3** were obtained with a monochromated X-ray source. However, the same tendency is observed, that is, doping with

cation resulted in a larger crystallite size. Compared to the respective M-doped samples, only a slight increase in D is observed for the (M,N) co-doped  $TiO_2$ . The  $d_{101}$  shows no obvious variation, and the result for the Nb-containing samples is also in good agreement with the result of Chapter 2, 3.1. This indicates a non-significant change in the lattice parameters due to the nitridation treatment.

#### 3.3.2 Morphology study

Fig 3.13 presents the comparison of the pore size distributions between the M-doped and (M,N) co-doped TiO<sub>2</sub> samples. The corresponding N<sub>2</sub> adsorption-desorption isotherms are shown in Figure S3.8, Page 196. It is shown that all co-doped samples present the type IV isotherm, with a hysteresis of type H2 in the relative pressure range between 0.4 and 0.8. The slight decrease in the specific surface area (Table 3.5) observed for the co-doped samples can be ascribed to the increase in the crystalline and particle size after nitridation.

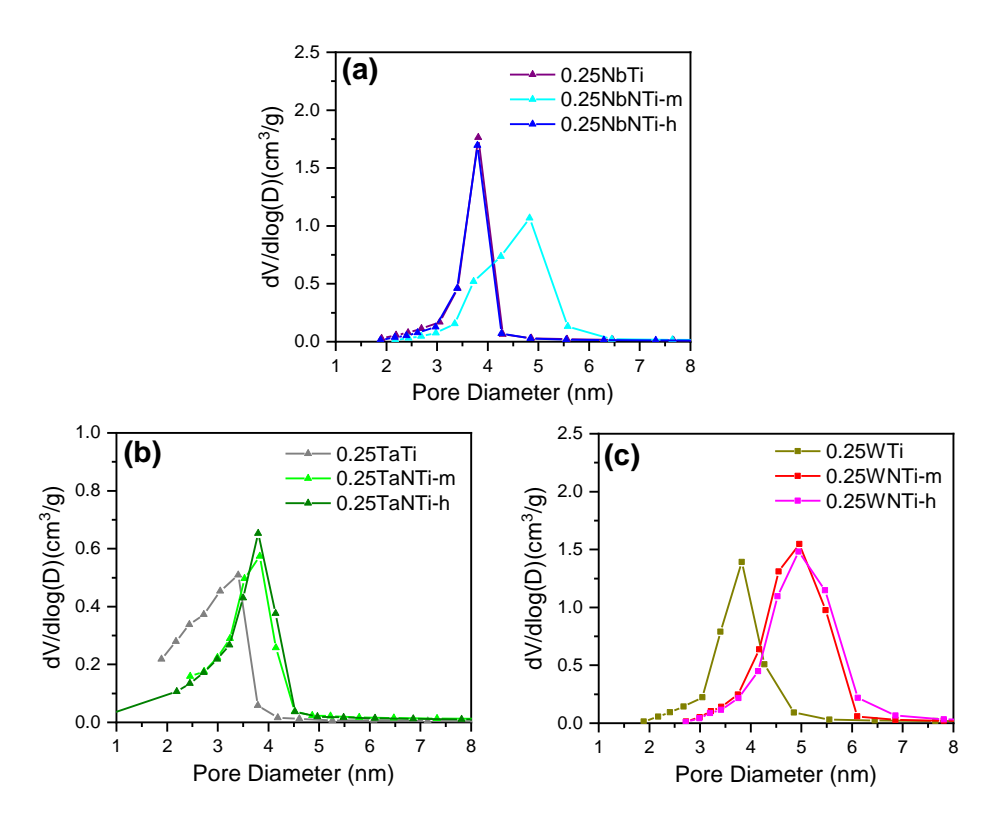


**Figure 3.13:** Distribution of pore diameter for the M-doped and (M,N) co-doped samples: (a) Nb-doped and (Nb,N) co-doped samples. (b) Ta-doped and (Ta,N) co-doped samples. (c) W-doped and (W,N) co-doped samples.

As discussed in Chapter 2 **3.2.2**, the pore diameter of TiO<sub>2</sub> was slightly enlarged due to the nitridation treatment. Here, a similar phenomenon is observed on the (M,N) co-doped TiO<sub>2</sub>. For the (Ta,N) and (W,N) co-doped samples, both mild and harsh nitridation (same temperature but different duration) result in pore diameter enlargement. For the (Nb,N) co-doped samples, only the mild nitridation leads to an increase in its pore diameter. Probably, certain small pores may recombine into large ones during the nitridation process. However, considering the tiny variation and the possible deviation in the measurement we cautiously

state that the thermal nitridation process does not significantly change the pore structure of the samples.

#### 3.3.3 Optical properties

# 3.3.3.1 UV-vis spectra of samples subjected to the same nitridation

First, we conducted nitridation of 0.25NbTi, 0.25TaTi and 0.25WTi samples under the same thermal condition (350°C, 12h), and recorded the UV-visible spectra of the resultant (M,N) co-doped TiO<sub>2</sub> powders in diffuse reflection mode. The absorption spectra converted in Kubelka-Munk unit are shown in **Figure 3.14**. The TiO<sub>2</sub> powder and the N-doped TiO<sub>2</sub> obtained under the same conditions (TiO<sub>2</sub>-350°C, 12h) are used as a reference.

Due to the limited thermal energy input, the N-doped sample only presents a slight increase in absorption before 500 nm. It is shown that the cation type has a significant effect on the light absorption properties of the resultant (M.N) co-doped samples. Compared to the N-doped sample, the (Ta,N) co-doped sample does not show any additional light absorption. However, both the Nb-doped and W-doped samples exhibit a significant increase in visible light absorption. In more detail, the increased absorption for the Nb-doped  $TiO_2$  is limited in the range before 550 nm, while the W-doped  $TiO_2$  presents absorption in the whole spectral range. The results indicate that the efficiency of the nitridation treatment for improving visible absorption of the (M,N) co-doped  $TiO_2$  follows the order: (W,N) > (Nb,N) > (Ta,N).

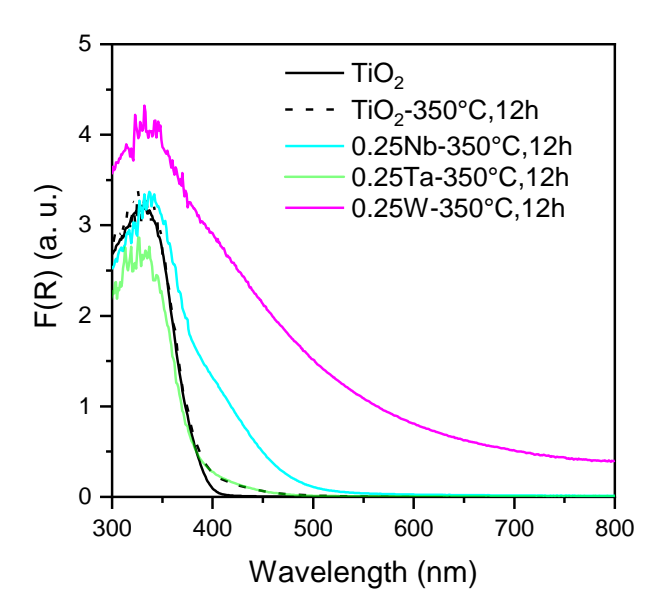


**Figure 3.14:** UV-visible absorption spectra of the different samples after the nitridation under the same thermal condition (350°C,12h).

# 3.3.3.2 UV-vis spectra of (M,N) co-doped $TiO_2$ subjected to mild and harsh nitridation

In order to have a better understanding of the influence of nitridation conditions and the doped cations on the light absorption properties of the (M,N) co-doped TiO<sub>2</sub>, all samples have been systematically studied by UV visible spectroscopy. We aimed to visualize the impact of the doping cation nature and concentration together with the nitridation condition.

The UV-Vis absorption spectra of the (Nb,N), (Ta,N) and (W,N) co-doped samples are presented in Figures 3.15 a, 3.15 d, and 3.15 g respectively. For each (M,N) family, the samples with 0.1 M/Ti and 0.25 M/Ti with nitridation under harsh and mild conditions are reported. As indicated in Chapter 2, mild conditions correspond to the sample with an increase of the visible absorption before 550 nm (yellow color) while harsh conditions induce absorption at longer wavelength (>550 nm; dark color). As reported in Table 3.1 of the experimental part of this chapter, after trying various combinations of temperature and duration for the nitridation process, we realized that mild and harsh conditions differ for the different (M,N) co-doped TiO<sub>2</sub> materials. For comparison purposes, in Figure 3.15, for each family of (M,N) co-doped sample we also reported the spectra of the N-doped TiO<sub>2</sub> (NTi samples) with similar mild and harsh conditions, as well as the one of the cation-doped 0.25MTi sample. The band gap energies of all the samples were calculated using the Tauc plot (Figure 3.15 b, 3.15 e and 3.15 h) and summarized in Table 3.6. Optical images (Figure 3.15 c, 3.15 f and 3.15 i) visualize the change in color of the samples in each (M,N) family with the nitridation conditions.

The (Nb,N) co-doped samples exhibit a higher visible absorption compared to the N-doped samples under the same thermal conditions. When decreasing the initial Nb concentration in  $TiO_2$ , the visible absorption of 0.1NbNTi-m and 0.1NbNTi-h is lower than that of 0.25NbNTi-m and 0.25NbNTi-h respectively, indicating a positive correlation between the doping concentration of Nb and the increase of visible absorption. It is shown that the absorption before 550 nm is related to the decrease in bandgap which is due to nitrogen doping. Under harsh nitridation conditions, the absorption is more intense in this region, however, no reduction of the  $E_g$  is observed for the 0.25NbNTi-h and 0.1NbNTi-h samples. Harsh nitridation conditions mainly increase the absorption at long wavelengths (> 500 nm) which was attributed in Chapter 2 to the generation of  $Ti^{3+}$  sites.

For the (Ta,N) co-doped samples the mild and hash thermal conditions for nitridation are determined as  $450^{\circ}$ C,1h and  $450^{\circ}$ C,12h respectively, which are slightly higher conditions when compared to the corresponding (Nb,N) co-doped TiO<sub>2</sub> samples. Similar to the (Nb,N) co-doped samples, a positive correlation between the doping concentration of Ta and the increase of visible absorption is observed. However, the different point is that 0.1TaNTi-m and 0.1TaNTi-h show no increase in visible absorption compared to the N-doped samples under the same thermal condition. Two different  $E_g$  values are observed on 0.1TaNTi-m and NTi-450°C 1h, the higher value could be ascribed to the original band gap of TiO<sub>2</sub>, and the lower one may be due to the insufficient and non-homogeneous N-doping. As observed for

(Nb,N) co-doped samples, for the same Ta concentration, no reduction of  $E_g$  is observed on the samples under harsh nitridation.

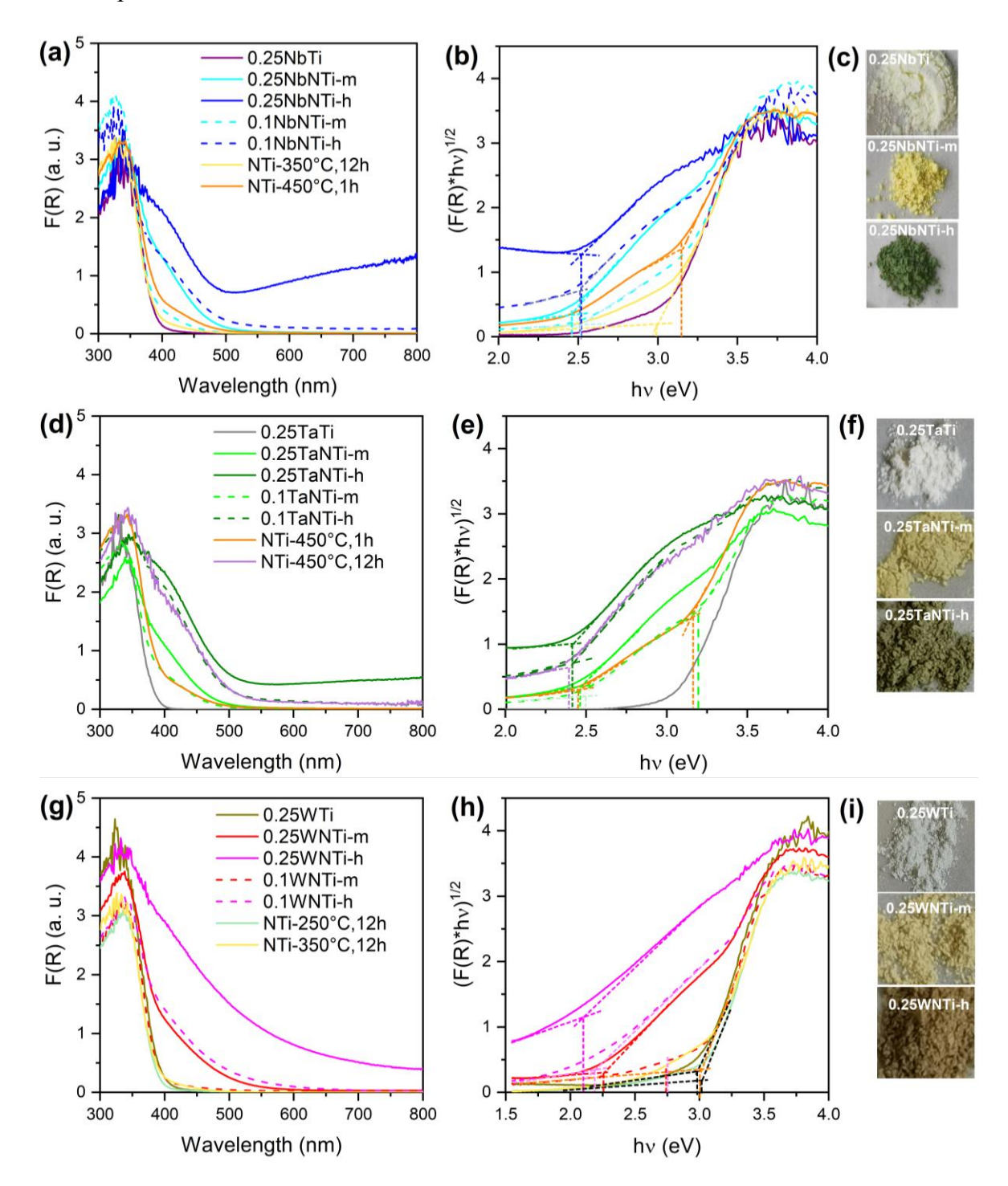


**Figure 3.15:** UV–visible absorption spectra (a,d,g), Tauc plots (b,e,h) and optical images (c,f,i) of the (Nb,N) co-doped samples subjected to mild (350°C, 12h) and harsh (450°C, 1h) nitridation (first row), of the (Ta,N) co-doped samples subjected to mild (450°C, 1h) and harsh (450°C, 12h) nitridation (second row), and of the (W,N) co-doped samples subjected to mild (250°C, 12h) and harsh (350°C, 12h) nitridation (third row).

For the W,N co-doped samples, the mild and harsh thermal conditions of nitridation are defined as  $250^{\circ}$ C,12h, and  $350^{\circ}$ C,12h, respectively. This indicates that a lower energy input is required for the nitrogen insertion, compared to the (Nb,N) and (Ta,N) co-doped samples. Under these thermal conditions, the N-doped samples present a negligible increase in visible absorption, with  $E_g$  almost similar to TiO<sub>2</sub>. For the (W,N) co-doped TiO<sub>2</sub>, even with a low doping concentration of W (0.1WNTi-m and 0.1WNTi-h), the visible absorption is higher than that of the N-doped samples and this absorption increases with the doping concentration of W. A reduction of  $E_g$  is observed on the (W,N) co-doped samples treated by harsh nitridation. Especially, a difference in the  $E_g$  value of 0.79 eV between 0.1WNTi-m and 0.1WNTi-h is noted.

The above results indicate that the nitridation process has effectively extended the absorption of the (M,N) co-doped  $TiO_2$  into the visible region. For the samples in each (M,N) family, two types of absorption spectra are observed depending on the thermal nitridation condition: (i) mild nitridation results in visible absorption before 550 nm. (ii) harsh nitridation further improves the absorption before 550 nm and also results in absorption after 550 nm. As discussed in Chapter 2 based on the (Nb,N) co-doped samples, the type-i absorption was attributed to nitrogen doping. For type-ii absorption, the absorption after 550 nm was mainly due to the introduction of defects in the band gap  $(Ti^{3+}$  and  $V_o^+)$  after the harsh nitridation. The results indicate that for both mild and harsh conditions for each (M,N) family, the facility for N-doping follows the order: W>Nb>Ta.

In each family of the (M,N) co-doped TiO<sub>2</sub>, all the 0.25MNTi samples exhibit higher absorption than 0.1MNTi, indicating an increasing cation concentration contributes to the improvement of absorption. Due to the relatively lower ability of Ta to promote N-doping, when the Ta concentration is low, 0.1TaNTi-m and 0.1TaNTi-h show almost the same absorption spectra as the corresponding N-doped samples. This reminds us that the visible absorption brought by the co-doping strategy strongly depends on the type of cation, the doping concentration, and the nitridation conditions that must be studied systematically.

From the point of view of the band gap structure, the  $E_g$  of all the (Nb,N) and (Ta,N) co-doped samples is near 2.5 eV. Since the VBT of the (M,N) co-doped TiO<sub>2</sub> is formed by the hybridization of O 2p and N 2p orbitals, it is reasonable to suppose that the N 2p states distribute similarly in the case of (Nb,N) and (Ta,N) co-doping. On the other hand, the  $E_g$  values of the (W,N) co-doped samples are smaller, This may indicate a different distribution of N 2p states in the (W,N) co-doped TiO<sub>2</sub> or a lowering of the CBM due to the W 5d orbitals. An exception (0.1WNTi-m) with larger  $E_g$  coud be explained by the insufficient N-doping due to the low W concentration and nitridation temperature.

In addition, in the case of (Nb,N) and (Ta,N) co-doping under harsh conditions, the intensity of absorption after 550 nm increases with the wavelength, while it decreases for 0.25WNTi-h. This may imply that the defects leading to longer wavelength absorption (>550 nm) in the (Nb,N) and (Ta,N) co-doped TiO<sub>2</sub> may be different from that in the (W,N) co-doped samples. Visually, both 0.25NbNTi-h and 0.25TaNTi-h exhibit a dark green color (**Figure 3.15 c and f**) while 0.25WNTi-h has a brownish color (**Figure 3.15 i**).

TiO <sub>2</sub> samples	$E_g \text{ (eV)} $ $(\pm 0.05)$	Nb doped TiO <sub>2</sub> samples	E <sub>g</sub> (eV) (±0.05)	Ta doped TiO <sub>2</sub> samples	$E_g(eV)$ $(\pm 0.05)$	W doped TiO <sub>2</sub> samples	E <sub>g</sub> (eV) (±0.05)
TiO <sub>2</sub>	3.06	0.1NbNTi	3.04	0.1TaNTi	3.02	0.1WNTi	2.97
NTi-250 12h	3.03	0.1NbNTi- <b>m</b>	2.52	0.1TaNTi- <b>m</b>	3.19/2.50	0.1WNTi- <b>m</b>	2.99
NTi-350 12h	3.01	0.1NbNTi- <b>h</b>	2.52	0.1TaNTi- <b>h</b>	2.42	0.1WNTi- <b>h</b>	2.20
NIT: 450 11	2 16/2 47	0.25NbNTi	3.08	0.25TaNTi	3.03	0.25WNTi	2.92
NTi-450 1h	3.16/2.47	0.25NbNTi- <b>m</b>	2.44	0.25TaNTi- <b>m</b>	2.47	0.25WNTi-m	2.26
NTi-450 12h	2.39	0.25NbNTi- <b>h</b>	2.50	0.25TaNTi- <b>h</b>	2.42	0.25WNTi- <b>h</b>	2.10
<b>m:</b> 350°C 12h							

**Table 3.6:** Band gap  $(E_q)$  determined by Tauc plot for the different samples.

**m:** 350°C 12h **h:** 450°C 1h

**m:** 450°C 1h **h:** 450°C 12h m: 250°C 12h h: 350°C 12h

#### 3.3.3.3 UV-vis spectra extended into the infrared region

Finally, we analyzed the UV-visible spectra extended to the infrared region for all the mentioned samples. The objective is to detect possible defect energy states located in the band gap, which may explain the difference in absorption at longer wavelengths.

The measurements were carried out between 300 to 2000 nm on the Perkin Elmer Lambda 950 spectrophotometer equipped with a 100 nm integrating sphere. In order to reduce signal noise in the infrared region, BaSO<sub>4</sub> powder was used as a reference for recording the baseline before the measurements of samples. The absorption spectra shown in **Figure 3.16** were obtained using the Kubelka-Munk equation.

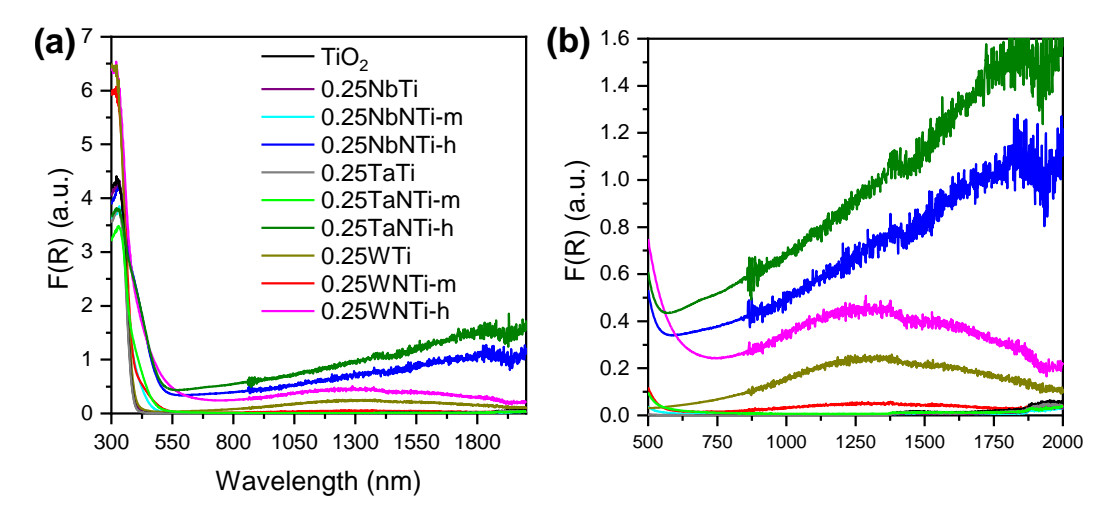


**Figure 3.16 :** (a) UV–visible absorption spectra recorded in the region of 300 to 2000 nm. (b) magnification on the spectral region of 500 to 2000 nm.

TiO<sub>2</sub>, 0.25NbTi, 0.25TaTi, as well as the associated (M,N) co-doped sample subjected to mild nitridation, exhibit negligible absorption in the infrared region. 0.25NbNTi-h and 0.25TaNTi-h exhibit similar spectral features, where the absorption increases with wavelength up to 2000 nm. The noise increases dramatically after 2000 nm due to absorption from molecules in the air, so we were unable to determine the central position of this absorption peak. However, this absorption is highly likely related to the

transition from the occupied  $Ti^{3+}$  energy state to the conduction band. In Chapter 2 we have confirmed the presence of  $Ti^{3+}$  in 0.25NbNTi-h by EPR characterization and according to previous studies, the  $Ti^{3+}$  energy levels are located ~0.8 to 0.5 eV below the conduction band. On the current UV visible IR spectra, the center of this transition is at a wavelength higher than 2000 nm (corresponding to energy transition < 0.62 eV).

All the W-containing samples present a broad peak centered on 1300 nm (corresponding to 0.95 eV), and a decrease in this peak intensity is observed for 0.25WNTi-m. We speculate that this absorption may correspond to another type of defect lying deeper in the bandgap of the W-containing TiO<sub>2</sub>, and the concentration of this defect may be reduced by the "mild" nitridation treatment. As indicated by the EPR result of the W-doped TiO<sub>2</sub>, we hypothesize that this defect state may related to the W<sup>5+</sup>.

#### 3.3.3.4 Conclusion on UV-vis spectra

In this part, we have thoroughly characterized the absorption properties of the synthesized (M,N) co-doped TiO<sub>2</sub>. The effect of the type and doping concentration of the cation, together with the nitridation conditions on the absorption behavior was analyzed. It is shown that the (M.N) co-doping strategy has successfully extended the absorption of TiO<sub>2</sub> materials into the visible region. By adjusting the nitridation conditions, the two different types of absorption features are observed on all the (M,N) co-doped TiO<sub>2</sub> samples. The mild and harsh conditions determined for each (M,N) family differ and indicate that the ability to promote on the N-doping follow the order W>Nb>Ta. Besides, it is shown that an increasing cation concentration improves absorption of the resultant (M,N) co-doped TiO<sub>2</sub>.

The (Nb,N) and (Ta,N) co-doped  $TiO_2$  show a similarity in absorption behavior. The band gap for all the (Nb,N) and (Ta,N) co-doped samples is ~2.5 eV, which is slightly larger than that of the (W,N) co-doped samples. The hypothesis behind this difference is that the N 2p states in the (W,N) co-doped  $TiO_2$  are probably higher in energy than that in the (Nb,N) and (Ta,N) co-doped samples or the CB minimum is lowered by the W 5d orbitals. Furthermore, the similarity of the absorption spectra between the (Nb,N) and (Ta,N) co-doped samples is also observed in the infrared region. With the harsh nitridation, both of them present an absorption increase with wavelength from 500 to 2000 nm, which is attributed to  $Ti^{3+}$ . On the other hand, the W-containing samples present a different behavior with a broad absorption peak at 1300 nm, which is hypothesized to be related to the generation of  $W^{5+}$  observed by EPR.

#### 3.3.4 Surface chemical composition by XPS

The surface chemical compositions of the (M,N) co-doped TiO<sub>2</sub> samples subjected to mild and harsh conditions were characterized by XPS and compared to the corresponding M-doped samples before nitridation. The atomic concentrations of the different elements are summarized in **Table 3.7.** 

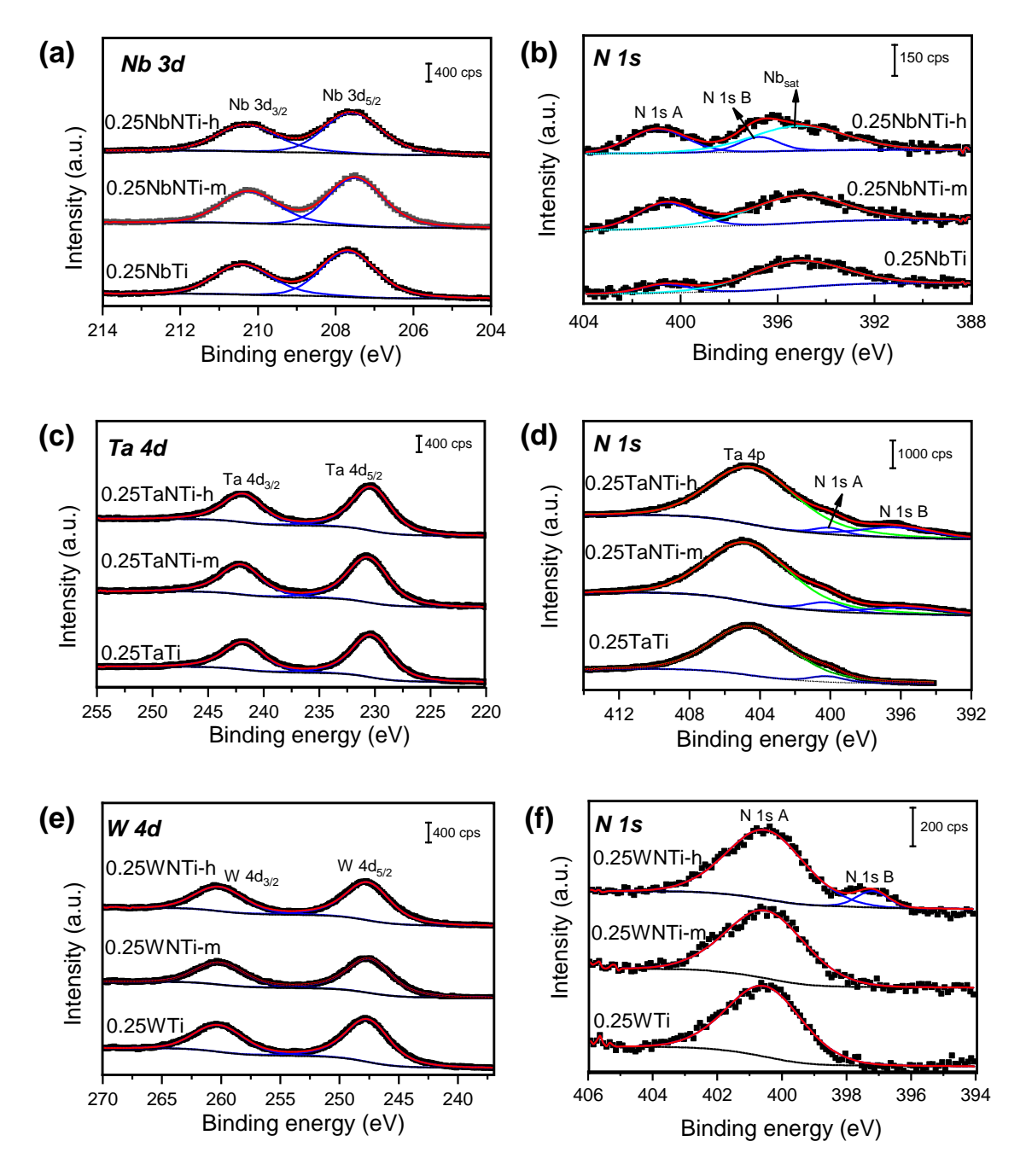


Figure 3.17: XPS spectra of Nb 3d (a) and N 1s (b) for the Nb-doped and (Nb,N) co-doped samples. XPS spectra of Ta 4d (c) and N 1s (d) for the Ta-doped and (Ta,N) co-doped samples. XPS spectra of W 4d (e) and N 1s (f) for the W-doped and (W,N) co-doped samples. (Red lines are the fitted signals, blue, green, cyan lines are the different contributions).

**Figure 3.17 a, 3.17 c** and **3.17 e** presents the spectral region of Nb 3d, Ta 4d, and W 4d for the (M,N) co-doped samples of 0.25NbNTi, 0.25TaNTi and 0.25WNTi, respectively. It is shown that all the (M,N) co-doped TiO<sub>2</sub> present the same characteristic peaks as their respective M-doped samples. The observed doublet is attributed to Nb<sup>5+</sup>, Ta<sup>5+</sup> and W<sup>6+</sup>, respectively. This suggests the stability of the cation during the nitridation. **Figure S3.9 and S3.10, Page 197,** show the Ti 2p region of the (Ta,N) and (W,N) co-doped TiO<sub>2</sub> (For the (Nb,N) co-doped samples, please see Chapter 2, **Figure 2.11 b**). It is observed that a small

contribution of Ti<sup>3+</sup> appears on the (Ta,N) co-doped samples, the ratio of Ti<sup>3+</sup> to total Ti increases with nitridation condition (1.3% for 0.25TaNTi-m, 3.3% for 0.25TaNTi-h). This confirms again a similar behavior for the (Nb,N) and (Ta,N) co-doped samples. For all the M-doped and (M,N) co-doped TiO<sub>2</sub>, the atomic ratio M/Ti is higher than the theoretical value (0.25), indicating a possible surface enrichment of cation.

**Figure 3.17 b, 3.17 d** and **3.17 f** present the spectral region of N 1s for the 0.25NbNTi, 0.25TaNTi and 0.25WNTi samples, respectively. The broad peaks that appear in **Figure 3.17 b** (395.2± 0.1 eV) and **Figure 3.17 d** (404.8± 0.1 eV) are attributed to the Nb 3p satellite peak and Ta 4p<sub>3/2</sub>, respectively. It is shown that the nitrogen species in a specific co-doped sample is determined by the type of cation as well as the associated thermal condition of nitridation. The co-doped samples under mild nitridation (0.25NbNTi-m, 0.25TaNTi-m and 0.25WNTi-m) present an increase of peak N 1s A with a binding energy of 400.5± 0.3 eV, indicating the presence of surface nitrogen or in interstitial sites. <sup>30,31</sup> However, an additional contribution of N 1s B, located at 395.6 eV, is also observed on 0.25TaNTi-m, indicating the appearance of substitutional nitrogen in this sample. <sup>43</sup> This may be ascribed to the higher thermal nitridation temperature for 0.25TaNTi-m (450°C) compared to 0.25NbNTi-m (350°C) and 0.25WNTi-m (250°C).

Sample	N %	Nb %	Ta %	W %	Ti %	N/M	M/Ti
0.25NbTi	0.2	6.4			18.8	0.03	0.34
0.25NbNTi-m	0.8	6.7			19.1	0.12	0.35
0.25NbNTi-h	1.3	6.6			18.5	0.18	0.36
0.25TaTi	0.5		7.1		16.1	0.07	0.44
0.25TaNTi-m	3.6		7.4		17.0	0.49	0.44
0.25TaNTi-h	3.9		6.7		15.8	0.58	0.43
0.25WTi	0.9			6.1	18.8	0.15	0.32
0.25WNTi-m	1.6			6.1	18.1	0.26	0.34
0.25WNTi-h	1.9			6.2	18.9	0.31	0.33

**Table 3.7:** Surface atomic concentrations of the M-doped and (M,N) co-doped samples.

For the (M,N) co-doped samples under harsh nitridation (0.25NbNTi-h, 0.25TaNTi-h and 0.25WNTi-h), both characteristic peaks of N 1s A and N 1s B are observed, further confirming that formation of substitutional nitrogen requires a higher thermal energy input. In addition, the binding energy of the N 1s B peak for 0.25WNTi-h (397.2 eV) is observed to be higher than that for 0.25NbNTi-h (396.8 eV) and 0.25TaNTi-h (395.9± 0.3 eV), which may be attributed to the stronger electronegativity of W than that of Nb and Ta.<sup>44</sup> Additionally, when comparing the spectrum of 0.25TaNTi-m and 0.25TaNTi-h, it is interesting to notice a decrease of N 1s A, while the N 1s B increases. This may suggest a transformation from interstitial nitrogen to substitutional nitrogen promoted by the harsh nitridation treatment.

Based on the information presented in **Table 3.7**, an increase in the N/M ratio is observed on all the (M,N) co-doped samples compared to the respective M-doped TiO<sub>2</sub>, indicating a successful N-doping through the thermal nitridation process. It should be noted

that the amount of N before nitridation is different for the different cations. It might be explained by a different surface chemistry brought by the different cations. By comparing, the (Nb,N) co-doped and (W,N) co-doped samples, the amount of N and the N/M ratio in the case of W as expected by the +VI charge of tungsten but this ratio remain far below the theoretical ones (1 for (Nb,N); 2 for (W,N)). However, a more significant increase in N amount is observed on the (Ta,N) co-doped samples (3.1% and 3.4% after the mild and harsh nitridation), which is unexpected. Since the (Ta,N) co-doped samples show lower absorption compared to the (Nb,N) and (W,N) co-doped TiO<sub>2</sub>, the total amount of N is expected to be lower. This is very likely due to the interference of the Ta 4p peak (**Figure 3.17 d**) in the data fitting, resulting in an overestimated N amount.

In summary, the XPS results have confirmed a successful nitrogen insertion for the (M.N) co-doped TiO<sub>2</sub> through the thermal nitridation process. The cations were kept at their highest oxidation states. A slight contribution of Ti<sup>3+</sup> was found on the (Nb,N) and (Ta,N) co-doped samples but not on the (W,N) co-doped samples. No new types of defects were detected by XPS. Thus, to correlate the different absorption behaviors and the possible defects in different samples, EPR analysis is supplemented in the following part.

### 3.3.5 Defects identification in the (M,N) co-doped TiO<sub>2</sub> samples

Figure 3.18 presents the EPR spectra of all the 0.25 M/Ti samples before and after nitridation (mild and harsh). Figure 3.18 a represents the signal normalized by the mass of the sample for semi-quantitative comparison and Figure 3.18 b is the high-resolution spectra with peak-to-peak normalization. First of all, a similarity of the spectral features between the Nb-containing and Ta-containing samples can be noticed on the large spectra in Figure 3.18 a. Both 0.25NbNTi-m and 0.25TaNTi-m keep a low overall intensity of the signals as 0.25NbTi and 0.25TaTi and TiO<sub>2</sub>. This suggests that the mild nitridation has little effect on the overall amount of paramagnetic defects in the samples and even reduces it slightly. The overall intensity of the EPR signal of (Nb,N) co-doped samples remains lower than that for (Ta,N) co-doped samples. For harsh conditions, a strong increase of the signal is observed for (Nb,N) and (Ta,N) co-doped TiO<sub>2</sub> as discussed later on high-resolution spectra, this is a composite signal that is composed of the signal of Vo<sup>+</sup> and a broad contribution attributed to a variety of Ti<sup>3+</sup> states.

Different spectral features appearing depending on the nitridation conditions are observed on W,N co-doped samples (**Figure 3.18 a**). Compared to 0.25WTi, the EPR signal almost completely disappears for 0.25WNTi-m. For harsh conditions, the EPR signal increases but to a lower extent when compared to (Nb,N) and (Ta,N) TiO<sub>2</sub>, and the broad signal of Ti<sup>3+</sup> is not observed in this case. The signal assigned to W<sup>5+</sup> (indicated by +) is observed on 0.25WNTi and 0.25WNTi-h, but not on 0.25WNTi-m.<sup>39,40</sup> Considering that the former two samples exhibit more intensive absorption peaks at 1300 nm on their UV-visible-IR spectra (as discussed in **3.3.3.3**), we can now more confidently relate these intermediate energy states to W<sup>5+</sup>.

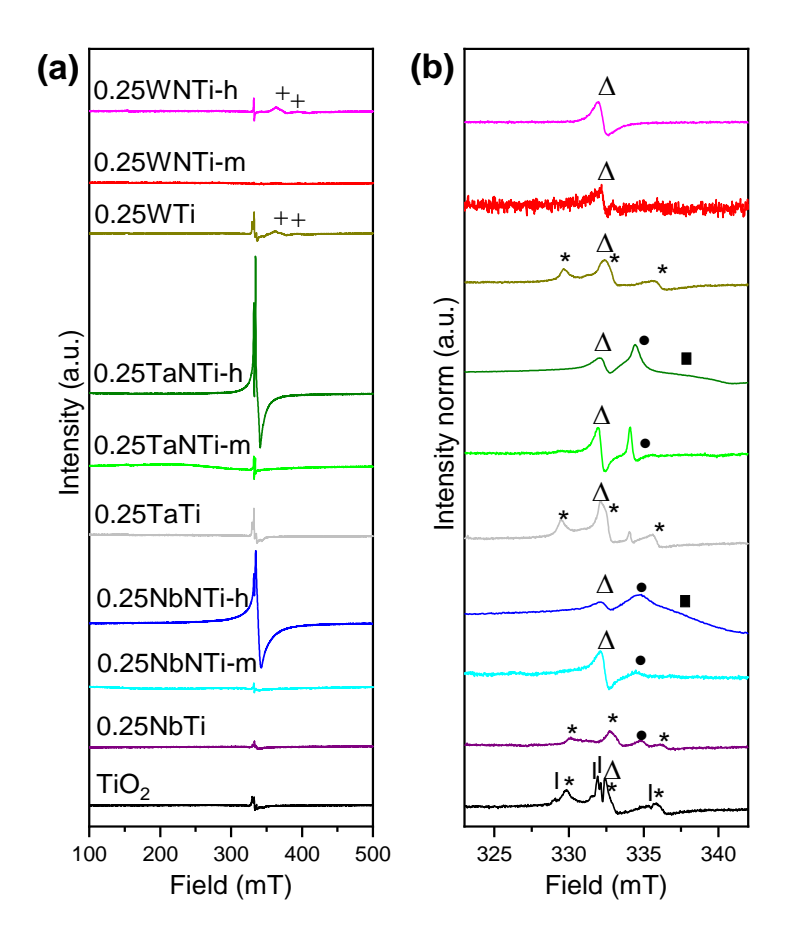


**Figure 3.18:** EPR for TiO<sub>2</sub>, M-doped TiO<sub>2</sub>, and (M,N) co-doped TiO<sub>2</sub>: (a) large range spectra normalized by the mass of the sample, (b) high-resolution spectra with peak-to-peak normalization.

The high-resolution spectra (**Figure 3.18 b**) show the effect of nitridation on defect evolution for different (M,N) co-doped  $TiO_2$ . As discussed in **3.1.6**, the signals observed for M-doped samples mainly originate from NO species (indicated by \*). This signal is higher for 0.25WTi in coherence with the XPS results. Besides, a reduction of the signal intensity of  $V_0^+$  (indicated by  $\Delta$ ) and a slight contribution of  $Ti^{3+}$  ( $\bullet$ ) (for 0.25NbTi) are observed. These defect variations are beneficial to compensate for the additional positive charge brought by the cation-doping.

Among the (M,N) co-doped samples, a similar evolution of defects with the nitridation condition is found for (Nb,N) and (Ta,N) co-doped  $TiO_2$ . In both cases, after the mild nitridation, the signal of  $V_O^+$  is observed to be stronger than that of the Nb and Ta-doped samples, and a slight signal of  $Ti^{3+}$  appears at the g value of 1.985 ( $\bullet$ ). However, it is noted that the overall concentration of the defects remains comparable to their M-doped counterpart, as illustrated on the large range spectra. Under the harsh nitridation, besides the significant increase in the overall signal intensity (as shown in the large spectra), it is observed that the signal of  $Ti^{3+}$  ( $\bullet$ ) is stronger than that of  $V_O^+$ , accompanied by a broad signal corresponding to  $Ti^{3+}$  in different sites appearing for both 0.25NbNTi-h and 0.25TaNTi-h. The results indicate a significant increase in the amount of  $Ti^{3+}$  after the harsh nitridation, which is consistent with the XPS results.

On the other hand, both 0.25WNTi-m and 0.25WNTi-h present the only signal of  $V_{O}^{+}$ , and the signal intensity is lower than their (Nb,N) and (Ta,N) counterpart. This implies a different charge compensation scheme in the case of (W,N) co-doping, in which  $T_{O}^{13}^{+}$  is absent. Although  $W_{O}^{5+}$  is detected, it cannot compensate for the additional positive charge due to the introduction of  $W_{O}^{6+}$  and the generation of  $V_{O}^{+}$ , since the number of N-dopants in the (W,N) co-doped samples is expected to be similar to that of the (Nb,N) co-doped samples (according to M/Ti values determined by XPS). Thus, another mechanism involving unidentified species such as cation vacancies could be involved in the case of (W,N) co-doping.

# 3.4 Conclusion on the (M,N) co-doped samples

The (M,N) co-doped TiO<sub>2</sub> materials were successfully synthesized by conducting a post-thermal nitridation in ammonia atmosphere based on the corresponding M-doped TiO<sub>2</sub> samples. In each (M,N) family, the nitridation condition was adjusted by a trial-error process to become mild and harsh, respectively. As the observation in Chapter 2 in the case of (Nb,N) co-doped samples, the mild and harsh nitridation led to a yellow and dark color, respectively. It is shown that the nitridation process does not change the phase structure of the TiO<sub>2</sub> materials with the pre-presence of the cation (M/Ti-0.25). All the (M,N) co-doped samples crystallized in pure anatase phase, as the respective M-doped sample. Since we have concluded that the cation doping suppresses the phases transition from anatase to rutile (XRD results in **3.1.1** and in-situ XRD results in **3.1.2**) while thermal nitridation promotes the increase of rutile (XRD results in Chapter 2, 3.1), the current results confirm a dominant role of cation in determining the phase structure of the (M,N) co-doped TiO<sub>2</sub>. Compared to the M-doped TiO<sub>2</sub>, modification of the morphology of the (M,N) co-doped samples by the nitridation process is limited. A slight increase in crystallite size (variation < 14.1%) is observed on the (M,N) co-doped samples, leading to a small loss of specific surface area (variation < 19.5%). In summary, by controlling the thermal condition for the air-annealing and nitridation process, all the produced (M,N) co-doped TiO<sub>2</sub> materials have a similar crystal structure and morphology.

The absorption properties of the synthesized (M,N) co-doped TiO<sub>2</sub> were characterized by UV-vis spectroscopy. As the (Nb,N) co-doped samples, two different types of absorption features are also observed on all the (Ta,N) and (W,N) co-doped samples. Mild nitridation resulted in an increase of visible absorption before 550 nm (yellow color), which is ascribed to N-doping. Harsh nitridation resulted in an increased visible absorption intensity with absorption that appeared after 550 nm (dark color), which is mainly attributed to the generation of defect states in the band gap. By comparing the absorption spectra of the (M,N) co-doped samples subjected to the same nitridation condition (350°C 12h), and the thermal energy input required for each (M,N) family to present yellow and dark color, we have concluded that the N-doping is promoted by the cation following the order: W>Nb>Ta. Besides, a positive correlation between the cation concentration and the visible absorption intensity of the co-doped sample was observed. The (Nb,N) and (Ta,N) co-doped samples show similar absorption behavior, with a band gap of ~2.5 eV. However, the (W,N) co-doped TiO<sub>2</sub> present a shorter band gap (2.26 eV for 0.25WNTi-m, 2.1 eV for 0.25WNTi-

h), which may be due to a different distribution of N 2p states or the lower energy of W 5d orbital. Besides, in the infrared region, an absorption that is expected to be related to Ti<sup>3+</sup> is observed on the (Nb,N) and (Ta,N) co-doped samples after harsh nitridation. The W-containing samples present a different signature with a broad absorption peak at 1300 nm, which can correspond to deeper states attributed to W<sup>5+</sup>.

The XPS results confirm a successful nitrogen insertion into the (M.N) co-doped TiO<sub>2</sub> through the nitridation treatment, and the formation of substitutional nitrogen requires a more harsh condition compared to that of interstitial nitrogen. The (W,N) as an increased amount of N compared to (Nb,N) samples. The EPR results confirmed a different behavior for the (W,N) sample: while Ti<sup>3+</sup> was generated under the harsh nitridation for Nb and Tabased samples, which is considered responsible for the absorption after 550 nm, for the (W,N) co-doped samples, the signal of Ti<sup>3+</sup> is absent regardless of the nitridation condition. Therefore, the charge compensation scheme for the (W,N) co-doping may involve Vo<sup>+</sup>,W<sup>5+</sup> and cation vacancies.

# 4. In-situ characterization of UV-visible properties during the thermal treatment.

As demonstrated, earlier in this chapter, the thermal treatment conditions depend on the cation and so far mild and harsh conditions have been determined by the trial-error method. Therefore, we tried to develop an *in-situ* method based on UV-spectroscopy, to monitor the change in the sample spectral properties during the annealing or nitridation processes in order to determine more precisely the critical temperature for nitrogen insertion and Ti<sup>3+</sup> defect generation and also to understand the thermodynamic behind these processes.

# 4.1 Experimental section

# 4.1.1 Apparatus

*In-situ* temperature-dependent spectra were obtained by recording the UV-visible spectra of the sample at different temperatures and under different atmospheres. The measurements were conducted in the 300-800 nm wavelength range using a Perkin Elmer Lambda 950 UV-vis spectrophotometer (**Figure 3.19 a**) equipped with a Diffuse Reflectance Accessory (Harrick, Praying Mantis). The sample is placed in a high-temperature reaction chamber (Harrick, **Figure 3.19 b**). The gas inlet and outlet are located on the top and bottom of the sample respectively, to force the gas to pass through the powder. In our experiment, air, nitrogen or ammonia were sent into the cell with a flow rate of 20 mL.min<sup>-1</sup>, and a vacuum was used to purge between these gases. The temperature control of the heating disc, placed below the chamber, is monitored with a K-type thermocouple.

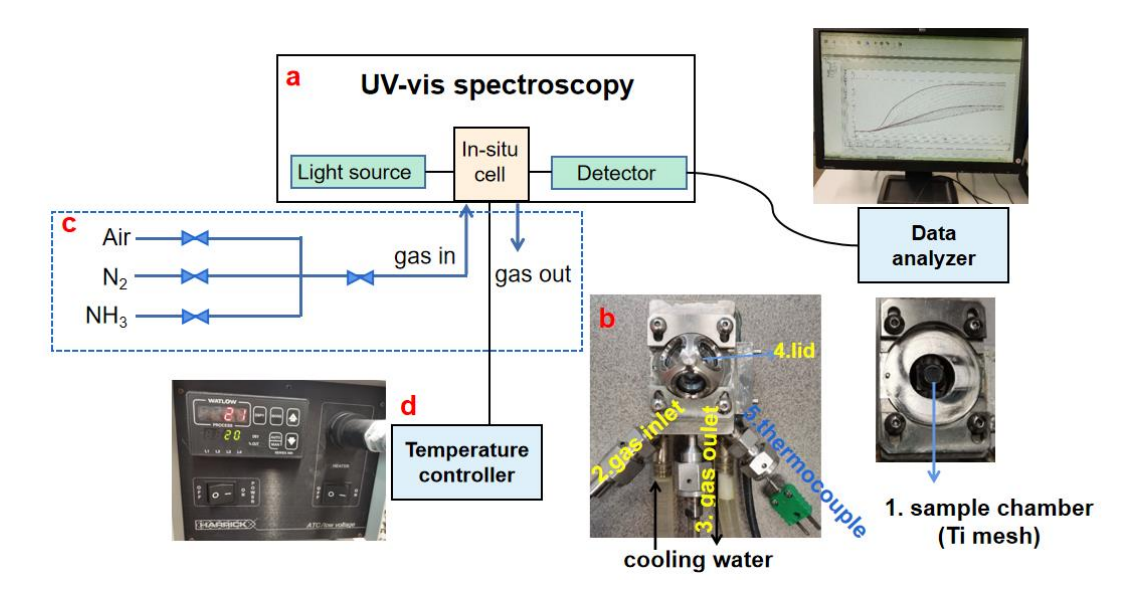


Figure 3.19: Schematic representation of the in-situ chamber and its different components

### 4.1.2 Calibration of temperature

The temperature indicated on the temperature controller was directly measured on the heating element by the thermocouple. However, our mesoporous TiO<sub>2</sub> has a low thermal conductivity, thus the actual temperature of the sample could be lower. Since the exact temperature of the sample surface is essential to determine the optimal thermal condition, it needs to be calibrated.

First, the temperature indicated by the temperature controller was calibrated using two nickel-based alloys with Curie temperatures of 163°C and 353°C, respectively. Below the Curie temperature, the material is ferromagnetic, and above it becomes paramagnetic. The transition between paramagnetic and ferromagnetic states is extremely precise in calibrating the temperature. The alloy was placed in the sample chamber and the temperature was increased to 500°C (set on the temperature controller) to ensure the alloy becomes paramagnetic. After fixing a magnet on the upper surface of the lid (**Figure 3.20 a**), the temperature of the heating disc was decreased with a ramp of 2°C.min<sup>-1</sup>. At the moment when the alloy jumped onto the magnet, the temperature on the controller was recorded for the calibration (190°C and 400°C the blue triangles in **Figure 3.20 c**).

Temperature calibration was also carried out by directly measuring the temperature of the sample powder with another thin K-type thermocouple (**Figure 3.20 b**) whose probe was carefully inserted into the  $TiO_2$  powder surface. Then, several points in the range of  $100^{\circ}$ C to  $600^{\circ}$ C (set on the temperature controller) were checked, and the data directly measured by the thermocouple are shown in **Figure 3.20 c** (black points). Below  $400^{\circ}$ C (set on the controller), the measured temperature follows a linear relationship and the real temperature is  $\approx 12\%$  lower than the one of the controller. While above  $400^{\circ}$ C, the measured temperature deviates slightly below. The temperature discussed in the following parts is the calibrated temperature indicating the surface temperature of the sample.

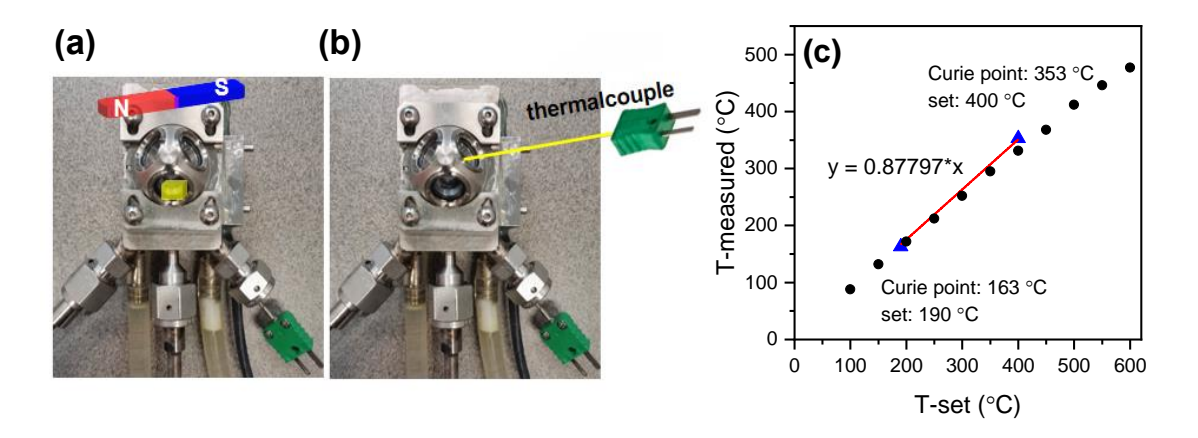


**Figure 3.20 :** Principle of temperature calibration by the Curie point of a magnet (a) and with a second thermocouple (b) and calibration curve (c)

#### 4.1.3 Data treatment

To describe the evolution of *in-situ* diffuse reflectance (DR) spectra with temperature for the different samples, the following values were extracted from the obtained spectra: i)  $R_{\lambda}$ , the reflectance value at a given wavelength  $\lambda$ . This parameter is used to follow the high wavelength absorption associated with the defects that lead to dark color. ii)  $\lambda_R$ , the wavelength corresponding to a given reflectance value of R. This parameter is mainly used to show the shift of the absorption edge with temperature, more or less representative of the bandgap evolution.

### 4.2 Results and discussion

#### 4.2.1 Cleaning pre-treatment

The *in-situ* DR spectra of  $TiO_2$  and M-doped  $TiO_2$  were first measured in air flow (20 mL.min<sup>-1</sup>). The first spectrum was recorded at room temperature (~22°C), then the temperature was increased up to 527°C (600°C on the temperature controller) with a ramp of 10°C.min<sup>-1</sup>. During this heating program, the spectra were recorded each 10min. Then, the heating was stopped and the spectrum was recorded again at room temperature.

**Figure 3.21 a and Figure 3.21 b-d** show the *in-situ* DR spectra of TiO<sub>2</sub> and M-doped TiO<sub>2</sub>. At room temperature, the absorption edge for TiO<sub>2</sub>, 0.25NbTi, 0.25TaTi and 0.25WTi is observed at 394 nm, 389 nm, 390nm, and 406nm, respectively. During the heating process, a red-shift of the absorption edge with the temperature increase is observed for all the samples. This temperature-dependent behavior is a typical semiconductor characteristic, which was also observed on other materials such as Ge, InP, InAs and BaTiO<sub>3</sub>. <sup>46–48</sup> A general explanation for this phenomenon is that the lattice vibration increases with the temperature, leading to larger interatomic spacing in the semiconductor lattice. Besides, the electron mobility increases with temperature, as a consequence the energy required for the electron to cross the bandgap decreased. <sup>49,50</sup>

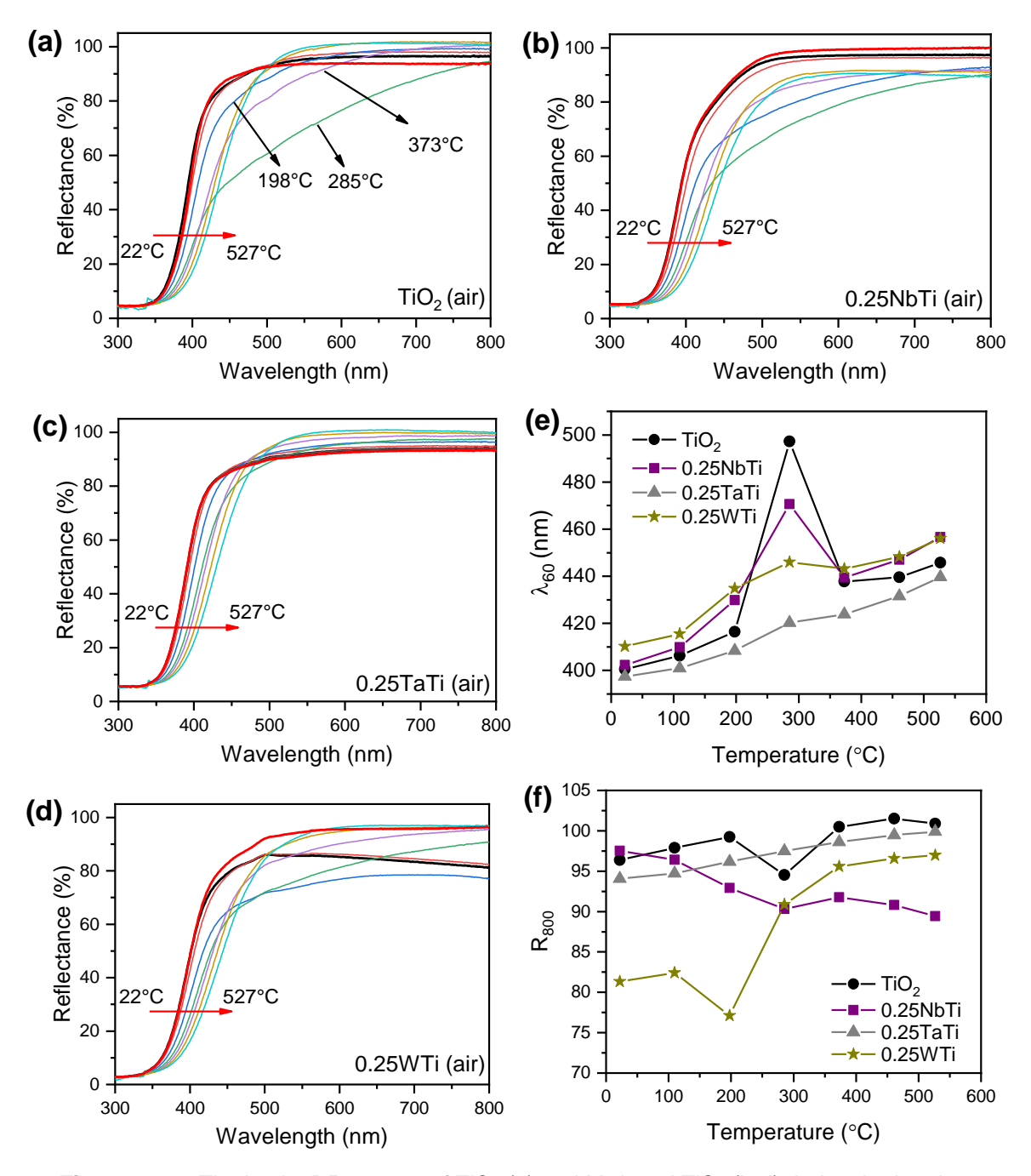


**Figure 3.21 :** The in-situ DR spectra of  $TiO_2$  (a) and M-doped  $TiO_2$  (b-d) during the heating program in air. Extracted values of  $\lambda_{60}$  (e) and  $R_{800}$  (f) as a function of the temperature. (Thick black lines are the spectra recorded at room temperature before heating; thick red lines are the spectra recorded after heating at room temperature)

An unexpected absorption is observed in the temperature range of 198°C to 373°C for all the samples (**Figure 3.21 e and f**), although it is less visible for 0.25TaTi. Considering that the current heating program was conducted under the air flow, we ruled out the possibility of defect generation instead, we suppose that the observed absorption may be due to contamination from the synthesis and/or adsorbed from the air. To verify our hypothesis, the same heating program was performed again for the TiO<sub>2</sub> sample. **Figure 3.22** shows that

the mentioned absorption disappeared, leaving only clear spectra that exhibit the evolution of the band gap with temperature.

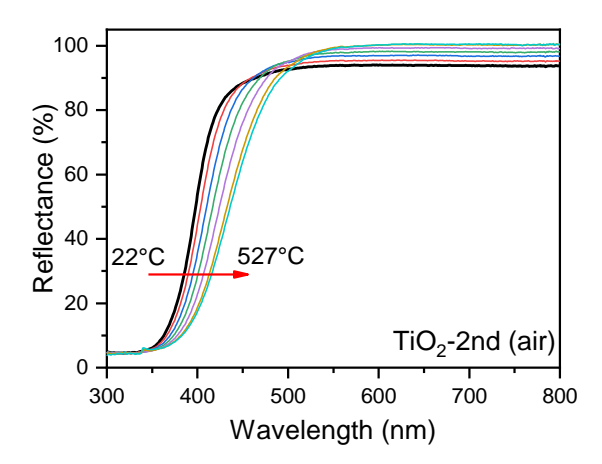


Figure 3.22: The in-situ DR spectra of TiO<sub>2</sub> during the heating program for the second time in air.

The TGA of the same samples indicated that the carbon species were removed in the same temperature range (**Figure S3.1**). The above result confirms that the removal of contamination is responsible for this feature. Therefore, in the following part to highlight the effect of the nitridation process on the resultant DR spectra (detail), an air cleaning pretreatment was performed *in-situ* for all samples before sending ammonia.

### 4.2.2 In-situ observation of nitridation process

### 4.2.2.1 Experimental part

To determine more precisely the thermal nitridation condition facilitating N-doping and the defects generation for TiO<sub>2</sub> and M-doped TiO<sub>2</sub> materials, *in-situ* DR spectroscopy measurements were conducted under ammonia flow (20 mL.min<sup>-1</sup>) and also under N<sub>2</sub> flow (20 mL.min<sup>-1</sup>) as a reference to take into account the shift of the absorption edge with the increasing temperature. The heating program is illustrated in **Figure 3.23** The sample was first heated up to 527°C under air with a ramp of 10°C.min<sup>-1</sup>, (cleaning) cooled down, then the chamber was purged and the DR spectra were recorded every 10 min during the heating process under NH<sub>3</sub> (or N<sub>2</sub>) at 2°C.min<sup>-1</sup>. Then, the spectrum was recorded again when the sample was cooled down to room temperature.

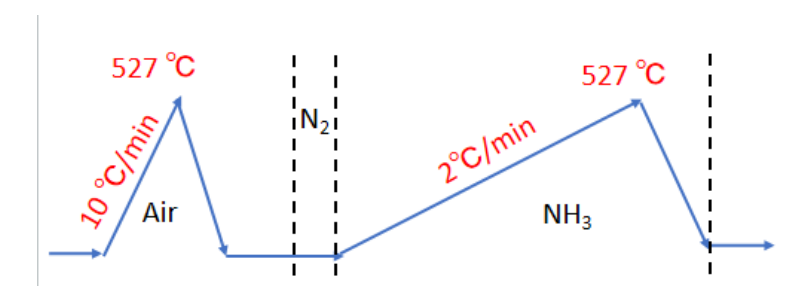
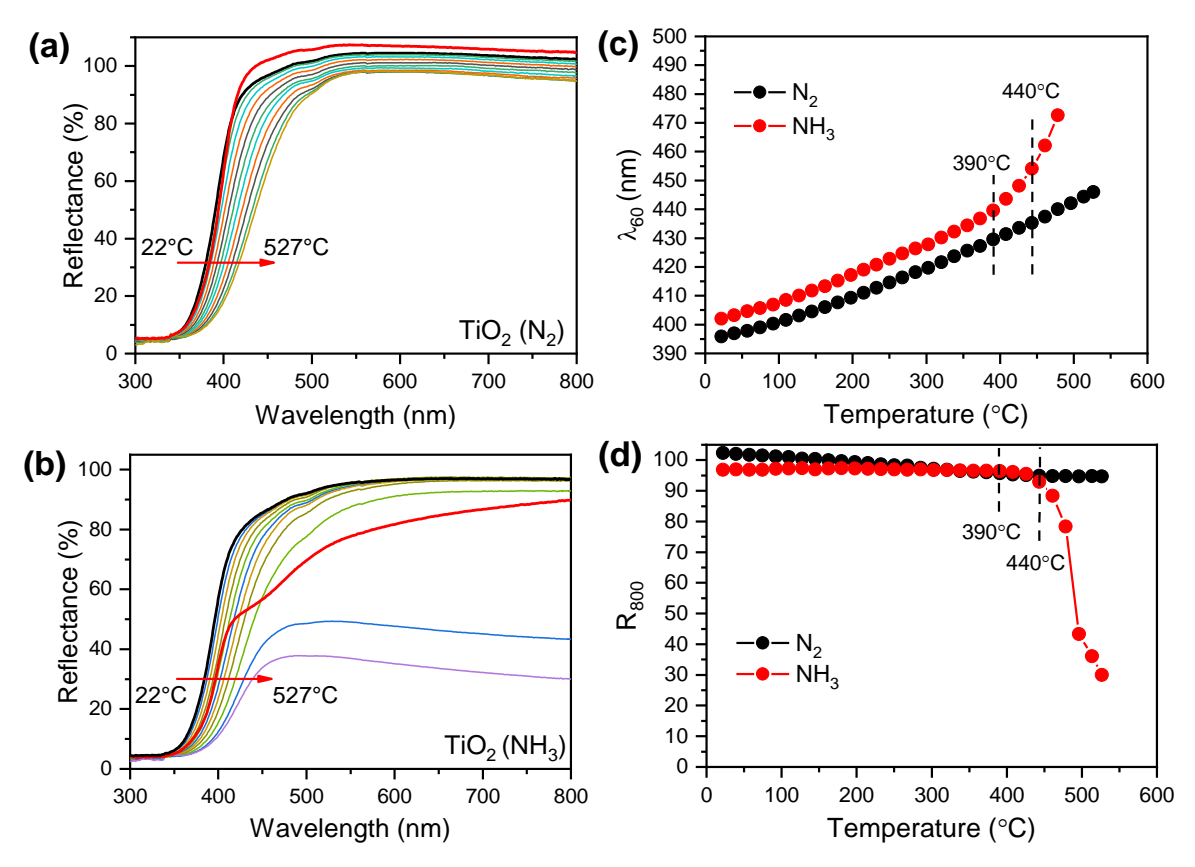


Figure 3.23: Heating program for nitridation process.

To follow the evolution of  $TiO_2$  samples during the heating program,  $\lambda_{60}$  and  $R_{800}$  are used in the following part. An increase of  $\lambda_{60}$  without a significant change of  $R_{800}$  can be an indication of N-doping in the interstitial position (yellow color appearance), while a significant decrease of  $R_{800}$  could indicate the generation of  $V_O^+$  and/or  $Ti^{3+}$ .

### 4.2.2.2 In situ nitridation of TiO<sub>2</sub>

Figure 3.24 a and b present the DR spectra of  $TiO_2$  measured in  $N_2$  and  $NH_3$ , respectively. The values of  $\lambda_{60}$  and  $R_{800}$  extracted from the spectra are presented in Figure 3.24 c and d, respectively. When  $TiO_2$  is heated in  $N_2$ , the absorption edge of the spectra is observed red-shifted with increasing temperature due to the reduction of the band gap during the heating process. As a result,  $\lambda_{60}$  increases almost linearly with temperature. On the other hand, a slight decrease of  $R_{800}$  with increasing temperature is observed, which is mainly due to the change in the height of the sample powder on the Ti mesh.



**Figure 3.24 :** In-situ DR spectra for TiO<sub>2</sub> during heating in N<sub>2</sub> (a) or NH<sub>3</sub> (b) atmosphere. Extracted values of  $\lambda_{60}$  (c) and R<sub>800</sub> (d) as a function of the temperature. (Thick black lines are the spectra recorded at room temperature before heating; thick red lines are the spectra recorded after heating at room temperature)

**Figure 3.24 b** shows the spectra measured during the heating under NH<sub>3</sub>. Before  $390^{\circ}$ C, the red-shift behavior is identical to that in N<sub>2</sub>. This suggests that a temperature lower than  $390^{\circ}$ C is not enough to promote N-doping. Then, above  $390^{\circ}$ C, the red-shift, as indicated by  $\lambda_{60}$  (**Figure 3.24 c**), increases. In addition, no simultaneous decrease of R<sub>800</sub> is observed (**Figure 3.24 d**). We suppose that the observed spectral characteristics could indicate the onset of N-doping. When the temperature is above  $440^{\circ}$ C, a significant decrease of reflectance after 550 nm is noted on the spectra, leading to a fast decrease in R<sub>800</sub>. This spectrum is consistent with the one of NTi-h, suggesting the generation of Ti<sup>3+</sup> defects defining the harsh nitridation conditions for TiO<sub>2</sub>, which is consistent with the harsh and mild synthesis conditions determined previously for TiO<sub>2</sub>.

When the sample is cooled down to room temperature after the nitridation process, the spectrum (thick red line in **Figure 3.24 b**) is similar to that of NTi-m. The appearance of absorption shoulder (~480 nm), indicates the creation of the second band gap after nitridation. This is in agreement with the result in Chapter 2, where the second band gap of NTi-m was determined at 2.47 eV by the Tauc plot. Visually, the sample took a yellow color, which indicates the successful nitrogen doping. It is noteworthy that the absorption after 550 nm disappeared during the cooling process, suggesting that the generated Ti<sup>3+</sup> defects disappeared. This can be due to the short nitridation duration in the *in-situ* chamber compared to the 12h nitridation at 450°C for NTi-h, which probably allows the Ti<sup>3+</sup> to be created only in the surface and that is consequently more prone to reoxidation.

The above results indicate that the nitridation process of TiO<sub>2</sub> was successfully transposed to the *in-situ* cell. By analyzing the evolution of the spectral response with temperature, it is possible to investigate the change of color related to the insertion of nitrogen and the generation of defects during the nitridation process. The technique of *in-situ* UV-visible spectroscopy is useful to determine the proper thermal nitridation condition for the preparation of N-doped TiO<sub>2</sub> with desired light absorption properties.

# 4.2.2.3 In situ nitridation of M-doped TiO<sub>2</sub>

In order to further understand the effect of doping cation nature on the nitridation process. The *in-situ* DR spectra of the M-doped materials were measured using the same heating program as that for TiO<sub>2</sub>. In particular, we expect to determine the temperature onset for mild and harsh conditions for each specific M-doped TiO<sub>2</sub>.

Figure 3.25, shows the temperature-dependent behaviors of the spectra for 0.25NbTi (a and b), 0.25TaTi (c and d) and 0.25WTi (e and f) in  $N_2$  (a,c,e) and  $NH_3$  (b,d,f) atmosphere. The evolution of parameters  $\lambda_{60}$  and  $R_{800}$  are presented in Figure 3.26 as well as the ones of  $TiO_2$ .

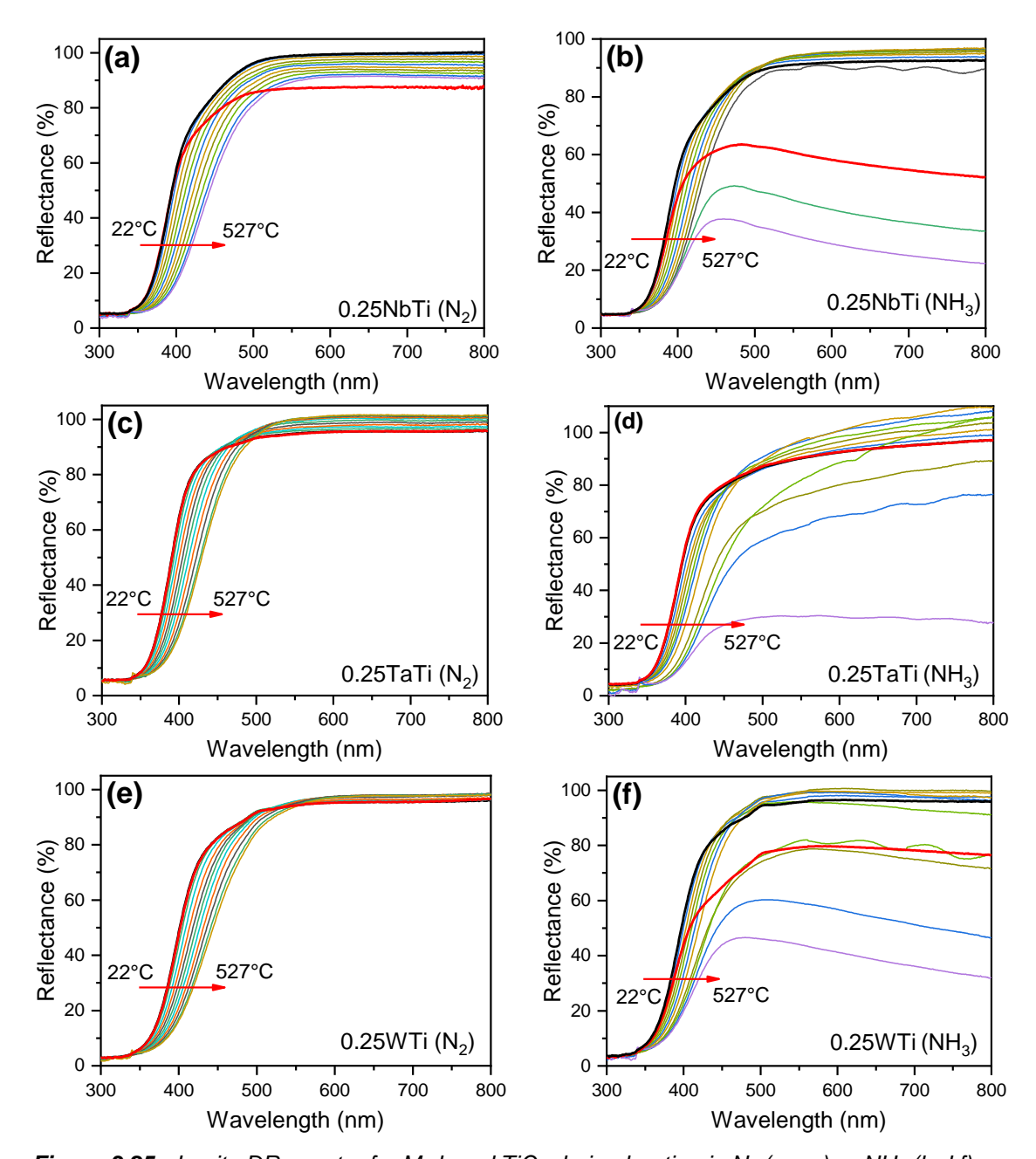


**Figure 3.25**: In-situ DR spectra for M-doped TiO<sub>2</sub> during heating in N<sub>2</sub> (a,c,e) or NH<sub>3</sub> (b,d,f) atmosphere. (Thick black lines are the spectra recorded at room temperature before heating; thick red lines are the spectra recorded after heating at room temperature)

Under  $N_2$ , all samples present a similar evolution with a red shift of the absorption related to the temperature increase. The final spectrum measured at room temperature (thick red line) shows the same absorption edge as the initial one (thick black line). No absorption at long wavelengths is observed for these conditions. When the samples are heated in  $NH_3$ , no additional red-shift of spectra is observed below  $340^{\circ}C$  (as shown by  $\lambda_{60}$  in **Figure 3.26** b), but after this value, the curves change differently for each samples:

For 0.25NbTi no significant increase  $\lambda_{60}$  is observed. But above 410°C the absorption at longer wavelength (represented by  $R_{800}$ ) associated to  $Ti^{3+}$  sites starts to increase. When getting back at room temperature the sample do not show any shoulder

- associated to the yellow color, and takes a grey color, which seems to indicate an unsuccessful N-doping.
- For 0.25TaTi sample, λ<sub>60</sub> increases around 340°C while no decrease of R<sub>800</sub> is observed as in the case of TiO<sub>2</sub>, which is an indication of the N-doping process related to the yellow color. The long wavelength absorption for this sample starts above 460°C. Nevertheless, when getting back to room temperature the sample is white and present the same spectra as before the test.
- For 0.25WTi sample,  $\lambda_{60}$  increases with a simultaneous decrease in  $R_{800}$  around 360°C. Indicating the generation of defects in the structure. When cooled down to room temperature, the sample exhibits a color of light brown when cooled to room temperature, which is close to that of 0.25WNTi-h but less intense and a small shoulder below the band gap can be observed.

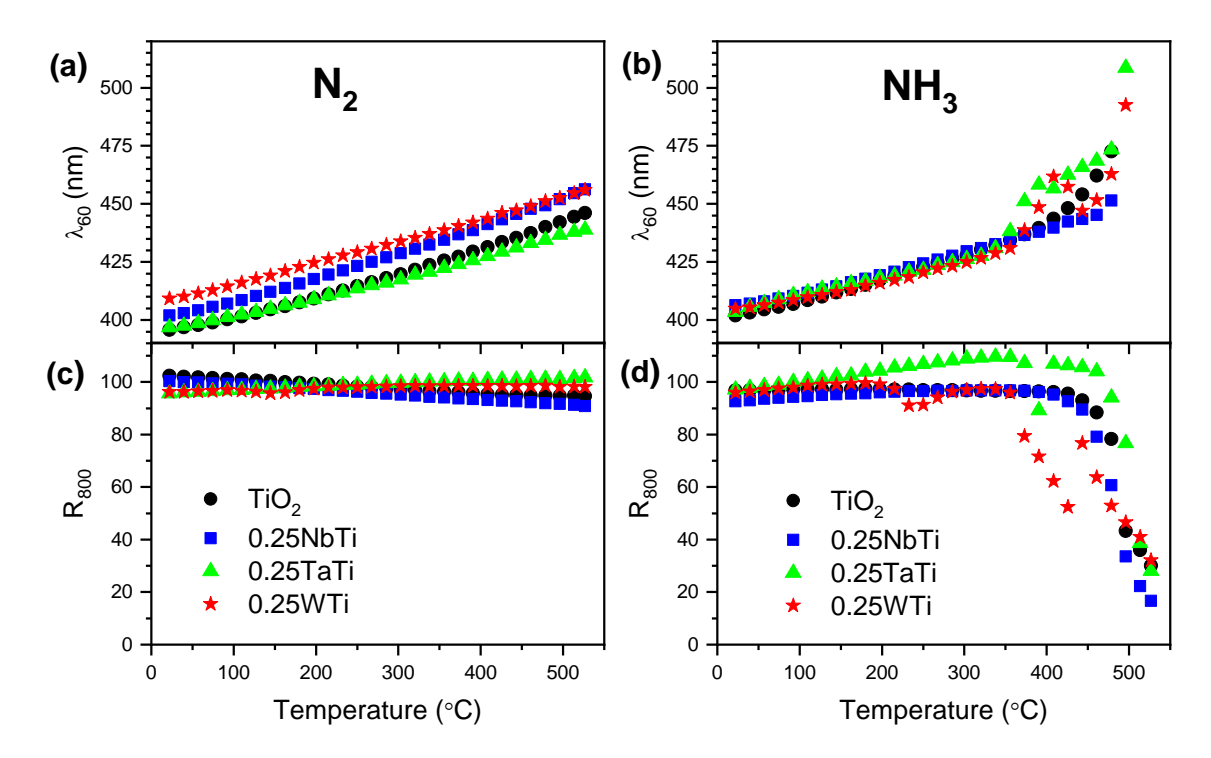


**Figure 3.26**: Values of  $\lambda_{60}$  and  $R_{800}$  extracted from **Figure 3.25** as a function of temperature.(a and c correspond to the spectra recorded in  $N_2$ ; b and d correspond to the spectra recorded in  $NH_3$ )

#### 4.2.2.4 Discussion on the in situ nitridation

The above results indicate that the nitrogen doping conditions are difficult to reproduce inside the *in-situ* chamber for the M-doped TiO<sub>2</sub> samples. The spectral characteristic corresponding to N insertion for mild nitridation is expected to appear at lower temperatures compared to TiO<sub>2</sub> but was not observed while the absorption at longer wavelengths appears on the spectra. It suggests that this second mechanism, related to Ti<sup>3+</sup>/W<sup>5+</sup> defects, is thermodynamically more favorable. The absorption at long wavelength, tracked by R<sub>800</sub>, appears at 360°C for 0.25WTi, 410°C for 0.25NbTi, 440°C for TiO<sub>2</sub> and 460°C for 0.25TaTi. An order that is quite logical when compared to the harsh conditions

defined previously in the chapter for each cation. Nevertheless, this dark color does not remain when getting back to room temperature suggesting only a surface reduction of the samples.

Several observations can explain the difference between nitridation in the in-situ chamber and the oven: In the oven, the mild nitridation duration is longer (12h for the Nbdoped and W-doped samples, 1h for the Ta-doped sample); in the in-situ chamber the duration at each temperature is way shorter and the mechanism behind the yellow color probably involves a slow diffusion step of nitrogen. The NH<sub>3</sub> is supposed to pass through the sample, but when the temperature increases the sample tend to retract and some opening appear between the sample and the side of the sample. This may be a preferential diffusion pass for the gas diffusion and consequently, only the surface of the sample is modified while the light beam penetrates several hundred nanometers in the sample at the analyzed wavelength. Furthermore, ammonia is a corrosive gas that can decompose in H<sub>2</sub> on a reaction that is catalyzed by Fe atoms and the chamber is constituted of stainless steel. At high temperatures, this reaction can favor the reduction of Ti<sup>4+</sup> which would explain the preferential appearance of the absorption at high wavelengths. Finally, we observed some cracks in the in-situ chamber, after several tests, which are probably due to ammonia corrosion. Although the pressure of ammonia flow used in the experiment is more than the atmospheric pressure, we cannot completely exclude the possibility that air could have entered the cell. This might explain the disappearance of the darker color of most of the samples during the cooling.

### 4.2.3 In-situ observation of the oxidation process

Although the nitridation process for the M-doped TiO<sub>2</sub> was not achieved probably due to the damage of *in-situ* cell, experiments under air flow are feasible. Thus, we conducted *in-situ* DR spectra measurements of the N-doped and (M.N) co-doped TiO<sub>2</sub> synthesized by the harsh nitridation under the air flow. The objective is to investigate the reversibility of the defects associated to the dark color during an oxidation process as we observed in Chapter 2 3.7.2 for the ERDT patterns of 0.25NbNTi-h after ozone treatment.

### 4.2.3.1 Experimental part

The heating program used for the measurements goes from room temperature to 527°C with a heating ramp of 2°C.min<sup>-1</sup> under air flow (20 mL.min<sup>-1</sup>) and the spectra were recorded every 10 min during the heating. When the sample was cooled to room temperature, the DR spectrum was measured again.

As observed in the results, the maximum reflectance for (M,N) co-doped  $TiO_2$  in the visible is lower than 60%, so  $\lambda_{20}$  was used to reflect the shift of absorption edge for the obtained spectra.  $R_{800}$  was used to describe the change of absorption after 550 nm, which is related to the evolution of  $Ti^{3+}$  or  $W^{5+}$  defects. It is important to remember that the spectral characteristics during the oxidation process could be influenced by the following factors: (i)

The increase of temperature will cause an overall red-shift of the spectra, leading to an increase of  $\lambda_{20}$ . (ii) The loss of nitrogen will cause a blue-shift of the absorption edge, resulting in a decrease of  $\lambda_{20}$ . (iii) The removal of Ti<sup>3+</sup> will result in a decrease of  $\lambda_{20}$  and an simultaneous increase of  $R_{800}$ .

#### 4.2.3.2 Results and discussion

Figure 3.27 a, b, c, d presents the DR spectra for NTi-h, 0.25NbNTi-h, 0.25TaNTi-h and 0.25WNTi-h measured during the heating program, respectively. The spectrum recorded at room temperature before (thick black line) and after (thick red line) the heating process are highlighted. For comparison purposes, the spectra of NTi-m, 0.25NbNTi-m, 0.25TaNTi-m and 0.25WNTi-m (measured with integrating sphere) are also shown in the figure (thick blue line). The evolution of the value of  $\lambda_{20}$  and  $R_{800}$  for each sample is shown in **Figure 3.27 e and f**, respectively.

When the temperature is below  $162^{\circ}\text{C}$ , a slight linear increase of  $\lambda_{20}$  and  $R_{800}$  is observed for all the samples. Then a notable difference can be observed for the 0.25WNTi-h sample with an increase of  $\lambda_{20}$  and a decrease of  $R_{800}$ . Considering the shape of the spectra, we think this sample contains a significant amount of carbon contamination as observed during our first test (the pre-cleaning procedure cannot be done before these oxidation tests). A rapid increase of  $R_{800}$  with the temperature, indicating the disappearance of the  $Ti^{3+}$  states, is observed for all co-doped samples around  $160\text{-}180^{\circ}\text{C}$ . Furthermore, several changes in the slope are observed and they might correspond to the reoxidation of surface and bulk  $Ti^{3+}$  or  $W^{5+}$ . For the NTi-h,  $R_{800}$  follows a more linear evolution. The  $\lambda_{20}$  indicator increases linearly with the temperature for all samples at the beginning as expected for a semi-conductor and as observed under  $N_2$  atmosphere. Then the  $\lambda_{20}$  started to decrease, indicating probably the removal of the yellow color centers. The temperatures of the inflection point are 110, 210, 240 and 270°C for 0.25WNTi-h, 0.25NbNTi-h, NTi-h, and 0.25TaNTi-h respectively. Again the order follows the general trend that was observed when defining the mild and harsh conditions at the beginning of Chapter 3.

These results indicate that the  $Ti^{3+}/W^{5+}$  centers, inducing the dark colors, can be removed at low temperatures (170°C) and does not depend on the co-doping cation. While the ones associated with the yellow color are more thermodynamically stable and their removal temperature depends on the cation. Indeed, when getting back to room temperature and as observed on the final spectra (bold red lines), NTi and 0.25TaNTi which have the highest inflection point temperature of  $\lambda_{20}$  are still visually yellow while 0.25NbNTi and 0.25WNTi almost get back to white color.

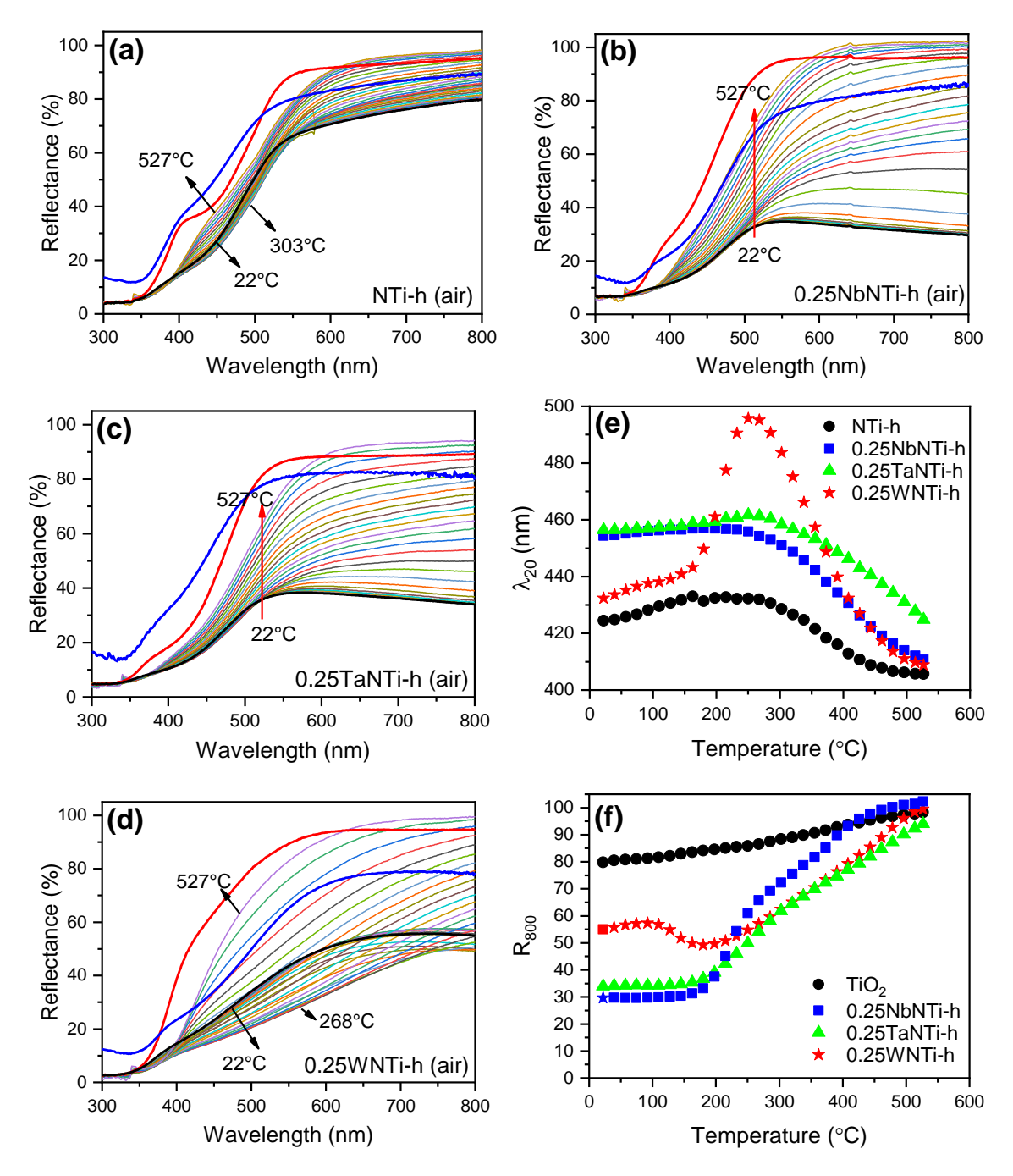


**Figure 3.27:** In-situ DR spectra for the N-doped  $TiO_2$  and the (M,N)-co-doped  $TiO_2$  samples subjected to harsh nitridation during heating in air: (a) for NTi-h, (b) for 0.25NbNTi-h, (c) for 0.25TaNTi-h and (d) for 0.25WNTi-h. (e) and (f) shows the extracted values of  $\lambda_{60}$  and  $R_{800}$  as a function of temperature, respectively. (Thick black lines are the spectra recorded at room temperature before heating; thick red lines are the spectra recorded after heating at room temperature, thick blue lines are the spectra of the N-doped and (M,N) co-doped samples treated by mild nitridation recorded at room temperature)

### 4.3 Conclusion on the in-situ UV-visible.

The *in-situ* chamber for UV visible spectroscopy allowed us to observe the spectral evolution of the sample as a function of the temperature up to 527°C. Unfortunately, for

technical reasons, the direct observation of the nitridation process under concentrated  $NH_3$  was not possible with this chamber, and a new cell must be designed if we aim to do it. Nevertheless, by studying the evolution of the sample as a function of the temperature in different atmospheres, we were able to observe different behavior of the M-doped samples, which confirmed the results presented earlier in Chapter 3. The two doping mechanism processes associated to nitrogen insertion and  $Ti^{3+}/W^{5+}$  appearance were identified. The latter ones appear at higher temperatures and were easily identified. Their appearance depends on the doping cation in the temperature order W < Nb < Ta.

The results of this original approach need to be complemented and other descriptors (derivative, Tauc plot) for the data treatment might provide more information. Nevertheless, we already observed that the appearance of the yellow color centers takes a longer time, probably due to diffusion phenomenon, but they are more stable to oxidation than the Ti<sup>3+</sup> centers. All these information can be useful to optimize the nitridation conditions in the future and go towards a multistep thermal process to favor the yellow color centers.

### 5. Conclusion

In conclusion, in this chapter, we have synthesized the M-doped TiO<sub>2</sub> materials *via* the sol-gel method described in chapter 2, in which a specific cation (Nb, Ta or W) has been successfully introduced into the lattice of TiO<sub>2</sub>. Based on the M-doped materials, the photocatalysts co-doped with cation and nitrogen were prepared by conducting a thermal nitridation in ammonia. Multiple characterization methods were used to understand the structures and properties of the prepared TiO<sub>2</sub> materials, due to the cation-doping and co-doping.

All the M-doped TiO<sub>2</sub> present a uniform spherical morphology similar to that of TiO<sub>2</sub>. It is observed that the particle size of TiO<sub>2</sub> nanoparticles for a specific M-doped sample increases with cation doping concentration, leading to a slight decrease in the BET-specific surface area. The *in-situ* TDXRD analysis showed that all the M-doped TiO<sub>2</sub> present higher anatase to rutile phase transition temperature compared to TiO<sub>2</sub> and this effect is more significant by increasing the doping cation concentration. For the M-doped TiO<sub>2</sub> with the same doping concentration, the values of  $T_{PT}$  follow the order: W>Ta>Nb. On the other hand, the observed phase segregation indicates a limited solubility of cations in the TiO<sub>2</sub> lattice at high temperatures.

The (M,N) co-doped TiO<sub>2</sub> materials were successfully synthesized by conducting a post-thermal nitridation in ammonia atmosphere based on the corresponding M-doped TiO<sub>2</sub> samples. In each (M,N) family, the mild and harsh nitridation conditions were determined by a trial-error process. As the observation in Chapter 2 in the case of (Nb,N) co-doped samples, the mild and harsh nitridation led to a yellow and dark color, respectively. It is shown that the nitridation process does not change the phase structure of the TiO<sub>2</sub> materials with the pre-presence of the cation (M/Ti-0.25). All the (M,N) co-doped samples crystallized in pure anatase phase. Compared to the M-doped TiO<sub>2</sub>, modification of the morphology of the (M,N) co-doped samples by the nitridation process is limited. In summary, by controlling

the thermal condition for the air-annealing and nitridation process, all the (M,N) co-doped TiO<sub>2</sub> materials have a similar crystal structure and morphology. The XPS results confirm a successful nitrogen insertion into the (M.N) co-doped TiO<sub>2</sub> through the nitridation treatment, and the formation of substitutional nitrogen requires a more harsh condition compared to that of interstitial nitrogen. The (W,N) has an increased amount of N compared to the (Nb,N) samples as expect by 6+ charge of W. The EPR results confirmed a different behavior for the (W,N) sample: while Ti<sup>3+</sup> was generated under the harsh nitridation for Nb and Ta-based samples, which is considered responsible for the absorption after 550 nm, for the (W,N) co-doped samples, the signal of Ti<sup>3+</sup> is absent regardless of the nitridation condition. Therefore, the charge compensation scheme for the (W,N) co-doping may involve V<sub>O</sub><sup>+</sup>,W<sup>5+</sup> and cation vacancies.

The absorption properties of the synthesized (M,N) co-doped TiO<sub>2</sub> were characterized by UV-vis spectroscopy. As the (Nb,N) co-doped samples, two different types of absorption features are also observed on all the (Ta,N) and (W,N) co-doped samples. Mild nitridation resulted in an increase of visible absorption before 550 nm (yellow color), which is ascribed to N-doping. Harsh nitridation resulted in an increased visible absorption intensity with absorption that appeared after 550 nm (dark color), which is mainly attributed to the generation of defect states in the band gap. Besides, a positive correlation between the cation concentration and the visible absorption intensity of the co-doped sample was observed. The (Nb,N) and (Ta,N) co-doped samples show similar absorption behavior, with a band gap of ~2.5 eV. However, the (W,N) co-doped TiO<sub>2</sub> presents a shorter band gap (2.26 eV for 0.25WNTi-m, 2.1 eV for WNTi-h), which may be due to a different distribution of N 2p states or the lower energy of W 5d orbital. Besides, in the infrared region, an absorption that is related to Ti<sup>3+</sup> is observed on the (Nb,N) and (Ta,N) co-doped samples after harsh nitridation. The W-containing samples present a different signature with a broad absorption peak at 1300 nm, which can correspond to deeper states attributed to W<sup>5+</sup>. By comparing the absorption spectra of the (M,N) co-doped samples subjected to the same nitridation condition (350°C 12h), but also by developing an original in-situ UV visible approach, we have determined that the N-doping is promoted by the cation following the order: W>Nb>Ta.

In the next chapter, all these samples which have a close morphology and phase structure, will be tested in photocatalytic experiments.

# 6. References

- (1) Lindgren, T.; Lu, J.; Hoel, A.; Granqvist, C.-G.; Torres, G. R.; Lindquist, S.-E. Photoelectrochemical Study of Sputtered Nitrogen-Doped Titanium Dioxide Thin Films in Aqueous Electrolyte. *Solar Energy Materials and Solar Cells* **2004**, *84* (1), 145–157. https://doi.org/10.1016/j.solmat.2004.02.044.
- (2) Pomoni, K.; Vomvas, A.; Trapalis, Chr. Dark Conductivity and Transient Photoconductivity of Nanocrystalline Undoped and N-Doped TiO<sub>2</sub> Sol-Gel Thin Films. *Thin Solid Films* **2008**, *516* (6), 1271–1278. https://doi.org/10.1016/j.tsf.2007.05.040.
- (3) Lindgren, T.; Lu, J.; Hoel, A.; Granqvist, C.-G.; Torres, G. R.; Lindquist, S.-E. Photoelectrochemical Study of Sputtered Nitrogen-Doped Titanium Dioxide Thin Films in Aqueous Electrolyte. Solar Energy Materials and Solar Cells 2004, 84 (1), 145–157. https://doi.org/10.1016/j.solmat.2004.02.044.
- (4) Sun, Q.; Cortie, D.; Zhang, S.; Frankcombe, T. J.; She, G.; Gao, J.; Sheppard, L. R.; Hu, W.; Chen, H.; Zhuo, S.; Chen, D.; Withers, R. L.; McIntyre, G.; Yu, D.; Shi, W.; Liu, Y. The Formation of Defect-Pairs for Highly Efficient Visible-Light Catalysts. *Adv. Mater.* **2017**, *29* (11), 1605123. https://doi.org/10.1002/adma.201605123.
- (5) Nakada, A.; Nishioka, S.; Vequizo, J. J. M.; Muraoka, K.; Kanazawa, T.; Yamakata, A.; Nozawa, S.; Kumagai, H.; Adachi, S.; Ishitani, O.; Maeda, K. Solar-Driven Z-Scheme Water Splitting Using Tantalum/Nitrogen Co-Doped Rutile Titania Nanorod as an Oxygen Evolution Photocatalyst. *J. Mater. Chem. A* **2017**, *5* (23), 11710–11719. https://doi.org/10.1039/C6TA10541F.
- (6) Yin, W.-J.; Tang, H.; Wei, S.-H.; Al-Jassim, M. M.; Turner, J.; Yan, Y. Band Structure Engineering of Semiconductors for Enhanced Photoelectrochemical Water Splitting: The Case of TiO<sub>2</sub>. *Phys. Rev. B* **2010**, *82* (4), 045106. https://doi.org/10.1103/PhysRevB.82.045106.
- (7) Na-Phattalung, S.; Harding, D. J.; Pattanasattayavong, P.; Kim, H.; Lee, J.; Hwang, D.-W.; Chung, T. D.; Yu, J. Band Gap Narrowing of TiO<sub>2</sub> Nanoparticles: A Passivated Co-Doping Approach for Enhanced Photocatalytic Activity. *Journal of Physics and Chemistry of Solids* **2022**, *162*, 110503. https://doi.org/10.1016/j.jpcs.2021.110503.
- (8) Brancho, J. J.; Bartlett, B. M. Challenges in Co-Alloyed Titanium Oxynitrides, a Promising Class of Photochemically Active Materials. *Chemistry of Materials* **2015**, *27* (21), 7207–7217. https://doi.org/10.1021/acs.chemmater.5b02357.
- (9) Nishioka, S.; Kobayashi, M.; Lu, D.; Kakihana, M.; Maeda, K. Selective Synthesis and Photocatalytic Oxygen Evolution Activities of Tantalum/Nitrogen-Codoped Anatase, Brookite and Rutile Titanium Dioxide. *BCSJ* **2019**, *92* (6), 1032–1038. https://doi.org/10.1246/bcsj.20190037.
- (10) Obata, K.; Irie, H.; Hashimoto, K. Enhanced Photocatalytic Activities of Ta, N Co-Doped TiO<sub>2</sub> Thin Films under Visible Light. *Chemical Physics* **2007**, *339* (1–3), 124–132. https://doi.org/10.1016/j.chemphys.2007.07.044.
- (11) Nakada, A.; Uchiyama, T.; Kawakami, N.; Sahara, G.; Nishioka, S.; Kamata, R.; Kumagai, H.; Ishitani, O.; Uchimoto, Y.; Maeda, K. Solar Water Oxidation by a Visible-Light-Responsive Tantalum/Nitrogen-Codoped Rutile Titania Anode for Photoelectrochemical Water Splitting and Carbon Dioxide Fixation. *ChemPhotoChem* **2019**, *3* (1), 37–45. https://doi.org/10.1002/cptc.201800157.
- (12) Thind, S. S.; Wu, G.; Chen, A. Synthesis of Mesoporous Nitrogen–Tungsten Co-Doped TiO<sub>2</sub> Photocatalysts with High Visible Light Activity. *Applied Catalysis B: Environmental* **2012**, *111–112*, 38–45. https://doi.org/10.1016/j.apcatb.2011.09.016.
- (13) Shen, Y.; Xiong, T.; Li, T.; Yang, K. Tungsten and Nitrogen Co-Doped TiO<sub>2</sub> Nano-Powders with Strong Visible Light Response. *Applied Catalysis B: Environmental* **2008**, *83* (3), 177–185. https://doi.org/10.1016/j.apcatb.2008.01.037.

- (14) Ramimoghadam, D.; Bagheri, S.; Abd Hamid, S. B. Biotemplated Synthesis of Anatase Titanium Dioxide Nanoparticles via Lignocellulosic Waste Material. *BioMed Research International* **2014**, *2014*, e205636. https://doi.org/10.1155/2014/205636.
- (15) Muniz, E. C.; Góes, M. S.; Silva, J. J.; Varela, J. A.; Joanni, E.; Parra, R.; Bueno, P. R. Synthesis and Characterization of Mesoporous TiO<sub>2</sub> Nanostructured Films Prepared by a Modified Sol–Gel Method for Application in Dye Solar Cells. *Ceramics International* **2011**, *37* (3), 1017–1024. https://doi.org/10.1016/j.ceramint.2010.11.014.
- (16) Shannon, R. D. Revised Effective Ionic Radii and Systematic Studies of Interatomic Distances in Halides and Chalcogenides. *Acta Cryst A* **1976**, *32* (5), 751–767. https://doi.org/10.1107/S0567739476001551.
- (17) Hanaor, D. A. H.; Sorrell, C. C. Review of the Anatase to Rutile Phase Transformation. *J Mater Sci* **2011**, *46* (4), 855–874. https://doi.org/10.1007/s10853-010-5113-0.
- (18) Arbiol, J.; Cerdà, J.; Dezanneau, G.; Cirera, A.; Peiró, F.; Cornet, A.; Morante, J. R. Effects of Nb Doping on the TiO<sub>2</sub> Anatase-to-Rutile Phase Transition. *Journal of Applied Physics* **2002**, *92* (2), 853–861. https://doi.org/10.1063/1.1487915.
- (19) Zaitsev, S. V.; Moon, J.; Takagi, H.; Awano, M. Preparation and Characterization of Nanocrystalline Doped TiO<sub>2</sub>. *Advanced Powder Technology* **2000**, *11* (2), 211–220. https://doi.org/10.1163/156855200750172321.
- (20) Buttersack, C. Modeling of Type IV and V Sigmoidal Adsorption Isotherms. *Physical Chemistry Chemical Physics* **2019**, *21* (10), 5614–5626. https://doi.org/10.1039/C8CP07751G.
- (21) Cong, Y.; Zhang, J.; Chen, F.; Anpo, M. Synthesis and Characterization of Nitrogen-Doped TiO<sub>2</sub> Nanophotocatalyst with High Visible Light Activity. *J. Phys. Chem. C* **2007**, *111* (19), 6976–6982. https://doi.org/10.1021/jp0685030.
- (22) Kubacka, A.; Colón, G.; Fernández-García, M. Cationic (V, Mo, Nb, W) Doping of TiO<sub>2</sub>—Anatase: A Real Alternative for Visible Light-Driven Photocatalysts. *Catalysis Today* **2009**, *143* (3–4), 286–292. https://doi.org/10.1016/j.cattod.2008.09.028.
- Znad, H.; Ang, M. H.; Tade, M. O. Ta/Ti-and Nb/Ti-Mixed Oxides as Efficient Solar Photocatalysts: Preparation, Characterization, and Photocatalytic Activity. *International Journal of Photoenergy* **2012**, *2012*, 1–9. https://doi.org/10.1155/2012/548158.
- Yue, J.; Suchomski, C.; Voepel, P.; Ellinghaus, R.; Rohnke, M.; Leichtweiss, T.; Elm, M. T.; Smarsly, B. M. Mesoporous Niobium-Doped Titanium Dioxide Films from the Assembly of Crystalline Nanoparticles: Study on the Relationship between the Band Structure, Conductivity and Charge Storage Mechanism. *J. Mater. Chem. A* **2017**, *5* (5), 1978–1988. https://doi.org/10.1039/C6TA06840E.
- (25) Fang, W.; Zhou, Y.; Dong, C.; Xing, M.; Zhang, J. Enhanced Photocatalytic Activities of Vacuum Activated TiO<sub>2</sub> Catalysts with Ti3+ and N Co-Doped. *Catalysis Today* **2016**, *266*, 188–196. https://doi.org/10.1016/j.cattod.2015.07.027.
- (26) Guillemot, F.; Porté, M. C.; Labrugère, C.; Baquey, C. Ti<sup>4+</sup> to Ti<sup>3+</sup> Conversion of TiO<sub>2</sub> Uppermost Layer by Low-Temperature Vacuum Annealing: Interest for Titanium Biomedical Applications. *Journal of Colloid and Interface Science* **2002**, *255* (1), 75–78. https://doi.org/10.1006/jcis.2002.8623.
- (27) Kubacka, A.; Colón, G.; Fernández-García, M. Cationic (V, Mo, Nb, W) Doping of TiO<sub>2</sub>–Anatase: A Real Alternative for Visible Light-Driven Photocatalysts. *Catalysis Today* **2009**, *143* (3), 286–292. https://doi.org/10.1016/j.cattod.2008.09.028.
- (28) Hellwig, M.; Milanov, A.; Barreca, D.; Deborde, J.-L.; Thomas, R.; Winter, M.; Kunze, U.; Fischer, R. A.; Devi, A. Stabilization of Amide-Based Complexes of Niobium and Tantalum Using Malonates as Chelating Ligands: Precursor Chemistry and Thin Film Deposition. Chem. Mater. 2007, 19 (25), 6077–6087. https://doi.org/10.1021/cm0630441.

- (29) Tao, Y.; De Luca, O.; Singh, B.; Kamphuis, A. J.; Chen, J.; Rudolf, P.; Pescarmona, P. P. WO<sub>3</sub>–SiO<sub>2</sub> Nanomaterials Synthesized Using a Novel Template-Free Method in Supercritical CO<sub>2</sub> as Heterogeneous Catalysts for Epoxidation with H<sub>2</sub>O<sub>2</sub>. *Materials Today Chemistry* **2020**, *18*, 100373. https://doi.org/10.1016/j.mtchem.2020.100373.
- (30) Asahi, R.; Morikawa, T.; Ohwaki, T.; Aoki, K.; Taga, Y. Visible-Light Photocatalysis in Nitrogen-Doped Titanium Oxides. *Science* **2001**, *293* (5528), 269–271. https://doi.org/10.1126/science.1061051.
- (31) Zeng, L.; Song, W.; Li, M.; Jie, X.; Zeng, D.; Xie, C. Comparative Study on the Visible Light Driven Photocatalytic Activity between Substitutional Nitrogen Doped and Interstitial Nitrogen Doped TiO<sub>2</sub>. *Applied Catalysis A: General* **2014**, *488*, 239–247. https://doi.org/10.1016/j.apcata.2014.09.041.
- (32) Sen, S. K.; Riga, J.; Verbist, J. 2s and 2p X-Ray Photoelectron Spectra of Ti<sup>4+</sup> Ion in TiO<sub>2</sub>. *Chemical Physics Letters* **1976**, *39* (3), 560–564. https://doi.org/10.1016/0009-2614(76)80329-6.
- (33) Materials | Free Full-Text | Electrochemical Corrosion Behavior of Ta<sub>2</sub>N Nanoceramic Coating in Simulated Body Fluid. https://www.mdpi.com/1996-1944/9/9/772 (accessed 2023-07-16).
- (34) Kong, L.; Wang, C.; Zheng, H.; Zhang, X.; Liu, Y. Defect-Induced Yellow Color in Nb-Doped TiO<sub>2</sub> and Its Impact on Visible-Light Photocatalysis. *J. Phys. Chem. C* **2015**, *119* (29), 16623–16632. https://doi.org/10.1021/acs.jpcc.5b03448.
- (35) Livraghi, S.; Chierotti, M. R.; Giamello, E.; Magnacca, G.; Paganini, M. C.; Cappelletti, G.; Bianchi, C. L. Nitrogen-Doped Titanium Dioxide Active in Photocatalytic Reactions with Visible Light: A Multi-Technique Characterization of Differently Prepared Materials. *J. Phys. Chem. C* **2008**, *112* (44), 17244–17252. https://doi.org/10.1021/jp803806s.
- (36) On the Origin of the Spectral Bands in the Visible Absorption Spectra of Visible-Light-Active TiO<sub>2</sub> Specimens Analysis and Assignments | The Journal of Physical Chemistry C. https://pubs.acs.org/doi/10.1021/jp901034t (accessed 2023-07-16).
- (37) Nakamura, I.; Negishi, N.; Kutsuna, S.; Ihara, T.; Sugihara, S.; Takeuchi, K. Role of Oxygen Vacancy in the Plasma-Treated TiO<sub>2</sub> Photocatalyst with Visible Light Activity for NO Removal. *Journal of Molecular Catalysis A: Chemical* **2000**, *161* (1), 205–212. https://doi.org/10.1016/S1381-1169(00)00362-9.
- (38) Zhang, Z.; Wang, X.; Long, J.; Gu, Q.; Ding, Z.; Fu, X. Nitrogen-Doped Titanium Dioxide Visible Light Photocatalyst: Spectroscopic Identification of Photoactive Centers. *Journal of Catalysis* **2010**, *276* (2), 201–214. https://doi.org/10.1016/j.jcat.2010.07.033.
- (39) Gorman, S.; Rickaby, K.; Lu, L.; Kiely, C. J.; Macphee, D. E.; Folli, A. A Combination of EPR, Microscopy, Electrophoresis and Theory to Elucidate the Chemistry of W- and N-Doped TiO<sub>2</sub> Nanoparticle/Water Interfaces. *Catalysts* **2021**, *11* (11), 1305. https://doi.org/10.3390/catal11111305.
- (40) Folli, A.; Bloh, J. Z.; Armstrong, K.; Richards, E.; Murphy, D. M.; Lu, L.; Kiely, C. J.; Morgan, D. J.; Smith, R. I.; Mclaughlin, A. C.; Macphee, D. E. Improving the Selectivity of Photocatalytic NOx Abatement through Improved  $O_2$  Reduction Pathways Using  $Ti_{0.909}W_{0.091}O_2N_x$  Semiconductor Nanoparticles: From Characterization to Photocatalytic Performance. *ACS Catal.* **2018**, 8 (8), 6927–6938. https://doi.org/10.1021/acscatal.8b00521.
- (41) Zhao, Z.; Goncalves, R. V.; Barman, S. K.; Willard, E. J.; Byle, E.; Perry, R.; Wu, Z.; Huda, M. N.; Moulé, A. J.; Osterloh, F. E. Electronic Structure Basis for Enhanced Overall Water Splitting Photocatalysis with Aluminum Doped SrTiO<sub>3</sub> in Natural Sunlight. *Energy Environ. Sci.* **2019**, *12* (4), 1385–1395. https://doi.org/10.1039/C9EE00310J.
- (42) Wang, Z.; Wen, B.; Hao, Q.; Liu, L.-M.; Zhou, C.; Mao, X.; Lang, X.; Yin, W.-J.; Dai, D.; Selloni, A.; Yang, X. Localized Excitation of Ti<sup>3+</sup> Ions in the Photoabsorption and Photocatalytic Activity of Reduced Rutile TiO<sub>2</sub>. *J. Am. Chem. Soc.* **2015**, *137* (28), 9146–9152. https://doi.org/10.1021/jacs.5b04483.

- (43) Yuan, B.; Wang, Y.; Bian, H.; Shen, T.; Wu, Y.; Chen, Z. Nitrogen Doped TiO<sub>2</sub> Nanotube Arrays with High Photoelectrochemical Activity for Photocatalytic Applications. *Applied Surface Science* **2013**, *280*, 523–529. https://doi.org/10.1016/j.apsusc.2013.05.021.
- (44) Allen, L. C. Electronegativity Is the Average One-Electron Energy of the Valence-Shell Electrons in Ground-State Free Atoms. *J. Am. Chem. Soc.* **1989**, *111* (25), 9003–9014. https://doi.org/10.1021/ja00207a003.
- (45) Encyclopedia of Materials: Science and Technology. ScienceDirect. http://www.sciencedirect.com:5070/referencework/9780080431529/encyclopedia-of-materials-science-and-technology (accessed 2023-08-06).
- (46) Mishra, V.; Warshi, M. K.; Kumar, R.; Sagdeo, P. R. Design and Development of In-Situ Temperature Dependent Diffuse Reflectance Spectroscopy Setup. *J. Inst.* **2018**, *13* (11), T11003. https://doi.org/10.1088/1748-0221/13/11/T11003.
- (47) Progress in Semiconductors. Vol. 4; Heywood: London, 1960.
- (48) Turner, W. J.; Reese, W. E.; Pettit, G. D. Exciton Absorption and Emission in InP. *Phys. Rev.* **1964**, *136* (5A), A1467–A1470. https://doi.org/10.1103/PhysRev.136.A1467.
- (49) Cox, P. A. *The Electronic Structure and Chemistry of Solids*; Oxford science publications; Oxford University Press: Oxford [Oxfordshire], 1987.
- (50) Ünlü, H. A Thermodynamic Model for Determining Pressure and Temperature Effects on the Bandgap Energies and Other Properties of Some Semiconductors. *Solid-State Electronics* **1992**, *35* (9), 1343–1352. https://doi.org/10.1016/0038-1101(92)90170-H.

Chapter- 4 Photocatalytic performance of M-doped TiO<sub>2</sub> and (M,N) co-doped TiO<sub>2</sub> (M=Nb, Ta or W) materials

# Summary

	1 1 1
1. Introduction.	
2. Photocatalytic performance for MB degradation	
2.1 Experimental part	145
2.2 Photocatalytic activities of M-doped materials	145
2.2.1 Effect of cation doping on the adsorption of MB	145
2.2.2 Photocatalytic degradation of MB under UV irradiation	147
2.3 Photocatalytic activities of (M,N) co-doped TiO <sub>2</sub>	147
2.3.1 Effect of co-doping on the adsorption for MB	147
2.3.2 Photocatalytic degradation of MB under UV irradiation	148
2.3.3 Photocatalytic degradation of MB under visible irradiation	150
2.4 Conclusion on photocatalytic MB degradation	151
3. Photocatalytic hydrogen production	152
3.1 Experimental part	152
3.1.1 Photocatalytic test platform	152
3.1.2 Analysis of products on compact GC	153
3.1.3 Data treatment	154
3.2 Photoreduction vs. chemical reduction for Pt co-catalyst deposition	155
3.2.1 Context	155
3.2.2 Experimental method for Pt deposition	155
3.2.3 Characterization of the Pt co-catalyst	156
3.2.4 Photocatalytic activity	158
3.3 Effect of M-doping and N-doping on the photocatalytic activities	160
3.3.1 Characterization of the co-catalyst	160
3.3.2 Photocatalytic activities	162
3.4 Effect of (M,N)-co-doping on the photocatalytic activities	163
3.4.1 Characterization of the co-catalyst	163
3.4.2 Photocatalytic activities	
3.5 Conclusion on photocatalytic hydrogen production	166
4. Photocatalytic performance for water oxidation	167
4.1 Experimental part	
4.2 Characterization of RuO <sub>x</sub> -deposited TiO <sub>2</sub> materials	
4.2.1 Elemental analysis	. 167

4.2.2 TEM characterization	168
4.2.3 XPS analysis	168
4.3 Photocatalytic activities for water oxidation	169
4.4 Conclusion on photocatalytic water oxidation.	170
5. Dual co-catalysts modified TiO <sub>2</sub> material	170
5.1 Context	170
5.2 Experimental part	171
5.2.1 Preparation of dual co-catalyst modified TiO <sub>2</sub>	171
5.2.2 Photocatalytic experiment	171
5.3 Photocatalytic activities of dual co-catalyst deposited TiO <sub>2</sub>	171
6. Conclusion	172
7. References	175

### 1. Introduction

This chapter presents the experimental results related to the photocatalytic performances of the materials synthesized in Chapter 3. First, the photocatalytic activities of the different M-doped and (M.N) co-doped  $TiO_2$  materials for MB degradation were evaluated to clarify the effect of different types of doping or co-doping on the resultant photocatalytic degradation activity. Besides, the influence of the defects ( $Ti^{3+}$ ,  $V_O^+$  and  $W^{5+}$ ,) on the photocatalytic degradation process was also discussed. Then, these materials were applied to the two half-reactions of photocatalytic water splitting: hydrogen and oxygen evolution reaction (HER and OER).

Water splitting is a thermodynamically uphill reaction ( $\Delta G = 237.2 \text{ kJ.mol}^{-1}$  at 25°C), requiring the transfer of multiple electrons, making it one of the most challenging reactions in chemistry. Even for the half-reactions, the use of cocatalysts and sacrificial agents is generally necessary. The function of the co-catalyst can be summarized as follows: (i) promoting charge separation and transfer by trapping photogenerated electrons or holes. (ii) serving as active sites and catalyzing a specific type of reaction. Previous studies have confirmed the effectiveness of platinum (Pt) and ruthenium oxide (RuO<sub>x</sub>) as benchmark cocatalysts in photocatalytic HER and OER, respectively. Thus, these two co-catalysts were utilized in this study.

Sacrificial agents can be categorized as sacrificial electron donors and sacrificial electron acceptors, which are used to scavenge photogenerated holes and electrons, respectively. Thermodynamically, oxidation (reduction) of the sacrificial electron donor (acceptor) is more favorable than water oxidation (reduction). In our study, methanol and NaIO<sub>3</sub> were used as the sacrificial agent in photocatalytic hydrogen production (eq. 4.1 to eq. 4.3)<sup>3</sup> and water oxidation reaction (eq 4.4 to eq. 4.6)<sup>4</sup>, respectively.

$$2H^+ + 2e^- \rightarrow H_2$$
 (HER: 0 V vs NHE) (eq. 4.1)

$$2CH_3OH + 2h^+ \rightarrow 2CH_3O^{\bullet} + 2H^+$$
 (h<sup>+</sup> scavenging: 0.48 V vs NHE) (eq. 4.2)

$$2CH_3OH \rightarrow 2CH_3O^{\bullet} + H_2$$
 ( $\Delta E: +0.48 \text{ V}$ ) (eq. 4.3)

$$2IO_3^- + 12H^+ + 12e^- \rightarrow 2I^- + 6H_2O$$
 (e<sup>-</sup> scavenging: 1.087 V vs NHE) (eq. 4.4)

$$6H_2O + 12h^+ \rightarrow 12H^+ + 3O_2$$
 (OER: 1.23 V vs NHE) (eq. 4.5)

$$2IO_3^- \rightarrow 2I^- + 3O_2$$
 ( $\Delta E: +0.143 \text{ V}$ ) (eq. 4.6)

# 2. Photocatalytic performance for MB degradation

# 2.1 Experimental part

The photocatalytic activity of the synthesized samples was evaluated by conducting the photocatalytic degradation of MB in aqueous solutions. Before the illumination, the photocatalyst and the MB solution were kept under stirring in the dark to ensure the absorption–desorption equilibrium. The experiments were carried out on the same set-up as illustrated in **Chapter 2, 4.1**, in which the evolution of the concentration of MB was monitored from the UV-Vis spectra measured by an immersion probe.

However, certain samples exhibit an increased MB adsorption in the dark, making the comparison between the different samples more difficult (detailed later). To avoid the complete absorption of MB molecules before turning on the illumination, the initial concentration of the MB solution used for the experiment was increased to 30.8 μmol.L<sup>-1</sup>, which is almost twice that of the value in Chapter 2 and only 20 mg of photocatalyst was used (-33%). The photocatalyst powder and 10 mL of MB solution (400 μmol.L<sup>-1</sup>) were added into 120 mL distilled water as the original solution. The measurements for the M-doped samples were performed only under UV illumination (365 nm, 25 mW.cm<sup>-1</sup>), while for the co-doped samples, the measurements under visible light illumination (450 nm, 46 mW.cm<sup>-1</sup>) were also conducted.

# 2.2 Photocatalytic activities of M-doped materials

### 2.2.1 Effect of cation doping on the adsorption of MB

# 2.2.1.1 Dark equilibrium adsorption curves

The adsorption of pollutants on the catalyst surface plays an important role in the photocatalytic activity. Within a certain range, an increase in adsorption for pollutants could promote photocatalytic degradation,<sup>5</sup> since the photogenerated active radicals could be able to react with pollutants in a more timely manner. However, excessive adsorption for pollutants may instead slow down the photocatalytic degradation reaction rate. In this case, the adsorbed pollutant may cover the surface of the catalyst, obstructing the contact of oxygen and water molecules with the catalyst surface and consequently suppressing the generation of active radicals, resulting in a reduction of photocatalytic activity.

**Figure 4.1 a** represents the adsorption-desorption equilibrium in the dark for the M-doped samples. For TiO<sub>2</sub>, the adsorption-desorption equilibrium was established within 10 mins, with a decrease of MB concentration of 34.7% due to the adsorption. For all the M-doped samples, the adsorption of MB was observed to took a longer time to reach adsorption-desorption equilibrium (> 60 min). In particular, 0.25WTi shows higher adsorption capacity than 0.25NbTi and 0.25TaTi, resulting in a decrease of the MB concentration by 85.3%. This indicates that the surface charge of the photocatalyst could be influenced by the doping of the cation.

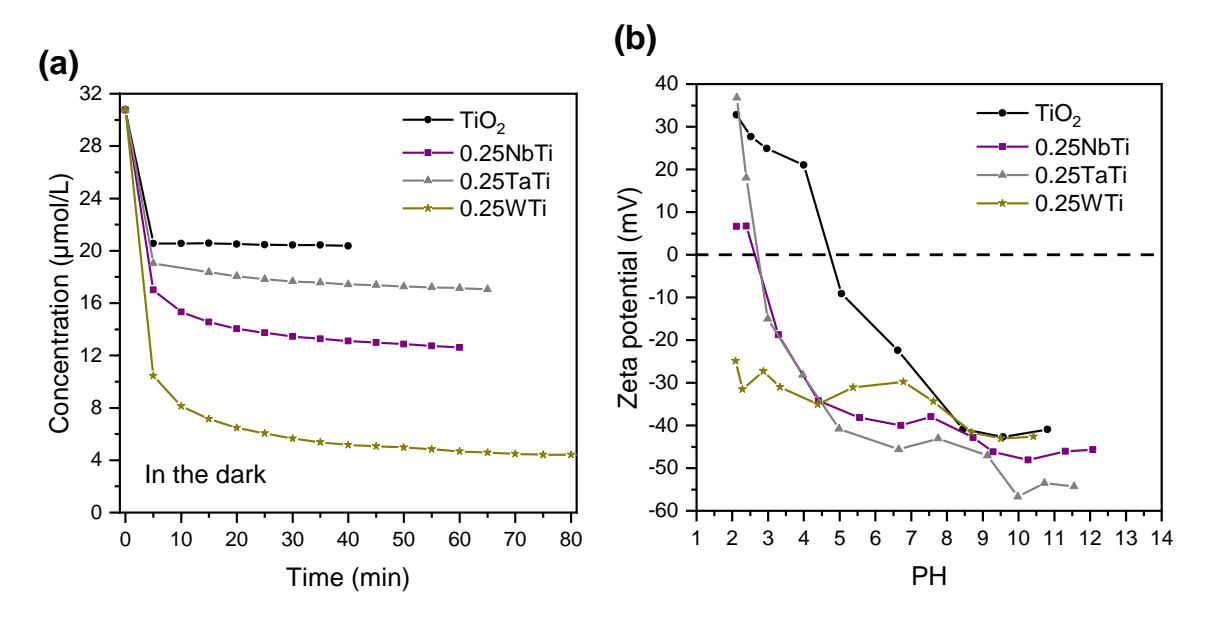


**Figure 4.1:** (a) Dark equilibrium adsorption curves of MB for TiO<sub>2</sub> and the M-doped samples. (b) Zeta potential of TiO<sub>2</sub> and the M-doped samples as a function of pH.

### 2.2.1.2 Zeta potential measurement

To evaluate the differences in surface charge between TiO<sub>2</sub> and the M-doped TiO<sub>2</sub>, the Zeta potential of the prepared materials was characterized. The measurements were carried out using a Zetasizer Nano ZS (Malvern Instruments Ltd. UK) with a laser Doppler electrophoresis technique. The sample container was connected through a capillary system, and with a peristaltic pump to a folded capillary cell (DTS 1060). The zeta potential was obtained from the electrophoretic mobility of the suspension due to the polar nature of the solvent. The suspension was prepared by dispersing 20 mg powder sample into 30 mL of distilled water. Each sample was measured three times at 30°C for each pH value, and the result was determined by the average value of the three tests. The pH titration was programmed from pH 12.3 to pH 2.04. To adjust the pH of the prepared suspension, sodium hydroxide (0.01 mol. L<sup>-1</sup> and 0.1 mol.L<sup>-1</sup>) and hydrochloric acid (0.01 mol L<sup>-1</sup> and 0.1 mol L<sup>-1</sup>) were used. The isoelectric point is the pH value where the zeta potential is zero.

The zeta potential curves for the M-doped samples are plotted in **Figure 4.1 b.** The degradation experiments were conducted without adding any acid or base, leading to a pH of the solution at ~5.9. At this pH, the zeta potential of the M-doped samples is more negative than that of TiO<sub>2</sub>, indicating more negative charge on the surface of the M-doped samples. The isoelectric points of TiO<sub>2</sub>, 0.25NbTi and 0.25TaTi are measured at pH 4.74, 2.59 and 2.79, respectively. For 0.25WTi, the isoelectric point is at a lower pH, out of the range of the apparatus. This suggests that W-doping results in a more negatively charged surface compared to Nb and Ta-doping. Considering that MB is a cationic dye,<sup>6</sup> which is preferentially adsorbed by the negatively charged surface, the result is in good accord with the MB adsorption behavior of the different samples shown in **Figure 4.1a.** 

### 2.2.2 Photocatalytic degradation of MB under UV irradiation

The photocatalytic degradation profiles and corresponding kinetics for the M-doped samples are presented in **Figure 4.2**. The kinetic constant k for the degradation was calculated as shown in Chapter 2, **4.2.2**. Under UV light irradiation, all samples should absorb a significant part of the photons at 365 nm. In this case, on the one hand, the photocatalytic activity should be determined by the efficiency of separation and transfer of the photogenerated charge carriers. On the other hand, the difference in MB adsorption could also affect the kinetic of photocatalytic degradation progress.

Under the current experimental condition,  $TiO_2$  was able to degrade about ~79% of the MB within 5h, with a kinetic constant k = 0.2814. On the opposite, a certain decrease of the activity is observed for all the M-doped samples, with k for 0.25NbTi, 0.25TaTi and 0.25WTi at 0.1872, 0.1008 and 0.1980, respectively. Considering that in Chapter 2, **4.2.2**, 0.25NbTi is more active for MB degradation compared to  $TiO_2$  under UV illumination, we suppose that the deterioration of photocatalytic activity observed on the M-doped samples could be mainly ascribed to the excessive adsorption of MB in these conditions. As mentioned, the coverage of the catalyst surface by MB molecules could inhibit the generation of active radicals. Based on the characterization in Chapter 3, the M-doped samples have a larger crystallite size and smaller surface area in comparison with  $TiO_2$ , this could also be a reason for their decreased photocatalytic activities.

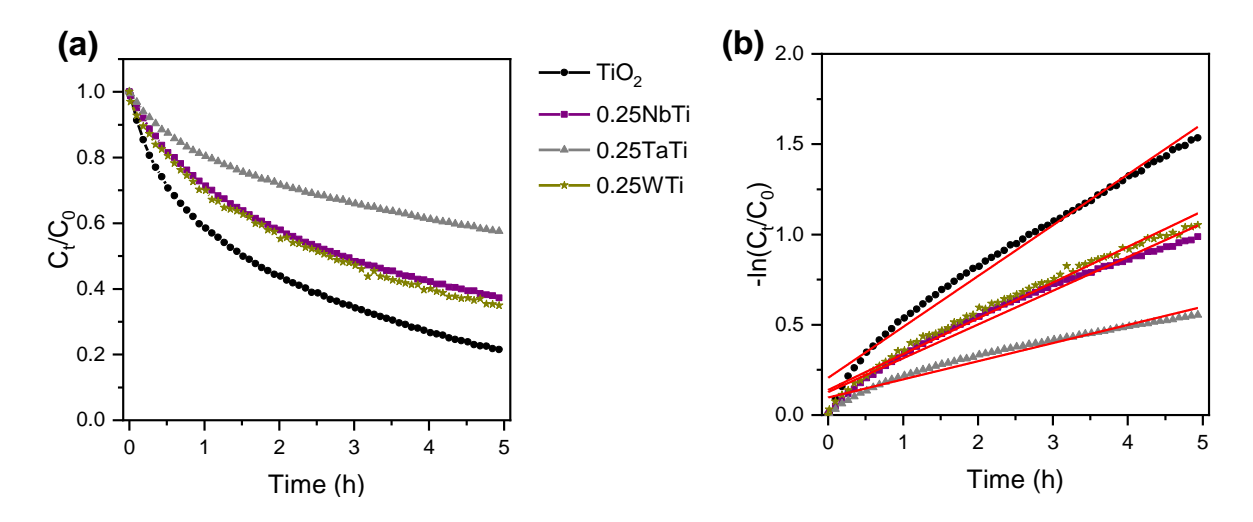


**Figure 4.2**: MB degradation profiles (a) and kinetics (b) for TiO<sub>2</sub> and the M-doped samples under the irradiation using UV LED (365 nm)

# 2.3 Photocatalytic activities of (M,N) co-doped TiO<sub>2</sub>

### 2.3.1 Effect of co-doping on the adsorption for MB

**Figure 4.3** presents the adsorption process of MB for the co-doped samples. Compared to the Nb-doped and Ta-doped samples, the adsorption of MB for the (Nb,N) co-

doped and (Ta,N) co-doped samples is observed to increase with the nitridation condition. Relatively, the increase is more obvious on the (Nb,N) co-doped samples, where the MB adsorption for 0.25NbNTi-m and 0.25NbNTi-h was increased by 26.4% and 40.1%, respectively, compared to 0.25NbTi. On the contrary, a slight decrease in the adsorption capacity is observed for the (W,N) co-doped samples, compared to the W-doped sample. The results indicate that the nitridation process could further modify the surface charge of the co-doped samples, and thus contribute to the different adsorption behavior. Nevertheless, the MB adsorption capacity of the different (M,N) co-doped samples follows the same order as that of the M-doped TiO<sub>2</sub>, that is, W>Nb>Ta.

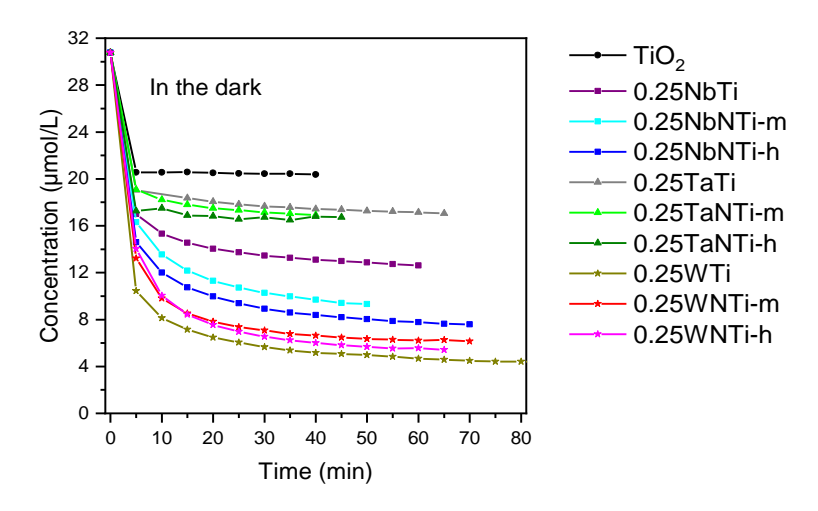


**Figure 4.3 :** Dark equilibrium adsorption curves of MB for TiO<sub>2</sub>, M-doped and (M,N) co-doped TiO<sub>2</sub> photocatalysts.

### 2.3.2 Photocatalytic degradation of MB under UV irradiation

The photocatalytic activities of the (M,N) co-doped  $TiO_2$  photocatalysts for MB degradation were first checked under UV irradiation. **Figure 4.4** presents the degradation profiles and associated kinetics for the different co-doped samples. The calculated kinetic constants k from these curves are summarized in **Table 4.1**. To have a better comparison, the k of M-doped  $TiO_2$  and  $TiO_2$  are presented as references, and the variations of k between the (M,N) co-doped  $TiO_2$  and the references were calculated.

As shown in **Figure 4.4. a and 4.4 b**, we found that the thermal condition of nitridation has an important effect on the photocatalytic activities of the (Nb,N) co-doped samples, which is in agreement with the result in Chapter 2. The photocatalytic degradation kinetics of 0.25NbNTi-m is 0.3384, which is increased by 80.8% compared to 0.25NbTi. One explanation could be that the co-doped sample synthesized by mild nitridation has a higher efficiency of photogenerated charge separation and transfer, which could minimize the negative effect caused by excessive MB adsorption. On the other hand, a deterioration of the activity is observed on 0.25NbNTi-h (k=0.1746), which could be ascribed to the generation of Ti<sup>3+</sup> during the harsh nitridation process.

A similar trend is observed on the (Ta, N) co-doped samples (**Figure 4.4 c and 4.4 d**). 0.25TaNTi-m exhibits a superior photocatalytic activity compared to 0.25TaTi, with a 20.8% increase in the degradation kinetics. On the other hand, an obvious deterioration of the activity is observed on 0.25TaNTi-h, leading to a 45.2% drop in the degradation kinetics. This indicates a similar influence on the photocatalytic properties of 0.25NbTi and 0.25TaTi with nitridation thermal conditions. In both cases of (Nb,N) and (Ta,N) co-doping, the harsh nitridation resulted in the deterioration of the photocatalytic activity.

Interestingly, a different effect of the thermal nitridation condition on the photocatalytic activity was observed for the (W,N) co-doped TiO<sub>2</sub> (**Figure 4.4 e and 4.4 f**). Similar to 0.25NbNTi-m and 0.25TaNTi-m, an increased degradation kinetic is observed on 0.25WNTi-m (47.3% increase compared to 0.25WTi). However, no significant deterioration of photocatalytic activity is observed on 0.25WNTi-h, and this sample produced with harsh nitridation still exhibits a photocatalytic activity 30% higher than 0.25WTi. All the W-containing samples have a fairly close surface area, crystalline size, and adsorption capacity for MB. Thus, the results of photocatalytic activities of the W-containing samples should be mainly determined by their intrinsic nature, such as dopants and defects. The EPR test has already confirmed the absence of Ti<sup>3+</sup> in the (W,N) co-doped samples, and the presence of W<sup>5+</sup> in 0.25WTi and 0.25WNTi-h, the latter probably have a less negative effect than Ti<sup>3+</sup> on the photocatalytic activity.

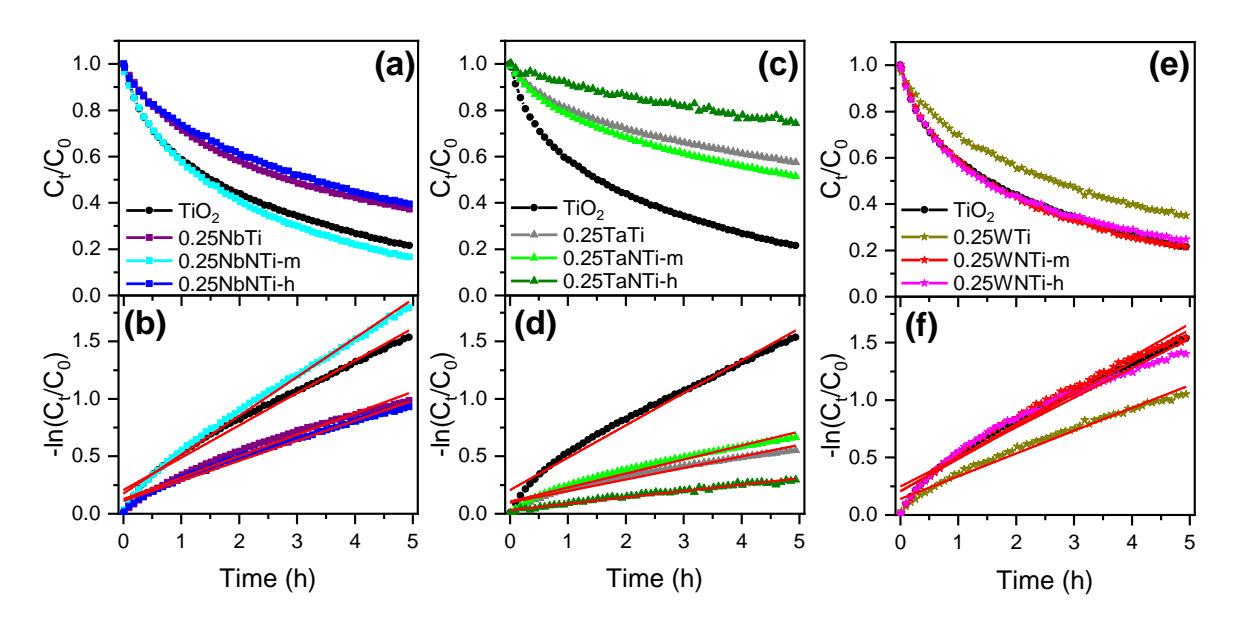


**Figure 4.4 :** MB degradation profiles and kinetics for TiO<sub>2</sub>, M-doped and (M,N) co-doped TiO<sub>2</sub> samples under the irradiation using UV LED (365 nm): (a, b) for Nb samples. (c, d) for Ta samples and (e, f) for W samples.

When comparing the photocatalytic activity of the (M,N) co-doped samples with the  $TiO_2$  reference, all the M-doped  $TiO_2$  show inferior degradation kinetics compared to  $TiO_2$ , following the order:  $TiO_2 > 0.25 WTi \approx 0.25 NbTi > 0.25 TaTi$ , which could be mainly due to the MB adsorption under the current test condition. For the 0.25MTi-m sample series, this detrimental effect might be compensated by the increase in efficiency of the separation and

transfer of the photogenerated charge carriers. 0.25NbTi-m and 0.25WTi-m still exhibit superior photocatalytic activity to TiO<sub>2</sub>. In particular, 20.3% of the increase in degradation kinetics was achieved by 0.25NbNTi-m. However, 0.25TaNTi-m is less active than TiO<sub>2</sub>, with degradation kinetics reduced by 56.7%. On the other hand, for the 0.25MTi-h sample series, 0.25WNTi-h is the only one that shows comparable degradation kinetics with TiO<sub>2</sub> (slightly decreased by 8.3%). The degradation kinetics of 0.25NbNTi-h and 0.25TaNTi-h decreased by 38.0% and 80.4%, respectively. Therefore, according to the results of the chapter-2, the nitridation condition plays an important role in determining the photocatalytic activity for the (Nb,N) co-doped and (Ta,N) co-doped TiO<sub>2</sub>. However, for the (W,N) co-doped TiO<sub>2</sub>, the photocatalytic degradation of MB is less affected by the thermal nitridation conditions.

In addition, by comparing the degradation kinetics of TiO<sub>2</sub> and the Nb-containing TiO<sub>2</sub> with the corresponding value obtained in Chapter 2, it is noted that all the samples are less performant under the current experimental condition. Our hypothesis is that the initial concentration of MB resulted in excessive MB adsorption on the sample surface, slowing the rate of active radical generation. In order to figure out the saturation level of the MB molecules adsorbed on the different sample surfaces, adsorption isotherm experiments are strongly recommended for future study. It can also help to compare the experimental results published by different research groups using the different initial MB concentrations.

<b>Table 4.1</b> : Pseudo first order of photo-degradation kinetic constant for all samples under the	
irradiation of UV LED (365 nm) and visible LED (450 nm).	

Sample	<i>k</i> -UV / h <sup>-1</sup>	variation vs TiO <sub>2</sub> (%)	variation vs M- doped TiO <sub>2</sub> (%)	<i>k</i> -visible / h <sup>-1</sup>
TiO <sub>2</sub>	0.2814			-
0.25NbTi	0.1872	-33.5		-
0.25NbNTi-m	0.3384	20.3	80.8	0.0672
0.25NbNTi-h	0.1746	-38.0	-6.7	0.0714
0.25TaTi	0.1008	-64.2		-
0.25TaNTi-m	0.1218	-56.7	20.8	0.0450
0.25TaNTi-h	0.0552	-80.4	-45.2	0.0552
0.25WTi	0.1980	-29.6		-
0.25WNTi-m	0.2916	3.6	47.3	0.1080
0.25WNTi-h	0.258	-8.3	30.3	0.1050

### 2.3.3 Photocatalytic degradation of MB under visible irradiation

The photocatalytic activities of the (M,N) co-doped samples were then evaluated under visible illumination (at 450 nm) (shown in **Figures 4.5 a** and **4.5 b**). In this case, the difference in visible light absorption for the specific sample will play an important role in determining its photocatalytic activity. The corresponding kinetic constants k are summarized in **Table 4.1.** 

For 0.25NbNTi-h and 0.25TaNTi-h, the increase of photon absorption in the visible range is supposed to compensate for the deterioration of photocatalytic activity caused by the generation of Ti<sup>3+</sup>. Consequently, their degradation kinetics are similar to that of 0.25NbNTi-m and 0.25TaNTi-m. The result of the (Nb,N) co-doped differs in that aspect from that obtained in Chapter 2, where 0.25NbNTi-m shows superior photocatalytic activity than 0.25NbNTi-h. This could be explained by the general decrease in degradation rate for the samples tested under the current experimental conditions, which may amplify the positive effect of the increase in photon absorption. For the (W,N) co-doped TiO<sub>2</sub>, there was no Ti<sup>3+</sup> generated during the nitridation treatment and these samples presented the higest visible light absorption at 450 nm. Although 0.25WNTi-h presents higher visible absorption compared to 0.25WNTi-m, the visible photocatalytic activity is similar.

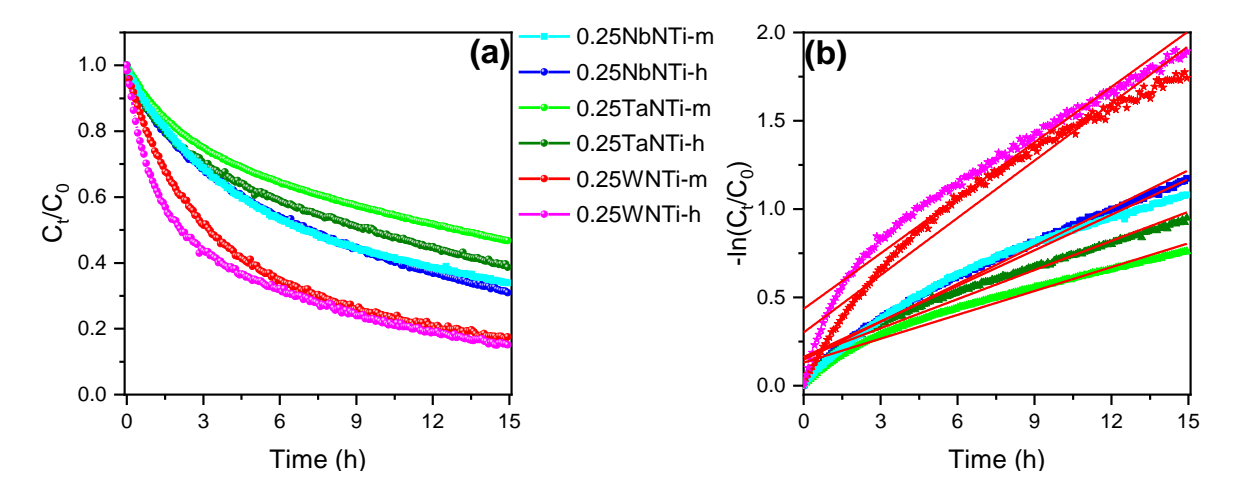


**Figure 4.5**: MB degradation profiles (a) and kinetics (b) for (M,N) co-doped samples under the irradiation with visible LED (450 nm):

# 2.4 Conclusion on photocatalytic MB degradation

In this part, the photocatalytic activities of the synthesized M-doped TiO<sub>2</sub> and (M,N) co-doped TiO<sub>2</sub> were evaluated by conducting MB degradation experiment. The results indicate that the photocatalytic activities of TiO<sub>2</sub> materials are significantly influenced by the synthetic strategy of cation doping or co-doping. The similarity in the photocatalytic behavior of (Nb,N) co-doped TiO<sub>2</sub> and (Ta,N) co-doped TiO<sub>2</sub> was observed. For both of them, nitridation conditions play an important role in determining the resultant photocatalytic activity. However, the nitridation condition does not significantly influence the activity of the (W,N) co-doped TiO<sub>2</sub>.

As discussed, the results obtained from the measurements under UV light are in general consistent with our conclusion in Chapter 2. It is supposed that the co-doped materials synthesized by the mild nitridation have a higher efficiency of the separation and transfer of photogenerated charge carriers, which could be mainly ascribed to the charge compensation effect between the cation and nitrogen dopants and lower density of crystalline defects. On the other hand, it is confirmed that the generation of Ti<sup>3+</sup> resulted in the

deterioration of the photocatalytic activity. Based on the fact that no significant decrease in degradation kinetics was observed on 0.25WNTi-h, we think that V<sub>O</sub><sup>+</sup> and W<sup>5+</sup> have negligible influence on the photocatalytic performance. Some results differ from the conclusions in Chapter 2, which could be attributed to the variation of the initial MB concentration used for the experiment. First, it is shown that all the M-doped TiO<sub>2</sub> were less active compared to TiO2, under the illumination of UV light. Considering that the surface of M-doped TiO<sub>2</sub> is more negatively charged compared to TiO<sub>2</sub> (as characterized by the Zeta potential test), a possible explanation is an excessive MB adsorption on the sample surface. Consequently, the generation of radicals involved in the degradation mechanism can be lowered. Under visible illumination, a similar photocatalytic activity between the co-doped samples produced by mild and harsh nitridation respectively (in the same (M,N) family). Besides, by comparing the photocatalytic activity of the (M,N) co-doped TiO<sub>2</sub> with that of TiO<sub>2</sub>, we can conclude that (Nb,N) co-doping is more beneficial to the improvement of photocatalytic activity compared to (Ta,N) or (W,N) co-doping, in the case of mild nitridation. While under visible light, (W,N) samples present the best activities, it should be noted that no Ti<sup>3+</sup> sites were identified for these (W,N) co-doped samples.

Another noteworthy point is that all the kinetics degradation fits are found unsatisfactory, especially under visible irradiation. The raw data for the different samples exhibit an arc-like shape, which indicates a slight decrease in the kinetics during the degradation process. The possible explanations are some residues of degraded MB molecules that remain attached to the surface and limit the activity over time or the fact that the catalyst particles surface charge changes over time and tends to diffuse toward the optical fiber probe. Consequently, they will change the light diffusion of the analyzing beam and create a problem of baseline compensation. Therefore, besides the nature of the photocatalyst itself, the adsorption of dye molecules on the catalyst surface also has an important influence on the photocatalytic activity. This effect should be taken into account for future photocatalytic studies to help for a better understanding of the mechanism of the photodegradation reaction and also help to determine the optimal conditions for the pollutant degradation.

# 3. Photocatalytic hydrogen production

# 3.1 Experimental part

# 3.1.1 Photocatalytic test platform

The photocatalytic hydrogen production was carried out on the set-up represented in **Figure 4.6** and **Figure 4.7**, The reaction was carried out in a reactor containing 120 mL of Milli-Q water/methanol mixture (90/10 %<sub>v.</sub>) under magnetic stirring (500 rpm). A water cooling system was connected to the photocatalytic cell to stabilize the temperature during the reaction. An Xe lamp (1000 W) equipped with an AM 1.5 filter was used as a simulated solar light source (100 mW.cm<sup>-2</sup> on the cell). In a typical test, 50 mg catalyst was used and before the illumination, the cell was purged with N<sub>2</sub> (N<sub>2</sub> 4.5, Linde) at a flow rate of 20

mL.min<sup>-1</sup> for 1h, to remove residual O<sub>2</sub> which might react with evolved H<sub>2</sub>. After this purge procedure, the light source of AM1.5 was switched on and the reaction products were analyzed online every 300 s by gas-phase compact-chromatograph (CompactGC).

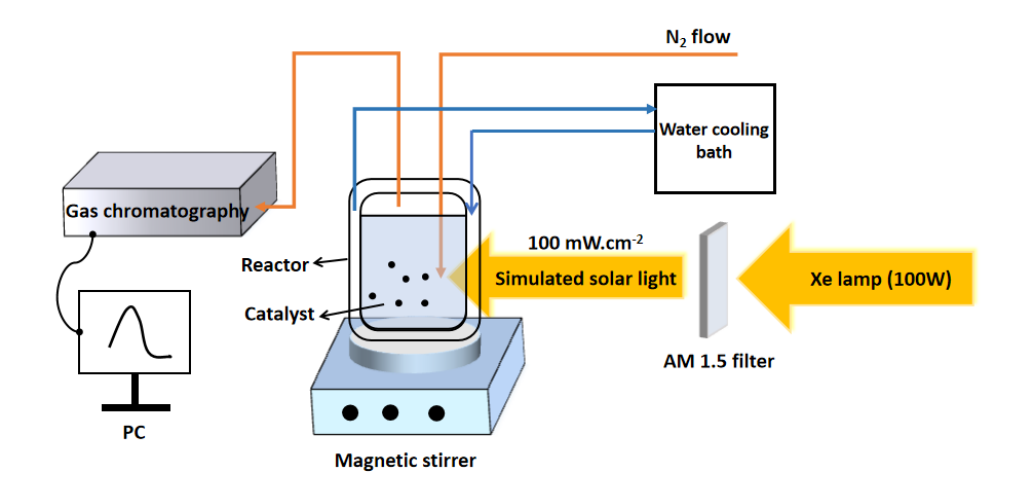


Figure 4.6: Scheme of the photocatalytic set-up.

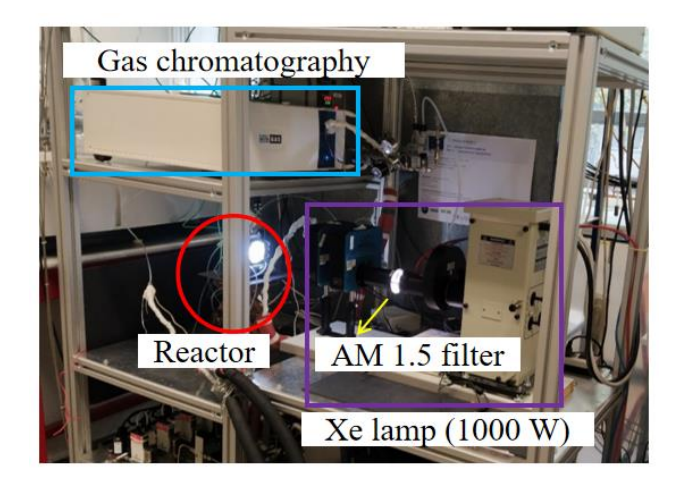


Figure 4.7: Photography of the photocatalytic set-up.

#### 3.1.2 Analysis of products on compact GC

The gaseous products of the photocatalytic reaction were analyzed by a CompactGC 4.0, (Global analyser solutions) controlled by Chromeleon 7 software. This instrument consists of three independent analytic modules (A, B and C). Modules A comprise a 10 m A Rtx-624 column, and a Flame Ionization Detector (FID), flushed with Helium (He 6.0, Linde) as carrier gas. It allows to monitor the carbon products. Module B comprises a Molsieve 5m\*0,32mm 5A column and a 3m\*0,32mm Rt-QBond, and a Thermal Conductivity Detector (TCD). Module B is flushed with Nitrogen (N<sub>2</sub> 4.5, Linde), enabling to follow the evolution of hydrogen. The automatic injection volume is 25µL for Module B. Module C is flushed with He (He 6.0, Linde), consists of a 1/16 \* 0,25m Hayesep N 60-80 pre-colum, a

1/16"\*1m XL Sulfur 60-80 column, a 1/16"\*1m Molsieve 5A, 60-80 column and a TCD detector. This module is used to monitor the evolution of oxygen and nitrogen. An automatic injection of  $100\mu$ L is conducted for Module C.

The chromatogram is a plot of signal (mV) detected by the GC module in the function of retention time (s). The peak corresponding hydrogen appears in the region of 0.32 to 0.42s on module B. The intensity was calibrated by diluting a calibration bottle of  $H_2$  in  $N_2$  (1000 ppm of  $H_2$ , Linde) at 100, 200, 300 and 400 ppm and the signal peak area recorded by module B is shown in **Figure 4.8 a.** 

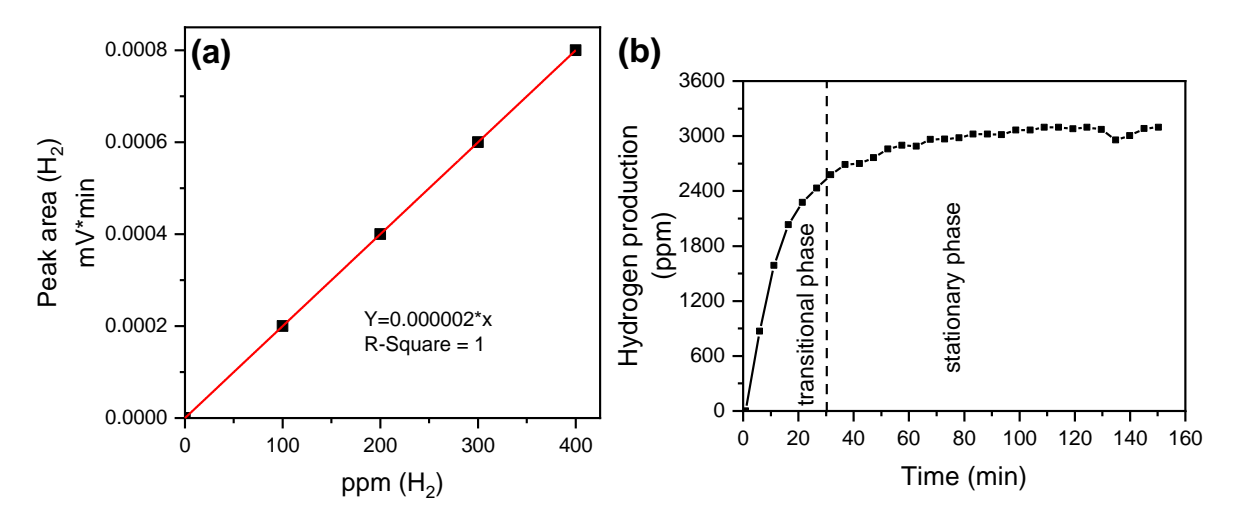


**Figure 4.8:** (a) Calibration curve obtained by recording the hydrogen peak area under flow of standard gas. (b) An exemplary curve of hydrogen production evolution over time.

#### 3.1.3 Data treatment

A typical evolution curve of hydrogen production as a function of time (TiO<sub>2</sub> as an example) is presented in **Figure 4.8 b**, which is obtained based on the data detected by GC (in ppm). The evolution curve includes two phases: a transitional phase (0 to 30 min), in which the H<sub>2</sub> produced by the photocatalytic reaction must saturate the solution in the cell and diffuse in the gas line before reaching the GC injector, leading to an increase of the detected hydrogen production. A stationary phase, characterized by a plateau, in which stable hydrogen production was obtained, in general, 30 min after the start of illumination.

The photocatalytic activity of a specific sample was evaluated using the hydrogen production rate ( $\mu$ mol.h<sup>-1</sup>.g<sup>-1</sup>), calculated by the following equation:

$$r_{H_2} = \frac{c_{H_2} * D_{V(N_2)}}{V_{m(N_2)} * m_{cata}}$$
 (eq. 4.7)

Where:  $C_{H2}$  is the average value of hydrogen concentration (in ppm) in the stationary phase extracted from the hydrogen production curve.  $D_{V(N2)}$  is the flow rate of  $N_2$  used during the experiment (20 mL.min<sup>-1</sup>),  $V_{m(N2)}$  is the molar volume of  $N_2$  (24.5 L.mol<sup>-1</sup> at 25°C), and  $m_{cata}$  is the mass of the catalyst (50 mg).

# 3.2 Photoreduction vs. chemical reduction for Pt co-catalyst deposition.

#### 3.2.1 Context

Various methods have been used to deposit co-catalysts on the surface of semiconductor catalysts, such as chemical reduction,<sup>7,8</sup> photoreduction,<sup>8–10</sup> atomic-layer deposition,<sup>11</sup> electrodeposition,<sup>12</sup> sputtering<sup>13</sup> and physical mixing<sup>14</sup>. Among them, the chemical reduction and photoreduction methods are more widely used because they do not require special equipment.

In the chemical reduction method, NaBH<sub>4</sub>, LiBH<sub>4</sub>, N<sub>2</sub>H<sub>4</sub>, LiAlH<sub>4</sub> *etc...*, are used as reducing agents.<sup>15</sup> During the synthesis process, metal ions precursor of co-catalysts are reduced in solution to metal (oxides) nanoparticles and deposited on the surface of support materials. By using this method, co-catalysts, such as Pt,<sup>16</sup> Au,<sup>17</sup> Ag,<sup>18</sup> have been successfully deposited on the TiO<sub>2</sub> surface to facilitate different photocatalytic reactions. For the photoreduction, the deposition of the co-catalyst is achieved by illuminating the supporting semiconductor and co-catalyst precursor in a simple slurry reactor. In this case, the metal ions in the co-catalyst precursor are reduced by the highly reductive photogenerated electrons without any additional reducing agent. Besides, it is shown that the particle size, geometrical distribution, and oxidation state of the deposited co-catalyst can be controlled by adjusting the reaction parameters.<sup>19–21</sup> When TiO<sub>2</sub> is used as support material, deposition of well-defined metal nanoparticles (Pt,<sup>2,15</sup> Au<sup>17,22</sup>, Pd<sup>23</sup>, etc.) as co-catalyst has been reported for different photocatalytic reactions, including hydrogen production, CO<sub>2</sub> reduction and pollutants degradation.

Comparisons in activities of photocatalysts decorated with cocatalysts, prepared by different methods, have been conducted in previous studies. Some authors claim that the photoreduction method improves the photocatalytic performances, <sup>21,24</sup> whereas the contrary has also been reported. <sup>25–27</sup> These conflicting conclusions could be because different experimental conditions may produce co-catalysts with different particle sizes, distribution, and oxidation states. Therefore, in the initial stage of our study, it is important to determine which method is more favorable for photocatalytic hydrogen production under the current experimental condition. In this part, photocatalytic activities of Pt-deposited TiO<sub>2</sub> prepared by the method of photoreduction (Pt-TiO<sub>2</sub>) and chemical reduction (Pt-TiO<sub>2</sub>-ch) are compared, using the TiO<sub>2</sub> synthesized via sol-gel method as reference material.

#### 3.2.2 Experimental method for Pt deposition

#### 3.2.2.1 chemical reduction

The chemical reduction deposition of Pt NPs is based on a method optimized in the laboratory by using NaBH<sub>4</sub> as a reducing agent. An aqueous solution of H<sub>2</sub>PtCl<sub>6</sub> (0.25 mol. L<sup>-1</sup>, raw material from Merck, 99.9%) was used as the precursor of Pt. To prepare our sample, labeled Pt-TiO<sub>2</sub>-ch, 300 mg of the synthesized TiO<sub>2</sub> was dispersed into 30 mL of distilled

water under magnetic stirring (500 rpm) for 15 min. 31 µL of the precursor solution of H<sub>2</sub>PtCl<sub>6</sub> was added to target a theoretical Pt loading of 0.5 wt.%. The stirring was kept for 45 min to permit a sufficient dispersion and adsorption of Pt ions on the surface of support TiO<sub>2</sub>. Then, 384 µL of freshly prepared NaBH4 solution (10 mmol.L<sup>-1</sup>, raw materal from Merck, 99.8%) was dropped into the mixture to promote the reduction of Pt ions. It was observed that a gray coloration appeared immediately, indicating a fast reduction. The gray suspension was stirred for 15 minutes to ensure a complete reaction. After this reduction step, the mixture is filtered and washed with distilled water 3 times. After drying in the oven for 24 hours at 80°C, the gray powder of Pt-TiO<sub>2</sub>-ch is finally recovered.

## 3.2.2.2 Photoreduction with in-situ photocatalytic activity test

In this method, both the deposition of Pt NPs through photoreduction and the photocatalytic hydrogen production test were achieved in the same suspension, using the aforementioned reactor and set-up. 50 mg synthesized TiO<sub>2</sub> and 5.3 µL of the precursor solution of H<sub>2</sub>PtCl<sub>6</sub> (0.25 mol.L<sup>-1</sup>, targeting a 0.5 wt.% Pt loading) were added into a 120 mL of Milli-Q water/methanol mixture (90/10, volume%) under magnetic stirring (500 rpm). Here, methanol was used as a sacrificial electron donor for both the photo-deposition of Pt NPs and the photocatalytic reaction for hydrogen production. After the photocatalytic reaction, the tested sample powder was recovered from the reactor by filtration with distilled water and dried at 80°C, and then used for characterization. The prepared samples are denoted as Pt-X (X is the sample name)

## 3.2.3 Characterization of the Pt co-catalyst

## 3.2.3.1 Elemental analysis

The Pt loading on the surface of  $TiO_2$  was determined by elemental analysis based on Inductively Coupled Plasma Atomic Emission Spectroscopy (ICP-AES). First, the powder samples were digested at about  $215^{\circ}C$  and 60 bar in a microwave digestion system (Multiwave 3000, Anton Paar, Austria) using an aqua regia mixture prepared with 2 mL HNO3 (Fluka, Trace SELECT >69%, Germany) and 4 mL HCl (Fluka, Trace-SELECT >37%, Germany). Secondly, analysis of diluted filtrates was carried out, after filtration of residual particles, by Inductively Coupled Plasma Optical Emission Spectroscopy (ICP-OES, Varian 720ES, France) at 214.423 nm (Pt). Multi-element standards were prepared by dilution of 1000 mg.L<sup>-1</sup> certified single element standards (CPI International, The Netherlands) in aqua regia to minimize matrix effect errors. A spike on a digested sample allowed checking that the recovered concentrations were  $100\% \pm 10\%$ . The deposition yield ( $\eta_{dep}\%$ ) is defined as the ratio between the deposited mass of Pt determined by ICP-AES and the theoretical mass of Pt introduced from synthesis (0.5 %).

The measured loading of Pt achieved by the chemical reduction method is the same as the theoretical value expected from the synthesis, giving a deposition yield of 100%. This suggests that the Pt ions introduced by H<sub>2</sub>PtCl<sub>6</sub> were completely reduced by NaBH<sub>4</sub> and successfully deposited on the surface of TiO<sub>2</sub>, using the current chemical reduction method.

By contrast, the deposition yield achieved by the photoreduction method shows a decrease almost by half ( $\eta_{dep}$ % = 48).

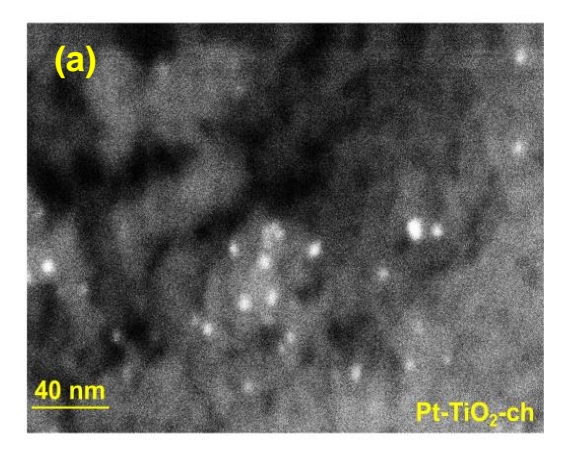
The difference in deposition yield can be explained by the respective reaction mechanisms of the two methods. In the chemical reduction process,  $[PtCl_6]^{2-}$  groups could be adsorbed first on the  $TiO_2$  surface and then reduced by NaBH<sub>4</sub> through the pathway shown in **eq. 4.8** <sup>28</sup>:

$$NaBH_4 + H_2PtCl_6 + 3H_2O \rightarrow Pt + H_3BO_3 + 5HCl + NaCl + 2H_2$$
 (eq. 4.8)

Due to the strong reducing capacity of NaBH<sub>4</sub>, the reduction of Pt ions could be achieved rapidly and sufficiently. However, for the photoreduction method, competition between the photoreduction of Pt ions and photocatalytic hydrogen production exists. The deposition of Pt NPs is thermodynamically more favorable than the photocatalytic hydrogen production with the redox potential required for the reduction of Pt (Pt<sup>4+</sup> to Pt<sup>2+</sup>, 0.68V vs. NHE; Pt<sup>2+</sup> to Pt<sup>0</sup>, 0.72V vs. NHE) lower than that the one of HER (0V vs. NHE).<sup>29</sup> Then, with the initial increase of Pt NPs deposited on the TiO<sub>2</sub> surface, could activate hydrogen production. Nevertheless, the negatively charged surface of TiO<sub>2</sub> (characterized by zeta potential) could favor the adsorption of H<sup>+</sup> against the one of [PtCl<sub>6</sub>]<sup>2-</sup>.

#### 3.2.3.2 SEM characterization

The morphology of the prepared samples was studied by SEM, chemical contrast was performed to highlight the distribution of Pt NPs deposited by the two methods (shown in **Figure 4.9**). It is observed that Pt NPs were spherically shaped in both samples. However, the distribution density and particle size of Pt NPs differ depending on the specific deposition method. The Pt NPs on the surface of Pt-TiO<sub>2</sub>-ch exhibit a higher density compared to that on Pt-TiO<sub>2</sub>. The observation is consistent with the elemental analysis result. Besides, the mean size of the Pt NPs deposited by chemical reduction and photoreduction is 6.7±1.4 nm (average on 15 particles) and 2.5±0.9 nm (average on 8 particles), respectively. Therefore, we can conclude that there is a direct impact of the deposition method on the morphology of resultant Pt NPs, in the aspects of both distribution density and particle size, which could further impact the photocatalytic performance of the Pt-TiO<sub>2</sub> photocatalysts.



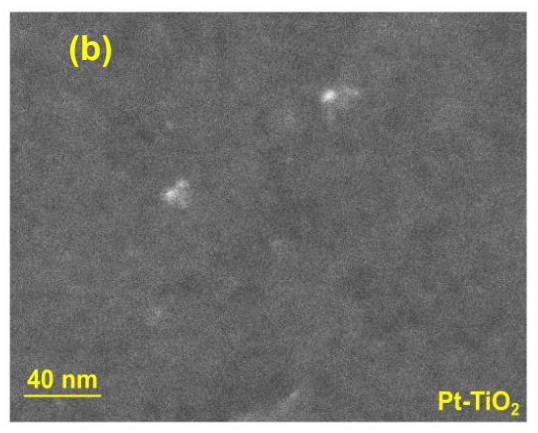
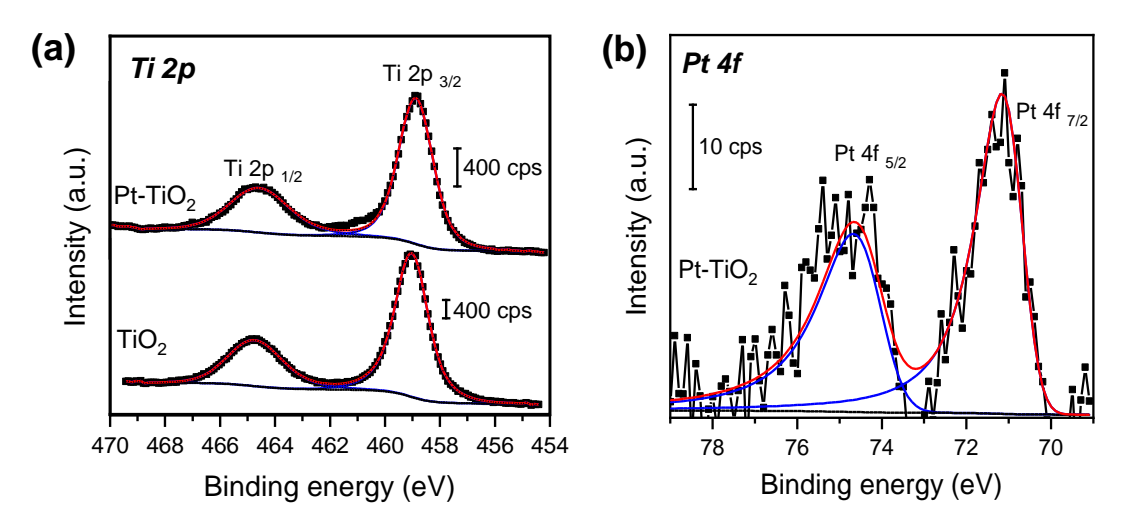


Figure 4.9: SEM images of Pt-TiO<sub>2</sub>-ch (a) and Pt-TiO<sub>2</sub> (b).

## 3.2.3.3 XPS analysis

The XPS analysis of the Pt-deposited  $TiO_2$  prepared by the photoreduction method is presented in **Figure 4.10**, with reference to the  $TiO_2$  before Pt-deposition. In the spectral region of Ti 2p (**Figure 4.10 a**), a doublet corresponding to the Ti  $2p_{3/2}$  and Ti  $2p_{1/2}$  of  $Ti^{4+}$ , 30 is observed on both  $TiO_2$  and Pt-TiO<sub>2</sub>. The oxidation state of the deposited Pt NPs was disclosed by the Pt 4f spectral region, as shown in **Figure 4.10 b**. A doublet peak located at 70.8 eV and 74.2 eV is observed, with an energy split of 3.3 eV. These two peaks are signed to Pt 4f  $_{7/2}$  and Pt 4f  $_{5/2}$  of the metallic Pt (Pt<sup>0</sup>), respectively. 8,31 This suggests a complete reduction of Pt from Pt<sup>4+</sup> to Pt<sup>0</sup> by the photogenerated electrons.



**Figure 4.10 :** XPS spectra of Ti 2p (a) and Pt 4f (b) region for Pt-TiO<sub>2</sub>. (Black points are the experiment data, red lines are the fitted signals, blue lines are different contributions).

On the other hand, although the XPS characterization for Pt-TiO<sub>2</sub>-ch still needs to be supplemented, we hypothesize that platinum oxides might be produced. According to the previous study in our group, in which the Pt NPs were deposited on the sol-gel synthesized TiO<sub>2</sub> surface using a similar chemical reduction method, both Pt<sup>0</sup> and Pt<sup>2+</sup> were observed.<sup>32</sup> Comparative studies on these two deposition methods for TiO<sub>2</sub> have been published by Lakshmanareddy *et al.* and Jiang *et al.* respectively. Both of them indicate that the photoreduction method was favorable for the formation of Pt<sup>0</sup>, whereas higher oxidation states of Pt<sup>2+</sup> and Pt<sup>4+</sup> were observed for the samples prepared by chemical reduction.<sup>8,21</sup> Lakshmanareddy *et al.* explained that the multiple Pt oxidation states produced by chemical reduction might be due to the multiple layers of Pt ions adsorbed on the TiO<sub>2</sub> surface. They proposed that only the upper layer of Pt ions could be reduced completely into Pt<sup>0</sup>, while the Pt ions in the deeper layer were partially reduced into Pt<sup>2+</sup> or maintained as Pt<sup>4+</sup>.

## 3.2.4 Photocatalytic activity

As mentioned, the photocatalytic activity of the samples for hydrogen production was conducted under AM1.5 illumination with the presence of methanol as a sacrificial electron donor. In the case of Pt-TiO<sub>2</sub> prepared by the photoceduction method, the photocatalytic test was conducted in the same suspension used for Pt deposition.

Figure 4.11 presents the hydrogen production rate using Pt-TiO<sub>2</sub>-ch and Pt-TiO<sub>2</sub> as catalysts, respectively. The synthesized TiO<sub>2</sub> samples are less active than the commercial P25 (4968 µmol.g<sup>-1</sup>h<sup>-1</sup>). A possible reason could be that the P25 particles are more separated due to the gas-phase synthetic procedure, and the heterojunction between anatase and rutile can facilitate charge separation.<sup>33</sup> It is noted that Pt-TiO<sub>2</sub> shows a better activity for hydrogen production (2590 μmol.g<sup>-1</sup>h<sup>-1</sup>) compared to Pt-TiO<sub>2</sub>-ch (1816 μmol.g<sup>-1</sup>h<sup>-1</sup>), although the Pt loading achieved by the photoreduction method is only ~50% that of chemical reduction. A previous study has proved an optimal Pt loading range of 0.2 to 1 wt.%, in which the photocatalytic activity of Pt-deposited TiO<sub>2</sub> samples shows little difference.<sup>34</sup> Thus, we suppose that in our case the photocatalytic activity could be mainly ascribed to the variation in particle size and oxidation state of the deposited Pt NPs. On the one hand, Pt-TiO<sub>2</sub> has a smaller size (2.58 nm) of Pt NPs on its surface, which is closer to the optimal size (~1 nm), as reported by both theoretical and experimental studies.<sup>34,35</sup> It is shown that the Pt NPs with smaller size could trap more effectively the photogenerated electron from TiO<sub>2</sub>, whereas the larger size ones could be more favorable for the formation of H-H bonds, together resulting in an optimal value at ~1 nm. Furthermore, the oxidation state of Pt<sup>0</sup> produced by the photoreduction method could promote photocatalytic hydrogen production, as shown by Jiang et al.<sup>21</sup>

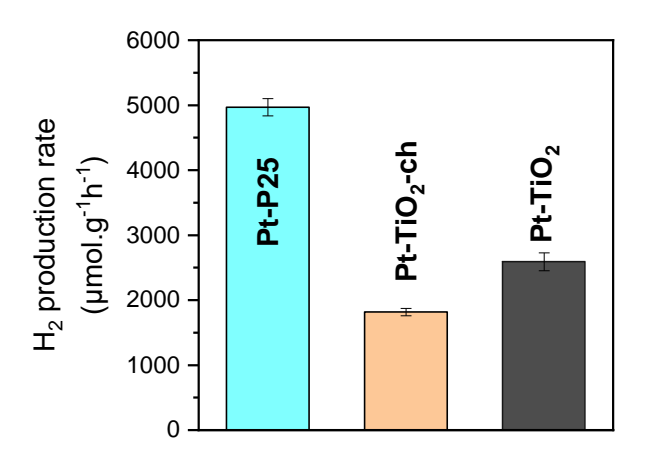


Figure 4.11: Photocatalytic hydrogen production rate for Pt-TiO<sub>2</sub>-ch and Pt-TiO<sub>2</sub>.

By using sol-gel synthesized TiO<sub>2</sub> as a reference material, we can conclude that the photoreduction method for the Pt-deposition is more favorable for hydrogen production under the current experimental parameters. Thus, this method was applied to prepare Pt-deposited M-doped, N-doped and (M,N) co-doped TiO<sub>2</sub> materials.

# 3.3 Effect of M-doping and N-doping on the photocatalytic activities

## 3.3.1 Characterization of the co-catalyst

#### 3.3.1.1 Elemental analysis

The Pt loading on the M-doped TiO<sub>2</sub> and the N-doped TiO<sub>2</sub> (Pt-NTi-m) determined by elemental analysis are presented in **Table 4.2**. it is shown that Pt-NTi-m and Pt-0.1NbTi have a similar Pt loading as Pt-TiO<sub>2</sub>, with a deposition yield of 42% and 46%, respectively. This probably indicates a limited modification of surface charge due to the mild nitridation or low concentration Nb-doping. On the other hand, a decrease of Pt loading is observed for all the 0.25MTi samples. In particular, the Pt loading of Pt-0.25NbTi and Pt-0.25TaTi dramatically decreases to 0.03 wt.%. This could be ascribed to the more negatively charged surface of the 0.25MTi samples, as analyzed by the zeta-potential tests, which limits the absorption of [PtCl<sub>6</sub>]<sup>2-</sup>. However, the decrease of Pt loading for Pt-0.25WTi is less, where the deposition yield is only decreased to 34%. A possible explanation is that W<sup>5+</sup> (detected by EPR) may bring more active sites for [PtCl<sub>6</sub>]<sup>2-</sup> adsorption.

Sample	Pt	m 0/	
	Theoretical	Measured	$\eta_{ m dep}\%$
Pt-TiO <sub>2</sub>	0.50	$0.24 \pm 0.005$	48 ± 1
Pt-0.1NbTi	0.50	$0.23 \pm 0.003$	$46 \pm 0.6$
Pt-0.25NbTi	0.50	$0.03 \pm 0.002$	$6\pm0.4$
Pt-0.25TaTi	0.50	$0.03 \pm 0.004$	$6 \pm 0.8$
Pt-0.25WTi	0.50	$0.17 \pm 0.008$	$34 \pm 1.6$
Dt NTi m	0.50	$0.21 \pm 0.011$	42 ± 2.2

Table 4.2: Pt loading for Pt-TiO<sub>2</sub>, Pt-MTi samples and Pt-NTi-m, determined by elemental analysis.

## 3.3.1.2 SEM and TEM characterization

The SEM images (**Figure 4.12**) reveal a striking difference in the morphology of Pt NPs in the case of M-doping and N-doping. Since we haven't characterized all the M-doped samples, Pt-0.25NbTi is used as a representative. Well-dispersed Pt NPs are observed on the surface of 0.25NbTi. There is no observable change in the particle size of the deposited Pt NPs between Pt-0.25NbTi (**Figure 4.12 b**) and Pt-TiO<sub>2</sub>(**Figure 4.12 a**) with the SEM resolution. However, for the N-doped sample, Pt NPs aggregation is noted to occur in some specific areas on the sample surface (**Figure 4.12 c**). The aggregate shown in **Figure 4.12 c** has a diameter of ~80 nm. This indicates a high inhomogeneity of the Pt distribution for Pt-NTi-m, even though it has a similar Pt loading as TiO<sub>2</sub>.

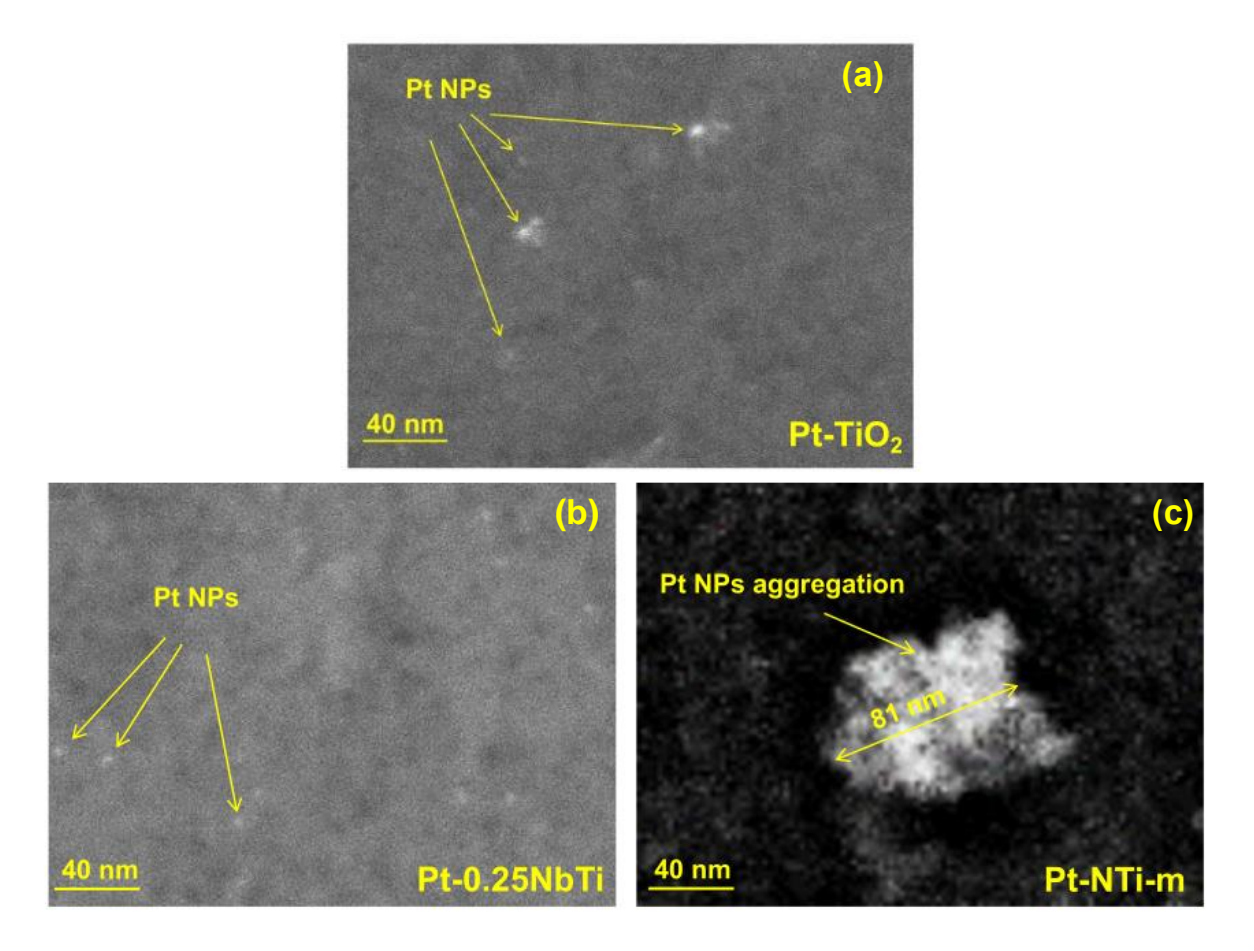


Figure 4.12: SEM images of Pt-TiO<sub>2</sub>(a), Pt-0.25NbTi (b) and Pt-NTi-m (c).

TEM images provide supplementary information on the Pt NPs deposited on  $TiO_2$  and 0.25 NbTi (**Figure 4.13**). We can easily observe that the Pt NPs on  $TiO_2$  are denser compared to those on 0.25 NbTi, indicating a higher Pt loading. This is consistent with the elemental analysis result. Besides, the mean particle size of the Pt NPs on  $TiO_2$  and 0.25 NbTi were calculated as  $1.73 \pm 0.7$  nm and  $1.91 \pm 0.7$  nm, respectively (average on 20 particles). The result confirms that the Nb-doping does not change the distribution and particle size of the Pt NPs, although the Pt loading is much lower than that of  $TiO_2$ .

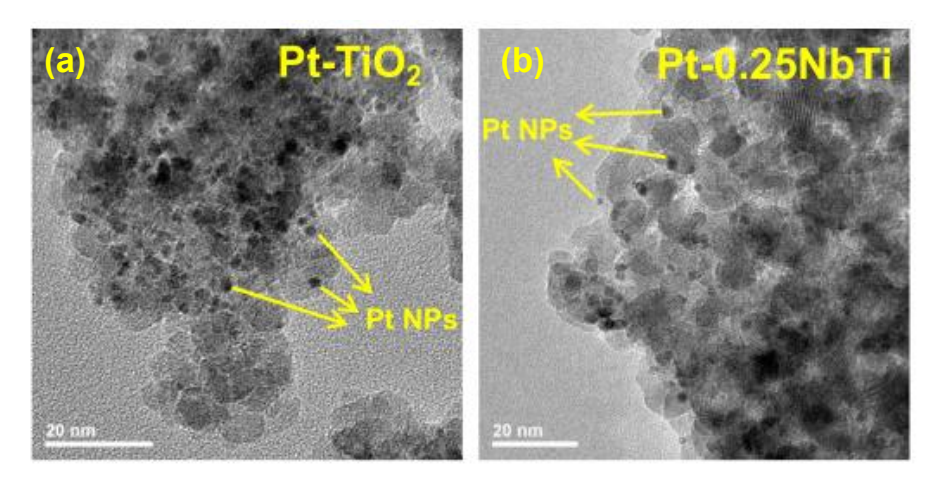


Figure 4.13: TEM images of Pt-TiO<sub>2</sub> (a) and Pt-0.25NbTi (b).

## 3.3.2 Photocatalytic activities

The photocatalytic hydrogen production rate of the Pt-MTi samples and Pt-NTi-m are shown in **Figure 4.14**, compared to Pt-TiO<sub>2</sub> as a reference. All samples are less active compared to Pt-TiO<sub>2</sub>. M-doping resulted in a significant decrease in the photocatalytic performance. For the Pt-0.25MTi sample family, it was observed that the performance of the samples dropped by 98% on average. The Pt-0.1MTi sample family exhibits better activity than their respective Pt-0.25MTi counterpart (93% loss in average). For Pt-NTi-m, the photocatalytic hydrogen production rate decreases "only" to 694 μmol.h<sup>-1</sup>g<sup>-1</sup>.

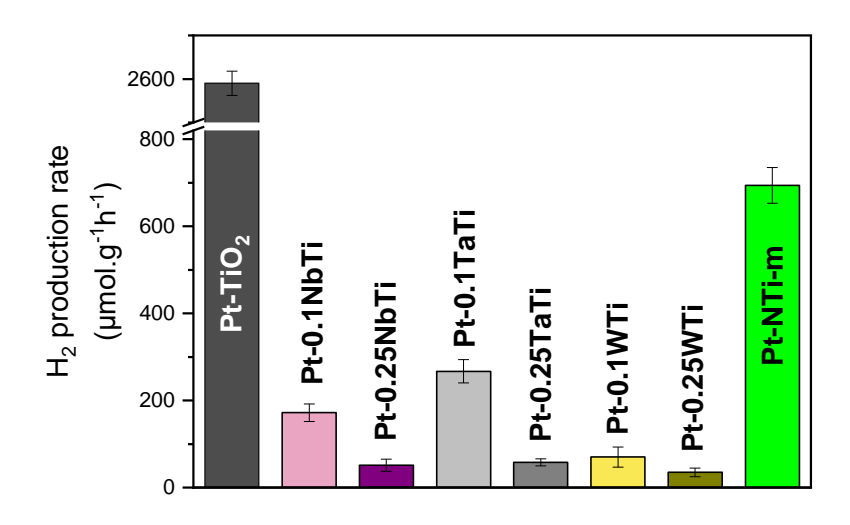


Figure 4.14: Photocatalytic hydrogen production rate of Pt-TiO<sub>2</sub>, Pt-MTi samples and Pt-NTi-m.

The Pt NPs on all the M-doped TiO<sub>2</sub> were distributed similarly to TiO<sub>2</sub>, that is, the Pt NPs were well dispersed on the sample surface without obvious change in particle size. Then, one of the reasons for the decrease of photocatalytic activity of the Pt-MTi samples could be the reduced Pt loading, as proved by ICP-AES. It is worth noting that Pt-0.1NbTi has almost the same Pt loading as Pt-TiO<sub>2</sub>, and significantly more than the Pt-0.25WTi and present also a better activity, even if it remains low compared to pure TiO<sub>2</sub>. On the other hand, the least performant sample is the Pt-0.25WTi, although it has a Pt loading ~6 times that of Pt-0.25NbTi and Pt-0.25TaTi. These results indicate the importance of controlling the distribution of co-catalyst its loading, but other properties might impact the activities of the Pt-MTi samples.

We propose two explanations for these differences: first, as predicted by the theoretical study,<sup>36</sup> the energy state of Nb 4d is quite close to the Ti 3d, while Ta 5d shows a slightly higher position and W 5d a slightly lower position. The hybridization between the cation d orbital and Ti 3d orbital modifies the CBB of M-doped TiO<sub>2</sub>, especially in the case with a high doping concentration. Consequently, the reducing power of the photogenerated electrons can be modified and will change the HER activity. This is consistent with the observed photocatalytic performance in both Pt-0.25MTi and Pt-0.1MTi families which show a better activity for Ta then Nb and finally W.

Secondly, both NTi and TiO<sub>2</sub> samples present a certain amount of rutile beside anatase. It is well known that the presence of these two phases significantly improve the charge separation in photocatalytic reaction. For the N-doped sample, an aggregation of Pt NPs was observed but this could be compensated by the presence of rutile and the visible light absorption brought by the N states above the VBT.

## 3.4 Effect of (M,N)-co-doping on the photocatalytic activities

The (Nb,N) co-doped samples were selected as representative, characterization of other co-doped materials needs to be completed in the future.

## 3.4.1 Characterization of the co-catalyst

#### 3.4.1.1 Elemental analysis

As shown in **Table 4.3,** Although the Pt loading of the (Nb,N) co-doped  $TiO_2$  was doubled compared to the Nb-doped sample, the deposition yield ( $\eta_{dep} = 12\%$ ) is still much lower than that of Pt-TiO<sub>2</sub> ( $\eta_{dep} = 48\%$ ). This indicates that the Pt loading was dominantly determined by the M-doping rather than the nitridation process.

Sample	Pt	wt.%	m . 0/	
	Theoretical	Actual	$\eta_{ m dep} \%$	
Pt-TiO <sub>2</sub>	0.50	$0.24 \pm 0.005$	48 ± 1	
Pt-0.25NbTi	0.50	$0.03 \pm 0.002$	$6 \pm 0.4$	
Pt-0 25NhNTi-m	0.50	$0.06 \pm 0.002$	12 + 0.4	

Table 4.3: Pt loading for Pt-TiO<sub>2</sub>, Pt-0.25NbTi and Pt-0.25NbNTi-m, determined by ICP-AES.

#### 3.4.1.2 SEM characterization

The morphology of the Pt NPs on the surface of the (Nb,N) co-doped  $TiO_2$  was characterized by SEM (**Figure 4.15**). As mentioned earlier, for Pt-0.25NbTi, the NPs were dispersed on the support surface in the form of separated particles. After the nitridation process, both separated Pt NPs and Pt NPs aggregation were observed on the sample surface, suggesting an increase of inhomogeneity of the Pt distribution due to the nitridation (similarly to the NTi sample). However, the size of Pt aggregates on the (Nb, N) co-doped sample (9.6 nm and 17.5 nm, in the dash frame in **Figure 4.15 b**) is smaller than that on the N-doped sample ( $\approx$ 80.0 nm).

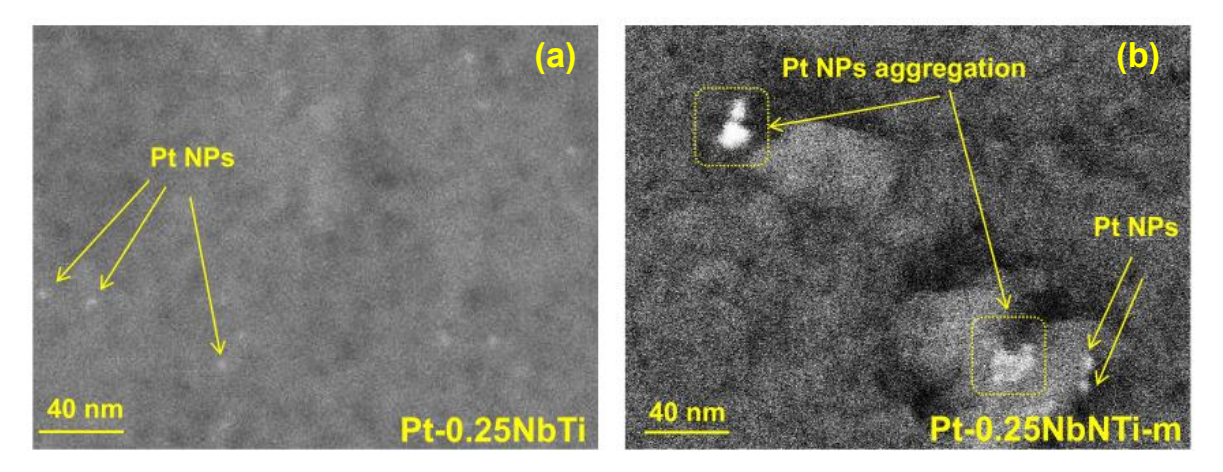
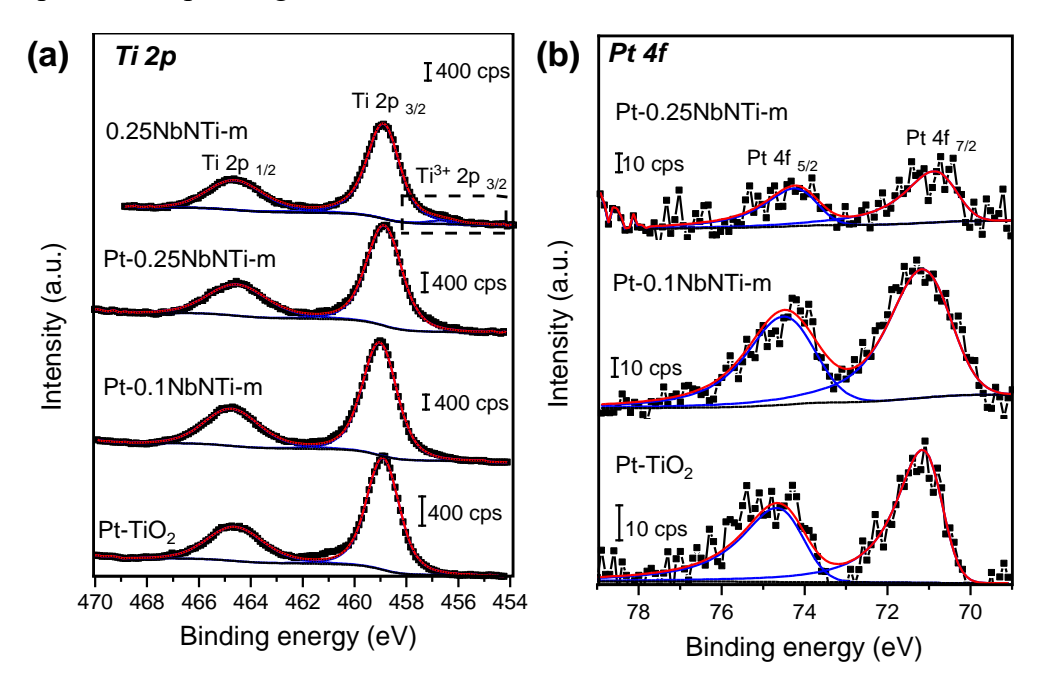


Figure 4.15: SEM images of Pt-0.25NbTi (a) and Pt-0.25NbNTi-m (b).

## 3.4.1.3 XPS analysis

The XPS spectra of the (Nb,N) co-doped TiO<sub>2</sub> deposited with Pt are presented in **Figure 4.16**, for comparison purposes, the spectra of Pt-TiO<sub>2</sub> and the co-doped sample (0.25NbNTi-m) without Pt deposition are used as reference.

In the spectral region of Ti (**Figure 4.16 a**), all the samples present two common peaks, corresponding to Ti<sup>4+</sup>. Besides, it is noted that the signal of Ti<sup>3+</sup> only appears on 0.25NbNTi-m but not on Pt-0.25NbNTi-m counterpart. This might indicate that the Ti<sup>3+</sup> could be oxidized into Ti<sup>4+</sup> during the photocatalytic test. The Nb 3d region for the Nb-containing samples is shown in **Figure S4.1 Page 198**, all three samples exhibit the same doublet peak corresponding to Nb<sup>5+</sup>.



**Figure 4.16:** XPS spectra of Ti 2p (a), and Pt 4f (b) region for Pt-deposited TiO<sub>2</sub> and (Nb,N) codoped TiO<sub>2</sub>. (Black points are the experiment data, red lines are the fitted signals, blue and green lines are different contributions).

The Pt 4f spectral region of the Pt-deposited samples is shown in **Figure 4.16 b**. A common doublet peak located at  $70.8 \pm 0.1$  eV and  $74.1 \pm 0.1$  eV is observed on the three samples, which is assigned to Pt<sup>0</sup>. This suggests that the Pt NPs exist exclusively in the form of metallic Pt, although the (Nb,N) co-doping can change the loading and distribution of Pt NPs. Furthermore, it is noted that the atomic concentration of Pt for Pt-TiO<sub>2</sub> (0.083%) and Pt-0.1NbNTi-m (0.085%) is more than three times that of Pt-0.25NbNTi-m (0.025%), which is consistent with the elemental analysis result.

## 3.4.2 Photocatalytic activities

The photocatalytic performances of the (M,N) co-doped TiO<sub>2</sub> materials are compared to their M-doped counterparts, as shown in **Figure 4.17** and **Table 4.4**. All the (Ta,N) co-doped and (W,N) co-doped samples are less active for hydrogen production compared to the respective M-doped samples. In particular, Pt-0.25WNTi-m does not produce detectable H<sub>2</sub>. For Pt-0.1TaNTi-m and Pt-0.1WNTi-m, a 50.6% and 60.0% decrease in activity occurred. On the contrary, (Nb,N) co-doped TiO<sub>2</sub> presents an improvement of 23.3% for Pt-0.1NbNTi-m and 60.8% for Pt-0.25NbNTi-m.

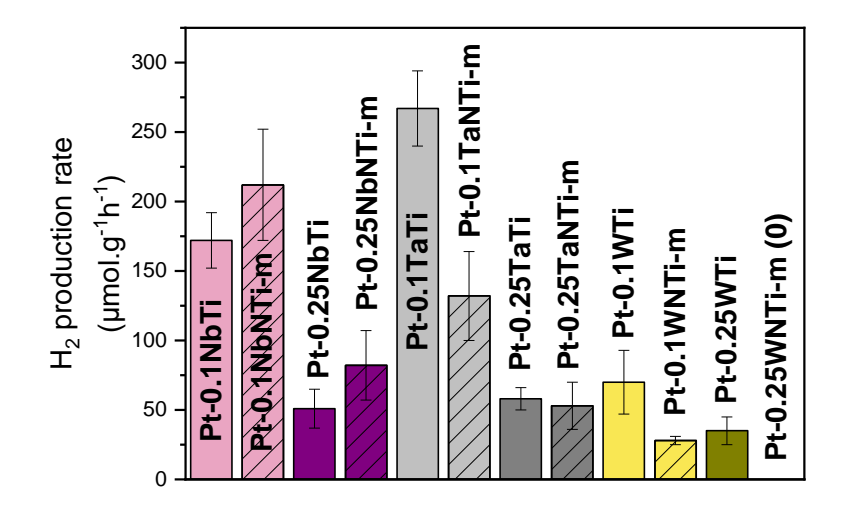


Figure 4.17: Photocatalytic hydrogen production rate of the Pt-MTi and Pt-MNTi samples.

So far, we have not completed the characterization of the Pt-deposited (Ta,N) codoped and (W,N) co-doped TiO<sub>2</sub> samples. Thus, the discussion is based on the following assumption that concluded from the result of (Nb,N) co-doped TiO<sub>2</sub>: First, the Pt-MNTi-m samples have a similar Pt-loading as the respective Pt-MTi samples, but the Pt NPs on the surface of the (M,N) co-doped TiO<sub>2</sub> is less dispersed compared to that on the M-doped samples. Two other opposing effects could also explain the photocatalytic activities of the Pt-deposited (M,N) co-doped TiO<sub>2</sub> samples. On the one hand, conducting co-doping effectively reduced the band gap of the co-doped materials, as confirmed in previous chapters. This contributes to the increase of photon absorption, resulting in a larger quantity of photogenerated electrons that could be used for photocatalytic reactions. In this regard, the results of MB degradation, indicate a more significant effect for Nb and W than for Ta co-doped samples, which can explain the improvement for (Nb,N) co-doped samples and

the decrease for (Ta,N) ones. On the other hand, the modification of the CBB, discussed above, may not have a strong influence on the photocatalytic MB degradation since the mechanism probably involves radicals generated by the photogenerated holes. In the case of HER, a decrease of CBB can have a stronger impact since the photogenerated electrons are involved in the HER reaction. This last aspect can explain the poor performances of (W,N) co-doped TiO<sub>2</sub> samples.

**Table 4.4**: Photocatalytic hydrogen production rate of the different samples shown in Figure 4.18, and the variation between Pt-MNTi-m samples and Pt-MTi samples.

Sample	r(H <sub>2</sub> ) / μmol.g-1h <sup>-1</sup>	variation vs M doped TiO <sub>2</sub> / %	
Pt-0.1NbTi	172		
Pt-0.1NbTi-m	212	23.3	
Pt-0.25NbTi	51		
Pt-0.25NbTi-m	82	60.8	
Pt-0.1TaTi	267		
Pt-0.1TaTi-m	132	-50.6	
Pt-0.25TaTi	58		
Pt-0.25TaTi-m	53	-8.6	
Pt-0.1WTi	70		
Pt-0.1WTi-m	28	-60.0	
Pt-0.25WTi	35		
Pt-0.25WTi-m	0	-100	

## 3.5 Conclusion on photocatalytic hydrogen production

In this part, the synthesized TiO<sub>2</sub>, M-doped TiO<sub>2</sub>, N-doped TiO<sub>2</sub> and (M,N) co-doped TiO<sub>2</sub> were applied to the photocatalytic hydrogen production, using Pt as co-catalyst and methanol as sacrificial electron donor. Starting from the sol-gel synthesized TiO<sub>2</sub>, the effect of Pt deposition methods (chemical reduction *vs* photoreduction) on the photocatalytic activity for hydrogen production was studied. It is shown that the photoreduction method is more favorable for hydrogen production (2590 µmol.g<sup>-1</sup>h<sup>-1</sup>), even though the actual Pt loading is only half that of chemical reduction. The superior activity is ascribed to the small size (~2.5 nm) and high dispertion of the Pt NPs produced by photoreduction, with an exclusive oxidation state of Pt<sup>0</sup>.

Using the Nb-doped and (Nb,N) co-doped samples as representatives, the effect of M-doping, N-doping and (M,N) co-doping on the photocatalytic activity for hydrogen production was studied. All the doped and co-doped materials show decreased activities compared to the undoped TiO<sub>2</sub>, the possible reasons responsible for the observed activity deterioration are the presence of rutile for TiO<sub>2</sub>-based samples and the shift of the CBB due to M-doping. Besides, it is found that a high cation doping concentration resulted in a significant loss of Pt loading, which could be ascribed to its more negatively charged surface. On the other hand, a certain aggregation of Pt NPs was found on the surface of the N-doped and (M.N) co-doped samples.

## 4. Photocatalytic performance for water oxidation

Compared to the photocatalytic hydrogen production reaction, the water oxidation reaction should be less affected by the downward shift of the CBB. Theoretically, the VBT of TiO<sub>2</sub> (~3.0 eV vs NHE) is much lower than the redox potential required for water oxidation (1.23 eV vs NHE), ensuring the thermodynamic feasibility for the photocatalytic reaction. Besides, using the M-doped TiO<sub>2</sub> and (M,N) co-doped TiO<sub>2</sub> materials as the photocatalysts for water oxidation is more frequently reported compared to hydrogen production.<sup>4,37–39</sup> Therefore, the photocatalytic performance of the mentioned materials was evaluated by conducting oxygen evolution reaction, using ruthenium oxide nanoparticles (RuO<sub>x</sub> NPs) as a co-catalyst.

## 4.1 Experimental part

The photocatalytic OER was carried out on the same experimental platform used for hydrogen production, and the RuO<sub>x</sub> NPs was deposited through a photo-deposition process which was combined with the photocatalytic test. In more detail, 50 mg of photocatalyst and 221 μL of the precursor solution RuCl<sub>3</sub> (3.4 mmol.L<sup>-1</sup>, targeting a 0.15 ‰. RuO<sub>x</sub> loading. The raw material is from Merck, 99.98%) were added into 120 mL of Milli-Q water containing 10 mmol.L<sup>-1</sup> NaIO<sub>3</sub> under magnetic stirring (500 rpm). Here, NaIO<sub>3</sub> plays the role of sacrificial electron acceptor for both photodeposition of RuO<sub>x</sub> NPs and photocatalytic OER. After the photocatalytic test, the sample was recovered by filtration with distilled water, dried at 80°C, and then used for characterization. The prepared samples are denoted as RuO<sub>x</sub>-X (X is the sample name). The photocatalytic activities were evaluated using the oxygen production rate, which was calculated by extracting data in the stationary phase of the oxygen evolution curve.

## 4.2 Characterization of $RuO_x$ -deposited $TiO_2$ materials

## 4.2.1 Elemental analysis

As shown in **Table 4.5**, the reference RuO<sub>x</sub>-TiO<sub>2</sub> has a RuO<sub>x</sub> loading of 0.11 wt.% (n  $_{\text{dep}} = 73\%$ ). It is observed that the high concentration M-doping resulted in a decrease in RuO<sub>x</sub> loading, especially in the case of Nb-doping ( $\eta_{dep} = 40\%$ ) and Ta-doping ( $\eta_{dep} = 20\%$ ), but the decrease is less significant than in the case of Pt photodeposition.

_		-	•	
Sampla	RuC	Ox wt.%	an 0/	
Sample	Theoretical	Actual	$\eta_{ m dep}\%$	

**Table 4.5** RuO<sub>x</sub> loading for RuO<sub>x</sub>-TiO<sub>2</sub> and RuO<sub>x</sub>-MTi samples determined by elemental analysis.

From the point of view of surface charge, the M-doped samples have a more negatively charged surface compared to  $TiO_2$ , which should be more favorable for the adsorption of  $Ru^{3+}$ . However, a more negatively charged surface also means that the capture of photogenerated electrons by  $IO_3^-$  may decrease. This probably leads to a decrease in the separation efficiency of the photogenerated charges, and thus limits the  $RuO_x$  deposition. These two opposite effects may determine the final actual  $RuO_x$  loading on a specific sample.

#### 4.2.2 TEM characterization

The morphology of the deposited RuO<sub>x</sub> NPs on TiO<sub>2</sub> and Ta-doped TiO<sub>2</sub> was characterized by TEM, as shown in **Figure 4.18**. The RuO<sub>x</sub> NPs, which are extremely fine, are observed to be dispersed on the surface of both samples. It seems that the RuO<sub>x</sub> NPs for RuO<sub>x</sub>-0.25TaTi are denser and have a larger particle size compared to that of RuO<sub>x</sub>-TiO<sub>2</sub>. However, it remains sub-nanometric and in the current image resolution and due to the poor contrast, it is difficult to determine the exact value of particle size.

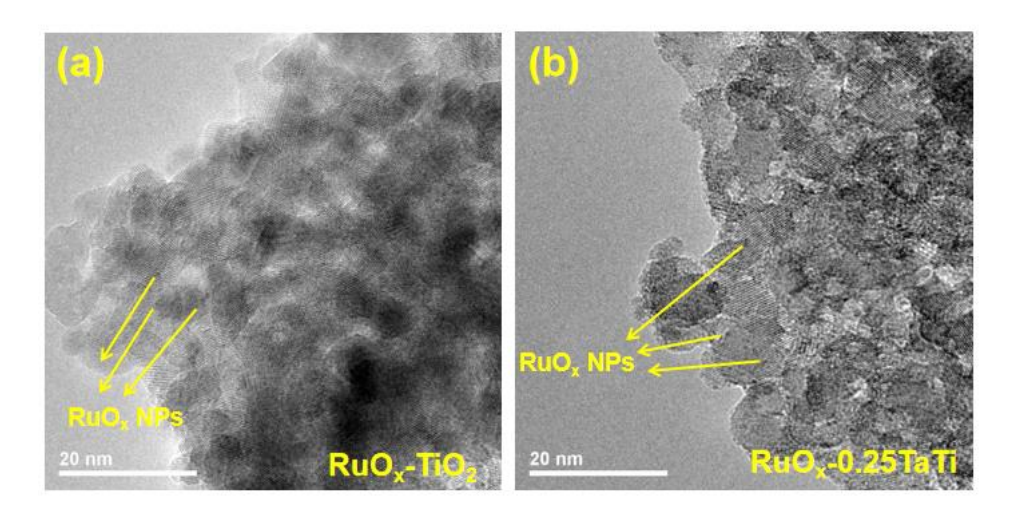


Figure 4.18: TEM images of RuO<sub>x</sub>-TiO<sub>2</sub> (a) and RuO<sub>x</sub>-0.25TaTi (b).

#### 4.2.3 XPS analysis

The XPS spectra of RuO<sub>x</sub>-TiO<sub>2</sub> are presented in **Figure 4.19**, with reference to TiO<sub>2</sub>. In the Ti 2p spectral region (**Figure S4.2**, **Page 198**), RuO<sub>x</sub>-TiO<sub>2</sub> shows the same characteristic peaks as TiO<sub>2</sub>, corresponding to Ti<sup>4+</sup>. In the region of O 1s (**Figure 4.19 a**), the peak ratio between O 1s B and O 1s A for RuO<sub>x</sub>-TiO<sub>2</sub> and TiO<sub>2</sub> is 0.51 and 0.23, respectively. The increased peak intensity of O 1s B for RuO<sub>x</sub>-TiO<sub>2</sub> might be due to the adsorbed oxygen on the deposited RuO<sub>x</sub> NPs, which provide the active sites for oxygen evolution. Besides, the other two peaks located at 528.8 eV and 530.2 eV are attributed to the oxygen in the O-Ru<sup>4+</sup> and O-Ru<sup>6+</sup> environment, respectively.<sup>40</sup>

**Figure 4.19 b** presents the spectral region of Ru 3d and C 1s. Two doublets that are attributed to Ru are observed. The first one displays the peaks at 281.5 eV and 285.6 eV, corresponding to the 3d  $_{5/2}$  and 3d  $_{3/2}$  of Ru<sup>4+</sup>,<sup>41</sup> and the second one with peaks located at

283.3 eV and 287.4 eV are assigned to Ru<sup>6+</sup>.<sup>42</sup> Therefore, the RuO<sub>x</sub> NPs deposited on the TiO<sub>2</sub> surface exist in the form of both RuO<sub>2</sub> and RuO<sub>3</sub>. The holes generated from the energy level in VB have a stronger oxidizing power that can lead to this higher oxidation state of Ru. Nevertheless, considering that the XPS analysis was done after the photocatalytic test, we cannot exclude that a part of RuO<sub>3</sub> was formed during the OER.

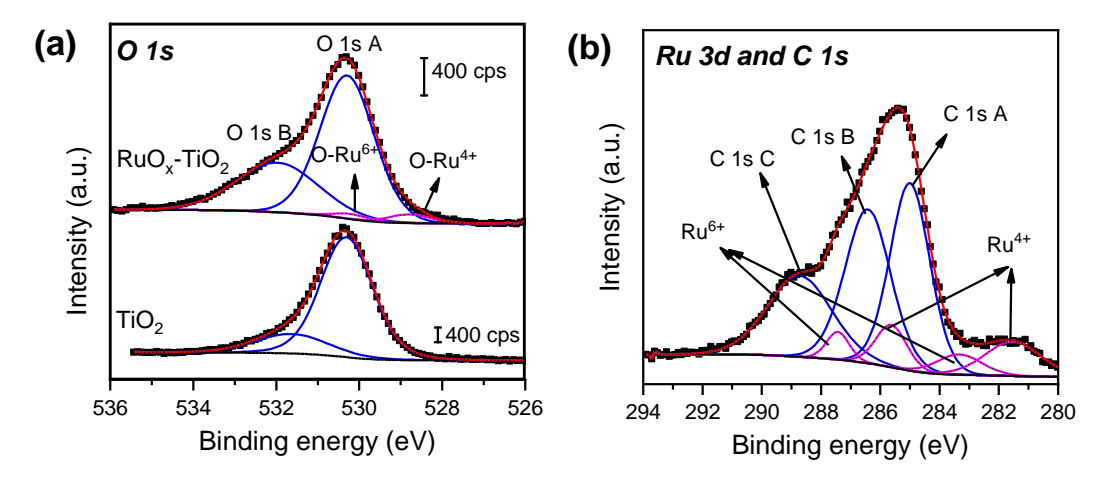


**Figure 4.19 :** XPS spectra of O 1s (a) and Ru 3d and C1s (b) region for RuO<sub>x</sub>-TiO<sub>2</sub> and TiO<sub>2</sub>. (Black points are the experiment data, red lines are the fitted signals, blue and magenta lines are different contributions).

## 4.3 Photocatalytic activities for water oxidation

The photocatalytic performances of RuO<sub>x</sub>-deposited TiO<sub>2</sub> materials are shown in **Figure 4.20.** The RuO<sub>x</sub>-TiO<sub>2</sub> shows an oxygen production rate of 14 μmol.g<sup>-1</sup>h<sup>-1</sup>. Improved photocatalytic activity is observed on RuO<sub>x</sub>-0.25NbTi and RuO<sub>x</sub>-0.25TaTi but not on RuO<sub>x</sub>-0.25WTi. In particular, RuO<sub>x</sub>-0.25Ta exhibits the highest oxygen production rate (49 μmol.g<sup>-1</sup>h<sup>-1</sup>) among all the tested samples, although it has the lowest RuO<sub>x</sub> loading. W-doped sample is the least active whether it was used for hydrogen production or water oxidation.

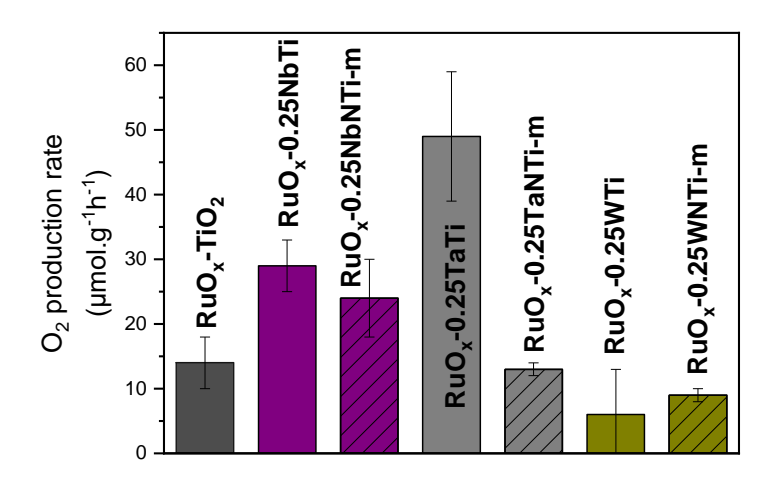


**Figure 4.20:** Photocatalytic oxygen production rate of RuO<sub>x</sub>-deposited TiO<sub>2</sub>, M-doped TiO<sub>2</sub> and (M,N) co-doped TiO<sub>2</sub>.

After the nitridation, no obvious change in the photocatalytic activity is observed on the (M,N) co-doped samples, considering the current experimental standard deviation. The only exception is for RuO<sub>x</sub>-0.25TaNTi-m which endures a significant decrease in oxygen production rate (13 µmol.g<sup>-1</sup>h<sup>-1</sup>) compared to the Ta-doped sample. This limited improvement due to co-doping suggests that the increase in photon absorption is counterbalanced by other properties. On the one hand, this is probably due to the change in the morphology (loading, particle size, oxidation state...) of the RuO<sub>x</sub> NPs that need to be investigated deeper. On the other hand, the introduction of N, raises the valence band top and this could reduce the oxidative power of photogenerated holes. To confirm the proposed hypothesis, systematic characterization of the RuO<sub>x</sub> NPs needs to be complemented.

## 4.4 Conclusion on photocatalytic water oxidation.

To conclude, we have applied the synthesized TiO<sub>2</sub>, M-doped and (M,N) co-doped TiO<sub>2</sub> materials to the photocatalytic water oxidation reaction. RuO<sub>x</sub> NPs were deposited on the sample surface as co-catalysts and NaIO<sub>3</sub> was used as a sacrificial electron acceptor to consume the photogenerated electrons. Sub-nanometric RuO<sub>x</sub> NPs were dispersed on the surface of TiO<sub>2</sub> and 0.25TaTi by the photo-deposition method which was combined with the in-situ photocatalytic test. Multiple oxidation states (Ru<sup>4+</sup> and Ru<sup>6+</sup>) of the RuO<sub>x</sub> NPs on the surface of TiO<sub>2</sub> were confirmed by XPS analysis. Compared to RuO<sub>x</sub>-TiO<sub>2</sub>, superior photocatalytic activity for water oxidation was observed on the Ta-doped and Nb-doped samples but not on the W-doped sample. However, no significant improvement was observed for the (M,N) co-doped samples. Nevertheless, more characterization is needed to reveal the correlation between the co-catalyst deposit, intrinsic defects, and photocatalytic activity.

## 5. Dual co-catalysts modified TiO<sub>2</sub> material

#### 5.1 Context

The utilization of dual co-catalysts has drawn significant attention in recent attempts to boost the photocatalytic performance of TiO<sub>2</sub>. Synergetic effects of components could facilitate the charge carrier separation and photocatalytic reaction kinetics. <sup>43</sup> In an ideal situation, co-catalyst promoting photocatalytic reduction and oxidation reaction (*i.e.* reduction co-catalyst and oxidation co-catalyst) are deposited separately onto the TiO<sub>2</sub> surface. It is expected that the photogenerated electrons and holes can be extracted simultaneously by the reduction co-catalyst and oxidation co-catalyst, respectively. Therefore, the charge separation efficiency could be further enhanced compared to the mono-cocatalyst counterpart. Numerous efforts have been devoted to depositing dual co-catalysts on TiO<sub>2</sub> over the past decade. <sup>44–47</sup> Using Pt and RuO<sub>2</sub> as the dual co-catalyst has been reported to effectively enhance the photocatalytic performance for hydrogen production, CO oxidation, and pollutant degradation. <sup>48–50</sup>

Encouraged by these successful precedents, we have conducted a preliminary attempt to deposit both Pt and RuO<sub>x</sub> NPs onto the surface of the sol-gel synthesized TiO<sub>2</sub>. The

activity of the dual co-catalyst decorated material was evaluated by conducting photocatalytic hydrogen production and water oxidation reaction, respectively.

## 5.2 Experimental part

## 5.2.1 Preparation of dual co-catalyst modified TiO<sub>2</sub>

The TiO<sub>2</sub> decorated with dual co-catalyst was prepared by a two-step photo-deposition method, in which Pt and RuO<sub>x</sub> NPs were successively deposited on the TiO<sub>2</sub> surface. Two different deposition sequences were conducted:

- (i) RuO<sub>x</sub> deposition first followed by Pt-deposition. Step-1 for RuO<sub>x</sub> deposition was carried out through the same procedure as described in **part 4.1**. Then the filtrated RuO<sub>x</sub>-deposited sample was used for the Pt-deposition in Step-2, the operation was the same as described in **part 3.2.2.2**. Since the whole sample cannot be recovered after the filtration, the quantity of H<sub>2</sub>PtCl<sub>6</sub> solution used in Step-2 was proportionally reduced, targeting a theoretical Pt loading of 0.5%. This sample was denoted as Pt-TiO<sub>2</sub>(RuO<sub>x</sub>).
- (ii) Pt deposition first followed by RuO<sub>x</sub>-deposition. Step-1 for Pt deposition was carried out through the same procedure as described in **part 3.2.2.2**. Then the filtrated Pt-deposited sample was used for the RuO<sub>x</sub>-deposition in Step-2, the operation was the same as described in **part 4.1**. Based on the sample mass after the filtration, the quantity of RuCl<sub>3</sub> solution and NaIO<sub>3</sub> used in Step-2 was also proportionally reduced, targeting a theoretical RuO<sub>x</sub> loading of 0.15%. The obtained sample is denoted as RuO<sub>x</sub>-TiO<sub>2</sub>(Pt).

## 5.2.2 Photocatalytic experiment

The prepared samples were used as catalysts for both photocatalytic hydrogen production and water oxidation reactions. For hydrogen production, the samples were tested in 120 mL Milli-Q water/methanol mixture (90/10, volume%). For water oxidation, the samples were tested in 120 mL Milli-Q water containing 10 mmol.L<sup>-1</sup> NaIO<sub>3</sub>.

## 5.3 Photocatalytic activities of dual co-catalyst deposited TiO<sub>2</sub>

**Figure 4.21 a** presents the photocatalytic activity of the dual co-catalyst deposited TiO<sub>2</sub> for hydrogen production, with reference to the Pt-deposited TiO<sub>2</sub>. The expected improvement of hydrogen production was not observed on the dual co-catalyst deposited TiO<sub>2</sub>, both of them were less active compared to Pt-TiO<sub>2</sub>. in particular, for RuO<sub>x</sub>-TiO<sub>2</sub>(Pt), the hydrogen production rate significantly dropped to 144 μmol.g<sup>-1</sup>h<sup>-1</sup>.

The oxygen production rates of the dual co-catalyst deposited  $TiO_2$  during the water oxidation reaction were compared to  $RuO_x$ - $TiO_2$ , as shown in **Figure 4.21 b**. It is noted that the photocatalytic activity of Pt- $TiO_2(RuO_x)$  was completely inhibited. On the other hand, a superior photocatalytic performance is observed on  $RuO_x$ - $TiO_2(Pt)$ , with an oxygen production rate  $\sim$ 3.6 times as  $RuO_x$ - $TiO_2$ .

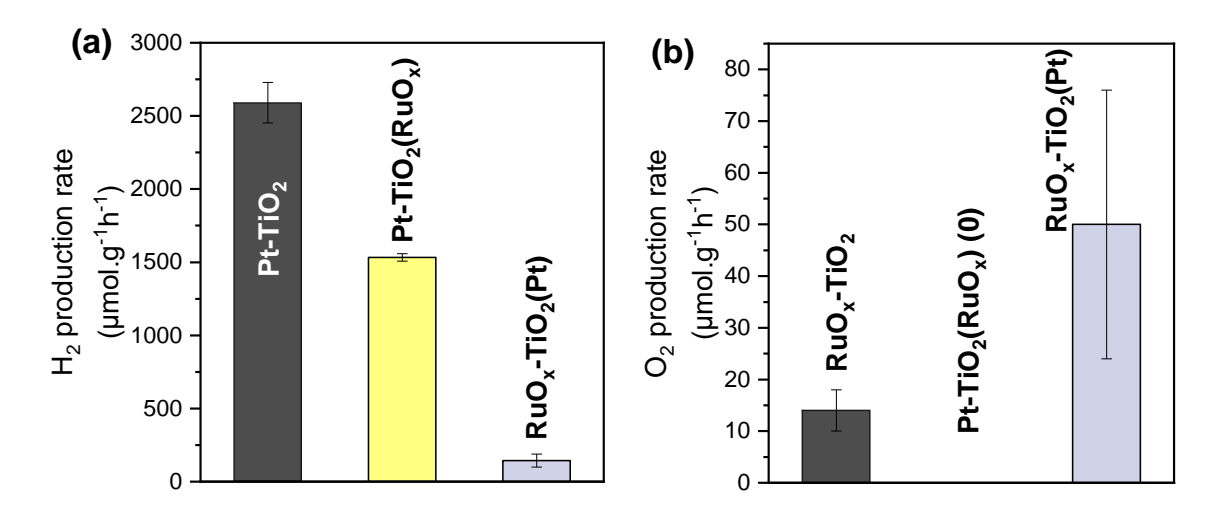


**Figure 4.21 :** Photocatalytic hydrogen (a) and oxygen (b) production rate of the TiO<sub>2</sub> deposited with dual co-catalyst.

From the result, we can conclude that the deposition sequence of Pt and RuO<sub>x</sub> plays an important role in determining the photocatalytic activity for a specific reaction. Depositing Pt after RuO<sub>x</sub> is more beneficial for hydrogen production, while the opposite sequence is more favorable for water oxidation. The above preliminary attempts suggest that the dual co-catalyst deposition strategy is promising to further enhance the photocatalytic activity of TiO<sub>2</sub> material, especially for water oxidation reactions. Therefore, it is worth applying it to the M-doped and (M,N) co-doped TiO<sub>2</sub> in the follow-up studies.

## 6. Conclusion

In conclusion, this chapter is devoted to the analysis of the photocatalytic results of the prepared M-doped and (M,N) co-doped catalysts for different types of photocatalytic reactions. In the first part, the photocatalytic activities of the M-doped and (M,N) co-doped samples were evaluated by degradation of MB. Then, the M-doped TiO<sub>2</sub> and the (M,N) co-doped TiO<sub>2</sub> produced by mild nitridation were applied to photocatalytic hydrogen production and photocatalytic water oxidation, respectively.

Based on the result of photocatalytic degradation of MB, we have concluded that the (Nb,N) co-doped TiO<sub>2</sub> and (Ta,N) co-doped TiO<sub>2</sub> exhibit similar photocatalytic behaviors, where the nitridation condition significantly influences the photocatalytic activity. On opposite, The photocatalytic performance of the (W,N) co-doped TiO<sub>2</sub> is hardly affected by the nitridation conditions. Under the illumination of UV light, a deterioration of photocatalytic activity was observed for (Nb,N) and (Ta,N) samples submitted to harsh nitridation, but not for 0.25WNTi-h. The result confirms that Ti<sup>3+</sup> could act as charge recombination centers, resulting in a decrease in the degradation rate. On the opposite, Vo<sup>+</sup> and W<sup>5+</sup> identified in Chapter 3 were proposed to have negligible influence on the photocatalytic degradation process. By comparing the photocatalytic results obtained in this chapter with those in Chapter 2, we have pointed out the important influence of MB adsorption on the experimental result of photocatalytic degradation. It is proposed that for a

higher MB/photocatalyst ratio, excessive dye molecules may be adsorbed on the sample surface. Consequently, the generation of radical species could be slowed down due to this coverage of the material surface by the adsorbed MB molecules (or their degradation products), leading to a decreased degradation rate. This phenomenon depends on the surface properties of the photocatalyst and zetametry indicates that M-doped samples suffered more than TiO<sub>2</sub> of this excessive adsorption of MB, since their surfaces are more negatively charged.

For the photocatalytic hydrogen production, Pt and methanol were used as co-catalyst and sacrificial electron donor, respectively. It was shown that the Pt-deposition method has a significant effect on the hydrogen production rate. Using TiO<sub>2</sub> as a reference material, we have found that the photoreduction method is more favorable for hydrogen compared to the chemical reduction method due to smaller co-catalyst particle size, the presence of Pt<sup>0</sup> (confirmed by XPS), and despite a lower loading. It was also observed that different doping strategies have a significant impact on the form of the deposited Pt NPs. A high concentration of Nb-doping resulted in a strong reduction of the Pt loading. This phenomenon was also ascribed to the more negative charge on the material surface. On the other hand, it is noted that Pt NPs tend to aggregate on the surfaces of N-doped and (Nb,N) co-doped TiO<sub>2</sub>. According to the photocatalytic results, all the materials subjected to doping and co-doping exhibit diminished activities compared to TiO2. The reasons might be the total absence of rutile in these samples compared to TiO<sub>2</sub> and N-doped TiO<sub>2</sub> and a change in the reductive power of the photogenerated electrons due to the shift of CBB caused by the d orbital of the doping cations. Except for the Nb-based samples, there is no obvious improvement in the photocatalytic activity of the (M,N) co-doped TiO<sub>2</sub> in comparison with their M-doped counterparts, which might be attributed to the aggregation of Pt NPs.

The synthesized TiO<sub>2</sub>, M-doped and (M,N) co-doped TiO<sub>2</sub> materials were also tested for photocatalytic water oxidation reaction, in which RuO<sub>x</sub> NPs and NaIO<sub>3</sub> were used as the co-catalyst and sacrificial electron acceptor. It is shown that extremely fine and dispersed RuO<sub>x</sub> NPs were successfully deposited on the surface of TiO<sub>2</sub> materials, by the photodeposition method. The oxygen production rates of the different samples indicate that the Ta-doped and Nb-doped TiO<sub>2</sub> are more advantageous for photocatalytic water oxidation. Similar to the photocatalytic hydrogen production reaction, no further enhancement of the activity was achieved on the (M,N) co-doped materials. This indicates that the increase in visible absorption does not contribute to an enhanced overall photocatalytic activity. Further characterizations are needed to reveal the correlation between the co-catalyst deposit, the intrinsic defects of the photocatalyst and the photocatalytic activity.

Finally, we have carried out a preliminary study of the photocatalytic properties of  $TiO_2$  deposited with both Pt and  $RuO_x$ . The co-catalysts were deposited successively by a 2-step photo-deposition method, and the photocatalytic activities of the prepared samples were evaluated by hydrogen production reaction and water oxidation reaction. It is shown that the deposition sequence of Pt and  $RuO_x$  has an important impact on the resultant photocatalytic activity for a specific type of reaction. Depositing Pt after  $RuO_x$  is more beneficial for hydrogen production, while the opposite sequence is more favorable for water oxidation.

The photocatalytic results suggest a prospect to further enhance the photocatalytic activity of  $TiO_2$  material by the strategy of dual co-catalyst deposition, especially for water oxidation reactions. We suppose that combining the strategy of dual co-catalyst deposition and doping/co-doping could be an interesting topic in the future.

## 7. References

- (1) Osterloh, F. E. Photocatalysis versus Photosynthesis: A Sensitivity Analysis of Devices for Solar Energy Conversion and Chemical Transformations. *ACS Energy Lett.* **2017**, *2* (2), 445–453. https://doi.org/10.1021/acsenergylett.6b00665.
- (2) McCrory, C. C. L.; Jung, S.; Ferrer, I. M.; Chatman, S. M.; Peters, J. C.; Jaramillo, T. F. Benchmarking Hydrogen Evolving Reaction and Oxygen Evolving Reaction Electrocatalysts for Solar Water Splitting Devices. *J. Am. Chem. Soc.* **2015**, *137* (13), 4347–4357. https://doi.org/10.1021/ja510442p.
- (3) Mureithi, A. W.; Sun, Y.; Mani, T.; Howell, A. R.; Zhao, J. Impact of Hole Scavengers on Photocatalytic Reduction of Nitrobenzene Using Cadmium Sulfide Quantum Dots. *Cell Reports Physical Science* **2022**, *3* (5), 100889. https://doi.org/10.1016/j.xcrp.2022.100889.
- (4) Breault, T. M.; Brancho, J. J.; Guo, P.; Bartlett, B. M. Visible Light Water Oxidation Using a Co-Catalyst Loaded Anatase-Structured Ti<sub>1-(5x/4)</sub>Nb<sub>x</sub>O<sub>2-y-δ</sub>N<sub>y</sub> Compound. *Inorg. Chem.* **2013**, *52* (16), 9363–9368. https://doi.org/10.1021/ic400932m.
- (5) Giorno, L. Membranes That Filter and Destroy Pollutants. Nat. Nanotechnol. 2022, 17 (4), 334–335. https://doi.org/10.1038/s41565-021-01064-2.
- (6) Al-Ghouti, M. A.; Al-Absi, R. S. Mechanistic Understanding of the Adsorption and Thermodynamic Aspects of Cationic Methylene Blue Dye onto Cellulosic Olive Stones Biomass from Wastewater. *Sci Rep* **2020**, *10* (1), 15928. https://doi.org/10.1038/s41598-020-72996-3.
- (7) Kang, J.-G.; Sohn, Y. Interfacial Nature of Ag Nanoparticles Supported on TiO<sub>2</sub> Photocatalysts. *J Mater Sci* **2012**, 47 (2), 824–832. https://doi.org/10.1007/s10853-011-5860-6.
- (8) Lakshmanareddy, N.; Navakoteswara Rao, V.; Cheralathan, K. K.; Subramaniam, E. P.; Shankar, M. V. Pt/TiO<sub>2</sub> Nanotube Photocatalyst Effect of Synthesis Methods on Valance State of Pt and Its Influence on Hydrogen Production and Dye Degradation. *Journal of Colloid and Interface Science* **2019**, *538*, 83–98. https://doi.org/10.1016/j.jcis.2018.11.077.
- (9) Ohyama, J.; Yamamoto, A.; Teramura, K.; Shishido, T.; Tanaka, T. Modification of Metal Nanoparticles with TiO<sub>2</sub> and Metal–Support Interaction in Photodeposition. *ACS Catal.* **2011**, *I* (3), 187–192. https://doi.org/10.1021/cs100072k.
- (10) Haselmann, G. M.; Baumgartner, B.; Wang, J.; Wieland, K.; Gupta, T.; Herzig, C.; Limbeck, A.; Lendl, B.; Eder, D. In Situ Pt Photodeposition and Methanol Photooxidation on Pt/TiO<sub>2</sub>: Pt-Loading-Dependent Photocatalytic Reaction Pathways Studied by Liquid-Phase Infrared Spectroscopy. *ACS Catal.* **2020**, *10* (5), 2964–2977. https://doi.org/10.1021/acscatal.9b05588.
- (11) Dasgupta, N. P.; Liu, C.; Andrews, S.; Prinz, F. B.; Yang, P. Atomic Layer Deposition of Platinum Catalysts on Nanowire Surfaces for Photoelectrochemical Water Reduction. *J. Am. Chem. Soc.* **2013**, *135* (35), 12932–12935. https://doi.org/10.1021/ja405680p.
- (12) Ma, L. L.; Cui, Z. D.; Li, Z. Y.; Zhu, S. L.; Liang, Y. Q.; Yin, Q. W.; Yang, X. J. The Fabrication of SnSe/Ag Nanoparticles on TiO<sub>2</sub> Nanotubes. *Materials Science and Engineering: B* **2013**, *178* (1), 77–82. https://doi.org/10.1016/j.mseb.2012.10.006.
- (13) Murata, A.; Oka, N.; Nakamura, S.; Shigesato, Y. Visible-Light Active Photocatalytic WO<sub>3</sub> Films Loaded with Pt Nanoparticles Deposited by Sputtering. *Journal of Nanoscience and Nanotechnology* **2012**, *12* (6), 5082–5086. https://doi.org/10.1166/jnn.2012.4894.
- (14) Bamwenda, G. R.; Tsubota, S.; Nakamura, T.; Haruta, M. Photoassisted Hydrogen Production from a Water-Ethanol Solution: A Comparison of Activities of Au-TiO<sub>2</sub> and Pt-TiO<sub>2</sub>. *Journal of Photochemistry and Photobiology A: Chemistry* **1995**, *89* (2), 177–189. https://doi.org/10.1016/1010-6030(95)04039-I.
- (15) Catalysts | Free Full-Text | Cocatalysts for Photocatalytic Overall Water Splitting: A Mini Review. https://www.mdpi.com/2073-4344/13/2/355 (accessed 2023-08-10).

- (16) Vaiano, V.; Iervolino, G.; Sannino, D.; Murcia, J. J.; Hidalgo, M. C.; Ciambelli, P.; Navío, J. A. Photocatalytic Removal of Patent Blue V Dye on Au-TiO<sub>2</sub> and Pt-TiO<sub>2</sub> Catalysts. *Applied Catalysis B: Environmental* **2016**, *188*, 134–146. https://doi.org/10.1016/j.apcatb.2016.02.001.
- (17) Liu, Y.; Xiao, Z.; Cao, S.; Li, J.; Piao, L. Controllable Synthesis of Au-TiO<sub>2</sub> Nanodumbbell Photocatalysts with Spatial Redox Region. *Chinese Journal of Catalysis* **2020**, *41* (1), 219–226. https://doi.org/10.1016/S1872-2067(19)63477-7.
- (18) Zhang, F.; Jin, R.; Chen, J.; Shao, C.; Gao, W.; Li, L.; Guan, N. High Photocatalytic Activity and Selectivity for Nitrogen in Nitrate Reduction on Ag/TiO<sub>2</sub> Catalyst with Fine Silver Clusters. *Journal of Catalysis* **2005**, *232* (2), 424–431. https://doi.org/10.1016/j.jcat.2005.04.014.
- (19) Busser, G. W.; Mei, B.; Muhler, M. Optimizing the Deposition of Hydrogen Evolution Sites on Suspended Semiconductor Particles Using On-Line Photocatalytic Reforming of Aqueous Methanol Solutions. *ChemSusChem* **2012**, *5* (11), 2200–2206. https://doi.org/10.1002/cssc.201200374.
- (20) Chen, X.; Chen, W.; Gao, H.; Yang, Y.; Shangguan, W. In Situ Photodeposition of NiO<sub>X</sub> on CdS for Hydrogen Production under Visible Light: Enhanced Activity by Controlling Solution Environment. *Applied Catalysis B: Environmental* **2014**, *152–153*, 68–72. https://doi.org/10.1016/j.apcatb.2014.01.022.
- (21) Jiang, X.; Fu, X.; Zhang, L.; Meng, S.; Chen, S. Photocatalytic Reforming of Glycerol for H<sub>2</sub> Evolution on Pt/TiO<sub>2</sub>: Fundamental Understanding the Effect of Co-Catalyst Pt and the Pt Deposition Route. *J. Mater. Chem. A* **2015**, *3* (5), 2271–2282. https://doi.org/10.1039/C4TA06052K.
- (22)  $J \mid Free Full-Text \mid Photocatalytic H_2 Production on Au/TiO_2$ : Effect of Au Photodeposition on Different TiO\_2 Crystalline Phases. https://www.mdpi.com/2571-8800/5/1/6 (accessed 2023-08-10).
- (23) Singhal, N.; Kumar, U. Noble Metal Modified TiO<sub>2</sub>: Selective Photoreduction of CO<sub>2</sub> to Hydrocarbons. *Molecular Catalysis* **2017**, *439*, 91–99. https://doi.org/10.1016/j.mcat.2017.06.031.
- (24) Gunji, T.; Tsuda, T.; Jeevagan, A. J.; Hashimoto, M.; Tanabe, T.; Kaneko, S.; Miyauchi, M.; Saravanan, G.; Abe, H.; Matsumoto, F. Visible Light Induced Decomposition of Organic Compounds on WO<sub>3</sub> Loaded PtPb Co-Catalysts. *Catalysis Communications* **2014**, *56*, 96–100. https://doi.org/10.1016/j.catcom.2014.07.013.
- (25) Li, J.; Xu, J.; Dai, W.-L.; Fan, K. Dependence of Ag Deposition Methods on the Photocatalytic Activity and Surface State of TiO<sub>2</sub> with Twistlike Helix Structure. *J. Phys. Chem. C* **2009**, *113* (19), 8343–8349. https://doi.org/10.1021/jp8114012.
- (26) Iizuka, K.; Wato, T.; Miseki, Y.; Saito, K.; Kudo, A. Photocatalytic Reduction of Carbon Dioxide over Ag Cocatalyst-Loaded ALa<sub>4</sub>Ti<sub>4</sub>O<sub>15</sub> (A = Ca, Sr, and Ba) Using Water as a Reducing Reagent. *J. Am. Chem. Soc.* **2011**, *133* (51), 20863–20868. https://doi.org/10.1021/ja207586e.
- (27) Abe, R.; Higashi, M.; Domen, K. Overall Water Splitting under Visible Light through a Two-Step Photoexcitation between TaON and WO3 in the Presence of an Iodate–Iodide Shuttle Redox Mediator. *ChemSusChem* **2011**, *4* (2), 228–237. https://doi.org/10.1002/cssc.201000333.
- (28) Van Rheenen, P. R.; McKelvy, M. J.; Glaunsinger, W. S. Synthesis and Characterization of Small Platinum Particles Formed by the Chemical Reduction of Chloroplatinic Acid. *Journal of Solid State Chemistry* **1987**, *67* (1), 151–169. https://doi.org/10.1016/0022-4596(87)90350-1.
- (29) Osaki, J.; Yoda, M.; Takashima, T.; Irie, H. Selective Loading of Platinum or Silver Cocatalyst onto a Hydrogen-Evolution Photocatalyst in a Silver-Mediated All Solid-State Z-Scheme System for Enhanced Overall Water Splitting. *RSC Adv 9* (71), 41913–41917. https://doi.org/10.1039/c9ra09421k.
- (30) Yue, J.; Suchomski, C.; Voepel, P.; Ellinghaus, R.; Rohnke, M.; Leichtweiss, T.; Elm, M. T.; Smarsly, B. M. Mesoporous Niobium-Doped Titanium Dioxide Films from the Assembly of Crystalline Nanoparticles: Study on the Relationship between the Band Structure, Conductivity and Charge Storage Mechanism. *J. Mater. Chem. A* **2017**, *5* (5), 1978–1988. https://doi.org/10.1039/C6TA06840E.

- (31) Shuzhong, D.; Fanhua, X.; Jingfa, D. The Adsorption of Oxygen and the Oxidation of Methanol on Silver-Platinum Alloys. *Journal of Catalysis* **1988**, *109* (1), 170–179. https://doi.org/10.1016/0021-9517(88)90195-9.
- (32) Marouazi, H. E. Élaboration, caractérisation et évaluation photocatalytique de matériaux de type TiO<sub>2</sub> dopé graphène.
- (33) Cao, F.; Xiong, J.; Wu, F.; Liu, Q.; Shi, Z.; Yu, Y.; Wang, X.; Li, L. Enhanced Photoelectrochemical Performance from Rationally Designed Anatase/Rutile TiO<sub>2</sub> Heterostructures. *ACS Appl. Mater. Interfaces* **2016**, *8* (19), 12239–12245. https://doi.org/10.1021/acsami.6b03842.
- (34) Dessal, C.; Martínez, L.; Maheu, C.; Len, T.; Morfin, F.; Rousset, J. L.; Puzenat, E.; Afanasiev, P.; Aouine, M.; Soler, L.; Llorca, J.; Piccolo, L. Influence of Pt Particle Size and Reaction Phase on the Photocatalytic Performances of Ultradispersed Pt/TiO<sub>2</sub> Catalysts for Hydrogen Evolution. *Journal of Catalysis* **2019**, *375*, 155–163. https://doi.org/10.1016/j.jcat.2019.05.033.
- (35) Wang, D.; Liu, Z.-P.; Yang, W.-M. Revealing the Size Effect of Platinum Cocatalyst for Photocatalytic Hydrogen Evolution on TiO<sub>2</sub> Support: A DFT Study. *ACS Catal.* **2018**, *8* (8), 7270–7278. https://doi.org/10.1021/acscatal.8b01886.
- (36) Yin, W.-J.; Tang, H.; Wei, S.-H.; Al-Jassim, M. M.; Turner, J.; Yan, Y. Band Structure Engineering of Semiconductors for Enhanced Photoelectrochemical Water Splitting: The Case of TiO<sub>2</sub>. *Phys. Rev. B* **2010**, *82* (4), 045106. https://doi.org/10.1103/PhysRevB.82.045106.
- (37) Nishioka, S.; Yanagisawa, K.; Lu, D.; Vequizo, J. J. M.; Yamakata, A.; Kimoto, K.; Inada, M.; Maeda, K. Enhanced Water Splitting through Two-Step Photoexcitation by Sunlight Using Tantalum/Nitrogen-Codoped Rutile Titania as a Water Oxidation Photocatalyst. *Sustainable Energy Fuels* **2019**, *3* (9), 2337–2346. https://doi.org/10.1039/C9SE00289H.
- (38) Nakada, A.; Nishioka, S.; Vequizo, J. J. M.; Muraoka, K.; Kanazawa, T.; Yamakata, A.; Nozawa, S.; Kumagai, H.; Adachi, S.; Ishitani, O.; Maeda, K. Solar-Driven Z-Scheme Water Splitting Using Tantalum/Nitrogen Co-Doped Rutile Titania Nanorod as an Oxygen Evolution Photocatalyst. *J. Mater. Chem. A* **2017**, *5* (23), 11710–11719. https://doi.org/10.1039/C6TA10541F.
- (39) Nishioka, S.; Kobayashi, M.; Lu, D.; Kakihana, M.; Maeda, K. Selective Synthesis and Photocatalytic Oxygen Evolution Activities of Tantalum/Nitrogen-Codoped Anatase, Brookite and Rutile Titanium Dioxide. *BCSJ* **2019**, *92* (6), 1032–1038. https://doi.org/10.1246/bcsj.20190037.
- (40) Manríquez, M. E.; Noreña, L. E.; Wang, J. A.; Chen, L.; Salmones, J.; González-García, J.; Reza, C.; Tzompantzi, F.; Hernández Cortez, J. G.; Ye, L.; Xie, H. One-Pot Synthesis of Ru-Doped ZnO Oxides for Photodegradation of 4-Chlorophenol. *International Journal of Photoenergy* **2018**, *2018*, e7605306. https://doi.org/10.1155/2018/7605306.
- (41) Huang, C. S.; Houalla, M.; Hercules, D. M.; Kibby, C. L.; Petrakis, L. Comparison of Catalysts Derived from Oxidation of Ruthenium-Thorium (Ru3Th7) with Impregnated Ruthenium/Thoria Catalysts. J. Phys. Chem. 1989, 93 (11), 4540–4544. https://doi.org/10.1021/j100348a030.
- (42) Kim, K. S.; Winograd, N. X-Ray Photoelectron Spectroscopic Studies of Ruthenium-Oxygen Surfaces. *Journal of Catalysis* **1974**, *35* (1), 66–72. https://doi.org/10.1016/0021-9517(74)90184-5.
- (43) Meng, A.; Zhang, L.; Cheng, B.; Yu, J. Dual Cocatalysts in TiO<sub>2</sub> Photocatalysis. *Advanced Materials* **2019**, *31* (30), 1807660. https://doi.org/10.1002/adma.201807660.
- Zhang, J.; Yu, Z.; Gao, Z.; Ge, H.; Zhao, S.; Chen, C.; Chen, S.; Tong, X.; Wang, M.; Zheng, Z.; Qin, Y. Porous TiO<sub>2</sub> Nanotubes with Spatially Separated Platinum and CoO<sub>x</sub> Cocatalysts Produced by Atomic Layer Deposition for Photocatalytic Hydrogen Production. *Angew Chem Int Ed Engl* **2017**, *56* (3), 816–820. https://doi.org/10.1002/anie.201611137.
- (45) Lin, H.; Zhang, K.; Yang, G.; Li, Y.; Liu, X.; Chang, K.; Xuan, Y.; Ye, J. Ultrafine Nano 1T-MoS<sub>2</sub> Monolayers with NiO<sub>x</sub> as Dual Co-Catalysts over TiO<sub>2</sub> Photoharvester for Efficient Photocatalytic Hydrogen

- Evolution. *Applied Catalysis B: Environmental* **2020**, 279, 119387. https://doi.org/10.1016/j.apcatb.2020.119387.
- (46) Li, B.; Li, Q.; Gupta, B.; He, C.; Yang, J. Boosting Visible-Light-Driven Catalytic Hydrogen Evolution via Surface Ti<sup>3+</sup> and Bulk Oxygen Vacancies in Urchin-like Hollow Black TiO<sub>2</sub> Decorated with RuO<sub>2</sub> and Pt Dual Cocatalysts. *Catal. Sci. Technol.* **2020**, *10* (23), 7914–7921. https://doi.org/10.1039/D0CY01706J.
- (47) Lin, Y.; Liu, Y.; Li, Y.; Cao, Y.; Huang, J.; Wang, H.; Yu, H.; Liang, H.; Peng, F. Dual Functional  $CuO_{1-x}$  Clusters for Enhanced Photocatalytic Activity and Stability of a Pt Cocatalyst in an Overall Water-Splitting Reaction. *ACS Sustainable Chem. Eng.* **2018**, *6* (12), 17340–17351. https://doi.org/10.1021/acssuschemeng.8b04889.
- (48) Cao, B.; Li, G.; Li, H. Hollow Spherical RuO<sub>2</sub>@TiO<sub>2</sub>@Pt Bifunctional Photocatalyst for Coupled *H*<sub>2</sub> Production and Pollutant Degradation. *Applied Catalysis B: Environmental* **2016**, *194*, 42–49. https://doi.org/10.1016/j.apcatb.2016.04.033.
- (49) Lin, F.; Zhang, Y.; Wang, L.; Zhang, Y.; Wang, D.; Yang, M.; Yang, J.; Zhang, B.; Jiang, Z.; Li, C. Highly Efficient Photocatalytic Oxidation of Sulfur-Containing Organic Compounds and Dyes on TiO<sub>2</sub> with Dual Cocatalysts Pt and RuO<sub>2</sub>. *Applied Catalysis B: Environmental* **2012**, *127*, 363–370. https://doi.org/10.1016/j.apcatb.2012.08.024.
- (50) Jiao, Y.; Jiang, H.; Chen, F. RuO<sub>2</sub>/TiO<sub>2</sub>/Pt Ternary Photocatalysts with Epitaxial Heterojunction and Their Application in CO Oxidation. *ACS Catal.* **2014**, *4* (7), 2249–2257. https://doi.org/10.1021/cs5001174.

# Conclusion and perspectives

In the context of an extension of application of renewable solar energy, photocatalysis appears as a promising technology for converting solar energy into storable chemical energy by water splitting process or for environmental remediation by advanced photocatalytic oxidation reactions. TiO<sub>2</sub> remains one of the most efficient and abundant photocatalyst with non-toxicity, low cost and good chemical stability. However, due to the wide band gap (3.2 eV for anatase), TiO<sub>2</sub> can only absorb photons in the UV region (~5% of the solar spectrum), which limits its overall photocatalytic activity.

In this work we studied the strategy of co-doping with cation-anion combination that has recently been proven, both theoretically and experimentally, effective in broadening the photoresponse of TiO<sub>2</sub> into the visible range. The co-doped materials were prepared via different synthetic methods and applied to promote different types of photocatalytic reactions. In order to boost a specific type of photocatalytic reaction, optimizing the selection of cation-anion is essential. However, so far, the role played by different cation-anion combination in determining the photoelectrochemical properties of the co-doped materials are still unclear. One of the barriers to our understanding of co-doped TiO<sub>2</sub> materials is that the results from different teams are not comparable. Besides the variation of cation-anion combination, different synthetic processes may result in a change in the particle sizes, surface area and phase structure of a specific co-doped photocatalyst, simultaneously influencing its property and photocatalytic performance. Thus, experimental comparative studies are needed to determine the cation-anion combination favorable for different reactions.

In this context, the objective of this thesis was to modify the electronic band structure of TiO<sub>2</sub> photocatalyst by co-doping with transition metals (M=Nb, Ta or W) and nitrogen, aiming at improving visible light response and photocatalytic activity of the (M,N) co-doped TiO<sub>2</sub> materials. In particular, efforts have been put on understanding the effect of the different types of doping/co-doping on the properties of the materials and their activities for specific photocatalytic reactions. By controlling the synthesis parameters, different (M.N) co-doped materials with comparable morphology and crystal structure were produced, allowing us to focus on the effect of co-doping itself.

Chapter 2 focused on the synthesis and characterization of TiO<sub>2</sub> nanoparticles codoped with (Nb,N), which is the most representative cation-anion combination. The emphasis was placed on the role of nitridation in determining the properties and photocatalytic activities for MB degradation of the (Nb,N) co-doped TiO<sub>2</sub> photocatalysts. By comparing the characterization results of the co-doped materials with that of TiO<sub>2</sub>, Nb or N-doped TiO<sub>2</sub>, we have proposed the charge compensation schemes for the different types of doping/co-doping.

By controlling the annealing parameters, TiO<sub>2</sub> and Nb-doped TiO<sub>2</sub> photocatalysts with comparable morphology were successfully prepared via a sol-gel method. Then, the nitrogen was introduced by a thermal nitridation treatment in an ammonia atmosphere to produce N-doped and (Nb,N) co-doped TiO<sub>2</sub>. The XRD results showed that the prepresence of Nb stabilized the anatase phase in the (Nb,N) co-doped samples, while the

nitridation process facilitated the increase of rutile proportion in the N-doped samples. the (Nb,N) co-doped  $TiO_2$  photocatalysts crystallized in pure anatase phase with a small particle size (< 10 nm) and consequently a large specific surface area (~120 m<sup>2</sup>g<sup>-1</sup>).

UV-vis spectroscopy results have shown an important effect of nitridation conditions on the light absorption properties of the N-doped and (Nb,N) co-doped TiO<sub>2</sub>. The mild nitridation produced yellow samples with the visible absorption limited in the region before 550 nm. On the other hand, the harsh nitridation contributed to a dark coloration with the visible absorption extended into longer wavelength (> 550 nm). XPS and EPR results revealed that different doping sites and associated defects are responsible for these two sets of UV-vis spectral characteristics. The mild nitridation process inserted the nitrogen species at the interstitial position in the lattice of NTi-m and 0.25NbNTi-m, and the latter showed a higher amount of nitrogen dopants due to the pre-presence of Nb. For 0.25NbNTi-m, the additional negative charge brought by the N<sup>3-</sup> was compensated by Nb<sup>5+</sup>. For NTi-m, the charge compensation was mainly achieved by V<sub>0</sub><sup>+</sup>. The harsh nitridation process introduced substitutional nitrogen into the TiO2 lattice in addition to the aforementioned interstitial nitrogen, and Ti3+ was proposed to be responsible for the absorption after 550 nm. For both N-doped and (Nb,N) co-doped materials, both V<sub>0</sub><sup>+</sup> and Ti<sup>3+</sup> centers associated with the substitutional nitrogen are involved in the charge compensation mechanism.

Combining the RDB-PAS, EPR and XPS results, we have proposed electronic band structures of the prepared materials. A broader distribution of N 2p states above the VBT was proposed for the (Nb,N) co-doped samples compared to their N-doped counterparts. This could be ascribed to the larger N-dopants amount due to the pre-presence of Nb. On the other hand, the harsh nitridation resulted in a decrease in the PAS signal for 0.25NbNTi-h, indicating that  $Ti^{3+}$  may act as charge recombination centers. Furthermore, we tried to figure out the coordination of Ti and Nb in the lattice of (Nb,N) co-doped  $TiO_2$  with XANES and VTC-XES measurements. The Nb K-edge XES spectra showed that the ligand-dependent peak (K $\beta$ ") evolved with the increasing nitridation temperature. However, the spectral characteristics observed on Ti K-edge are independent of the nitridation conditions. The results indicated that the formation of Nb-N bonds could be more favorable compared to that of Ti-N bonds.

The photocatalytic activities of the prepared materials have been evaluated by conducting photocatalytic degradation of MB under the illumination of UV, visible and simulated solar light (AM 1.5G), respectively. We have found that the nitridation conditions play an important role in determining the photocatalytic activities. Both N-doping and (Nb,N) co-doping enhanced the visible light activities of TiO<sub>2</sub>. For the samples after mild nitridation, 0.25NbNTi-m exhibited the best activity under the illumination of visible light and simulated solar light, which could be attributed to the band gap narrowing due to (Nb,N) co-doping. On the contrary, the samples submitted to harsh nitridation conditions (NTi-h and 0.25NbNTi-h) suffered from deterioration of photocatalytic activities when compared to their counterparts treated under mild conditions, which could be attributed to the generation of Ti<sup>3+</sup> acting as charge recombination centers.

Chapter 3 presents a comparative study aiming at understanding the role of cation in the M-doped and (M,N) co-doped TiO<sub>2</sub> materials (M=Nb, Ta or M). We selected Ta because it is from the same column as Nb in the periodic table, thus we expected similar physicochemical properties between them. W<sup>6+</sup> theoretically brought more positive charge into the TiO<sub>2</sub> lattice, thus more nitrogen was expected to be introduced by the nitridation.

The M-doped samples were synthesized via a sol-gel method as mentioned in Chapter 2. Morphological characterizations showed that all the M-doped  $TiO_2$  present similar spherical morphology as  $TiO_2$ . In a specific M-doped  $TiO_2$  family, the particle size increases with the doping concentration, consequently slightly reducing the BET-specific surface area. An *in-situ* TDXRD technique was applied to reveal the evolution of the crystal structure of a specific M-doped  $TiO_2$  with increasing temperature. The results confirmed an inhibition of phase transition from anatase to rutile due to the M-doping. In a specific M-doped family, the phase transition temperature ( $T_{PT}$ ) increased with the cation doping concentration. For the M-doped  $TiO_2$  doped with different types of cation but with the same doping concentration, the values of  $T_{PT}$  follow the order: W>Ta>Nb. Besides, the observed phase segregation phenomenon indicated a decrease in the cation solubility in the  $TiO_2$  lattice with temperature.

Based on the M-doped TiO<sub>2</sub>, the (M,N) co-doped samples were obtained through a thermal nitridation in ammonia. For each (M,N) family, we have determined the mild and harsh nitridation conditions by a trial-error process to present the yellow and dark samples. respectively. Compared to the M-doping process, modification of the morphology and crystal structure of the (M,N) co-doped samples by the nitridation process is limited. All the (M,N) co-doped TiO<sub>2</sub> materials (M/Ti-0.25) have a similar phase structure, particle size and BET surface area. The XPS results confirmed a successful nitrogen insertion into the (M.N) co-doped TiO<sub>2</sub> through thermal nitridation, and the formation of substitutional nitrogen requires more harsh condition compared to that of interstitial nitrogen. As expected, due to the 6+ charge of W, a larger amount of nitrogen was observed on (W,N) co-doped samples in comparison with the (Nb,N) samples. The EPR results demonstrated a similar doping mechanism between (Nb,N) and (Ta,N) co-doping, in which Ti<sup>3+</sup> was generated under harsh nitridation. As mentioned in Chapter 2, this defect is considered to be responsible for the longer wavelength absorption after 550 nm. However, a different behavior was observed on the (W,N) co-doped samples. No Ti<sup>3+</sup> was generated during the nitridation process regardless of the thermal condition. Instead, W<sup>5+</sup> was generated under the harsh nitridation condition. Thus, the charge compensation scheme for the (W,N) codoping may involve  $V_0^+$ ,  $W^{5+}$  and cation vacancies.

According to the results of UV-vis spectra, the (Ta,N) and (W,N) co-doped samples also present two types of absorption features, as observed on (Nb,N) co-doped samples, depending on the nitridation conditions. Mild nitridation resulted in an increase of visible absorption before 550 nm (yellow color), which is ascribed to N-doping. Harsh nitridation resulted in an increased visible absorption intensity with absorption that appeared after 550 nm (dark color), which is mainly attributed to the generation of defect states in the band gap. Besides, in each (M,N) co-doped family, the visible absorption intensity was observed

to increase with the cation doping concentration, which indicates a promotion of nitrogen doping due to the pre-presence of cation. This promotion effect was proposed to follow the order: W>Nb>Ta, based on the comparison of the visible absorption intensity of the (M,N) co-doped samples treated by the same nitridation condition (350°C 12h). By extending the measurement range into the infrared region, we have observed the absorption peak related to Ti³+ on the (Nb,N) and (Ta,N) co-doped samples after harsh nitridation. For the W-containing samples, an absorption peak at 1300 nm, which might be attributed to W⁵+ was observed. Especially, the signal of W⁵+ is more intense on the (W,N) co-doped sample treated by harsh nitridation. On the other hand, all the (Nb,N) and (Ta,N) co-doped samples show a similar band gap value (~2.5 eV). However, (W,N) co-doping resulted in a further reduced band gap (2.26 eV for 0.25WNTi-m, 2.1 eV for WNTi-h), which may be due to a different distribution of N 2p states or the lower energy of W 5d orbital.

In addition, we have developed an *In-situ* temperature-dependent UV visible spectroscopy technique to visualize the process of N-doping and defect generation for the TiO<sub>2</sub> materials during the thermal treatment. The nitridation process of TiO<sub>2</sub> was successfully transposed into the *in-situ* cell. 390°C and 440°C were determined to present the spectral characteristics as those produced by mild and harsh nitridation, respectively. In the case of M-doped samples, the appearance of the yellow color centers was not observed. Nevertheless, by oxidation process of the (M,N) co-doped samples, we have observed that the defects associated to dark color (Ti<sup>3+</sup>/W<sup>5+</sup>) can be removed by heating the (M,N) co-doped materials in air flow at ~170°C, which is not influenced by the type of cation. On the other hand, the nitrogen doping species related to the yellow color are more thermodynamically stable.

In Chapter 4, the M-doped TiO<sub>2</sub> and (M,N) co-doped TiO<sub>2</sub> discussed in Chapter 3 were used to catalyze three different types of photocatalytic reactions: MB degradation, hydrogen production and water oxidation. The (Nb,N) and (Ta,N) co-doped TiO<sub>2</sub> presented similar photocatalytic behaviors for the degradation of MB, where the nitridation condition significantly influences the resultant photocatalytic activity. Under the UV illumination, the harsh nitridation resulted in a deterioration of photocatalytic activity for the (Nb,N) and (Ta,N) co-doped samples but not for the (W,N) co-doped sample. Combining XPS and EPR results shown in Chapter 3, we have concluded that Ti<sup>3+</sup> acts as charge recombination centers whereas V<sub>O</sub><sup>+</sup> and W<sup>5+</sup> negligibly influence the photocatalytic degradation kinetics. Besides, a decreased degradation rate was observed on all the M-doped TiO<sub>2</sub> compared to the undoped TiO<sub>2</sub>, which is inconsistent with the results in Chapter 2. Considering the higher MB/photocatalyst ratio in the experimental condition in Chapter 4, we proposed that excessive MB molecules may be adsorbed on the surface of the M-doped samples due to their negatively charged surface, as indicated by the zeta potential test. Consequently, the generation of radical species could be slowed down since the corresponding reaction sites may be already occupied by MB molecules (or their degradation products). Actually, by comparing the experimental results in Chapter 4 with those in Chapter 2, we supposed that the activities of all the tested samples were limited to a certain extent due to the aforementioned excessive adsorption of MB.

Then the activities of the prepared photocatalysts were evaluated by catalyzing photocatalytic hydrogen production and water oxidation reactions, respectively. For hydrogen production, Pt NPs were deposited on the sample surface by a photo-reduction method as co-catalyst for enhancing the reaction kinetics. This deposition method produced dispersed Pt NPs with smaller particle sizes compared to the chemical reduction method. The XPS results showed an exclusive oxidation state of Pt<sup>0</sup> for the deposited Pt NPs. It was observed that the surface chemical properties modified by doping/co-doping significantly influence the Pt deposition process. A high concentration of Nb-doping led to a drop in Pt loading, which could be ascribed to the more negative surface charge. On the other hand, the introduction of nitrogen resulted in the aggregation of Pt NPs on the surface of N-doped and (Nb,N) co-doped samples. The photocatalytic results showed a decrease in activity for all the M-doped and (M,N) co-doped samples compared to TiO<sub>2</sub> and N-doped TiO<sub>2</sub>. The possible reason could be the absence of rutile compared to TiO<sub>2</sub> or the downward shift of CBB due to the M-doping.

For water oxidation, extremely fine RuO<sub>x</sub> NPs were photo-deposited on the sample surface as co-catalyst. The experimental results showed that the Nb-doped and Ta-doped samples are more favorable for catalyzing water oxidation, and we did not observe any further increase in oxygen production on the (M,N) co-doped materials. Finally, we demonstrated a prospect of dual co-catalyst deposition for further improving the photocatalytic activity of TiO<sub>2</sub> material used in water splitting. The TiO<sub>2</sub> decorated with Pt and RuO<sub>x</sub> NPs successively was observed more active for water oxidation compared to the one decorated with mono co-catalyst.

Based on the conclusion of this work, several perspectives could be considered in future studies:

- Although we have made efforts to control the calcination and nitridation parameters to ensure a similar phase structure and morphology between different samples, the presence of rutile can not be avoided completely for the undoped TiO<sub>2</sub> and the N-doped TiO<sub>2</sub>. Since the heterojunction constructed with anatase and rutile may facilitate charge separation. The influence of the rutile phase on photocatalytic results, but also the amorphous layer (not taken into account in our case), still remains a debate in the community and requires further study.
- We have discussed the charge compensation scheme for each (M,N) co-doped family. However, the types of involved dopants and defects were mainly determined by XPS and EPR, which are unable to detect cation vacancies. Indeed, considering the high cation doping concentration (M/Ti=0.25) and the limited amount of N dopants (N/M < 0.6), the presence of cation vacancies is highly possible. Thus, we hope that future studies to reveal the effect of cation vacancies on the charge compensation scheme and the photocatalytic activity.
- For a more comprehensive understanding of the band structure of different (M,N) co-doped TiO<sub>2</sub> materials, further characterization should be focused on determining the position of their CBB and VBT. This could help us to better explain the photocatalytic experimental results, especially for hydrogen production reactions.

- Ultraviolet Photoelectron Spectroscopy (UPS) and Mott-Schottky plot by electrochemical impedance spectroscopy measurements could be useful techniques for this purpose.
- Although we successfully synthesized TiO<sub>2</sub> nanoparticles by sol-gel method with a small particle size (~5 nm for TiO<sub>2</sub>; < 12 nm for the doped samples), the SEM/TEM results indicted an agglomeration of TiO<sub>2</sub> nanoparticles, which may limit the charge carrier transfer efficiency and reduce the surface area. This agglomeration might be related to the calcination procedure. Therefore, it is necessary to further optimize the preparation method to promote the dispersion of the nanoparticles as much as possible. The synthetic methods without calcination, such as hydrothermal and sovothermal could be a possible solution.
- In our experiment of hydrogen production and water oxidation, the distribution and loading amount of the co-catalyst was difficult to control. Thus the photocatalytic activity of a specific sample was determined together by the properties of the photocatalyst itself and the co-catalyst NPs mophology. To make the co-catalyst on the surface of M-doped and (M,N) co-doped samples comparable with that of TiO<sub>2</sub>, the photo-deposition method should be optimized. But for this a clear understanding of surface properties of the co-doped sample is necessary. This last point also have a strong influence on the photocatalytic reaction as demonstrated in the case of MB degradation and it will need to be taken more into account.
- Combining co-doping strategy and dual co-catalyst deposition could be an interesting topic for developing advanced TiO<sub>2</sub>-based material used for water splitting. Enhanced activity was already observed on the TiO<sub>2</sub> decorated by Pt and RuO<sub>x</sub> NPs. Further characterization of the dual co-catalyst should be supplemented. The effect of co-catalyst loading, distribution, and oxidation states on the photocatalytic results need to be figured out.

The results presented in this thesis were used for one accepted publication:

Marchal, C., Mary, C., Hammoud, L., Xi, Q., Toufaily, J., Hamieh, T., Suhadolnik, L., Fornasiero, P., Colbeau-Justin, C., Caps, V., Cottineau, T., Keller, V. 2022. A Parametric Study of the Crystal Phases on Au/TiO<sub>2</sub> Photocatalysts for CO<sub>2</sub> Gas-Phase Reduction in the Presence of Water. Catalysts, 12(12), p.1623.

A second one, based on the results of Chapter 2, was submitted in june 2023 to Chemistry of Material and is now under revision.

## Annexes

## Chapter 2

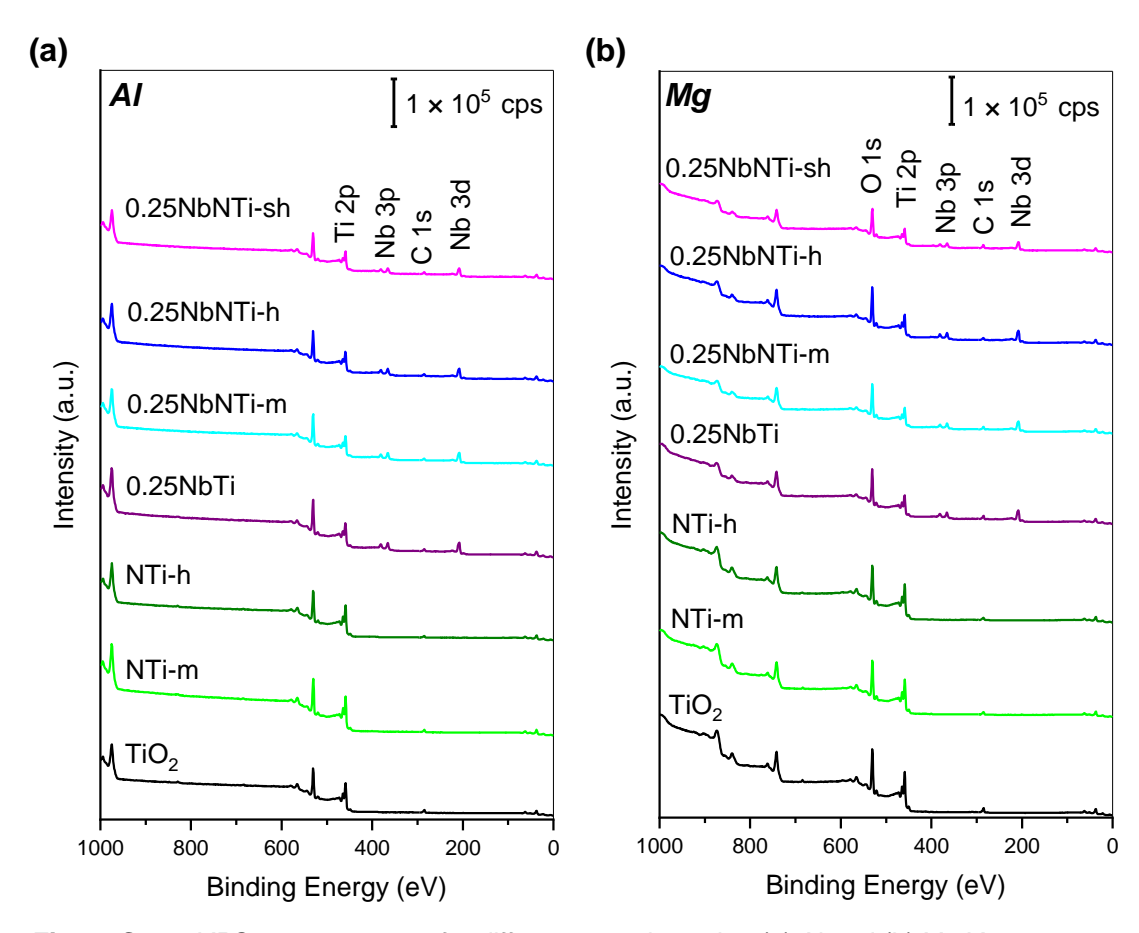
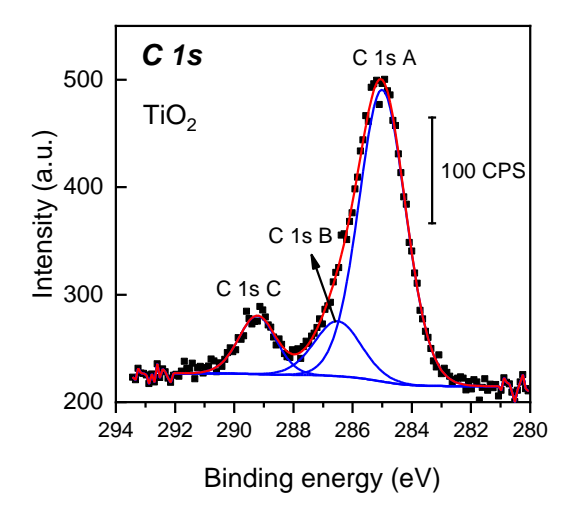


Figure S2.1: XPS survey spectra for different samples using (a) Al and (b) Mg X-ray source.



**Figure S2.2**: XPS spectra of C 1s region for TiO<sub>2</sub>. (Black points are the experiment data, black, blue and red lines are the baseline, the individual peak contributions, and the fitted signals).

Table S2.1: Peak fitting details for XPS related to Figure 2.11 and 2.12.

Sample ID	Ele	ment/Transition	Position	FWH M	Line shape	R.S. F.	% Conc
TiO <sub>2</sub> O	Ti	Ti <sup>4+</sup> 2p <sub>3/2</sub>	459.018	1.42	LF(0.7,0.75,24,240)	5.22	25.4
	0	O 1s-A	530.327	1.47	LF(1,0.9,25,400)	2.93	45.7
	0	O 1s-B	531.653	2.04	LF(1,0.9,25,400)	2.93	10.3
N		$N_{i}$	400.547	2.39	GL(30)	1.8	0.2
Ti	Ti	$Ti^{4+} 2p_{3/2}$	459.239	1.40	LF(0.7,0.75,24,240)	5.22	26.7
NTi-m	0	O 1s-A	530.537	1.44	LF(1,0.9,25,400)	2.93	46.7
IN 11-111	0	O 1s-B	531.785	2.16	LF(1,0.9,25,400)	2.93	12.5
	N	$N_{i}$	400.828	2.37	GL(30)	1.8	0.6
	Ti	$Ti^{4+} 2p_{3/2}$	458.775	1.42	LF(0.7,0.75,24,240)	5.22	27.0
	0	O 1s-A	530.092	1.45	LF(1,0.9,25,400)	2.93	48.4
NTi-h	О	O 1s-B	531.433	2.08	LF(1,0.9,25,400)	2.93	10.8
	NI	$N_{i}$	400.440	3.00	GL(30)	1.8	0.6
	N	$N_{\rm s}$	396.267	2.54	GL(30)	1.8	0.6
	T.	$Ti^{4+} 2p_{3/2}$	459.266	1.49	LF(0.7,0.75,24,240)	5.22	18.0
	Ti	$Ti^{3+} 2p_{3/2}$	457.169	1.34	LF(0.7,0.75,24,240)	5.22	0.8
	NII	Nb <sup>5+</sup> 3d <sub>5/2</sub>	207.748	1.62	LF(1.5,1,25,240)	4.86	6.4
0.25NbTi	Nb	Nb satellite	395.230	4.58	GL(30)		0
	0	O 1s-A	530.548	1.52	LF(1,0.9,25,400)	2.93	42.6
	О	O 1s-B	531.464	2.23	LF(1,0.9,25,400)	2.93	17.0
	N	$N_{i}$	400.676	2.32	GL(30)	1.8	0.2
	Tr:	$Ti^{4+} 2p_{3/2}$	459.106	1.49	LF(0.7,0.75,24,240)	5.22	18.5
	Ti	$Ti^{3+} 2p_{3/2}$	456.834	1.34	LF(0.7,0.75,24,240)	5.22	0.6
O OSNIL NUTE	NIL	$Nb^{5+} 3d_{5/2}$	207.571	1.62	LF(1.5,1,25,240)	4.86	6.7
0.25NbNTi-	Nb –	Nb satellite	395.135	4.61	GL(30)		0
m	0	O 1s-A	530.404	1.55	LF(1,0.9,25,400)	2.93	49.0
		O 1s-B	531.569	2.08	LF(1,0.9,25,400)	2.93	11.3
	N	$N_{i}$	400.635	2.80	GL(30)	1.8	0.8
	Tr:	$Ti^{4+} 2p_{3/2}$	459.204	1.53	LF(0.7,0.75,24,240)	5.22	17.5
	Ti —	$Ti^{3+} 2p_{3/2}$	456.999	1.38	LF(0.7,0.75,24,240)	5.22	1.0
	NII-	$Nb^{5+} 3d_{5/2}$	207.636	1.69	LF(1.5,1,25,240)	4.86	6.6
0.25NbNTi-	Nb —	Nb satellite	395.11	4.60	GL(30)		0
h	0	O 1s-A	530.485	1.57	LF(1,0.9,25,400)	2.93	45.3
		O 1s-B	531.571	2.20	LF(1,0.9,25,400)	2.93	14.3
	NI	$N_{i}$	400.969	2.80	GL(30)	1.8	0.9
	N –	$N_s$	396.771	1.93	GL(30)	1.8	0.4
0.25NbNTi-sh	TD:	$Ti^{4+} 2p_{3/2}$	459.118	1.69	LF(0.7,0.75,24,240)	5.22	18.2
	Ti	Ti <sup>3+</sup> 2p <sub>3/2</sub>	457.015	1.52	LF(0.7,0.75,24,240)	5.22	1.2
	Nb	$Nb^{5+} 3d_{5/2}$	207.532	1.88	LF(1.5,1,25,240)	4.86	5.6
		$Nb^{4+} 3d_{5/2}$	205.672	1.81	LF(1.5,1,25,240)	4.86	0.4
		Nb satellite	395.409	4.60	GL(30)		0
		O 1s-A	530.41	1.58	LF(1,0.9,25,400)	2.93	44.3
	О	O 1s-B	531.684	2.01	LF(1,0.9,25,400)	2.93	11.9
		Ni	400.232	2.50	GL(30)	1.8	0.2
	N	N <sub>s</sub>	396.527	2.11	GL(30)	1.8	1

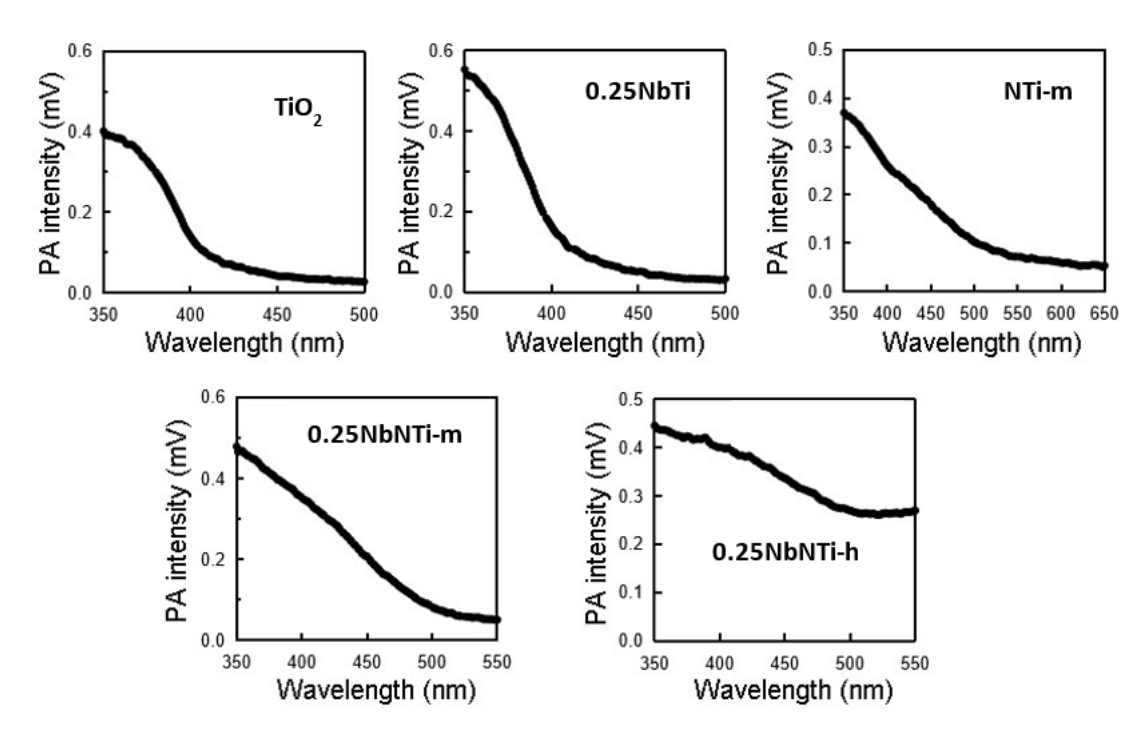


Figure \$2.3: PA spectra for different samples.

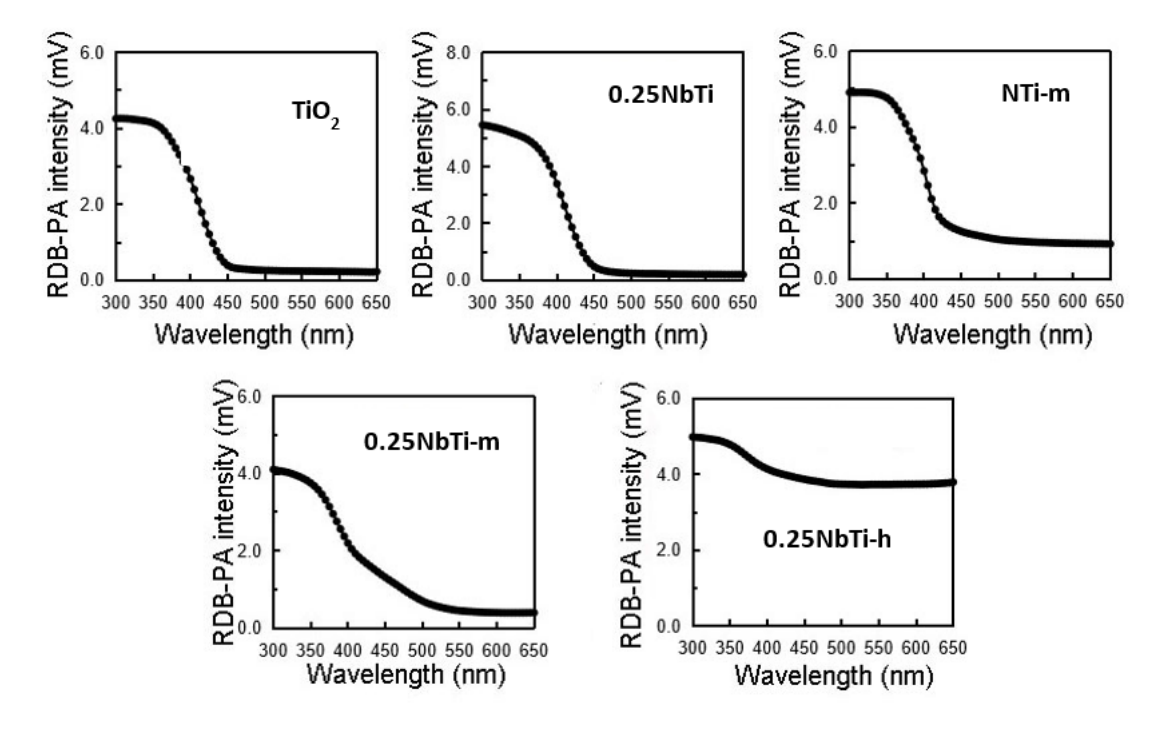


Figure S2.4: RDB-PA spectra for different samples.

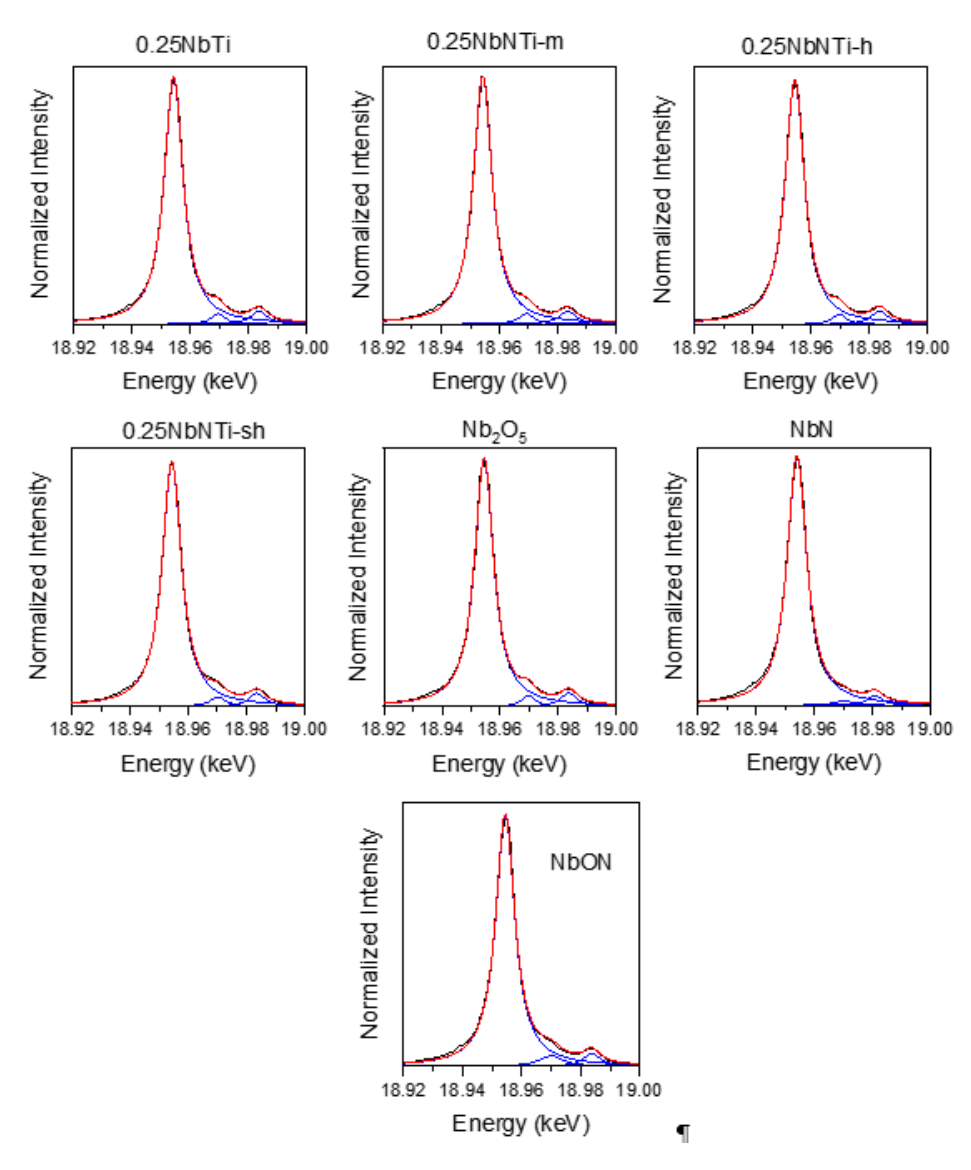


Figure S2.5: Peak fitting for X-ray emission spectra for different samples using Lorentz function.

## Chapter 3

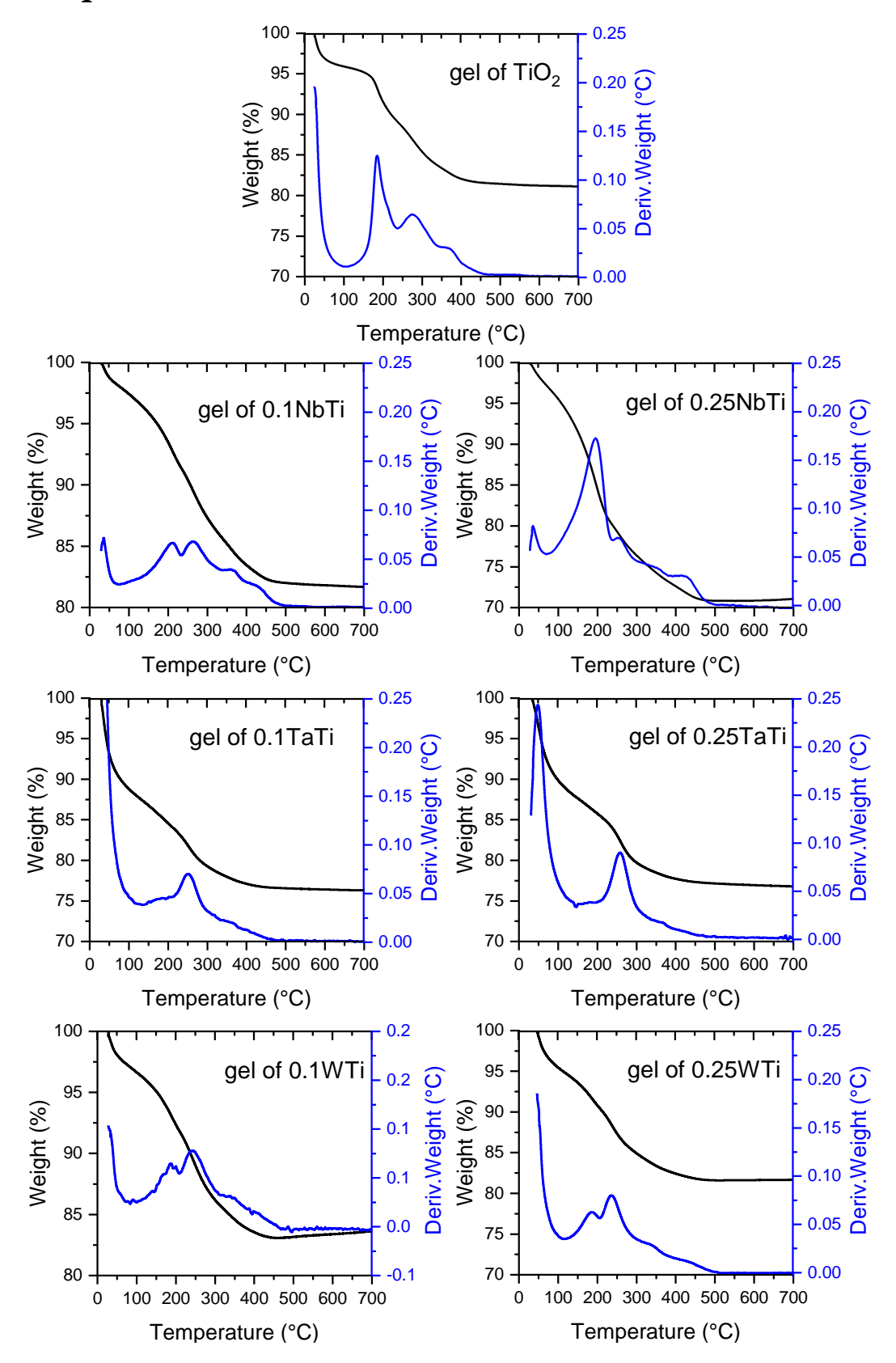


Figure S3.1: Thermogravimetric analysis of the gel of TiO<sub>2</sub> and the M-doped samples.

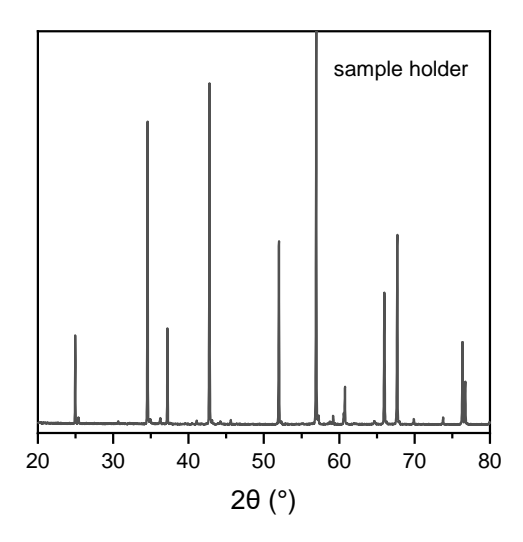
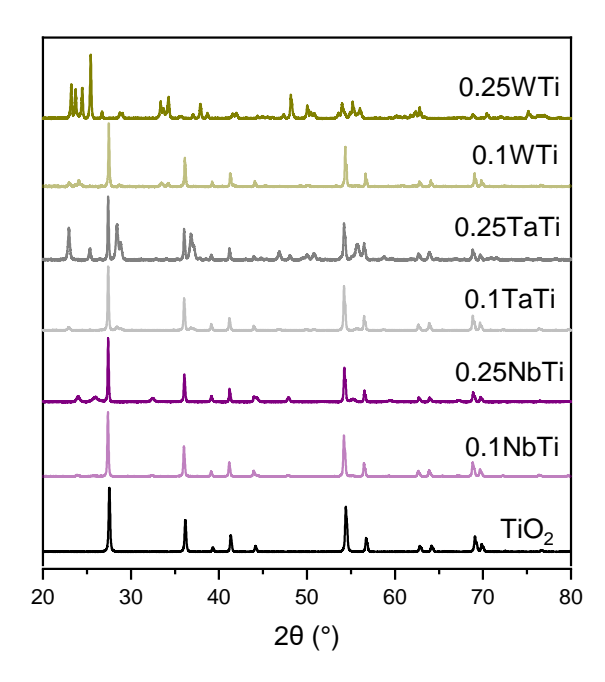
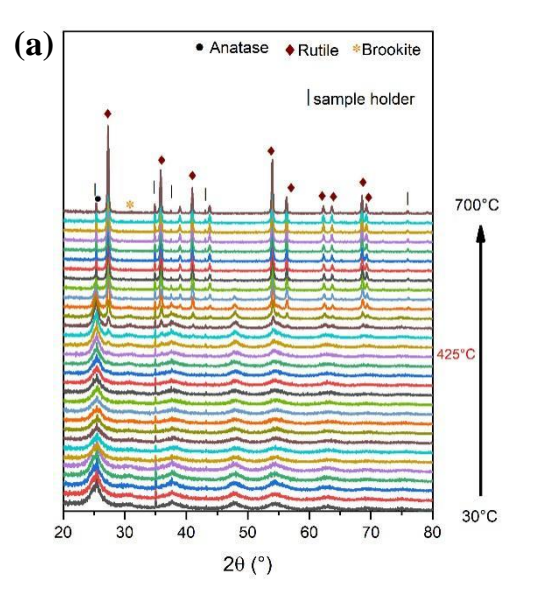
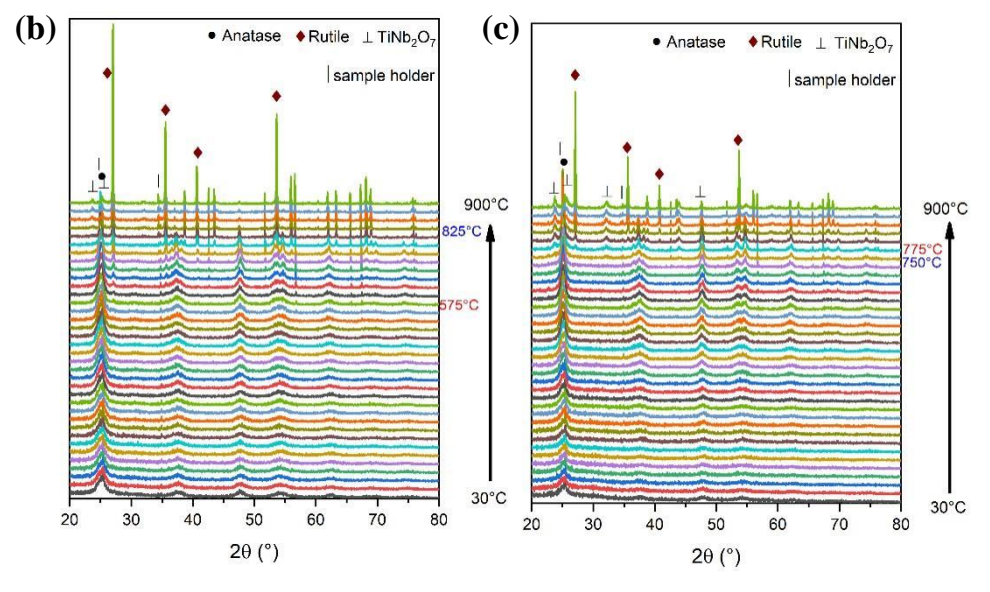


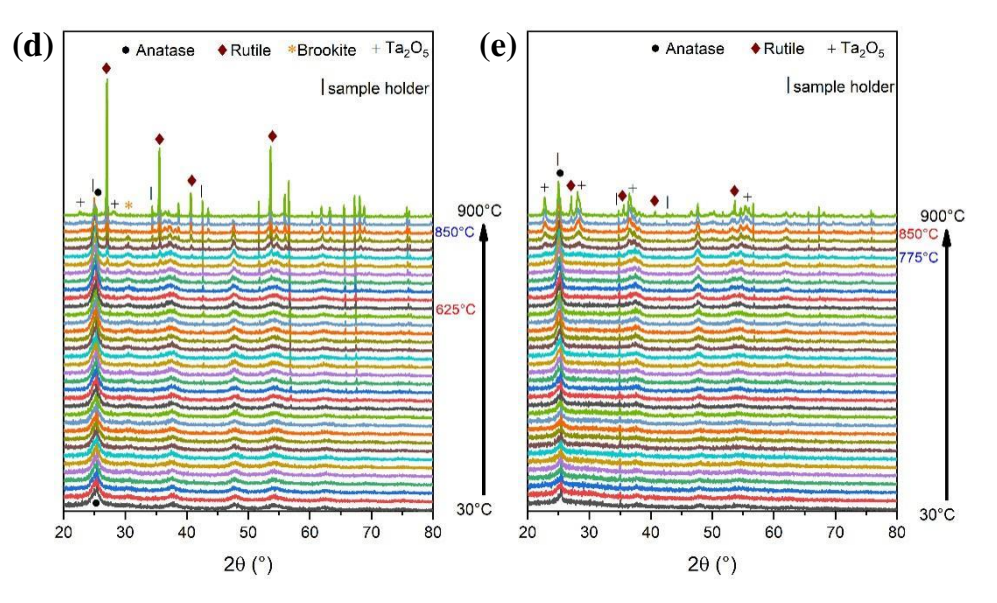
Figure \$3.2: XRD pattern of the sample holder used for the in-situ TDXRD measurement.



**Figure S3.3:** XRD patterns for different samples after the TDXRD measurement recorded again at room temperature.







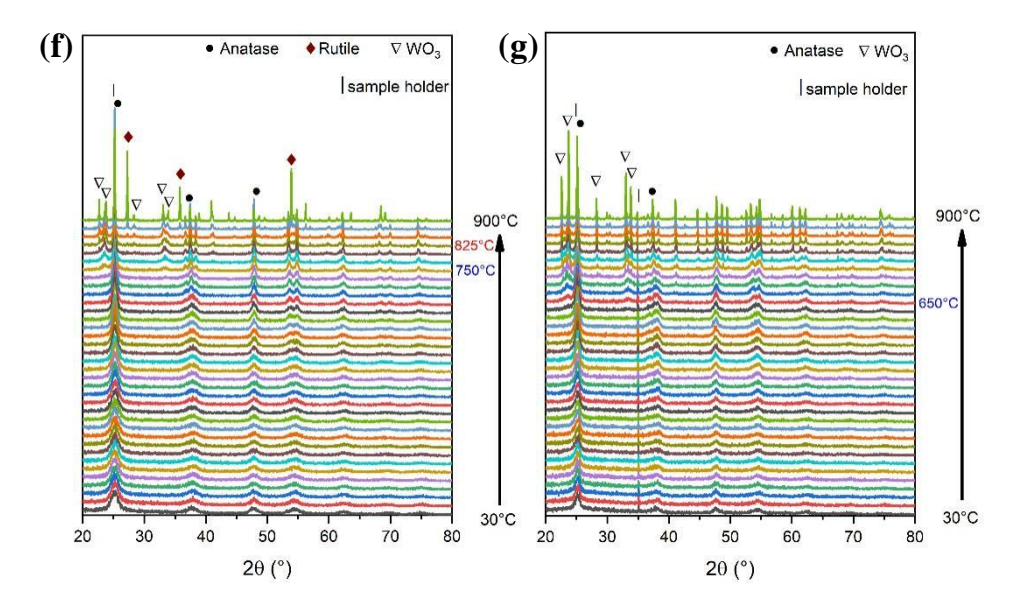


Figure S3.4: The raw TDXRD patterns for different samples stacked with the increase of temperature. (a) for TiO<sub>2</sub>; (b) and (c) for 0.1NbTi and 0.25NbTi; (d) and (e) for 0.1TaTi and 0.25TaTi; (f) and (g) for 0.1WTi and 0.25WTi. The phase transition temperature (T<sub>PT</sub>) is marked in red, and the phase segregation temperature (T<sub>PS</sub>) is marked in blue.

**Table S3.1**: atomic concentrations of the cation and titanium for the cation-doped samples determined by SEM-EDX.

Sample ID	Ti	Nb	Ta	W	cation/Ti
0.1NbTi	90.6	9.4			0.103
0.25NbTi	82.0	18.0			0.220
0.1TaTi	91.7		8.3		0.091
0.25TaTi	82.7		17.3		0.209
0.1WTi	91.4			8.6	0.094
0.25WTi	81.8			18.2	0.222

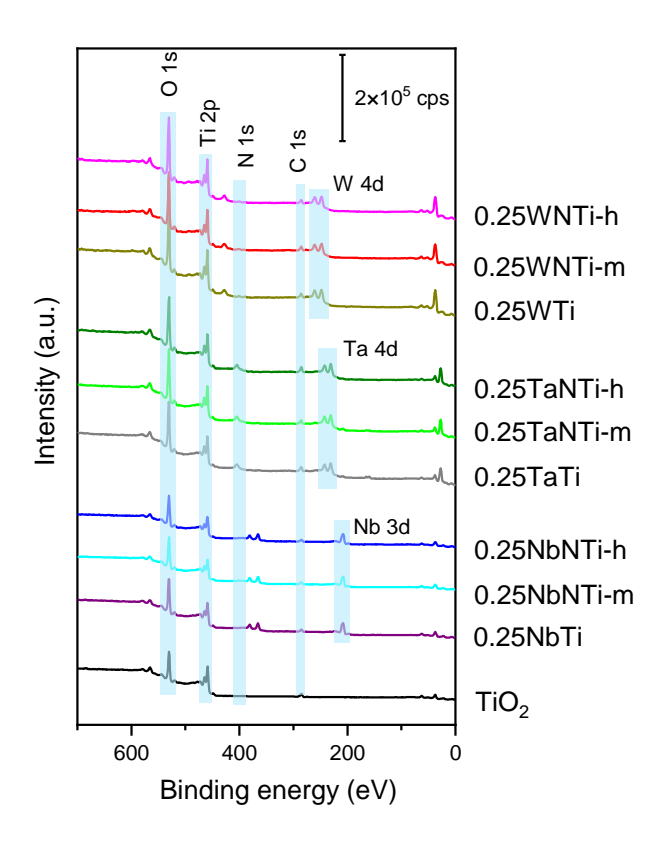
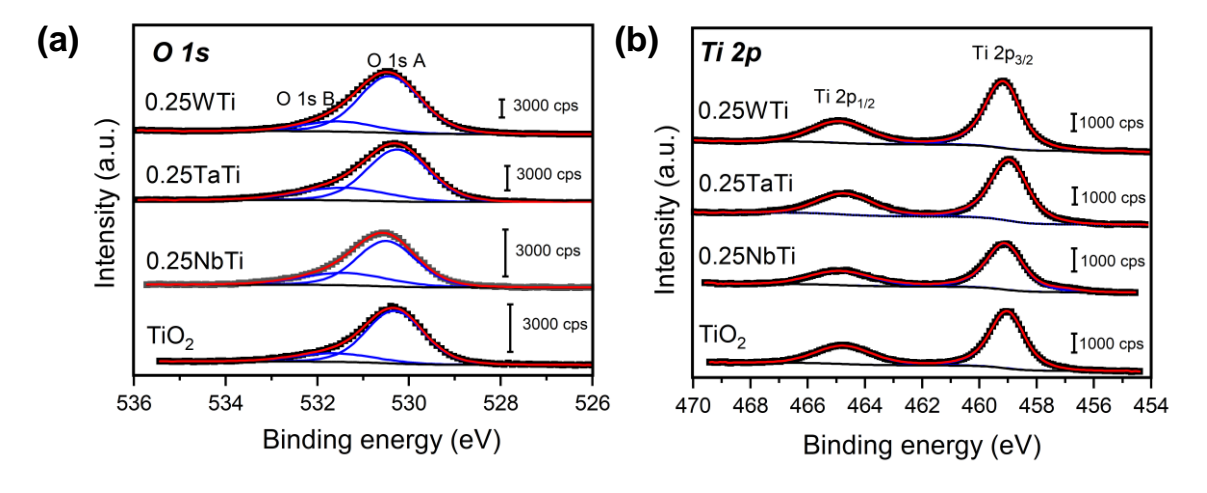


Figure S3.5: XPS survey spectra for different samples discussed in Chapter 3..



**Figure S3.6:** XPS spectra of O 1s (a) and Ti 2p (b) region for TiO<sub>2</sub> and M-doped samples. (Black points are the experiment data, red lines are the fitted signals, blue lines are different contributions).

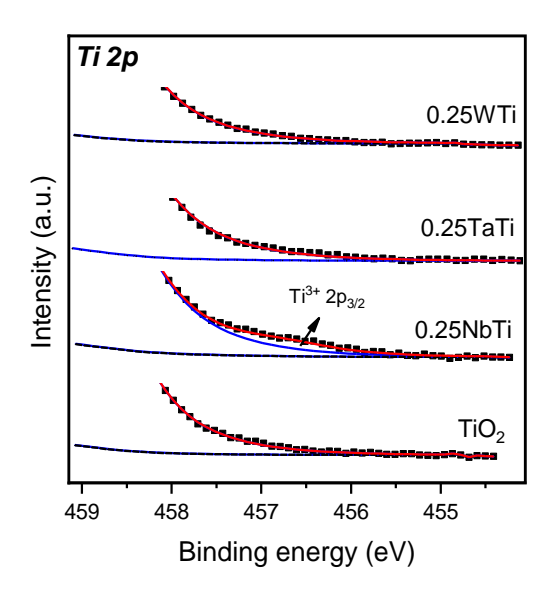
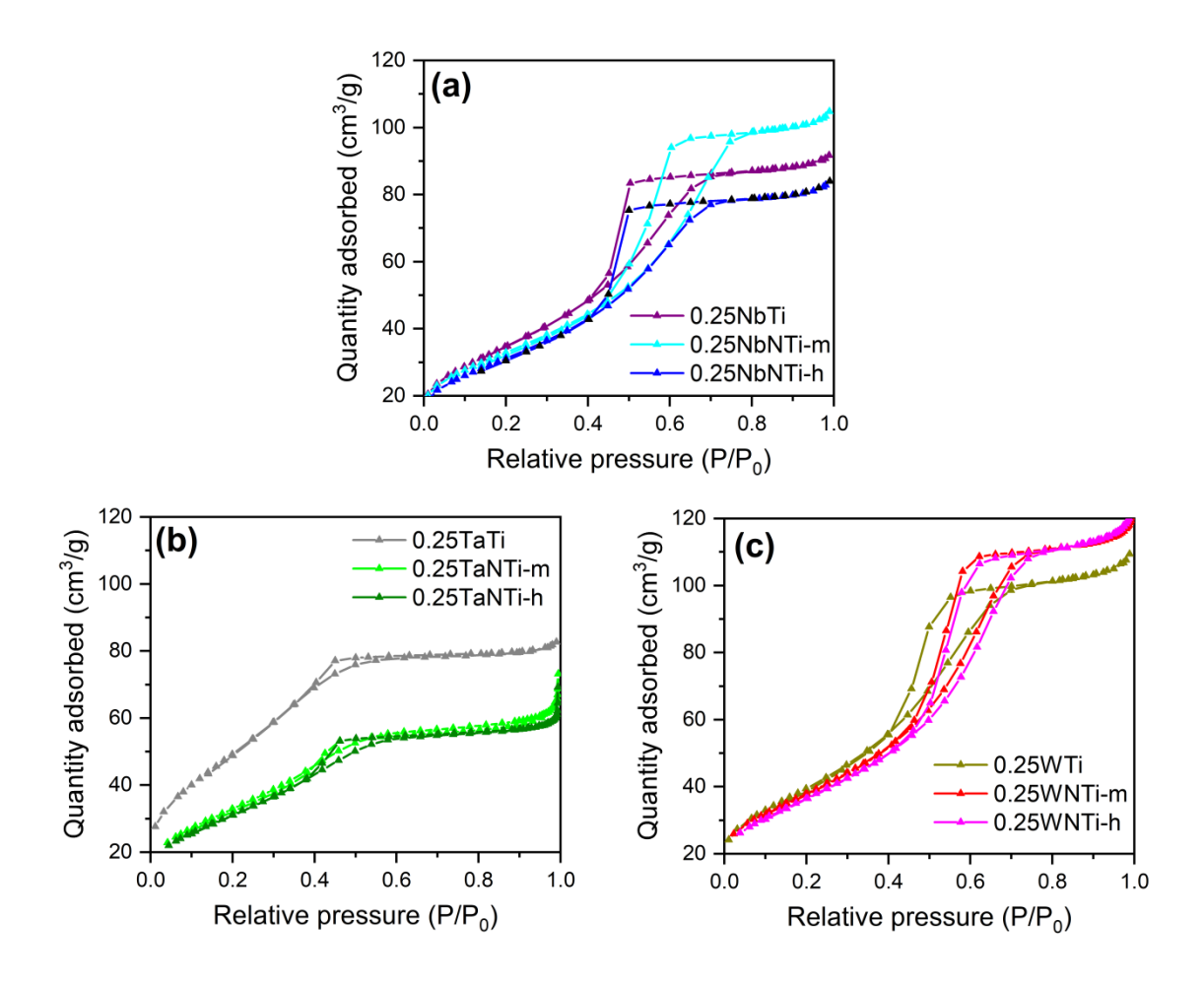
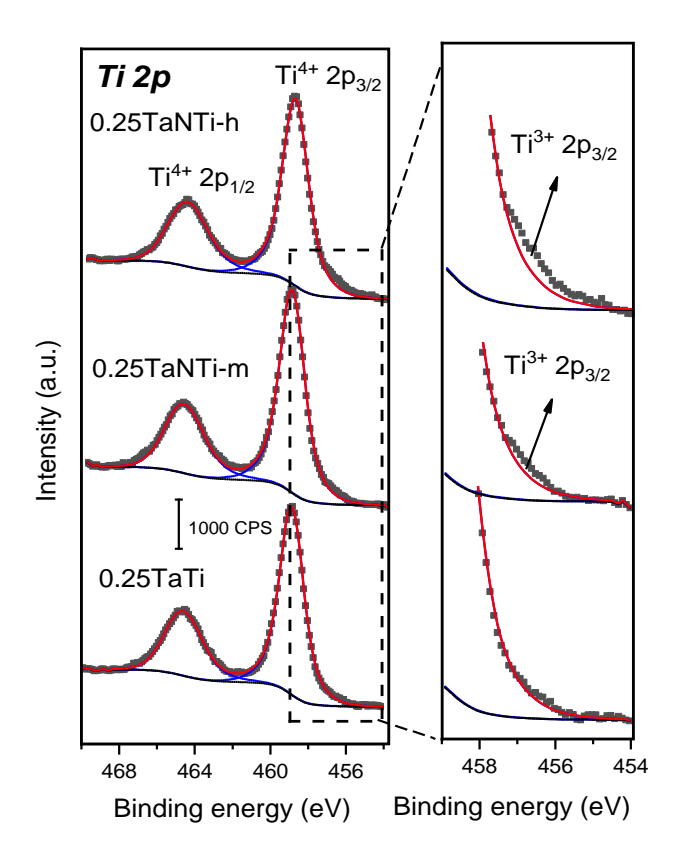


Figure \$3.7: Magnification on the Ti 2p XPS region for the M-doped samples.



**Figure 3.8:** N<sub>2</sub> sorption isotherms for the M-doped and (M.N) co-doped samples: (a) Nb-doped and (Nb,N) co-doped samples. (b) Ta-doped and (Ta,N) co-doped samples. (c) W-doped and (W,N) co-doped samples.



**Figure S3.9:** XPS spectra of Ti 2p region for Ta-doped and (Ta,N) co-doped samples. (Black points are the experiment data, red lines are the fitted signals, blue lines are different contributions).

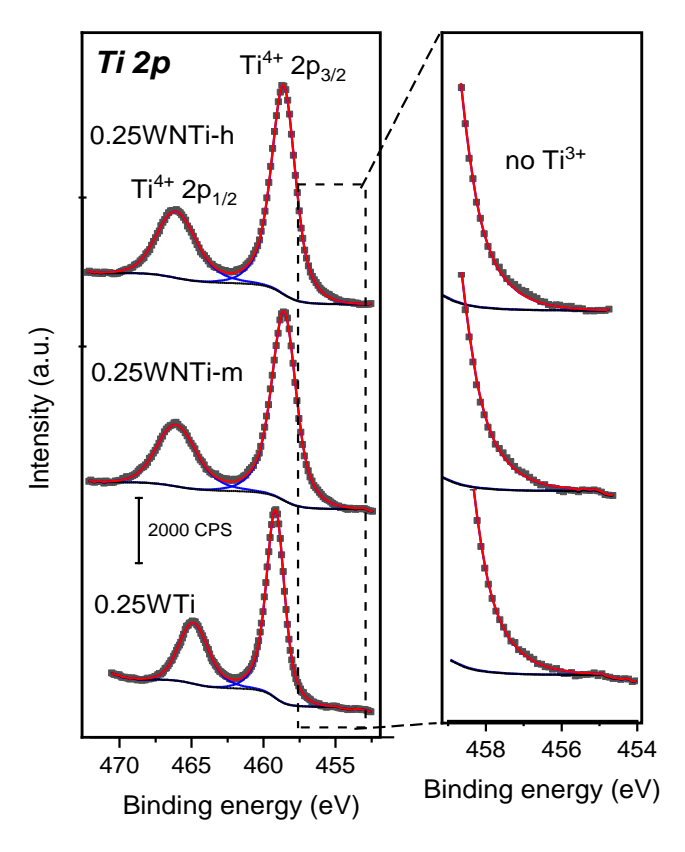


**Figure S3.10:** XPS spectra of Ti 2p region for the W-doped and (W,N) co-doped samples. (Black points are the experiment data, red lines are the fitted signals, blue lines are different contributions).

## Chapter 4

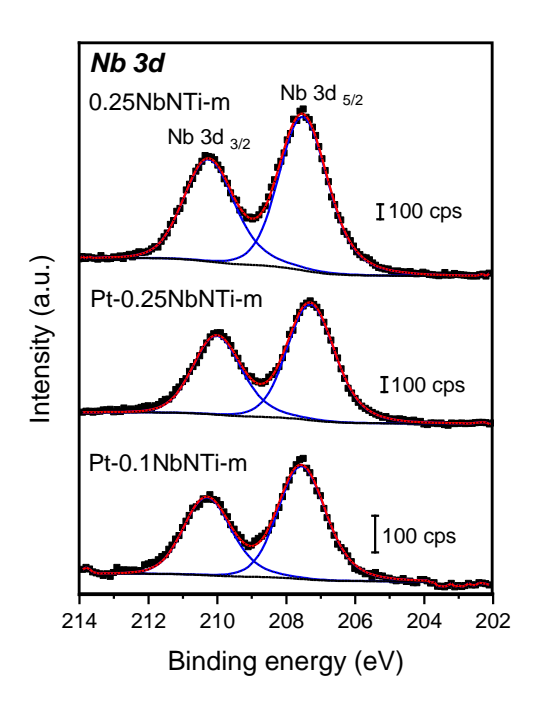


**Figure S4.1:** XPS spectra of Nb 3d region for (Nb,N) co-doped TiO<sub>2</sub> and Pt-deposited (Nb,N) co-doped TiO<sub>2</sub>. (Black points are the experiment data, red lines are the fitted signals, blue and green lines are different contributions).

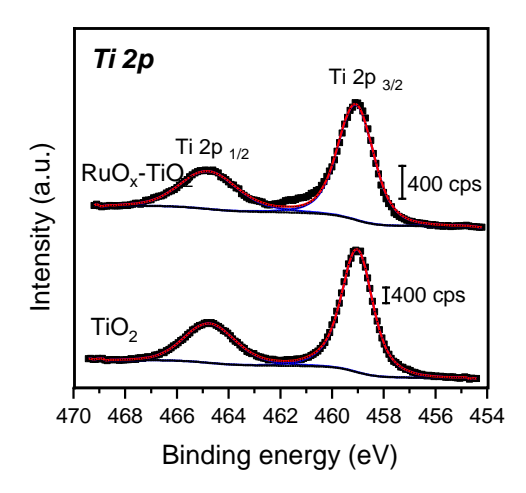


**Figure S4.2:** XPS spectra of Ti 2p for  $RuO_x$ -TiO<sub>2</sub> and TiO<sub>2</sub>. (Black points are the experiment data, red lines are the fitted signals, blue and magenta lines are different contributions).



## **Qingyang XI**



## TiO<sub>2</sub> co-dopé avec des métaux de transition et de l'azote pour la photocatalyse à large spectre activé par la lumière solaire

## Résumé

La photocatalyse est une technologie prometteuse dans le domaine de la conversion de l'énergie solaire, qui peut être utilisée pour l'assainissement de l'environnement et la production de carburant solaire. Dans ce contexte, la thèse présente des travaux visant à développer des photocatalyseurs TiO<sub>2</sub> co-dopés aux métaux de transition (M = Nb, Ta ou W) et à l'azote avec une réponse à la lumière solaire à large spectre.

Des nanoparticules de TiO<sub>2</sub> co-dopées (M,N) ont été synthétisées via une méthode sol-gel suivie d'un processus thermique de nitruration dans une atmosphère d'ammoniac. La présence préalable de cations a favorisé l'insertion de l'azote et augmenté l'absorption de la lumière visible par les matériaux co-dopés. En ajustant les conditions de nitruration thermique, l'absorption visible peut être déplacée dans la région avant 550 nm ou étendue à de plus grandes longueurs d'onde. En comparant les résultats de caractérisation du TiO<sub>2</sub> codopé (Nb,N), (Ta,N) et (W,N), le rôle du cation dans la détermination du processus de dopage N et de la génération de défauts a été étudié. Ensuite les échantillons codopés (M,N) synthetisé avec les differentes conditions de nitruration ont été testé pour la dégradation du MB et les réactions de craquage de l'eau. Dans le premier cas, les résultats on montrées une amélioration de la conversion activée par la lumière visible en particulier pour le TiO<sub>2</sub> co-dopé (Nb,N). D'autre part, les dopants Nb et Ta ont favorisé efficacement l'oxydation photocatalytique de l'eau.

<u>Mots-clés:</u> Photocatalyse, TiO<sub>2</sub> co-dopé, Dégradation, Production d'hydrogène, Oxydation de l'eau.

## Résumé en Anglais

Photocatalysis is a promising technology in the field of solar energy conversion, which can be used for environmental remediation and solar fuel production. In this context, the thesis presents works aiming at developing transition metal (M=Nb, Ta or W) and nitrogen co-doped TiO<sub>2</sub> photocatalysts with broad spectrum solar light response.

(M,N) co-doped TiO<sub>2</sub> nanoparticles were synthesized via a sol-gel method followed by a thermal nitridation process in ammonia. The pre-presence of cation promoted nitrogen insertion and increased visible light absorption of the co-doped materials. By adjusting the nitridation conditions, the visible absorption could be shifted in the region before 550 nm or extended at longer wavelengths. By comparing the characterization results of (Nb,N), (Ta,N) and (W,N) co-doped TiO<sub>2</sub>, the role of cation in determining the N-doping process and defect generation was studied. Co-doped (M,N) samples synthesized with different nitriding conditions were then tested for MB degradation and water-splitting reactions. In the first case, the results showed an improvement in conversion activated by visible light, particularly for (Nb,N) co-doped TiO<sub>2</sub>. On the other hand, the Nb and Ta dopants effectively promoted the photocatalytic oxidation of water.

**Key words:** Photocatalysis, Co-doped TiO<sub>2</sub>, Degradation, Hydrogen production, Water oxidation.